

**INSIGHTS INTO STRUCTURE, DYNAMICS OF THIOREDOXIN
REASSEMBLY AND DYNEIN LIGHT CHAIN 8 AND IONIZATION STATES
OF THIAMIN COFACTOR BY MAS NMR SPECTROSCOPY**

by

Sivakumar Paramasivam

A dissertation submitted to the Faculty of the University of Delaware in partial fulfillment of the requirements for the degree of Doctor of Philosophy in Chemistry and Biochemistry

Spring 2011

Copyright 2011 Sivakumar Paramasivam
All Rights Reserved

UMI Number: 3640294

All rights reserved

INFORMATION TO ALL USERS

The quality of this reproduction is dependent upon the quality of the copy submitted.

In the unlikely event that the author did not send a complete manuscript and there are missing pages, these will be noted. Also, if material had to be removed, a note will indicate the deletion.



UMI 3640294

Published by ProQuest LLC (2014). Copyright in the Dissertation held by the Author.

Microform Edition © ProQuest LLC.

All rights reserved. This work is protected against unauthorized copying under Title 17, United States Code



ProQuest LLC.
789 East Eisenhower Parkway
P.O. Box 1346
Ann Arbor, MI 48106 - 1346

**INSIGHTS INTO STRUCTURE, DYNAMICS OF THIOREDOXIN
REASSEMBLY AND DYNEIN LIGHT CHAIN 8 AND IONIZATION STATES
OF THIAMIN COFACTOR BY MAS NMR SPECTROSCOPY**

by

Sivakumar Paramasivam

Approved:

Klaus H. Theopold, Ph.D.
Chair of the Department of Chemistry and Biochemistry

Approved:

George H. Watson, Ph.D.
Dean of the College of Arts and Sciences

Approved:

Charles G. Riordan, Ph.D.
Vice Provost for Graduate and Professional Education

I certify that I have read this dissertation and that in my opinion it meets the academic and professional standard required by the University as a dissertation for the degree of Doctor of Philosophy.

Signed:

Tatyana Polenova, Ph.D.
Professor in charge of dissertation

I certify that I have read this dissertation and that in my opinion it meets the academic and professional standard required by the University as a dissertation for the degree of Doctor of Philosophy.

Signed:

Cecil Dybowski, Ph.D.
Member of dissertation committee

I certify that I have read this dissertation and that in my opinion it meets the academic and professional standard required by the University as a dissertation for the degree of Doctor of Philosophy.

Signed:

Colin Thorpe, Ph.D.
Member of dissertation committee

I certify that I have read this dissertation and that in my opinion it meets the academic and professional standard required by the University as a dissertation for the degree of Doctor of Philosophy.

Signed:

Alexander J. Vega, Ph.D.
Member of dissertation committee

I certify that I have read this dissertation and that in my opinion it meets the academic and professional standard required by the University as a dissertation for the degree of Doctor of Philosophy.

Signed:

John C. Williams, Ph.D.
Member of dissertation committee

I certify that I have read this dissertation and that in my opinion it meets the academic and professional standard required by the University as a dissertation for the degree of Doctor of Philosophy.

Signed:

Frank Jordan, Ph.D.
Member of dissertation committee

ACKNOWLEDGMENTS

There are a number of people who contributed to my growth and knowledge in the graduate school. I would like to thank all of them in the chronological order I met them.

First of all, I would like to thank my advisor Dr. Tatyana Polenova for giving me an opportunity to join her group as a graduate student and work in the field of biological solid-state NMR spectroscopy. Her constant advice and guidance have helped me a lot in completing this dissertation. The pace with which she thinks of new ideas and executes them with full attention to every detail has always inspired me. Moreover, her broad knowledge in almost all branches of science and engineering and also her unique ability to get to the bottom of the problem quickly is something special and an inspiration for everyone starting in science.

Next I would like to thank Dr. Cecil Dybowski for expanding my knowledge in NMR through multiple discussions and lectures. There were a number of times I went to his office without any prior notice and he was always there to teach me something I could not understand myself. This is a quality which makes him an ideal teacher. I thank him for all his time and also for serving in my dissertation committee. I should also thank him for his wonderful book on NMR spectroscopy, which I used heavily during my course work.

Then I would like to thank Dr. Alexander Vega for being part of our group more than anything else so that we all got a chance to interact with him. His contributions to solid-state NMR are very well-known to everybody in the field. Things that impress me most are his simplicity and ability to look at things from a different viewpoint, not only in NMR but also in life.

Next I thank Dr. Colin Thorpe for being on my dissertation committee. I was also quite lucky that I got a chance to interact with him and his group in the Eggshell membrane project. His excitement at learning and discovering new things has always impressed me.

I would like to thank Dr. John Williams for serving in my dissertation committee and also for the wonderful collaboration on the DLC8 and other related projects. Even though I did not interact much with him directly, I have learnt a lot of NMR from him through some of the classic papers he published in the mid 90s when he was working in solid-state NMR.

I would like to thank Dr. Frank Jordan for joining my dissertation committee on a very short notice during my second committee meeting. I was lucky that I got involved in a collaborative project on solid-state NMR studies of Thiamin between our lab and his group and had a chance to interact with him. I have been truly amazed by his long-standing commitment to improve our understanding of thiamin chemistry.

I thank Dr. Steve Bai for his long-lasting help with the solution NMR measurements. I thank Dr. Olga Dmitrenko for her excellent collaboration on the DFT calculations we used in the thiamin project.

I would like to thank all the present and the past group members of the Polenova group for the wonderful scientific environment they provided over the years. There are too many to name them all. The likes of Wenlin Huang, Shangjin Sun, and Guangjin Hou provided an ideal atmosphere and company to do science. I also thank Vera Vladimirova, not just for her lab management but also for the motherly love and kindness she has for everyone in the group.

Last but not least, I thank Pat McMahon, John Famiglietti, and Jim Draper. Their help with computer and instrument-related problems have been of great value in running our lab efficiently.

I also thank Susan Cheadle for all her help with administrative work.

There are a quite a few people from NMR groups outside UD that I would like to acknowledge. I thank Dr. Benjamin Wylie, and Dr. Trent Franks (from Prof. Chad Rienstra's group at UIUC) for their help with numerical simulations. I also thank Dr. Mikhail Veshtort (Columbia University) for his help with SPINEVOLUTION simulations. I thank Dr. Anand Balakrishnan (Rutgers University) for his collaboration in the thiamin project and also for all the fruitful discussions.

TABLE OF CONTENTS

LIST OF TABLES	xii
LIST OF FIGURES	xiv
ABBREVIATIONS	xxi
ABSTRACT	xxiii
1. GENERAL INTRODUCTION	1
1.1 Structural and Dynamics Studies of Solid Proteins using MAS NMR Spectroscopy	1
1.2 <i>E. coli</i> Thioredoxin	5
1.3 Dynein Light Chain 8	6
1.4 MAS NMR of Ionization States	8
1.5 Scope of the Dissertation	9
1.6 References	11
2. STRUCTURAL STUDIES OF <i>E. COLI</i> THIOREDOXIN REASSEMBLY BY MAS NMR SPECTROSCOPY	13
2.1 Introduction	13
2.2 Experimental Methods	16
2.2.1 Materials	16
2.2.2 Sample Preparation	17
2.2.3 Solid-State NMR Spectroscopy	18
2.3 Results and Discussion	21
2.3.1 DARR Build-up Curves	21
2.3.2 Summary of Distance Constraints	27
2.4 Conclusions	39
2.5 References	40

3.	DYNAMICS STUDIES OF <i>E. COLI</i> THIOREDOXIN REASSEMBLY BY MAS NMR SPECTROSCOPY	42
3.1	Introduction	42
3.2	Experimental Methods	44
3.2.1	Sample Preparation	44
3.2.2	Solid-State NMR Spectroscopy	44
3.2.3	¹⁵ N ROCSA Experiment.....	44
3.2.4	¹⁵ N ROCSA Numerical Simulations.....	46
3.2.5	3D DIPSHIFT Experiment.....	47
3.2.6	R18 ₁ ⁷ Numerical Simulations.....	49
3.2.7	¹⁵ N T ₁ Experiment.....	51
3.2.8	¹³ C- ¹³ C Correlation Spectra at Variable Temperatures.....	53
3.3.	Results and Discussion.....	54
3.3.1	¹⁵ N Chemical Shift Anisotropy.....	54
3.3.1.1	Dynamic Averaging of the ¹⁵ N Chemical Shift Anisotropy	60
3.3.1.2	Secondary Structure Dependence.....	63
3.3.1.3	Effect of Hydrogen Bonding	67
3.3.2	NH Dipolar Order Parameters	71
3.3.2.1	Dynamic Averaging of NH Dipolar Couplings.....	76
3.3.2.2	Comparison with Solution NMR Order Parameters	79
3.3.2.3	NH Bond Lengths and Hydrogen Bonding.....	81
3.3.3	¹⁵ N Longitudinal Relaxation Rates (R ₁).....	81
3.3.4.	Correlation Between Solid-State NH Dipolar Order Parameters and ¹⁵ N R ₁	86
3.3.5	Dynamics on Intermediate Time Scales.....	90
3.4	Conclusions	95
3.5	References	96
4.	MAS NMR STUDIES OF DYNEIN LIGHT CHAIN 8.....	98
4.1	Introduction	98
4.2	Experimental Methods.....	101

4.2.1	Sample Preparation	101
4.2.2	Solid-State NMR Spectroscopy	101
4.2.3	¹⁵ N ROCSA Experiment.....	101
4.2.4	¹⁵ N ROCSA Numerical Simulations.....	102
4.2.5	3D DIPSHIFT Experiment.....	102
4.2.6	NH Dipolar Lineshape Simulations	103
4.2.7	HN-CAHA Dipolar Experiment	104
4.2.8	HN-CAHA Dipolar Lineshape Simulations.....	105
4.3	Results and Discussion.....	110
4.3.1	¹⁵ N Chemical Shift Anisotropy Tensors of Dynein Light Chain 8	110
4.3.2	Solid-State NMR NH Dipolar Order Parameters of Dynein Light Chain 8.....	116
4.3.3	HN-CAHA Dipolar Lineshapes of Dynein Light Chain 8.....	120
4.4	Conclusions	133
4.5	References	134
5.	MAS NMR SPECTROSCOPIC AND DENSITY FUNCTIONAL THEORY STUDIES OF IONIZATION STATES OF THIAMIN.....	137
5.1	Introduction	137
5.2	Experimental Methods	140
5.2.1	Materials	140
5.2.2	Preparation of Solid-State NMR Samples.....	140
5.2.3	Solid-State NMR Spectroscopy	140
5.2.4	¹³ C, ¹⁵ N CSA Numerical Simulations	142
5.2.5	Density Functional Theory Calculations.....	143
5.3	Results and Discussion.....	144
5.3.1	Selective Labeling of Thiamin Analogs.....	144
5.3.2	Assignments of ¹³ C Resonances in Different Ionization States of Thiamin	145
5.3.3	¹³ C and ¹⁵ N Chemical Shift Anisotropy Tensors in Different Ionization States of Thiamin: MAS NMR Spectroscopy	146
5.3.4	¹³ C, ¹⁵ N CSA Tensors in Thiamin Hydrochloride: Density Functional Theory	151

5.3.5	^{13}C , ^{15}N CSA Tensors in Thiamin: Density Functional Theory	153
5.3.6	Relative Orientations of ^{13}C , ^{15}N CSA Tensors in the Thiamin Molecular Frame	157
5.4	Conclusions	159
5.5	References	160
6.	ASSIGNMENT OF IONIZATION AND TAUTOMERIC STATES IN THE THIAMIN DIPHOSPHATE FAMILY OF ENZYMES BY MAS NMR SPECTROSCOPY	162
6.1	Introduction	162
6.2	Experimental Methods	163
6.2.1	Materials	163
6.2.2	Solid-State NMR Spectroscopy	163
6.3	Results and Discussion	164
6.3.1	^{13}C CPMAS NMR on ThDP-Dependent Enzymes	164
6.3.1.1	^{13}C CPMAS NMR Spectra of ThDP-YPDC Complex	164
6.3.1.2	^{13}C CPMAS NMR Spectra of ThDP-E1p Complex	168
6.3.1.3	^{13}C CPMAS NMR Spectra of ThDP-E1o Complex	170
6.3.2	^{15}N CPMAS NMR on ThDP-dependent Enzymes	171
6.3.2.1	^{15}N CPMAS NMR Spectra of ThDP-E1p Complex	172
6.3.2.2	^{15}N CPMAS NMR Spectra of ThDP-YPDC Complex	175
6.4	Conclusions	177
6.5	References	178
	Appendix	180
	PERMISSION LETTERS	181

LIST OF TABLES

Table 2.1	Summary of Inter-Residue Distance Constraints for the C-Terminal Fragment of the U- ¹⁵ N-1-73/U- ¹³ C, ¹⁵ N-74-108-labeled <i>E. coli</i> Thioredoxin Reassembly.....	32
Table 2.1	Summary of Inter-Residue Distance Constraints for the C-Terminal Fragment of the U- ¹⁵ N-1-73/U- ¹³ C, ¹⁵ N-74-108-labeled <i>E. coli</i> Thioredoxin Reassembly (continued).....	33
Table 2.1	Summary of Inter-Residue Distance Constraints for the C-Terminal Fragment of the U- ¹⁵ N-1-73/U- ¹³ C, ¹⁵ N-74-108-labeled <i>E. coli</i> Thioredoxin Reassembly (continued).....	34
Table 2.1	Summary of Inter-Residue Distance Constraints for the C-Terminal Fragment of the U- ¹⁵ N-1-73/U- ¹³ C, ¹⁵ N-74-108-labeled <i>E. coli</i> Thioredoxin Reassembly (continued).....	35
Table 2.1	Summary of Inter-Residue Distance Constraints for the C-Terminal Fragment of the U- ¹⁵ N-1-73/U- ¹³ C, ¹⁵ N-74-108-labeled <i>E. coli</i> Thioredoxin Reassembly (continued).....	36
Table 2.2	Comparison of the Total Number of Inter-Residue Distance Correlations of the C-Terminal Fragment of the U- ¹⁵ N-1-73/U- ¹³ C, ¹⁵ N-74-108-labeled <i>E. coli</i> Thioredoxin Reassembly with few other Uniformly ¹³ C, ¹⁵ N- labeled Proteins reported in the Literature.....	36
Table 3.1	Summary of ¹⁵ N Chemical Shift Parameters for the C-terminal Fragment of U- ¹⁵ N-1-73/U- ¹³ C, ¹⁵ N-74-108-labeled <i>E. coli</i> Thioredoxin Reassembly.....	59
Table 3.2	Summary of the Statistical Mean (±Standard Deviation) of the Backbone Amide ¹⁵ N CSA Parameters of U- ¹⁵ N-1-73/U- ¹³ C, ¹⁵ N-74-108 <i>E. coli</i> Thioredoxin Reassembly as a Function of Secondary Structure Type.....	65

Table 3.3	Summary of the Statistical Mean (\pm Standard Deviation) of the Backbone Amide ^{15}N CS Parameters of U- ^{15}N -1-73/U- ^{13}C , ^{15}N -74-108 <i>E. coli</i> Thioredoxin Reassembly with respect to Hydrogen Bond Interactions.....	69
Table 3.4	Summary of Backbone NH Dipolar Order Parameters for the C-Terminal Fragment of the U- ^{15}N -1-73/U- ^{13}C , ^{15}N -74-108 <i>E. coli</i> Thioredoxin Reassembly.....	75
Table 3.5	Summary of Backbone ^{15}N R_1 values for the C-terminal Fragment of the U- ^{15}N -1-73/U- ^{13}C , ^{15}N -74-108 <i>E. coli</i> Thioredoxin Reassembly.....	86
Table 4.1	Summary of the ^{15}N Chemical Shift Parameters for DLC8.....	116
Table 4.2	Summary of Backbone NH Order Parameters for DLC8.	119
Table 4.3.	Summary of T-MREV-4 HN-CAHA Lineshape Fit Parameters for the 11 Residues of DLC8.	124
Table 4.4.	Comparison of SSNMR Φ Values of DLC8 Residues Against X-ray- and TALOS-Based Values.....	130
Table 5.1	Experimental and Computed J_{CH} Couplings for the 2,6'- ^{13}C /4'- ^{15}N Th•HCl and Th	145
Table 5.2	Experimental and Computed ^{13}C and ^{15}N CSA Parameters for 2,6'- ^{13}C /4'- ^{15}N Th•HCl and Th	149

LIST OF FIGURES

Figure 2.1:	A) Amino acid sequence and secondary structure of <i>E. coli</i> thioredoxin generated by PDBsum using the PDB file 2trx.ent. B) Tertiary structure. The N-terminal fragment is shown in blue; the C-terminus is in yellow. Arg-73 at the cleavage site is represented using the stick representation. (Adapted from ref. [29] with permission).....	16
Figure 2.2:	3D ^{13}C - ^{13}C - ^{13}C (A) and NCACX (B) pulse sequences for inter-residue ^{13}C - ^{13}C correlations. The inter-residue correlations emerge during the 200 ms DARR mixing in both experiments.	20
Figure 2.3:	DARR spectra of U- ^{15}N -1-73/U- ^{13}C , ^{15}N -74-108 <i>E. coli</i> thioredoxin reassembly acquired with (A) 100 ms, (B) 200 ms, (C) 300 ms, and (D) 400 ms. Several representative inter-residue correlations are shown in each spectrum. (Adapted from ref. [30] with permission).....	23
Figure 2.4:	Intensity build-up curves for DARR cross-peaks in U- ^{15}N -1-73/U- ^{13}C , ^{15}N -74-108 <i>E. coli</i> thioredoxin reassembly for (a) one-bond, (b) two-bond, (c) sequential, (d) medium-, (e) long-range correlations. (Adapted from ref. [30] with permission).....	24
Figure 2.5:	Several representative 2D F2-F3 planes of 3D ^{13}C - ^{13}C - ^{13}C (A), and 3D NCACX (B) spectra of U- ^{15}N -1-73/U- ^{13}C , ^{15}N -74-108 <i>E. coli</i> thioredoxin reassembly. The chemical shift of the first nucleus (^{13}C A or ^{15}N) is indicated at the top (F1). Assigned cross peaks correspond to inter-residue correlations.	28
Figure 2.6:	2D ^{13}C - ^{13}C PDS correlation spectrum (aliphatic region) of U- ^{15}N -1-73/U- ^{13}C , ^{15}N -74-108 <i>E. coli</i> thioredoxin reassembly with the mixing time of 500 ms. Assigned cross peaks represent the majority of the inter-residue correlations identified in this work.....	29
Figure 2.7:	2D ^{13}C - ^{13}C PDS correlation spectrum (carbonyl region) of U- ^{15}N -1-73/U- ^{13}C , ^{15}N -74-108 <i>E. coli</i> thioredoxin reassembly with the mixing time of 500 ms. Assigned cross peaks represent the majority of the inter-residue correlations identified in this work.....	30

Figure 3.1:	3D NCA-ROCSA pulse sequence for site-specific ^{15}N CSA recoupling.....	46
Figure 3.2:	3D DIPSHIFT-NCA pulse sequence for site-specific measurements of NH dipolar couplings. NH dipolar recoupling is performed by $R18_1^7$ symmetry-based scheme.	48
Figure 3.3:	Simulation of NH $R18_1^7$ lineshape with i) Model A: only NH dipolar coupling constant (10.83 kHz) ii) Model B: NH DCC and amide proton CSA ($\delta_\sigma = 8$ ppm, $\eta_\sigma = 1.0$, $\beta = 10^\circ$, $\gamma = 0$) iii) Model C: NH DCC and amide proton CSA and T_{2RF} (1.0 ms). In all three cases, the NH dipolar splitting remains the same.	51
Figure 3.4:	3D ^{15}N T_1 -NCA pulse sequence employed for site-specific ^{15}N T_1 measurements of the C-terminal fragment of the U- ^{15}N -1-73/U- ^{13}C , ^{15}N -74-108 <i>E. coli</i> thioredoxin complex. The T_1 relaxation takes place during the τ delay.....	53
Figure 3.5:	The first 2D NCA plane of the 3D ROCSA/NH-dipolar/ R_1 -NCA spectrum. A total of 27 peaks were resolved for the C-terminal fragment of U- ^{15}N -1-73/U- ^{13}C , ^{15}N -74-108 labeled <i>E. coli</i> thioredoxin reassembly.	55
Figure 3.6:	Site-specific backbone amide ^{15}N ROCSA lineshapes encompassing residues I75-A93 of the C-terminal fragment of U- ^{15}N -1-73/U- ^{13}C , ^{15}N -74-108 labeled <i>E. coli</i> thioredoxin reassembly. The experimental lineshapes are in black, the numerical simulations in red.	56
Figure 3.7:	Site-specific backbone amide ^{15}N ROCSA lineshapes encompassing residues L94-N106 of the C-terminal fragment of U- ^{15}N -1-73/U- ^{13}C , ^{15}N -74-108 labeled <i>E. coli</i> thioredoxin reassembly. The experimental lineshapes are in black, the numerical simulations in red.	57
Figure 3.8:	Variation of backbone amide ^{15}N δ_σ as a function of residue number in U- ^{15}N -1-73/U- ^{13}C , ^{15}N -74-108 <i>E. coli</i> thioredoxin reassembly.....	58
Figure 3.9:	Variation of the principal components of the backbone amide ^{15}N CSA tensor as a function of residue number in U- ^{15}N -1-73/U- ^{13}C , ^{15}N -74-108 <i>E. coli</i> thioredoxin reassembly.....	58

Figure 3.10: A histogram of the deviation of the principal components of the ^{15}N CSA tensor for the two secondary structure types from their mean values. The dashed line indicates the mean value over 26 residues in U- ^{15}N -1-73/U- ^{13}C , ^{15}N -74-108 <i>E. coli</i> thioredoxin reassembly.....	66
Figure 3.11: A histogram of the deviation of the principal components of the ^{15}N CSA tensor for hydrogen-bonded and non-hydrogen-bonded residues. The dashed line indicates the mean value over 26 residues in U- ^{15}N -1-73/U- ^{13}C , ^{15}N -74-108 <i>E. coli</i> thioredoxin reassembly.....	70
Figure 3.12: Site-specific backbone amide NH R18 ₁ ⁷ lineshapes encompassing residues I75-A93 of the C-terminal fragment of U- ^{15}N -1-73/U- ^{13}C , ^{15}N -74-108 <i>E. coli</i> thioredoxin reassembly. The experimental lineshapes are in black, the numerical simulations in red. The zero-frequency peak was not included in the fit.....	73
Figure 3.13: Site-specific backbone amide NH R18 ₁ ⁷ lineshapes encompassing residues L94-N106 of the C-terminal fragment of U- ^{15}N -1-73/U- ^{13}C , ^{15}N -74-108 <i>E. coli</i> thioredoxin reassembly. The experimental lineshapes are in black, the numerical simulations in red. The zero-frequency peak was not included in the fit.....	74
Figure 3.14: Variation of backbone NH dipolar order parameter as a function of residue number in U- ^{15}N -1-73/U- ^{13}C , ^{15}N -74-108 <i>E. coli</i> thioredoxin reassembly.	77
Figure 3.15: Comparison of solid-state NH dipolar order parameters with generalized solution order parameters for the C-terminal fragment of U- ^{15}N -1-73/U- ^{13}C , ^{15}N -74-108 <i>E. coli</i> thioredoxin reassembly.....	80
Figure 3.16: ^{15}N T_1 decay curves obtained from the 3D T_1 -NCA experiment in U- ^{15}N -1-73/U- ^{13}C , ^{15}N -74-108 <i>E. coli</i> thioredoxin reassembly. The experimental points were fit to exponential functions.....	84
Figure 3.17: Variation of ^{15}N R_1 values as a function of residue number in U- ^{15}N -1-73/U- ^{13}C , ^{15}N -74-108 <i>E. coli</i> thioredoxin reassembly.....	85
Figure 3.18: Correlation between ^{15}N R_1 and solid-state NH order parameters in the C-terminal fragment of U- ^{15}N -1-73/U- ^{13}C , ^{15}N -74-108 <i>E. coli</i> thioredoxin reassembly.	88

Figure 3.19: Summary of correlation time for fast internal motions using the model-free formalism in U- ¹⁵ N-1-73/U- ¹³ C, ¹⁵ N-74-108 <i>E. coli</i> thioredoxin reassembly	90
Figure 3.20: Overlay of 2D ¹³ C- ¹³ C DARR spectra of U- ¹⁵ N-1-73/U- ¹³ C, ¹⁵ N-74-108 <i>E. coli</i> thioredoxin reassembly at -5 °C (black) and -35 °C (red).	93
Figure 3.21: Intensity variation of DARR cross peaks as a function of temperature for different secondary structure elements of C-terminal fragment of U- ¹⁵ N-1-73/U- ¹³ C, ¹⁵ N-74-108 <i>E. coli</i> thioredoxin reassembly. Reproduced with permission from ref [44].	94
Figure 4.1: Amino acid sequence and secondary structure of <i>Drosophila</i> dynein light chain 8 generated by PDBsum from the X-ray coordinates deposited in the PDB file 2PG1. Residues M1, S2, D3 and R4 are not included.	99
Figure 4.2: 3D HN-CAHA pulse sequence for site-specific backbone torsion angle Φ measurements. ¹ H- ¹⁵ N and ¹ H- ¹³ C dipolar recoupling is performed using the T-MREV-4 scheme.....	105
Figure 4.3: The first 2D NCA plane of the 3D ROCSA (or DIPSHIFT or HN-CAHA)-NCA spectrum of DLC8. A total of 15 cross-peaks were resolved.	112
Figure 4.4: Site-specific backbone amide ¹⁵ N ROCSA lineshapes for 15 residues of DLC8. The experimental lineshapes are in black, the numerical simulations in red.	114
Figure 4.5: Variation of backbone amide ¹⁵ N δ_σ as a function of the residue number.	115
Figure 4.6: Variation of the principal components of the backbone amide ¹⁵ N CSA tensor as a function of the residue number.....	115
Figure 4.7: Site-specific backbone amide NH R18 ₁ ⁷ ROCSA lineshapes for 15 residues of DLC8. The experimental lineshapes are in black, the numerical simulations in red. The zero-frequency peak was not included in the fit.....	118
Figure 4.8: Variation of SSNMR NH dipolar order parameters in DLC8 as a function of the residue number.....	120

Figure 4.9:	Site-specific HN-CAHA dipolar lineshapes for ten residues under analysis in DLC8. The experimental lineshapes are in black, the numerical simulations are in red.....	123
Figure 4.10:	Simulated T-MREV-4 HN-CAHA dipolar lineshapes for varying Φ_H from 10° to 180° . The value of Γ_2 was fixed at 4.0 ms^{-1} . HN and HC dipolar couplings were fixed at their rigid limit values. Note that the T-MREV-4 lineshapes are symmetric with respect to $\Phi_H = 80^\circ$ in the range 30° - 130°	126
Figure 4.11:	RMSD plot of simulated HN-CAHA dipolar lineshape with $\Phi_H = 140^\circ$. The value of Γ_2 is fixed at 2.0 ms^{-1} . NH and CH dipolar couplings were fixed at their rigid limit values.....	128
Figure 4.12:	Comparison of site-specific Φ values of DLC8 determined from solid-state NMR experiments with X-ray and TALOS values	131
Figure 5.1:	Various ionization and tautomerization states of ThDP bound to enzymes. (Adapted from ref. [24] with permission)	138
Figure 5.2:	Chemical structures of Th•HCl and Th with $^{13}\text{C}/^{15}\text{N}$ enrichment at positions C2, C6' and N4'. (Adapted from ref. [24] with permission).....	144
Figure 5.3:	^{13}C ROCSA and slow-MAS spectra of Th•HCl and Th: experimental (black) and simulated (red). (a) ROCSA spectrum of C2 of Th•HCl. (b) ROCSA spectrum of C6' of Th•HCl. (c) Slow-MAS spectrum of C2 and C6' of Th•HCl at 2900 Hz MAS frequency. (d) ROCSA spectrum of C2 of Th. (e) ROCSA spectrum of C6' of Th. (f) Slow-MAS spectrum of C2 and C6' of Th at 2075 Hz MAS frequency. (Adapted from ref. [24] with permission).....	147
Figure 5.4:	^{15}N ROCSA spectra of Th•HCl and Th: experimental (black) and simulated (red). (a) N4' of Th•HCl. (b) N4' of Th. (Adapted from ref. [24] with permission).....	148
Figure 5.5:	Deviation of the A) C6' and B) N4' chemical shift tensor components upon deprotonation from Th•HCl to Th.....	151

- Figure 5.6: Correlation between the principal components δ_{ii} of the calculated (DFT) and the experimental (MAS NMR) chemical shift anisotropy tensors of Th•HCl and Th: (a) ^{13}C of C2 and C6', (b) ^{15}N of 4' with chloride anions, and (c) ^{15}N of N4' without chloride anions. The solid lines in all three figures indicate perfect agreement ($\delta_{\text{cal}} = \delta_{\text{exp}}$), and the dotted lines are the least-square fits: (a) $\delta_{\text{cal}} = 1.05 * \delta_{\text{exp}} - 4.88$, $R^2 = 0.99$, (b) $\delta_{\text{cal}} = 0.94 * \delta_{\text{exp}} + 7.86$, $R^2 = 0.98$; and (c) $\delta_{\text{cal}} = 1.03 * \delta_{\text{exp}} - 20.28$, $R^2 = 0.94$. (Adapted from ref. [24] with permission)..... 156
- Figure 5.7: Structures of Th.HCl (a) and Th (b) used for DFT calculations and depicting orientations of C6' and N4' CSA tensors. For both atoms, the third principal component (δ_{33} for C6', δ_{22} for N4') is perpendicular to 4'-aminopyrimidine plane. (Adapted from ref. [24] with permission)..... 158
- Figure 6.1: ^{13}C CPMAS NMR spectra of YPDC with a) unlabeled ThDP (control spectrum), b) only [$^{13}\text{C}2, ^{13}\text{C}6'$]-ThDP, c) [$^{13}\text{C}2, ^{13}\text{C}6'$]-ThDP and pyruvamide (100 mM). The broad resonance at ~166 ppm is from excess pyruvamide. d) [$^{13}\text{C}2, ^{13}\text{C}6'$]-ThDP and acetyl phosphinate (60 mM). All spectra were acquired at 5 °C with 16,384 transients and 5 s recycle delay..... 166
- Figure 6.2: ^{13}C CPMAS NMR spectra of E1p reconstituted with [$^{13}\text{C}2$]-ThDP or [$^{13}\text{C}2, ^{13}\text{C}6'$]-ThDP. E1p reconstituted with: a) [$^{13}\text{C}2$]-ThDP, b) [$^{13}\text{C}2$]-ThDP and additional 10 mM methyl acetylphosphonate, c) [$^{13}\text{C}2, ^{13}\text{C}6'$]-ThDP and additional 10 mM methyl acetylphosphonate. The spectra were acquired at 15 °C with 16,384 transients and recycle delay was 10 s (spectrum a) and 5 s (spectra b and c)..... 169
- Figure 6.3: ^{13}C CPMAS NMR spectra of *E. coli* 2-oxoglutarate dehydrogenase E1 reconstituted with [$^{13}\text{C}2, ^{13}\text{C}6'$]-ThDP. a) Spectrum acquired at pH 7.0 at 8 °C with 32,768 transients. b) Spectrum acquired at pH 8.0 at 10 °C with 28,900 transient. Recycle delay was 5 s for both spectra..... 171

Figure 6.4:	^{15}N CPMAS NMR spectra of E1p reconstituted with [$^{15}\text{N}4'$]-ThDP at pH 7.0. E1p reconstituted with: a) 3 eq. [$^{15}\text{N}4'$]-ThDP and additional 10 mM methyl acetylphosphonate at $-25\text{ }^{\circ}\text{C}$. b) 3 eq. [$^{15}\text{N}4'$]-ThDP at $-25\text{ }^{\circ}\text{C}$. c) 1 eq. [$^{15}\text{N}4'$]-ThDP at $-23\text{ }^{\circ}\text{C}$. The spectra a sum of 30,720 transients (spectrum a), 16,384 scans (spectrum b), and 14,336 transients (spectrum c); the recycle delay was 5 s. All spectra were processed with 50 Hz exponential broadening.....	173
Figure 6.5:	^{15}N CPMAS NMR spectra of E1p reconstituted with [$^{15}\text{N}4'$]-ThDP at pH 8.0. E1p reconstituted with: a) 3 eq. [$^{15}\text{N}4'$]-ThDP and additional 10 mM methyl acetylphosphonate. b) 3 eq. [$^{15}\text{N}4'$]-ThDP. The spectra were acquired at $-25\text{ }^{\circ}\text{C}$ with 32,768 scans and 5 s recycle delay. Both spectra were processed with 100 Hz exponential broadening.....	174
Figure 6.6:	^{15}N CPMAS NMR spectra of YPDC reconstituted with [$^{15}\text{N}4'$]-ThDP with: a) in the presence of 60 mM acetyl phosphinate. b) in the presence of 300 mM pyruvamide. c) nothing added. The spectra were acquired at $-25\text{ }^{\circ}\text{C}$ with a) 57,344 scans and 4 s recycle delay, b) 23,552 scans with 5 s recycle delay, c) 27, 648 transients with 5 s recycle delay. All spectra were processed with 50 Hz exponential broadening.....	176

ABBREVIATIONS

MAS NMR	Magic Angle Spinning Nuclear Magnetic Resonance
SSNMR	Solid-State Nuclear Magnetic Resonance
<i>E. COLI</i>	<i>Escherichia coli</i>
DLC8	Dynein Light Chain 8
DHC	Dynein Heavy Chain
DIC	Dynein Intermediate Chain
DLIC	Dynein Light Intermediate Chain
DFT	Density Functional Theory
PDB	Protein Data Bank
PEG	Poly ethylene glycol
DARR	Dipolar Assisted Rotational Resoance
PDS	Proton Driven Spin Diffusion
TPPI	Time Proportional Phase Incrementation
TPPM	Two Pulse Phase Modulation
CW	Continuous Wave
SPECIFIC-CP	SPECtrally Induced Filtering In Combination with Cross Polarization
CSA	Chemical Shift Anisotropy
ROCSA	Recoupling Of Chemical Shift Anisotropy
NOE	Nuclear Overhauser Effect
T-MREV	Transverse- Mansfield, Rhim, Elleman, Vaughan

ThDP	Thiamin Diphosphate
AP	Aminopyrimidine
APH+	Aminopyrimidinium
IP	Iminopyrimidine
YI	Ylide
CD	Circular Dichroism
YPDC	Yeast Pyruvate Decarboxylase

ABSTRACT

Magic angle spinning (MAS) NMR spectroscopy has found applications as a versatile technique in chemistry and biochemistry to probe structure and dynamics of materials and biological systems. In recent years, MAS NMR spectroscopy has been rapidly developing as a method for atomic-resolution structural characterization of proteins and protein assemblies that are insoluble and difficult to crystallize. A number of laboratories including ours are working on developments of MAS technologies that would enable analysis of complex biological systems.

In this dissertation, the applications of MAS NMR approaches to two types of problems in structural biology and biochemistry are demonstrated. First, structural and dynamics studies of two proteins, *E. coli* thioredoxin reassembly and dynein light chain 8 (DLC8) in the solid state are carried out yielding atomic-level details, as discussed in Chapters 2, 3, and 4. Second, ionization and tautomeric states of thiamin diphosphate cofactor (ThDP) in large protein, ThDP-dependent family of enzymes are probed using MAS NMR spectroscopy, described in Chapters 5 and 6.

Chapter 1

GENERAL INTRODUCTION

1.1 Structural and Dynamics Studies of Solid Proteins using MAS NMR Spectroscopy

Protein structure is central to its biological function. Proteins must fold rapidly and reliably to a specific structure to carry out their biological tasks. The native, folded conformation of protein molecules is determined by several factors such as their amino acid sequence, intra- as well as inter-molecular interactions, and also the properties of the solvent medium. Knowledge of how proteins perform a particular biological function requires knowledge of their structure. This knowledge relies on appropriate structural biology tools to probe the protein conformation in atomic detail. X-ray crystallography and solution NMR have long been used for the atomic-resolution structure of proteins. However, there are a number of systems, which the two methods cannot address because of their stringent requirements for sample conditions. X-ray crystallography requires long-range molecular order, which is achieved in the crystalline state. However, systems such as membrane proteins, and amyloid fibrils generally do not crystallize and thus are not amenable to X-ray diffraction methods. Solution NMR methods require that the size of the molecule does not exceed a certain limit because of the inherent problems associated with detection of NMR signal with increasing size due to fast spin-spin relaxation causing broadening of resonance lines beyond detection in large proteins.

Solid-state NMR spectroscopy is as an alternative method to both X-ray crystallography and solution NMR spectroscopy. Unlike X-ray crystallography, solid-state NMR spectroscopy does not require long-range order and hence single crystals are not required for structural characterization. In addition, there is no fundamental limitation on the size of the molecule, which makes it suitable for large molecular systems such as proteins and protein assemblies. Notwithstanding the potential of the technique to yield structures of large biological molecules, application of solid-state NMR methods to proteins remained quite limited until recently because of the inherently low resolution of NMR spectra in the solid state.

Magic angle spinning (MAS) is an experimental technique which was designed in the early years of NMR to improve the resolution of solid-state NMR spectra by rapid sample spinning about an axis which is inclined at the angle of 54.74° with respect to the static magnetic field [1,2]. Even though this technique has been known for several decades, only in the last two decades with development of new pulse sequence methods in synchronization with sample spinning [3,4], MAS NMR has matured tremendously to permit applications in characterization of not only biomolecules but also inorganic materials, polymers, glasses and other solids and solid-like systems. With the advent of new sample preparation protocols combined with developments in pulse sequence methodology, the resolution of MAS spectra in solid state is now quite comparable to that of solution NMR spectra. This makes MAS NMR a feasible method for studying uniformly and extensively enriched proteins containing hundreds or thousands of atoms whose frequencies have to be recorded and analyzed.

The first step in any NMR-based protein structural study (either solid or solution) is the resonance assignment, i.e., attribution of each peak in the spectra to a particular atom in the protein molecule. While this process is straightforward for small molecules with a few atoms, it is a tedious and a time-consuming one for macromolecules such as proteins due to overlap of NMR resonances and/or possible ambiguities when amino acid sequence is repetitive. Resonance assignment is quite often the bottleneck in NMR-based protein structure determination protocols. However, recent developments in multidimensional MAS NMR methods have made it possible to resolve the ambiguity with several chemical shift correlation spectra and to assign the resonances of each atom in a residue unequivocally [5,6].

Partial ^{13}C NMR assignments of a protein in the solid state were first reported for uniformly ^{13}C , ^{15}N -labeled BPTI by McDermott et al. in 2000 [7]. Complete structure determination of SH3 domain was reported by Castelani et al. in 2002 by primarily using two-dimensional ^{13}C - ^{13}C NMR on sparsely ^{13}C -labeled samples grown in glycerol medium [8]. Since then, MAS NMR has emerged as a powerful alternative tool to both X-ray crystallography and solution NMR spectroscopy for complete structural characterization of proteins.

One of the main advantages of solid-state NMR in general is its inherent ability to retain the anisotropic nature of the various NMR interactions, which bear important structural information such as inter-atomic distances and details of the local electronic environment at each nuclear site. This anisotropic information is usually lost in solution state due to the molecular tumbling, and hence their measurement is not often straightforward by solution NMR methods.

The direct access of the anisotropic information by a suitable pulse sequence has made MAS NMR a powerful tool to address complex problems in structural biology. For example, structurally important interatomic distances can be directly extracted from dipolar lineshapes [9] or magnetization dephasing trajectories [10]. Similarly, full access to the chemical shift tensor by MAS NMR methods has made it a unique tool to characterize several important biomolecular properties of proteins such as hydrogen bonding interactions and secondary structure type in terms of CSA tensors of the appropriate nuclei. In particular, it is now possible to make reliable predictions of protein secondary structure on a per-residue basis with the isotropic chemical shifts of backbone nuclei [11].

NMR based methods are not only important for structural studies, but also provide dynamics information. In this respect, both solution and solid-state NMR complement X-ray crystallography, with the latter mainly being used for studies of static structures. In particular, solid-state NMR can probe internal dynamics of proteins directly in the absence of overall rotational Brownian tumbling motion, which overrides the internal motion in the solution state. MAS NMR can probe dynamic processes on a wide range of time scales from picoseconds to seconds [12]. The dynamical information is obtained by probing the various anisotropic lineshapes, couplings, and relaxation rates. With these measurements combined with appropriate theoretical formalisms [13,14], both the amplitude and the time scale of the internal motion can be determined on a per-residue basis in a protein.

Despite these inherent capabilities of MAS NMR methods, there have been only a few reports in the literature on structural and dynamics studies of proteins using MAS NMR. In particular, MAS NMR studies of uniformly labeled samples are

notably scarce [15-17]. Uniformly labeled systems present a number of technical challenges such as severe spectral overlap and the complicated spin dynamics due to multi-spin couplings. Hence, methodology development and applications are particularly necessary to circumvent the technical challenges and set the protocols for MAS NMR characterization of uniformly labeled protein samples.

With this overall goal, we have applied MAS NMR spectroscopy to the structural and dynamics studies of two uniformly labeled protein systems; one of them is differentially enriched *E. coli* thioredoxin complex and the other is dynein light chain 8 DLC8, a subunit of dynein complex. The biological roles of these two proteins are summarized in the following sections.

1.2 *E. coli* Thioredoxin

Thioredoxin is a ubiquitous, multifunctional protein. It is responsible for redox regulation of protein function and signaling via the thiol redox center. Thioredoxins from different organisms possess conserved active site residues C-G-P-C forming a disulfide bridge in the oxidized form (thioredoxin-S₂), which is reduced by NADPH and the flavoprotein thioredoxin reductase to form thioredoxin-(SH₂) containing two thiol groups. Thioredoxin-(SH₂) is a powerful protein disulfide reductase, and thioredoxin catalyzes dithiol-disulfide exchange reactions.

E. coli thioredoxin is a 108- amino acid residue protein. The crystal structure of the oxidized form of the protein as the Cu²⁺ complex has been solved by Katti et al. at 1.68 Å resolution [18]. No crystal structure has been obtained for the reduced form of *E. coli* thioredoxin. Solution NMR has been applied to study both oxidized and reduced forms. Dyson et al. [19] reported the solution NMR structure of the reduced *E. coli* thioredoxin, which was found to be similar to the X-ray structure of the

oxidized form with differences in the local conformation of the active site loop. It was concluded that the subtle differences in the active site conformation have important implications for the mechanism of thioredoxin as protein disulfide oxidoreductase. Stone et al. [20] reported a detailed comparative study of backbone dynamics in the oxidized and the reduced form by solution NMR spectroscopy. The results indicated that both forms exhibit almost identical dynamics behavior on the picosecond to nanosecond time scale.

One of the interesting properties of *E. coli* thioredoxin is that it reassembles to form a noncovalent complex in vitro from the complementary fragments, with a preserved tertiary structure displaying minor conformational adjustments near the cleavage sites [21]. Recently, Yang et al. used differentially enriched *E. coli* thioredoxin reassembly cleaved at R73 to develop MAS NMR methods for structural characterization of intermolecular interfaces [15]. With its interesting properties, a wide range of biological functions, and a thermodynamically stable three dimensional structure, *E. coli* thioredoxin presents an excellent model protein for the application of new MAS NMR methodologies in structural and dynamics investigations using uniform labeling.

1.3 Dynein Light Chain 8

Cargo transport inside a cell is primarily driven by three classes of motor proteins; kinesin, dynein, and myosin. These motor proteins move along the polymeric cytoskeletal structures, microtubules (kinesin and dynein) and actin (myosin), by successive binding and unbinding, powered by energy derived from the hydrolysis of ATP. Microtubules are polar, with their minus ends situated close to the nucleus. The plus ends spread outward from the cell center in a radial organization. Kinesin-class

motors move toward the plus-end of the microtubule and thus bring cargo toward the cell periphery. In contrast, dynein motors move toward the minus-end of the microtubule and hence are used to move cargo toward nucleus. While kinesin and myosin have been proposed to be robust and highly efficient transporters, dynein tries to achieve the same level of efficiency with the help of other protein complexes such as dynactin [22]. The architecture of cytoplasmic dynein is quite complex and the molecular weight of the complex is 2 MDa. Dynein complex consists of heavy chains (DHCs), intermediate chains (DICs), and several light chains (DLCs). The DHCs bind to the microtubule and are responsible for the motor activity. Dynein motor activity can be regulated either directly or indirectly. For example, phosphorylation of its partner protein dynactin has been reported to influence dynein's ATPase activity [23]. Removal of DIC from rat testis leads to four-fold enhancement of ATPase activity [24]. Thus DICs act as a negative regulator of the motor activity. The dynein light chains (DLC) are also involved in a number of regulatory functions of the dynein complex. In addition to being an integral part of the dynein complex, DLCs also bind to a number of other proteins. This observation led to the hypothesis that DLCs might play an important role in directing the dynein complex to various cellular cargo. However, recent X-ray studies have shown that DLCs do not bind to the cargo [25].

The large molecular weight of dynein complex makes it prohibitive for solution NMR characterization. Moreover, the complexes of dynein and dynactin with microtubules cannot be crystallized and, hence, the use of X-ray crystallography is also quite limited in expanding our knowledge of the dynein motor activity on the microtubules, which is not yet completely understood.

In this respect, MAS NMR is a viable alternative to study the dynein complex as well as dynein-dynactin-microtubule interactions. As a first step, we apply MAS NMR methods to study details of structural and backbone dynamics of the 89-residue DLC8 subunit of dynein. Recently, our group (Sun et al.) has studied the CAP-Gly domain of mammalian dynactin and its interaction with paclitaxel-stabilized microtubules at atomic-level detail [26]. The long-term goal of these studies in our laboratory is to expand MAS NMR methods to other integral parts of the dynein, as well as to dynactin complexes, with the aim to achieve atomic-level understanding dynein's motor activity and its binding to cellular cargo.

1.4 MAS NMR of Ionization States

Acid/base reactions are of great importance in every branch of chemistry and biochemistry. In particular, knowledge of the pK_a of ionizable groups is crucial in understanding the structure-function relationships of proteins and other biomolecules [27]. Moreover, the ionization state of a functional group strongly influences many of the drug-receptor interactions. Despite the significance of knowledge of ionization states, methods to assign charges for ionizable groups such as carboxyl, amino, and imidazole groups are still difficult in proteins.

NMR chemical shift parameters are exquisitely sensitive to the protonation state of ionizable groups [28]. Isotropic chemical shifts measured by solution NMR methods have long been used for the determination of pK_a of amino acids, proteins, ligands and other molecules containing acidic or basic groups. However, as in the case of carboxylate groups of amino acids, the changes in the isotropic chemical shift between protonated and deprotonated states are sometimes rather small and quite difficult to detect [29]. In contrast, solid-state NMR can measure the full chemical

shift tensor of ionizable groups both in protonated and deprotonated states and thus all three principal components of the chemical shift tensor can be used for characterization of ionization states.

Thiamin diphosphate (ThDP) is an important cofactor in sugar metabolism and it interconverts between various ionization and tautomeric states during the catalytic cycle of the enzyme [30,31]. Not all of these ionization or tautomeric states have been completely characterized by spectroscopic methods. Defining proton positions with X-ray crystallography is not possible. The large molecular weight of ThDP-dependent enzymes on the order of 160-250 kDa excludes the possibilities of chemical shift measurements using solution NMR methods. Hence MAS NMR is an attractive method to characterize the various ionization and tautomeric states of ThDP in complex with enzymes with full access to chemical shift anisotropy tensors of the key atoms.

1.5 Scope of the Dissertation

This thesis work is broadly focused on the application of MAS NMR methods to the following problems:

- i) structural and dynamics studies of uniformly labeled proteins in the solid state;
- ii) characterization of ionization and tautomeric states of thiamin diphosphate.

A brief outline of the following chapters is given below.

In chapter 2, structural studies of U-¹⁵N-1-73/¹⁵N-¹³C-74-108 of *E. coli* thioredoxin reassembly using MAS NMR correlation methods are presented.

In chapter 3, internal backbone dynamics of U-¹⁵N-1-73/¹⁵N-¹³C-74-108 of *E. coli* thioredoxin reassembly studied by MAS NMR are discussed in terms of site-

specific backbone amide ^{15}N CSA tensors, amide NH dipolar lineshapes, and amide ^{15}N longitudinal relaxation rates.

In chapter 4, internal backbone dynamics studies for a select number of residues of dynein light chain 8 is presented with site-specific backbone amide ^{15}N CSA tensors, amide NH dipolar lineshapes. A site-specific backbone torsion angle ϕ measurement is reported using HN-CAHA correlated dipolar lineshapes.

In chapter 5, two of the ionization states (aminopyrimidine and aminopyrimidinium) of thiamin diphosphate are characterized in terms of the full ^{15}N and ^{13}C chemical shift anisotropy parameters of the key atoms, using MAS NMR and density functional theory (DFT) methods.

In chapter 6, MAS NMR is applied to elucidate the ionization and tautomeric states of thiamin diphosphate in three enzyme systems (yeast pyruvate decarboxylase, the E1 component of the pyruvate, and 2-oxoglutarate dehydrogenase complexes from *Escherichia coli*).

1.6 References

- (1) Andrew, E. R.; Bradbury, A.; Eades, R. G. *Nature* **1959**, *183*(4678), 1802-1803.
- (2) Lowe, I. J. *Phys. Rev. Lett.* **1959**, *2*(7), 285-287.
- (3) Lee, Y. K.; Kurur, N. D.; Helmle, M.; Johannessen, O. G.; Nielsen, N. C.; Levitt, M. H. *Chem. Phys. Lett.* **1995**, *242*(3), 304-309.
- (4) Bennett, A. E.; Rienstra, C. M.; Auger, M.; Lakshmi, K. V.; Griffin, R. G. *J. Chem. Phys.* **1995**, *103*(16), 6951-6958.
- (5) Baldus, M.; Petkova, A. T.; Herzfeld, J.; Griffin, R. G. *Mol. Phys.* **1998**, *95*(6), 1197-1207.
- (6) Takegoshi, K.; Nakamura, S.; Terao, T. *Chem. Phys. Lett.* **2001**, *344*(5-6), 631-637.
- (7) McDermott, A.; Polenova, T.; Bockmann, A.; Zilm, K. W.; Paulsen, E. K.; Martin, R. W.; Montelione, G. T. *J. Biomol. NMR* **2000**, *16*(3), 209-219.
- (8) Castellani, F.; van Rossum, B.; Diehl, A.; Schubert, M.; Rehbein, K.; Oschkinat, H. *Nature* **2002**, *420*(6911), 98-102.
- (9) Zhao, X.; Eden, M.; Levitt, M. H. *Chem. Phys. Lett.* **2001**, *342*(3-4), 353-361.
- (10) Gullion, T.; Schaefer, J. *J. Magn. Reson.* **1989**, *81*(1), 196-200.
- (11) Cornilescu, G.; Delaglio, F.; Bax, A. *J. Biomol. NMR* **1999**, *13*(3), 289-302.
- (12) Krushelnitsky, A.; Reichert, D. *Prog. NMR Spec.* **2005**, *47*(1-2), 1-25.
- (13) Lipari, G.; Szabo, A. *J. Am. Chem. Soc.* **1982**, *104*(17), 4546-4559.
- (14) Lipari, G.; Szabo, A. *J. Am. Chem. Soc.* **1982**, *104*(17), 4559-4570.
- (15) Yang, J.; Tasayco, M. L.; Polenova, T. *J. Am. Chem. Soc.* **2008**, *130*(17), 5798-807.
- (16) Li, S.; Zhang, Y.; Hong, M. *J. Magn. Reson.* **2010**, *202*(2), 203-10.
- (17) Lange, A.; Becker, S.; Seidel, K.; Giller, K.; Pongs, O.; Baldus, M. *Angew. Chem. Int. Ed.* **2005**, *44*(14), 2089-92.
- (18) Katti, S. K.; LeMaster, D. M.; Eklund, H. *J. Mol. Biol.* **1990**, *212*(1), 167-84.
- (19) Dyson, H. J.; Gippert, G. P.; Case, D. A.; Holmgren, A.; Wright, P. E. *Biochemistry* **1990**, *29*(17), 4129-4136.
- (20) Stone, M. J.; Chandrasekhar, K.; Holmgren, A.; Wright, P. E.; Dyson, H. J. *Biochemistry* **1993**, *32*(2), 426-435.
- (21) Yu, W. F.; Tung, C. S.; Wang, H.; Tasayco, M. L. *Protein Sci.* **2000**, *9*(1), 20-28.
- (22) Mallik, R.; Gross, S. P. *Curr. Biol.* **2004**, *14*(22), R971-82.
- (23) Kumar, S.; Lee, I. H.; Plamann, M. *J. Biol. Chem.* **2000**, *275*(41), 31798-31804.
- (24) Kini, A. R.; Collins, C. A. *Cell Motil. Cytoskeleton* **2001**, *48*(1), 52-60.
- (25) Williams, J. C.; Roulhac, P. L.; Roy, A. G.; Vallee, R. B.; Fitzgerald, M. C.; Hendrickson, W. A. *PNAS* **2007**, *104*(24), 10028-33.
- (26) Sun, S. J.; Siglin, A.; Williams, J. C.; Polenova, T. *J. Am. Chem. Soc.* **2009**, *131*(29), 10113-10126.

- (27) Gardiennet-Doucet, C.; Henry, B.; Tekely, P. *Prog. NMR Spec.* **2006**, *49*(2), 129-149.
- (28) Bachovchin, W. W.; Roberts, J. D. *J. Am. Chem. Soc.* **1978**, *100*(26), 8041-8047.
- (29) Gu, Z.; McDermott, A. *J. Am. Chem. Soc.* **1993**, *115*(10), 4282-4285.
- (30) Nemeria, N.; Baykal, A.; Joseph, E.; Zhang, S.; Yan, Y.; Furey, W.; Jordan, F. *Biochemistry* **2004**, *43*(21), 6565-75.
- (31) Nemeria, N.; Chakraborty, S.; Baykal, A.; Korotchkina, L. G.; Patel, M. S.; Jordan, F. *PNAS* **2007**, *104*(1), 78-82.

Chapter 2

STRUCTURAL STUDIES OF *E. COLI* THIOREDOXIN REASSEMBLY BY MAS NMR SPECTROSCOPY

2.1 Introduction

Recent developments in magic angle spinning (MAS) NMR spectroscopy have made it a complementary tool to both X-ray crystallography and solution NMR methods for biomolecular structure determination. Structural studies of biological solids inherently lacking long-range order, such as membrane proteins [1-4], macromolecular assemblies [5-8], and amyloid fibrils [9-13], are now amenable to MAS NMR methods. A number of structural studies using MAS NMR have been reported in the literature in the last few years. Many of them have employed sparsely labeled samples for a number of technical reasons [11,12,14,15], while only a few reports focused on uniformly labeled systems [16,17]. The early work by Castellani et al. [18,19] on SH3 domain of α -spectrin (2002, 2003) and the subsequent study by Zech et al. [20] on ubiquitin (2005) showed that complete protein structure determination in the solid state was possible by using dipolar-based carbon-carbon distance constraints acquired on 1,3- and 2-glycerol labeled samples at moderate MAS frequencies. This type of labeling strategy greatly reduces the number of trivial intra-residue correlations typically observed in ^{13}C - ^{13}C correlation spectra due to the differential enrichment of the directly bonded ^{13}C nuclei. As a consequence, the resolution of the non-trivial inter-residue cross peaks improves significantly, which makes their resonance assignments less ambiguous. In addition, this labeling was

thought to be necessary not only for reducing the spectral congestion, but also to avoid the so-called dipolar truncation problem [21,22], which is generally defined as the attenuation of polarization transfer between weakly dipolar-coupled spins (i.e., nuclei separated by long distances) in the presence of the strong dipolar couplings, such as one-bond interactions. Dipolar truncation was conceived to be a serious limitation in the uniformly labeled protein samples for the measurement of structurally important inter-residue carbon-carbon distances, which are usually greater than 3-4 Å.

However, later research demonstrated that some homonuclear recoupling sequences are less susceptible to dipolar truncation effects and can be used for establishing inter-residue connectivities in uniformly labeled samples. In particular, our group reported observation of a number of inter-residue distance constraints on the 108-residue uniformly U-¹⁵N,¹³C *E. coli* thioredoxin [23] using spin-diffusion-based carbon-carbon methods [24] or their variants [25]. Later, Lange et al. [17] reported the complete structure determination of the 38-residue U-¹⁵N,¹³C kalitoxin using proton-proton spin-diffusion experiments for establishing long-range connectivities. Later theoretical studies by Grommek et al. [26] showed that dipolar truncation does not seriously affect the proton-driven carbon-carbon spin-diffusion based polarization transfer methods. Even though the proton-proton spin diffusion can take place over longer distances than proton-driven carbon-carbon spin diffusion and thus yield connectivities even longer than demonstrated by Lange et al., it suffers from low sensitivity due to a number of intermediate selective ¹H-¹³C polarization transfer steps.

In 2005, shortly after we observed lack of dipolar truncation in spin diffusion experiments on U-¹⁵N,¹³C *E. coli* thioredoxin [23], we initiated structural investigations of the 35-residue long C-terminal fragment of the U-¹⁵N-1-73/U-

^{13}C , ^{15}N -74-108 *E. coli* thioredoxin using proton-driven carbon-carbon spin-diffusion method (or its variants) as a principal tool to acquire structure defining inter-residue distance constraints. Thioredoxin is a well-behaved model system for the development of new methodologies in solid-state NMR. The X-ray [27] and solution NMR [28] structures of *E. coli* thioredoxin have been reported in the literature. The solid-state resonance assignments of ^{13}C and ^{15}N chemical shifts of the intact *E. coli* thioredoxin as well as the reassembled thioredoxin complex have been previously reported by our group [23,29,30]. The primary, secondary, and tertiary structures of *E. coli* thioredoxin from the PDB file 2trx are shown in Figure 2.1. This chapter focuses on experiments, spectral analysis, and resonance assignments of the inter-residue correlations in the context of structural studies of the 35-residue C-terminal fragment of the U- ^{15}N -1-73/U- ^{13}C , ^{15}N -74-108 *E. coli* thioredoxin reassembly.

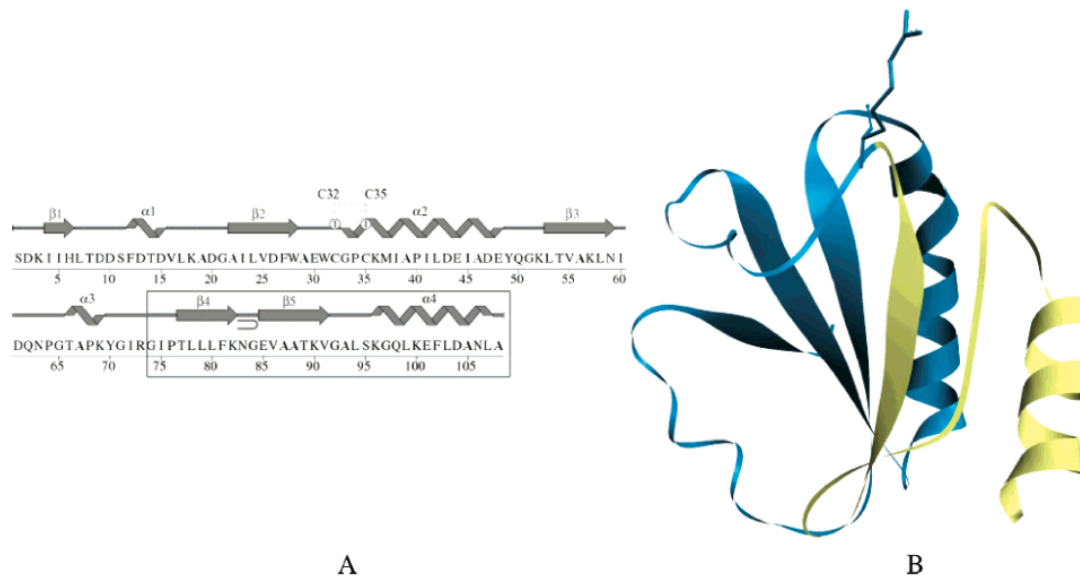


Figure 2.1: A) Amino acid sequence and secondary structure of *E. coli* thioredoxin generated by PDBsum using the PDB file 2trx.ent. B) Tertiary structure. The N-terminal fragment is shown in blue; the C-terminus is in yellow. Arg-73 at the cleavage site is represented using the stick representation. (Adapted from ref. [29] with permission)

2.2 Experimental Methods

The sample preparation procedure has been discussed in detail by Marulanda et al. [29]. A brief summary is presented here.

2.2.1 Materials

All chemicals were from Sigma. U- $^{13}\text{C}_6$ -glucose and $^{15}\text{NH}_4\text{Cl}$ were from Cambridge Isotope Laboratories. Rich media for *E. coli* cultures were from Oxoid, Inc. All reagents were used without further purification.

2.2.2 Sample Preparation

Overexpression and purification of isotopically enriched thioredoxin was reported previously [23,29]. For the preparation of differentially enriched thioredoxin reassembly, two batches of thioredoxin were expressed and purified: one containing uniformly ^{13}C , ^{15}N isotopically labeled protein, and another containing uniform ^{15}N isotopic labels. The final yields of the purified protein were 40 and 100 mg/l of minimal media for the U- ^{13}C , ^{15}N -enriched and U- ^{15}N enriched thioredoxin, respectively. Each protein batch was subsequently proteolytically cleaved at the Arg-73 site, as reported previously [31]. Subsequently, the complementary fragments consisting of the *N*-terminal portion encompassing residues 1–73 and of the *C*-terminal portion encompassing residues 74–108 were purified. The ^{13}C , ^{15}N -enriched fragment was then reconstituted with its complementary ^{15}N -enriched counterpart, resulting in 1–73(U- ^{15}N)/74–108(U- ^{13}C , ^{15}N) reassembled thioredoxin. Samples for MAS NMR spectroscopy were prepared by controlled precipitation of the differentially enriched reassembly with the polyethylene glycol (PEG) 4000, using the protocols reported previously [23,29]. A solution of PEG-4000 containing 10 mM NaCH_3COO and 1 mM NaN_3 (pH 3.5) was slowly added to a solution containing 70 mg/ml thioredoxin in 10 mM phosphate buffer (pH 7.0), until no further protein precipitation was observed; the final concentration of PEG-4000 was estimated to be 30–35%. A nearly complete precipitation with yields better than 95% was achieved after 24 h, as estimated by the residual absorbance of the supernatant at 280 nm. The PEG precipitate was centrifuged, the supernatant was removed, and the resulting sample was transferred into a 3.2 mm rotor. The sample was sealed using a bottom spacer and top spinner, according to the standard procedures. The final amount of the

hydrated precipitated thioredoxin sample packed in the NMR rotors was 6-7 mg of 1-73(U-¹⁵N)/74-108(U-¹³C, ¹⁵N).

2.2.3 Solid-State NMR Spectroscopy

All SSNMR spectra presented in this chapter were acquired at 14.1 T on a narrow bore Varian InfinityPlus spectrometer operating at Larmor frequencies of 599.5 MHz for ¹H, 150.8 MHz for ¹³C, and 60.8 MHz for ¹⁵N. The instrument was outfitted with a 3.2 mm T3 MAS probe. The MAS frequency was 10 kHz for all experiments, and was controlled to be within ± 1 Hz by a Varian MAS controller. The temperature was kept at -15 °C. The temperature reported includes a MAS frequency-dependent correction determined experimentally by using PbNO₃ as the temperature sensor [32]. The conditions pertaining to the individual experiments are given below.

Dipolar-assisted rotational resonance (DARR) [25] build-up measurements were conducted with mixing times of 5, 10, 20, 50, 100, 150, 200, 250, 300, and 400 ms. The 2D ¹³C-¹³C proton-driven spin-diffusion (PDS) spectrum was collected with the mixing time of 500 ms. Two 3D ¹³C-¹³C-¹³C spectra were acquired with 10 ms for the first DARR mixing and 200 or 500 ms for the second DARR mixing periods. The 2D spectra (for build-up curve measurements) were typically collected as (1000 x 512) matrices with 32 scans. The 10 ms x 200 ms 3D ¹³C-¹³C-¹³C spectrum was collected as (1000 x 128 x 128) matrix with 16 scans. The 10 ms x 500 ms 3D ¹³C-¹³C-¹³C spectrum were collected as (1000 x 128 x 96) matrix with 32 scans. The ¹³C excitation frequency was set at 100.0 ppm for the 2D, and at 72.0 ppm for the 3D experiments.

Time proportional phase incrementation (TPPI) method was used for frequency discrimination in the indirect dimension in all experiments. The typical pulse lengths were 3.1 (¹H), 4.8-5.0 (¹³C) μ s. The ¹H-X (X=¹³C, ¹⁵N) cross polarization

was performed with a linear (76-100% for ^{13}C and 68-100% for ^{15}N) amplitude ramp; the ^1H rf field was 57 kHz, while the center of the ramp on the heteronucleus was Hartmann-Hahn matched to the first spinning sideband. The contact times were 1.25-1.60 ms. The DARR experiment employed the $n = 1$ mixing condition. 80.6 kHz TPPM [33] decoupling was used during evolution in the direct dimension; the TPPM pulse width was 6.0 μs

The 3D N-CA-CX spectrum was collected as (1333 x 64 x 32) matrix with 128 scans. SPECIFIC-CP [34] was used for NCA transfer. The rf field strength for ^{15}N was 27 kHz, and the ^{13}C field was tangentially ramped 83-100% with the center of the ramp being 17 kHz; the contact time was 6.0 ms. 87 kHz CW decoupling was applied during SPECIFIC-CP. 200 ms DARR mixing time used for CA-CX transfer. The excitation frequency was set at 119.9 ppm for ^{15}N , and at 58.4 ppm for ^{13}C .

^{13}C , ^{15}N chemical shifts were referenced with respect to adamantane and ammonium chloride used as external referencing standards, and following the protocol described by Marcombe and Zilm [35]. All spectra were processed with a 60° or 90° sine-bell apodization function and followed by a Lorentzian-to-Gaussian transformation in all dimensions. A forward linear prediction to twice the number of experimental points was employed in the indirect dimension followed by zero-filling.

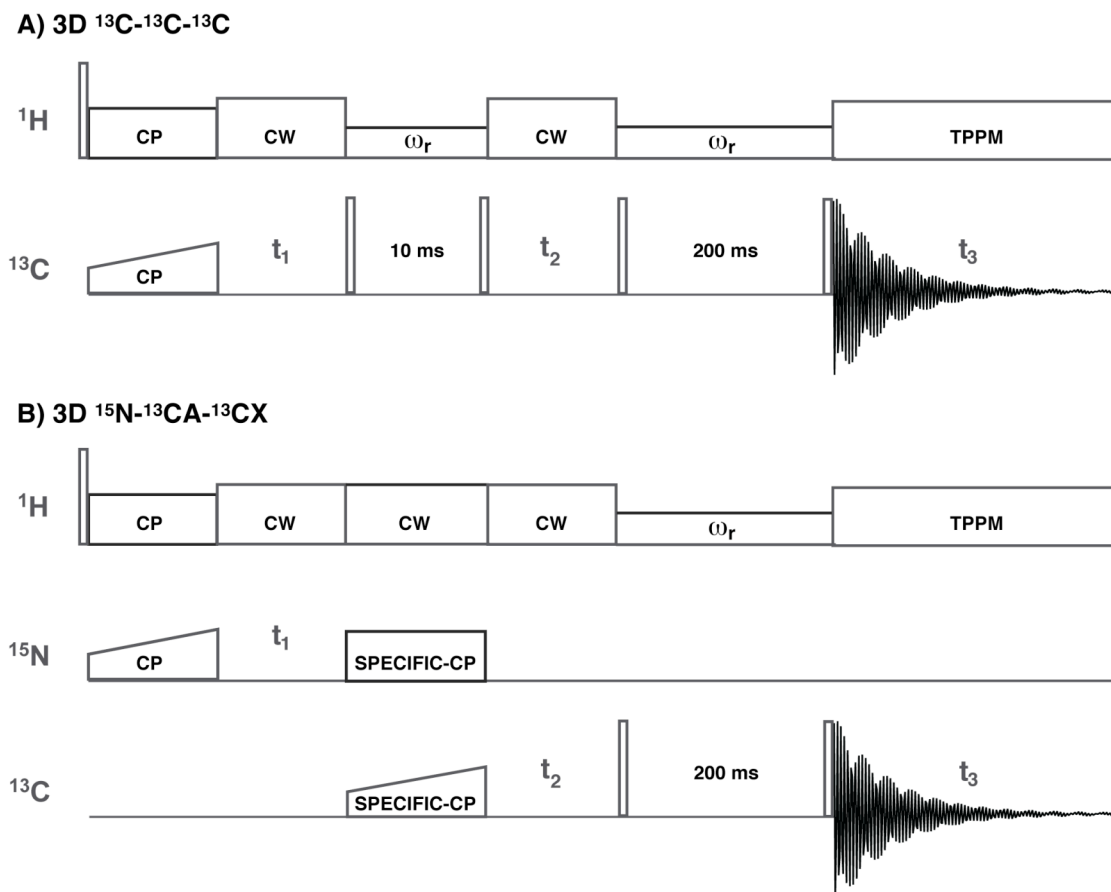


Figure 2.2: 3D ^{13}C - ^{13}C - ^{13}C (A) and NCACX (B) pulse sequences for inter-residue ^{13}C - ^{13}C correlations. The inter-residue correlations emerge during the 200 ms DARR mixing in both experiments.

2.3 Results and Discussion

2.3.1 DARR Build-up Curves

Spin-diffusion-based polarization transfer methods have long been used for the observation of dipolar correlations in many systems in the solid state. In a conventional proton-driven spin-diffusion (PDSD) experiment the ^1H decoupling field is switched off. This causes homogeneous line broadening of the ^{13}C resonances due to ^1H - ^{13}C and ^1H - ^1H dipolar interactions, which allows a pair of ^{13}C resonances with different chemical shifts to overlap with each other and thus the rotational resonance condition necessary for dipolar recoupling to be achieved. In 2001, Takegoshi et al. [25] introduced a dipolar-assisted rotational resonance (DARR) sequence whereby ^1H rf irradiation is applied during the mixing period with intensity ν_1 satisfying the rotary resonance condition $\nu_1 = n\nu_R$ ($n=1$ or 2) for the recovery of the ^1H - ^{13}C dipolar interaction (which would otherwise be averaged to zero by MAS), and which assists the polarization transfer between a pair of ^{13}C nuclei. The DARR sequence showed significant increase in the polarization transfer efficiency and enhanced cross-peak intensities in the ^{13}C - ^{13}C correlation spectra compared to PDSD method, with generally faster polarization transfer dynamics. In the same work, it was also shown that ^1H - ^1H dipolar coupling is indispensable for efficient DARR transfer.

In both PDSD and DARR experiments, at short mixing times (5-20 ms at 14.1 T), the magnetization from a ^{13}C spin diffuses over a limited distance corresponding typically to only one-bond or two-bond intra-residue correlations. However, for structural studies, inter-residue correlations are more informative. To obtain inter-residue correlations in ^{13}C - ^{13}C correlation spectra, one needs to use long spin-diffusion

mixing times (≥ 100 ms) in PDS and DARR experiments so that magnetization can be transferred over longer distances.

Hence, as a first step toward acquiring inter-residue constraints for structural studies, a series of 2D ^{13}C - ^{13}C dipolar correlation spectra were acquired on the C-terminal fragment of the U- ^{15}N -1-73/U- ^{13}C , ^{15}N -74-108 *E. coli* thioredoxin reassembly with DARR mixing times of 5, 10, 15, 20, 50, 100, 150, 200, 250, 300, and 400 ms. The spectra with 100-400 ms mixing times are presented in Figure 2.3 with several representative inter-residue correlations labeled on the graphs. The build-up curves of one-bond, two-bond, sequential, medium- ($|i - j| \geq 2,3,4$), and long-range ($|i - j| > 4$) correlations as a function of DARR mixing time are presented in Figure 2.4.

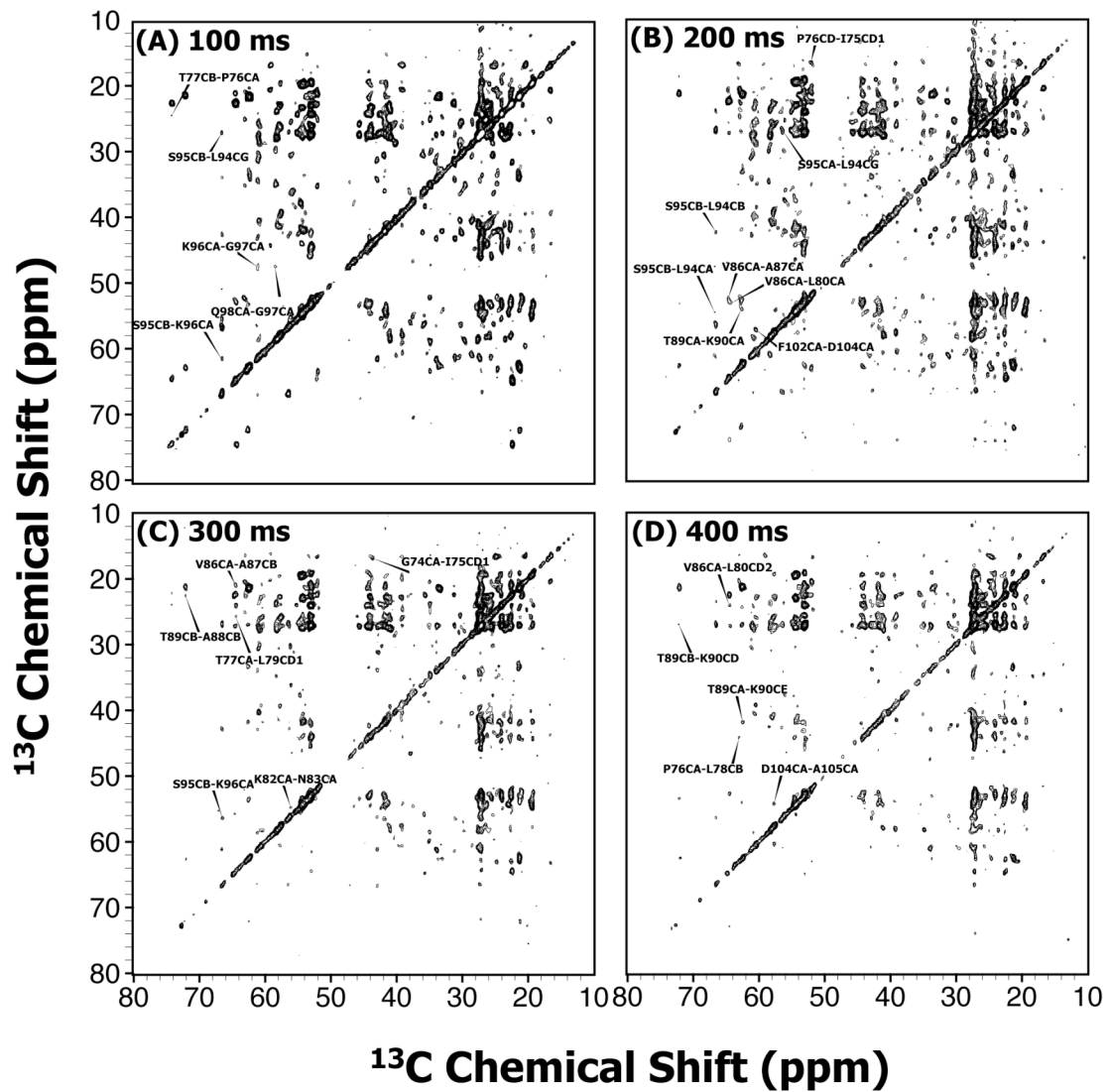


Figure 2.3: DARR spectra of $\text{U-}^{15}\text{N-1-73/U-}^{13}\text{C,}^{15}\text{N-74-108}$ *E. coli* thioredoxin reassembly acquired with (A) 100 ms, (B) 200 ms, (C) 300 ms, and (D) 400 ms. Several representative inter-residue correlations are shown in each spectrum. (Adapted from ref. [30] with permission)

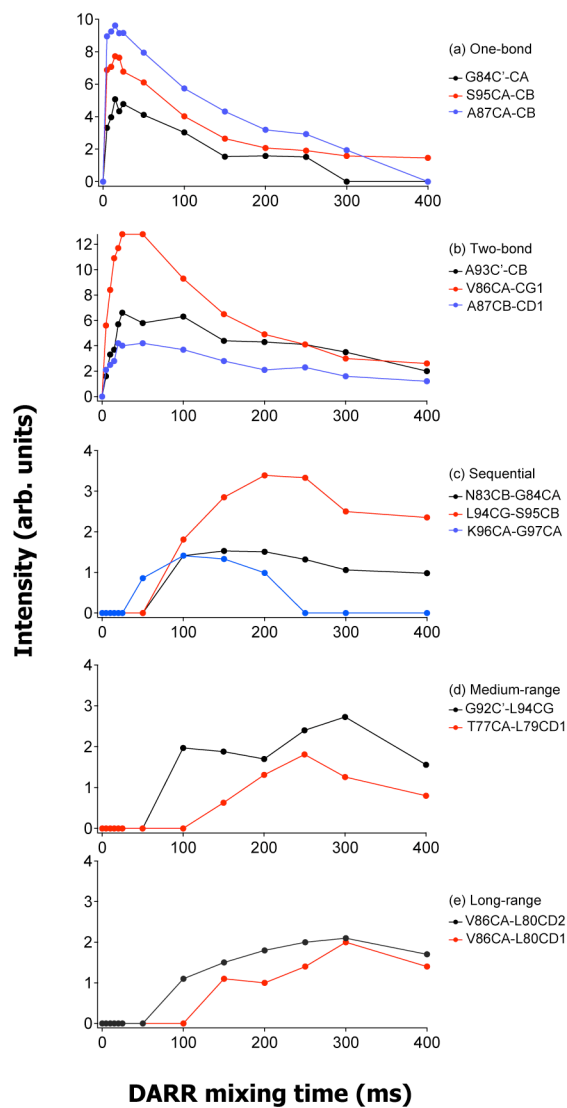


Figure 2.4: Intensity build-up curves for DARR cross-peaks in $U\text{-}^{15}\text{N}\text{-}1\text{-}73/U\text{-}^{13}\text{C},^{15}\text{N}\text{-}74\text{-}108$ *E. coli* thioredoxin reassembly for (a) one-bond, (b) two-bond, (c) sequential, (d) medium-, (e) long-range correlations. (Adapted from ref. [30] with permission)

It is clear from Figure 2.4 that the one-bond correlations such as $C\alpha-C\beta$ and $C\alpha-C\gamma$ build up very fast and reach their maximum around 10-15 ms, and then decay with a time constant of several hundred milliseconds. However, it is important to note that the one-bond correlations do not always decay to zero and significant intensity in the corresponding cross peaks is present even at long mixing times along with other inter-residue correlations thus contributing to spectral congestion. In this respect, 1,3- and 2-glycerol labeled samples are advantageous since dilute isotopic labels result in reducing the number of one-bond correlations, thus significantly alleviating the spectral congestion in ^{13}C - ^{13}C correlation spectra at long mixing times.

The two-bond correlations such as $C\beta-C\gamma$ and $C\alpha-C\delta$ reach the maximum intensity around 25-30 ms and their decay is slow compared to that of one-bond correlations at higher mixing times. The sequential correlations start emerging around 50-100 ms and reach their maximum intensities around 200-250 ms. The exact profiles of their build-up curves appear to depend on the type of the two carbon nuclei correlated through dipolar interaction. For example, conformation-independent sequential contacts like $C\alpha(i) - C\alpha(i+1)$ show up very early, around 50 ms, whereas $C\alpha(i)$ contacts with side-chain carbon atoms belonging to the next residue, as well as side-chain/side-chain contacts, reach their maximum at slightly longer mixing times because of the longer distances. The decrease in the sequential cross-peak intensity takes about three times longer compared to that of the one-bond correlations.

The medium- ($|i - j| \geq 2,3,4$) and long-range ($|i - j| > 4$) correlations take even longer mixing times (200-400 ms) to build up. It is important to examine the relative intensities of the cross-peaks at different mixing times. At 200 ms, the intensities of a number of sequential correlations are equal to, or exceed, the intensities of one-bond cross-peaks. At 300 ms, the medium- and long-range correlations grow and become of intensities equal to or greater than those for one-bond and sequential cross-peaks. This indicates that at mixing times longer than 200-300 ms, medium- and long-range distance correlations can be detected in the DARR spectra providing nontrivial distance constraints. These results in conjunction with the previous experimental work by our group and others thus indicate that dipolar truncation is weak in ^{13}C - ^{13}C DARR spectra. The theoretical studies by Grommek et al. employing both analytical calculations and numerical simulations demonstrated that dipolar truncation does not strongly influence the proton-driven spin-diffusion (PDSD) experiments. In that work, it was shown that the zeroth-order average Hamiltonian of the dipolar interaction of the two carbons coupled to a proton bath under PDSD mixing is zero due to MAS and the polarization transfer between the two carbon nuclei is promoted by the nonzero first-order average Hamiltonian terms which have very little dipolar truncation effects. The magnitude of the first-order term scales inversely with the MAS frequency. Thus at moderate spinning speeds (such as 10 kHz used in our work) polarization transfer between distant carbon nuclei does not suffer from dipolar truncation effects while spin-diffusion mixing schemes are used. Therefore, the experimental and the theoretical results in aggregate indicate the feasibility of DARR and PDSD experiments for measurement of long inter-residue distance constraints in multiply labeled proteins.

2.3.2 Summary of Distance Constraints

The resonance assignments of the ^{13}C and ^{15}N chemical shifts in the 35-residue long C-terminal fragment of the U- ^{15}N -1-73/U- ^{13}C , ^{15}N -74-108 *E. coli* thioredoxin reassembly were achieved using a combination of two-dimensional homonuclear and heteronuclear correlation spectra by Marulanda et. al. [29]. The high resolution of cross-peaks in the N-C and C-C correlation spectra acquired with short mixing times made this possible. However, at longer spin-diffusion mixing times, the sequential and other inter-residue carbon-carbon correlations build up very quickly, the spectra become heavily congested, and the number of degeneracies for each cross-peak increases in both dimensions. Hence, it is not always possible to make confident inter-residue resonance assignments only with 2D C-C spectra, except for some outliers. For this reason, we have employed two 3D experiments; N-CA-CX and C-C-C. The pulse sequences for these two experiments are shown in Figure 2.2 In the N-CA-CX experiment, each CA atom in a residue interacts during the long spin-diffusion mixing time with any other carbon atom CX in the protein, and the CA-CX cross peak is resolved by the amide nitrogen N attached to CA. In the C-C-C experiment, the second C1-(C2-C3) mixing time is longer (200 or 500 ms in our experiments) than the first (C1-C2)-C3 mixing time which is typically set to 10 ms to observe one-bond correlations. Thus each long-range C2-C3 interaction is resolved by the C1 chemical shift, which is attached to C2.

2D planes of 3D NCACX and C-C-C spectra with few representative inter-residue correlations are presented in Figure 2.5 In Figure 2.6 and 2.7, a 2D C-C PDS spectrum acquired with 500 ms mixing time is presented along with most of the inter-residue correlations assigned in this work.

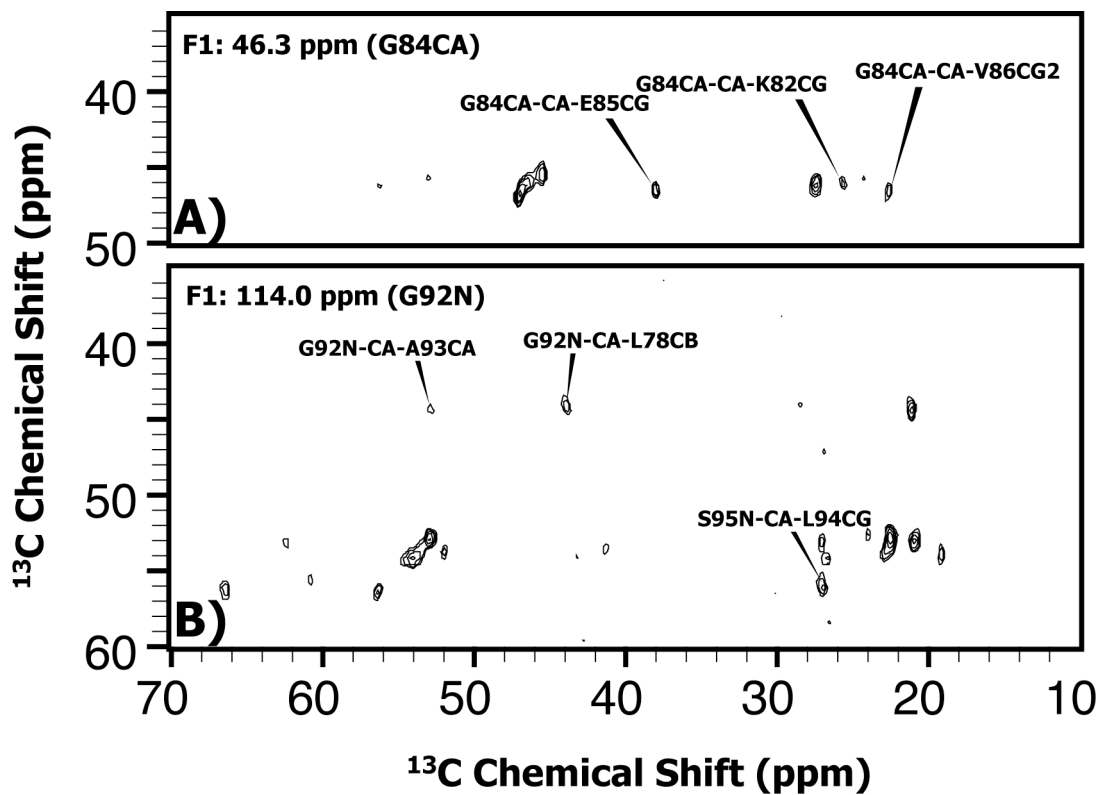


Figure 2.5: Several representative 2D F2-F3 planes of 3D ^{13}C - ^{13}C - ^{13}C (A), and 3D NCACX (B) spectra of U- ^{15}N -1-73/U- ^{13}C , ^{15}N -74-108 *E. coli* thioredoxin reassembly. The chemical shift of the first nucleus (^{13}C or ^{15}N) is indicated at the top (F1). Assigned cross peaks correspond to inter-residue correlations.

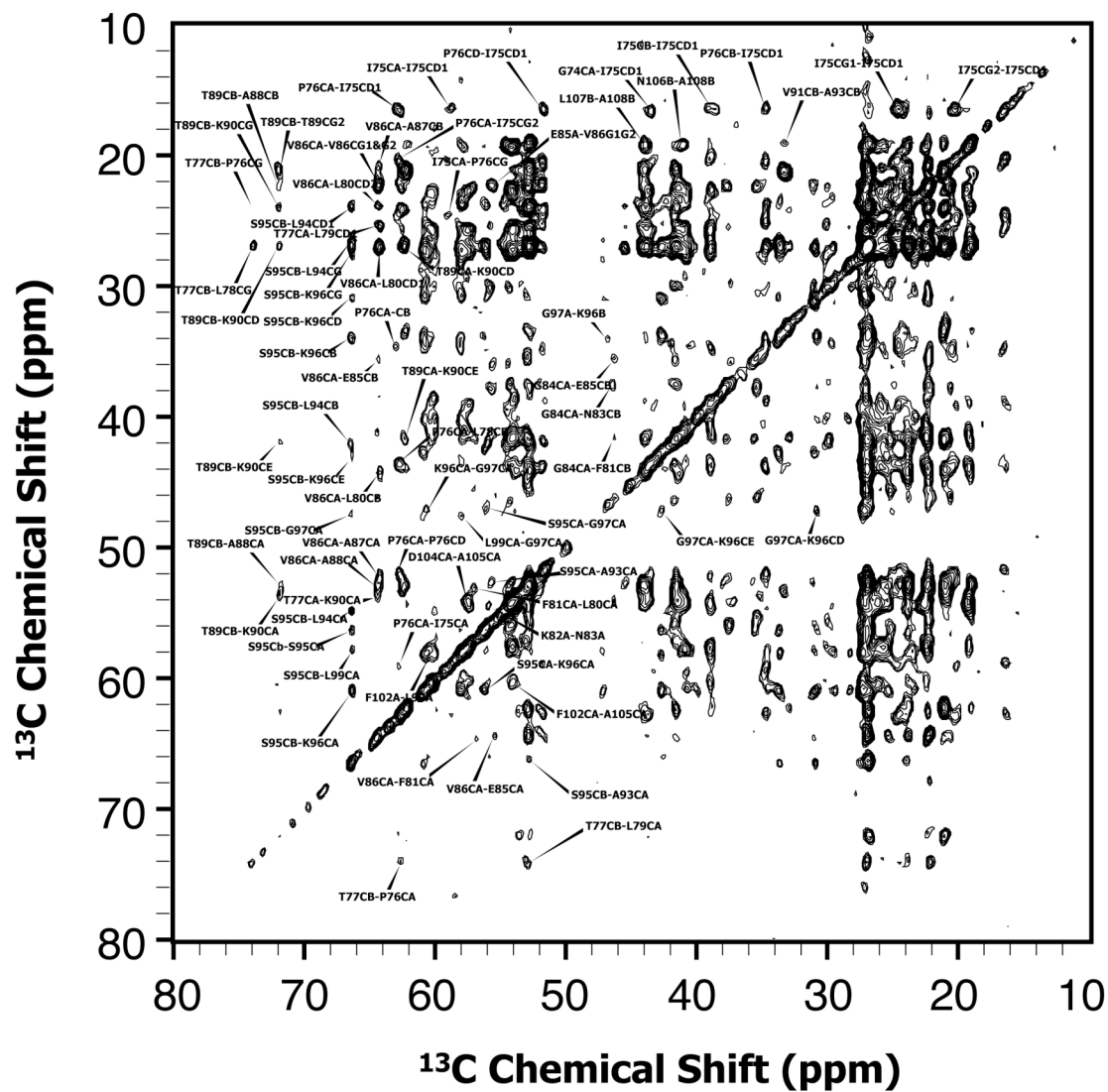


Figure 2.6: 2D ^{13}C - ^{13}C PDS correlation spectrum (aliphatic region) of U- ^{15}N -1-73/U- ^{13}C , ^{15}N -74-108 *E. coli* thioredoxin reassembly with the mixing time of 500 ms. Assigned cross peaks represent the majority of the inter-residue correlations identified in this work.

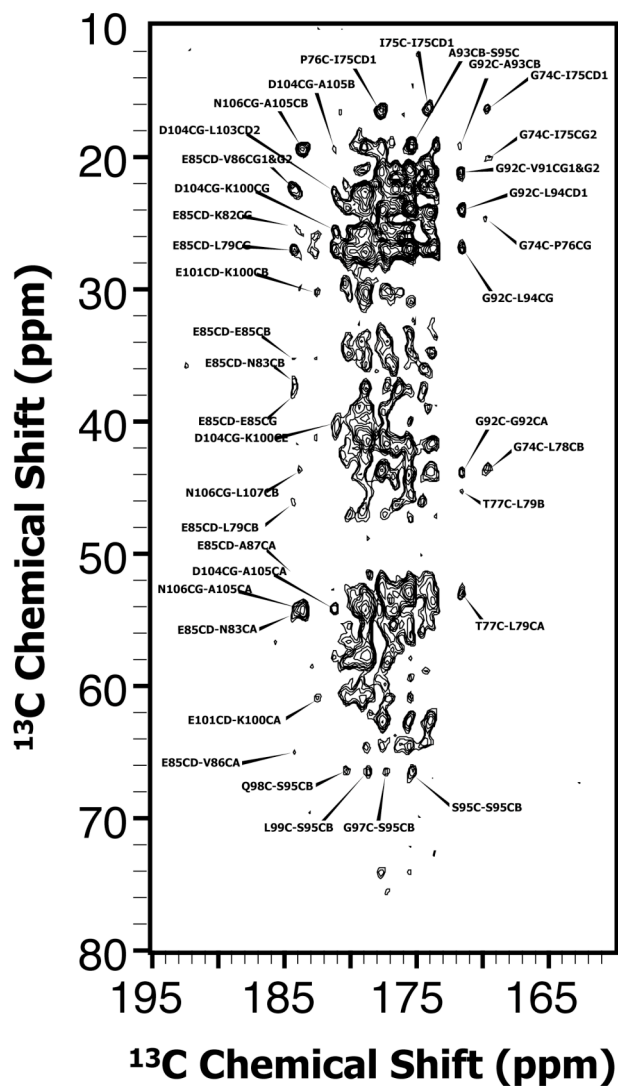


Figure 2.7: 2D ^{13}C - ^{13}C PDS correlation spectrum (carbonyl region) of $\text{U-}^{15}\text{N-1-73}/\text{U-}^{13}\text{C},^{15}\text{N -74-108}$ *E. coli* thioredoxin reassembly with the mixing time of 500 ms. Assigned cross peaks represent the majority of the inter-residue correlations identified in this work.

In total, we have assigned 121 inter-residue ^{13}C - ^{13}C correlations in the U- ^{15}N -1-73/U- ^{13}C , ^{15}N -74-108 *E. coli* thioredoxin complex using a combination of 2D and 3D spectra with long spin-diffusion mixing times. Of the 121, 73 are sequential, 39 are medium-, and 9 are long-range contacts. A summary of all the inter-residue constraints is given in Table 2.1.

Table 2.1 Summary of Inter-Residue Distance Constraints for the C-Terminal Fragment of the U-¹⁵N-1-73/U-¹³C,¹⁵N-74-108-labeled *E. coli* Thioredoxin Reassembly.

#	Atom1	Atom2	Type
1	G74CA	I75CD1	sequential
2	G74CO	I75CG2	sequential
3	G74CO	I75CD1	sequential
4	G74CO	P76CG	medium
5	G74CO	L78CB	medium
6	I75CD1	P76CO	sequential
7	I75CD1	P76CA	sequential
8	I75CD1	P76CD	sequential
9	I75CA	T77CA	medium
10	I75CA	P76CG	sequential
11	I75CA	P76CA	sequential
12	P76CG	T77CB	sequential
13	P76CA	L78CB	medium
14	P76CA	T77CB	sequential
15	T77CB	L78CG	sequential
16	T77CB	L79CA	medium
17	T77CO	L79CA	medium
18	T77CO	L79CB	medium
19	T77CA	L79CD1	medium
20	L78CB	G92CA	long
21	L79CB	E85CD	long
22	L79CG	E85CD	long
23	L80CB	V86CA	long
24	L80CD1	V86CA	long
25	L80CD2	V86CA	long
26	L80CB	F102CG	long
27	L80CA	F81CA	sequential
28	F81CB	G84CA	medium

Table 2.1 Summary of Inter-Residue Distance Constraints for the C-Terminal Fragment of the U-¹⁵N-1-73/U-¹³C,¹⁵N-74-108-labeled *E. coli* Thioredoxin Reassembly (continued).

#	Atom1	Atom2	Type
29	F81CA	V86CA	long
30	K82CA	N83CA	sequential
31	K82CG	E85CD	medium
32	K82CG	G84CA	medium
33	K82CD	N83CA	sequential
34	N83CB	G84CA	sequential
35	N83CB	E85CD	medium
36	N83CA	E85CD	medium
37	G84CA	V86CA	medium
38	G84CA	E85CB	sequential
39	G84CA	E85CG	sequential
40	G84CA	V86CB	medium
41	G84CA	V86CG2	medium
42	K85CA	V86CA	sequential
43	K85CD	A87CA	medium
44	K85CD	V86CG1	sequential
45	K85CB	V86CA	sequential
46	V86CA	A87CA	sequential
47	V86CA	A87CB	sequential
48	V86CA	A88CA	medium
49	V86CA	A88CB	medium
50	A87CA	A88CO	sequential
51	A88CA	F102CA	long
52	A88CA	T89CG2	sequential
53	A88CB	T89CB	sequential
54	T89CB	K90CA	sequential
55	T89CB	K90CE	sequential
56	T89CB	K90CD	sequential

Table 2.1 Summary of Inter-Residue Distance Constraints for the C-Terminal Fragment of the U-¹⁵N-1-73/U-¹³C,¹⁵N-74-108-labeled *E. coli* Thioredoxin Reassembly (continued).

#	Atom1	Atom2	Type
57	T89CB	K90CG	sequential
58	T89CA	K90CD	sequential
59	T89CA	K90CE	sequential
60	K90CD	V91CG1&2	sequential
61	K90CA	V91CG1&2	sequential
62	K90CO	V91CG1&2	sequential
63	K90CG	V91CG1&2	sequential
64	V91CG1/CG2	A93CA	sequential
65	V91CG1/CG2	G92CO	sequential
66	V91CG1/CG2	G92CA	sequential
67	V91CB	A93CB	medium
68	G92CA	A93CA	sequential
69	G92CA	A93CB	sequential
70	G92CO	A93CB	sequential
71	G92CO	L94CG	medium
72	G92CO	L94CD	medium
73	A93CA	S95CB	medium
74	A93CA	L94CD1	sequential
75	A93CA	S95CA	medium
76	A93CB	S95CO	medium
77	A93CB	L94CA	sequential
78	A93CO	L94CA	sequential
79	L94CA	S95CB	sequential
80	L94CB	S95CB	sequential
81	L94CG	S95CB	sequential
82	L94CG	S95CA	sequential
83	L94CD1	S95CB	sequential
84	S95CA	K96CA	sequential

Table 2.1 Summary of Inter-Residue Distance Constraints for the C-Terminal Fragment of the U-¹⁵N-1-73/U-¹³C,¹⁵N-74-108-labeled *E. coli* Thioredoxin Reassembly (continued).

#	Atom1	Atom2	Type
85	S95CA	G97CA	medium
86	S95CB	K96CA	sequential
87	S95CB	L99CA	medium
88	S95CB	G97CA	medium
89	S95CB	K96G	sequential
90	S95CB	K96D	sequential
91	S95CB	K96B	sequential
92	S95CB	K96E	sequential
93	S95CB	G97CO	medium
94	S95CB	Q98CO	medium
95	S95CB	L99CO	medium
96	K96CA	G97CA	sequential
97	K96CB	G97CA	sequential
98	K96CE	G97CA	sequential
99	K96CG	G97CA	sequential
100	K96CD	G97CA	sequential
101	G97CA	L99CA	medium
102	G97CA	Q98CA	sequential
103	G97CA	Q98CO	sequential
104	G97CO	Q98CA	sequential
105	L99CA	F102CA	medium
106	L99CA	K100CA	sequential
107	K100CA	E101CD	sequential
108	K100CE	D104CG	medium
109	K100CB	E101CD	sequential
110	K100CG	D104CG	medium
111	F102CA	A105CA	medium
112	F102CA	D104CA	medium

Table 2.1 Summary of Inter-Residue Distance Constraints for the C-Terminal Fragment of the U-¹⁵N-1-73/U-¹³C,¹⁵N-74-108-labeled *E. coli* Thioredoxin Reassembly (continued).

#	Atom1	Atom2	Type
113	L103CD2	D104CG	sequential
114	D104CA	A105CA	medium
115	D104CG	A105CB	medium
116	A105CA	N106CG	sequential
117	A105CA	D104CG	sequential
118	N106CG	L107CB	sequential
119	N106CG	A105CB	sequential
120	N106CB	A108CB	medium
121	L107CB	A108CB	sequential

The total number of 121 inter-residue correlations is significantly smaller than the number of distance constraints normally required for NMR protein structure calculations. A comparison of the number of distance constraints with the few other uniformly ¹³C,¹⁵N- labeled proteins reported in the literature is given in Table 2.2.

Table 2.2 Comparison of the Total Number of Inter-Residue Distance Correlations of the C-Terminal Fragment of the U-¹⁵N-1-73/U-¹³C,¹⁵N-74-108-labeled *E. coli* Thioredoxin Reassembly with few other Uniformly ¹³C,¹⁵N- labeled Proteins reported in the Literature.

Sample	# of residues	Sequential	Medium	Long	Total
Thioredoxin (current work)	35	73	39	9	121
GB1 (ref. [14])	56	182	40	45	267
HNP-1 (ref. [16])	30	129	45	96	270
KTX (ref. [17])	32	6	7	15	28

Even though the number of sequential and medium-range distance constraints is reasonably sufficient, the number of the long-range constraints is significantly lower than necessary. It is clear from Figures 2.5 and 2.6 that there are many cross-peaks that are unassigned and correspond to inter-residue correlations especially in C α -C β , C β -C β , C β -C γ regions of the 2D ^{13}C - ^{13}C correlation spectra. Due to the severe resonance overlap, these cross-peaks cannot be assigned unambiguously with only 2D spectra. 3D spectra such as C-C-C, NCACX, and NCOCX have to be used heavily to resolve them in the third dimension. However, in the 3D experiments the cross-peak intensity decreases substantially because of the additional polarization-transfer step. For example, in NCACX spectra, the cross peaks are only 50% of original intensity in 2D due to the first N-CA transfer step; N-CO transfer efficiency is usually lower than that of N-CA. Similarly, in C-C-C experiments, the first C-C mixing with short mixing times (10 ms) which is used to resolve the inter-residue cross peaks scales the intensity to only about 20-25% of their original values in 2D spectra. Due to the low sensitivity of the 3D experiments on the U- ^{13}C , ^{15}N -74-108 C-terminal fragment of *E. coli* thioredoxin (which is only one third [2-2.5 mg] of the total amount of the protein in the rotor), the 3D cross peaks have low intensity which makes the resonance assignments of inter-residue cross-peaks quite difficult. Only 24 of the 121 correlations have been assigned confidently in the 3D NCACX and C-C-C experiments.

Due to the low number of distance constraints, our preliminary attempts at structure calculation of 35-residue C-terminal fragment of *E. coli* thioredoxin using simulated annealing did not yield good convergence. The β -sheet structure consisting

of β 4- β 5 was not at all defined because of the insufficient number of inter-strand correlations.

To improve the quality of the structure derived from SSNMR spectra, we need more distance constraints, in particular long-range correlations. We are planning to revisit this issue with the following approaches. First, at higher magnetic fields the inherent sensitivity and the resolution of 2D and 3D correlation spectra increase significantly. Hence, high-field measurement of correlation spectra of the *E. coli* thioredoxin complex is one possible approach to alleviate the sensitivity problem. Second, very fast MAS is a recently emerging technique in solid-state NMR, in which the sample is spun at frequencies of 40 kHz and above to achieve line narrowing in the proton dimension. A number of studies have recently been reported for recoupling dipolar interactions at very fast MAS [36-38]. Our group (Hou et al. [39]) has recently developed *R*-symmetry based ^{13}C - ^{13}C recoupling sequences for MAS frequencies of 40 kHz and higher. These recoupling sequences have higher polarization-transfer efficiencies than conventional PDS and DARR under high MAS conditions and can be used for establishing intra-residue as well as inter-residue correlations. In addition, nonuniform sampling techniques in which the sampling interval between consecutive dwell points during data collection is modified in a specifically designed nonuniform manner to reduce the experimental time and increase the sensitivity are now beginning to be applied in solid-state NMR. Thus, high-field measurements combined with techniques such as fast-MAS and nonuniform data collection are a promising approach to SSNMR studies of samples with low sensitivity. In the future, we shall be pursuing work along these lines to improve the quality of SSNMR *E. coli* thioredoxin structure.

2.4 Conclusions

Structural studies of a 35-residue C-terminal fragment of the U-¹⁵N-1-73/U-¹³C, ¹⁵N -74-108 *E. coli* thioredoxin complex have been performed using ¹³C-¹³C dipolar-based distance constraints acquired by PDS and DARR mixing schemes. A number of inter-residue correlations identified in this work show that dipolar truncation does not significantly affect the spin-diffusion based polarization-transfer schemes such as PDS and DARR, even in uniformly labeled samples. However, the small number of acquired distance constraints, which is mainly because of the inherently low sensitivity of the *E. coli* thioredoxin complex used in this work, did not permit a full structure calculation. High-field measurements combined with very fast MAS techniques and nonuniform sampling are expected to alleviate the sensitivity problem and this study will be continued in the future.

2.5 References

- (1) Park, S. H.; De Angelis, A. A.; Nevzorov, A. A.; Wu, C. H.; Opella, S. J. *Biophys. J.* **2006**, *91*(8), 3032-42.
- (2) Park, S. H.; Prytulla, S.; De Angelis, A. A.; Brown, J. M.; Kiefer, H.; Opella, S. J. *J. Am. Chem. Soc.* **2006**, *128*(23), 7402-3.
- (3) Frericks, H. L.; Zhou, D. H.; Yap, L. L.; Gennis, R. B.; Rienstra, C. M. *J. Biomol. NMR* **2006**, *36*(1), 55-71.
- (4) Hong, M. *Structure* **2006**, *14*(12), 1731-40.
- (5) Sun, S.; Siglin, A.; Williams, J. C.; Polenova, T. *J. Am. Chem. Soc.* **2009**, *131*(29), 10113-26.
- (6) Goldbourn, A.; Gross, B. J.; Day, L. A.; McDermott, A. E. *J. Am. Chem. Soc.* **2007**, *129*(8), 2338-44.
- (7) Egawa, A.; Fujiwara, T.; Mizoguchi, T.; Kakitani, Y.; Koyama, Y.; Akutsu, H. *PNAS* **2007**, *104*(3), 790-5.
- (8) Paik, Y.; Yang, C.; Metaferia, B.; Tang, S.; Bane, S.; Ravindra, R.; Shanker, N.; Alcaraz, A. A.; Johnson, S. A.; Schaefer, J.; O'Connor, R. D.; Cegelski, L.; Snyder, J. P.; Kingston, D. G. *J. Am. Chem. Soc.* **2007**, *129*(2), 361-70.
- (9) Jaroniec, C. P.; MacPhee, C. E.; Bajaj, V. S.; McMahon, M. T.; Dobson, C. M.; Griffin, R. G. *PNAS* **2004**, *101*(3), 711-6.
- (10) Tycko, R. *Q. Rev. Biophys.* **2006**, *39*(1), 1-55.
- (11) Van Melckebeke, H.; Wasmer, C.; Lange, A.; Ab, E.; Loquet, A.; Bockmann, A.; Meier, B. H. *J. Am. Chem. Soc.* **2010**, *132*(39), 13765-75.
- (12) Wasmer, C.; Lange, A.; Van Melckebeke, H.; Siemer, A. B.; Riek, R.; Meier, B. H. *Science* **2008**, *319*(5869), 1523-1526.
- (13) Chimon, S.; Ishii, Y. *J. Am. Chem. Soc.* **2005**, *127*(39), 13472-3.
- (14) Franks, W. T.; Wylie, B. J.; Schmidt, H. L. F.; Nieuwkoop, A. J.; Mayrhofer, R.-M.; Shah, G. J.; Graesser, D. T.; Rienstra, C. M. *PNAS* **2008**, *105*(12), 4621-4626.
- (15) Chen, B.; Tycko, R. *Protein Sci.* **2010**, *19*(4), 716-30.
- (16) Li, S.; Zhang, Y.; Hong, M. *J. Magn. Reson.* **2010**, *202*(2), 203-10.
- (17) Lange, A.; Becker, S.; Seidel, K.; Giller, K.; Pongs, O.; Baldus, M. *Angew. Chem. Int. Ed.* **2005**, *44*(14), 2089-92.
- (18) Castellani, F.; van Rossum, B.; Diehl, A.; Schubert, M.; Rehbein, K.; Oschkinat, H. *Nature* **2002**, *420*(6911), 98-102.
- (19) Castellani, F.; van Rossum, B. J.; Diehl, A.; Rehbein, K.; Oschkinat, H. *Biochemistry* **2003**, *42*(39), 11476-83.
- (20) Zech, S. G.; Wand, A. J.; McDermott, A. E. *J. Am. Chem. Soc.* **2005**, *127*(24), 8618-26.
- (21) Hodgkinson, P.; Emsley, L. *J. Magn. Reson.* **1999**, *139*(1), 46-59.
- (22) Ladizhansky, V. *Solid State Nucl. Magn. Reson.* **2009**, *36*(3), 119-28.

- (23) Marulanda, D.; Tasayco, M. L.; Cataldi, M.; Arriaran, V.; Polenova, T. *J. Phys. Chem. B* **2005**, *109*(38), 18135-18145.
- (24) Szeverenyi, N. M.; Sullivan, M. J.; Maciel, G. E. *J. Magn. Reson.* **1982**, *47*(3), 462-475.
- (25) Takegoshi, K.; Nakamura, S.; Terao, T. *Chem. Phys. Lett.* **2001**, *344*(5-6), 631-637.
- (26) Grommek, A.; Meier, B. H.; Ernst, M. *Chem. Phys. Lett.* **2006**, *427*(4-6), 404-409.
- (27) Katti, S. K.; LeMaster, D. M.; Eklund, H. *J. Mol. Biol.* **1990**, *212*(1), 167-84.
- (28) Dyson, H. J.; Gippert, G. P.; Case, D. A.; Holmgren, A.; Wright, P. E. *Biochemistry* **1990**, *29*(17), 4129-4136.
- (29) Marulanda, D.; Tasayco, M. L.; McDermott, A.; Cataldi, M.; Arriaran, V.; Polenova, T. *J. Am. Chem. Soc.* **2004**, *126*(50), 16608-20.
- (30) Yang, J.; Paramasivam, S.; Marulanda, D.; Cataldi, M.; Tasayco, M. L.; Polenova, T. *Magn. Reson. Chem.* **2007**, *45 Suppl 1*, S73-83.
- (31) Yu, W. F.; Tung, C. S.; Wang, H.; Tasayco, M. L. *Protein Sci.* **2000**, *9*(1), 20-28.
- (32) Neue, G.; Dybowski, C. *Solid State Nucl. Magn. Reson.* **1997**, *7*(4), 333-336.
- (33) Bennett, A. E.; Rienstra, C. M.; Auger, M.; Lakshmi, K. V.; Griffin, R. G. *J. Chem. Phys.* **1995**, *103*(16), 6951-6958.
- (34) Baldus, M.; Petkova, A. T.; Herzfeld, J.; Griffin, R. G. *Mol. Phys.* **1998**, *95*(6), 1197-1207.
- (35) Morcombe, C. R.; Zilm, K. W. *J. Magn. Reson.* **2003**, *162*(2), 479-86.
- (36) Zhou, D. H.; Shea, J. J.; Nieuwkoop, A. J.; Franks, W. T.; Wylie, B. J.; Mullen, C.; Sandoz, D.; Rienstra, C. M. *Angew. Chem. Int. Ed.* **2007**, *46*(44), 8380-3.
- (37) Zhou, D. H.; Shah, G.; Cormos, M.; Mullen, C.; Sandoz, D.; Rienstra, C. M. *J. Am. Chem. Soc.* **2007**, *129*(38), 11791-801.
- (38) Zhou, D. H.; Shah, G.; Mullen, C.; Sandoz, D.; Rienstra, C. M. *Angew. Chem. Int. Ed.* **2009**, *48*(7), 1253-6.
- (39) Hou, G.; Yan, S.; Sun, S.; Han, Y.; Byeon, I. J.; Ahn, J.; Concel, J.; Samoson, A.; Gronenborn, A. M.; Polenova, T. *J. Am. Chem. Soc.* **2011**, *133*(11), 3943-53.

Chapter 3

DYNAMICS STUDIES OF *E. COLI* THIOREDOXIN REASSEMBLY BY MAS NMR SPECTROSCOPY

3.1 Introduction

X-ray crystallography and NMR spectroscopy are the two well-established methods to determine structures of biological macromolecules, such as proteins and protein assemblies, at atomic resolution. Among the two, NMR has the additional advantage that it can study dynamics present in proteins on a wide range of time scales, ranging from picoseconds to seconds and slower, in a site-specific manner [1-3]. Solid-state NMR spectroscopy offers an additional advantage, in that it can probe internal dynamics in proteins directly in the absence of global tumbling [4,5]. There are multiple dynamics probes in solid-state NMR, such as the anisotropic lineshape measurements (dipolar, chemical shift anisotropy (CSA), quadrupolar) as well as relaxation measurements (T_1 , T_2 , $T_{1\rho}$), all of which provide detailed glimpse on internal dynamics on various time scales. Historically, deuterium (^2H) lineshape measurements have been widely used in the studies of internal motions of specific sites labeled with deuterium, because of its small quadrupolar interaction ($\nu_Q = 167$ kHz for a static deuteron). However, this method has the disadvantage that multiple sites cannot be investigated simultaneously because of the resonance overlap. This hampers the applications of deuterium NMR spectroscopy to protein backbone dynamics studies, where typically lineshapes from most (or all) of the residues in a protein molecule would have to be recorded and analyzed under the same experimental

conditions in a given sample to get residue-specific information on the backbone and/or sidechain mobility. In some cases, ^2H line shapes can be recorded in multidimensional experiments where additional ^{13}C and/or ^{15}N chemical shift dimensions are introduced to attain the necessary resolution; but these studies still remain rare [6-8]. Dipolar and CSA lineshapes measurements present another dynamics probe and have the advantage that they can be measured in a site-specific manner in multidimensional experiments containing one or more dimensions correlating chemical shifts and an additional dimension where the dipolar or CSA interactions are recorded through recoupling methods. From the various anisotropic interactions, i.e., N-H or C-H dipolar, and ^{15}N , ^{13}C , or ^1H chemical shift interactions, one can derive not only site-specific dynamic information but also important structural insight. For example, a hydrogen bond interaction between an NH and a CO group in the protein backbone affects to a significant extent the NH bond length as well as the chemical shift tensors of the corresponding amide proton, amide nitrogen, and the carbonyl carbon. A set of these parameters measured with high accuracy can be a valuable source of information in characterizing hydrogen bond interactions. In this regard, measurement of anisotropic lineshapes in a protein by solid-state NMR has important applications in both structural and dynamics studies [9-11].

Even though CSA and dipolar lineshape measurements in small molecules have been in practice for a long time, with numerous examples of applications in small inorganic and organic molecules and materials, there are only a handful of reports to date where comprehensive backbone dynamics studies of solid proteins have been performed in a site-specific manner by anisotropic lineshape measurements using magic angle spinning (MAS) NMR spectroscopy [13-16].

In this chapter, we will present the anisotropic lineshapes (amide ^{15}N CSA and amide NH dipolar couplings) and relaxation parameters (amide ^{15}N R_1) of the 35-residue C-terminal fragment of U- ^{15}N -1-73/U- ^{13}C , ^{15}N -74-108 labeled *E. coli* thioredoxin reassembly measured by MAS NMR, and we will discuss the results in the context of structure and internal backbone dynamics of this complex.

3.2 Experimental Methods

3.2.1 Sample Preparation

The sample preparation protocols have been described in Chapter 2.

3.2.2 Solid-State NMR Spectroscopy

All SSNMR spectra presented in this chapter were acquired at 14.1 T on a narrow bore Varian InfinityPlus spectrometer operating at Larmor frequencies of 599.8 MHz for ^1H , 150.8 MHz for ^{13}C , and 60.8 MHz for ^{15}N . The instrument was outfitted with a 3.2 mm T3 MAS probe. The MAS frequency was 10 kHz for all experiments, and was controlled to be within ± 1 Hz by a Varian MAS controller. The temperature was kept at -15 °C. The temperature reported includes a MAS frequency-dependent correction determined experimentally by using PbNO_3 as the temperature sensor [17]. The conditions pertaining to the individual experiments are given below or in the figure captions.

3.2.3 ^{15}N ROCSA Experiment

The ^{15}N CSA recoupling was achieved by the symmetry-based ROCSA [18] method. The pulse sequence for the 3D NCA-ROCSA experiment is shown in Figure

3.1. The excitation frequencies were set at 122.4 ppm for ^{15}N and at 55.5 ppm for ^{13}C . Eighteen ROCSA points were acquired with the dwell time equal to one rotor period, and 64 ^{15}N t_2 points with acquired with the dwell time of 120 μs . 128 scans were added to record each point in the indirect dimensions of the 3D spectra. ^1H 90 pulse width was 2.78 μs . The contact time for the ^1H - ^{15}N CP was 1.6 ms. The ^1H radio frequency field strength was 51 kHz, the ^{15}N field was linearly ramped 70-100% with the center of the ramp being 41 kHz. The ROCSA sequence was used with a window $\tau_a = 3.29 \mu\text{s}$, and 42.8 kHz rf irradiation was employed. The Z-filter pulses were placed after the ROCSA block; the rf field strength was 50 kHz. The Z-filter delay was set equal to one rotor period. XY-16 decoupling on the ^{13}C channel was performed with the rf field strength of 50 kHz. 100 kHz CW decoupling was performed on the ^1H channel during ROCSA. SPECIFIC-CP [19] for ^{15}N - ^{13}C transfer was utilized. The ^{13}C field was tangentially ramped 90-100% with the center of the ramp being 35 kHz; the rf field strength for ^{15}N was 25 kHz; the contact time was 6.2 ms. 100 kHz CW decoupling was applied during SPECIFIC-CP. The Z-filter pulses were incorporated on the ^{13}C channel immediately after SPECIFIC-CP; the rf field strength was 67.9 kHz. 90 kHz TPPM decoupling [20] was applied during the t_3 evolution; the TPPM pulse width was 5.4 μs .

The NCA dimension was processed with a 60° sine-bell apodization function, followed by a Lorentzian-to-Gaussian transformation in both dimensions. A forward linear prediction to twice the number of the experimental points was employed in the ^{15}N dimension followed by zero-filling up to 256 points. The ROCSA dimension was processed with 200 Hz exponential linebroadening.

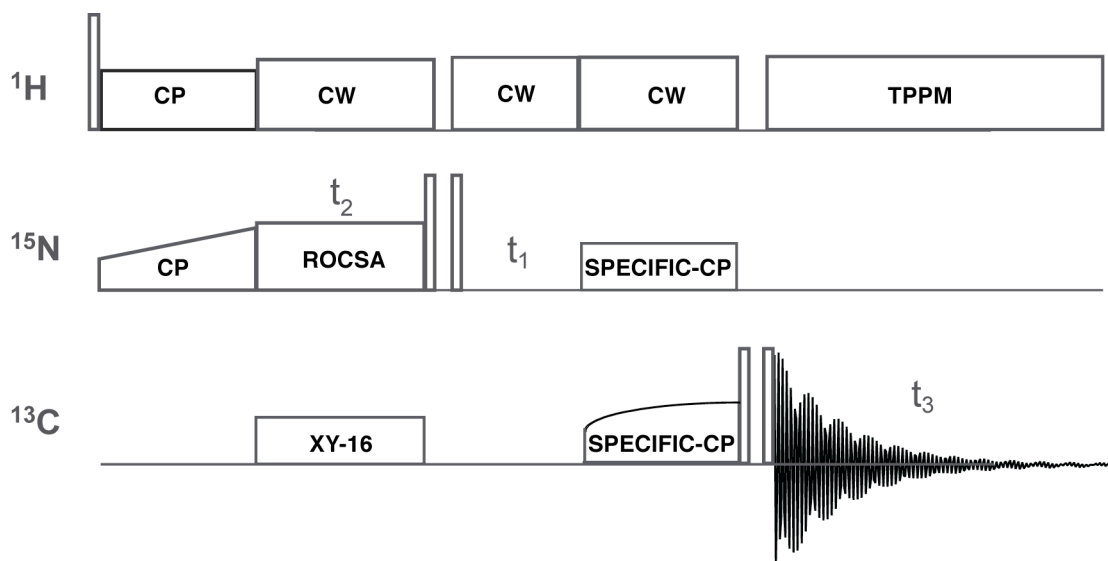


Figure 3.1: 3D NCA-ROCSA pulse sequence for site-specific ^{15}N CSA recoupling.

3.2.4 ^{15}N ROCSA Numerical Simulations

Numerical simulations of the ROCSA lineshapes were performed on a single spin system using SIMPSON [21] with repulsion 320 powder angle set and 36 γ -angles. The rest of the conditions were exactly the same as in the experiment. The ROCSA lineshapes were fitted using MINUIT with the SIMPLEX method with three adjustable parameters: i) reduced anisotropy (δ_σ) ii) asymmetry parameter (η_σ) iii) exponential linebroadening parameter which accounts for the exponential decay of the magnetization due to the various relaxation processes during ^{15}N ROCSA evolution. The linebroadening parameter was optimized with an upper limit set according to the slope of the edges of the lineshapes. The uncertainties in the fitting parameters were determined using the Monte Carlo method. First, the root-mean-square-deviation (RMSD) between the experimental and the best-fit FID was calculated as follows.

Then, to the best-fit FID, gaussian random noise scaled by the RMSD was added, and the Fourier transform of the resulting signal was fitted by MINUIT. This process was repeated 100 times and the standard deviation (σ) of the distribution of the best-fit parameters was analyzed. To take into account the covariance between parameters, the 2σ of the distribution is reported as the uncertainty for each parameter. As reported in the literature, the asymmetry parameter (η_σ) and the linebroadening parameter are observed to be strongly covariant in the backbone ^{15}N ROCSA lineshape simulations [22].

3.2.5 3D DIPSHIFT Experiment

The 3D NCA-DIPSHIFT experiment was performed with a pulse sequence shown in Figure 3.2. The ^1H - ^{15}N dipolar recoupling was achieved by the symmetry based $\text{R}18_1^7$ sequence [23]. The excitation frequencies were set at 122.4 ppm for ^{15}N and at 55.5 ppm for ^{13}C . Sixteen dipolar points were acquired with the dwell time equal to one rotor period, and 64 ^{15}N t_2 points with acquired with the dwell time of 120 μs . 128 scans were added to acquire each point in the indirect dimensions of the 3D spectra. ^1H 90 pulse width was 2.78 μs . The contact time for the ^1H - ^{15}N CP was 1.6 ms. The ^1H radio frequency field strength was 50 kHz, the ^{15}N field was linearly ramped 70-100% with the center of the ramp being 40 kHz. An $\text{R}18_1^7$ block was used for ^1H - ^{15}N dipolar recoupling; the rf field was 90 kHz. The total length of the 2τ period was set equal to 32 rotor periods. SPECIFIC-CP [19] for ^{15}N - ^{13}C CA transfer was utilized. The ^{13}C field was tangentially ramped 90-100% with the center of the ramp being 35 kHz; the rf field strength for ^{15}N was 25 kHz; the contact time was 6.2 ms. 90 kHz TPPM decoupling [20] was applied during the t_3 evolution; the TPPM pulse width was 5.1 μs .

The NCA dimension was processed with a 60° sinebell apodization function, followed by a Lorentzian-to-Gaussian transformation in both dimensions. A forward linear prediction to twice the number of the experimental points was employed in the ^{15}N dimension followed by zero-filling up to 256 points.

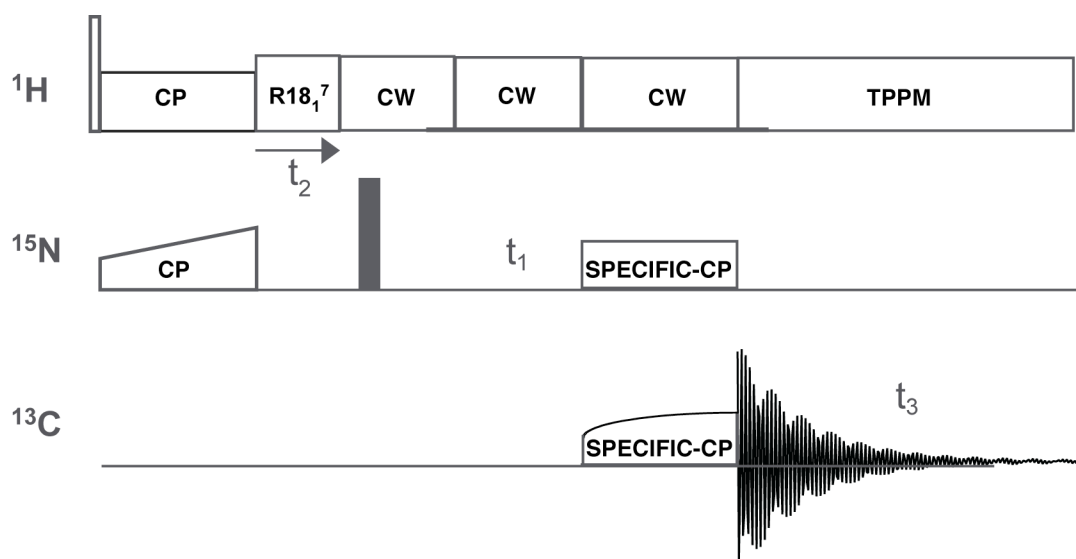


Figure 3.2: 3D DIPSHIFT-NCA pulse sequence for site-specific measurements of NH dipolar couplings. NH dipolar recoupling is performed by $\text{R}18_1^7$ symmetry-based scheme.

3.2.6 R18₁⁷ Numerical Simulations

Numerical simulations of the R18₁⁷ dipolar lineshapes were performed on an isolated ¹H-¹⁵N spin pair using SIMPSON with repulsion 168 powder angle set and 3 γ -angles. The rest of the conditions were exactly the same as in the experiment. The R18₁⁷ lineshapes were fitted manually with two adjustable parameters: i) the ¹H-¹⁵N dipolar coupling constant (d_{NH}) and ii) the exponential linebroadening parameter.

In general, the R18₁⁷ dipolar lineshapes depend not only on the NH dipolar coupling but also on the ¹H CSA of the amide proton, as this interaction is also recoupled by R18₁⁷. This introduces four additional parameters: δ_{σ} and η_{σ} for the amide proton CSA tensor, as well as β and γ angles, which describe the orientations of the NH dipolar vector in the CSA frame. Moreover, the dipolar lineshapes are also sensitive to the residual proton-proton interactions, which can be modeled as a relaxation process during dipolar evolution [24]. This requires yet an additional parameter, namely the differential relaxation time constant ($T_{2\text{RF}}$). Overall, six parameters are required to describe the R18₁⁷ experimental lineshapes completely. However, numerical simulations indicate that the dipolar splitting in the R18₁⁷ spectra is determined only by the NH dipolar coupling; the rest of the parameters (amide proton CSA, $T_{2\text{RF}}$) affect only the central peak intensity and the overall broadening of the R18₁⁷ lineshape as shown in Figure 3.3. All the numerical simulations in Figure 3.3 were performed using SPINEVOLUTION 3.3.3. [25]. Therefore, in the final set of simulations we decided to include only the ¹H-¹⁵N dipolar coupling constant (d_{NH}) and the exponential linebroadening parameter.

The numerical simulation of all the *E. coli* thioredoxin NH R18₁⁷ lineshapes were performed with only with two adjustable parameters, NH dipolar coupling

constant and an exponential linebroadening parameter. The linebroadening parameter was optimized according to slope of the outer doublets of the experimental R18₁⁷ spectra. The uncertainty in the dipolar coupling was manually estimated to be within ± 300 Hz for all residues.

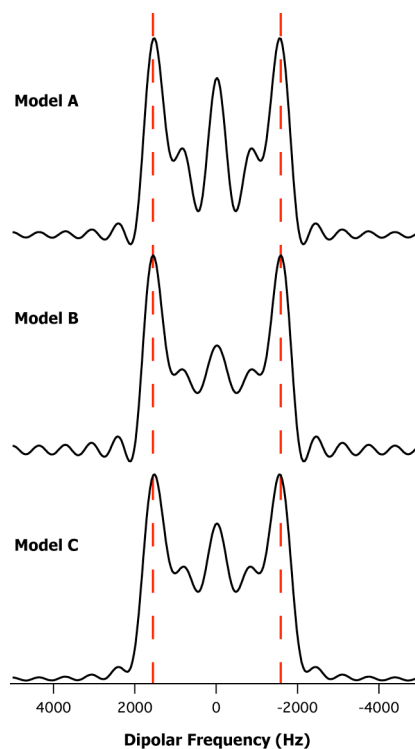


Figure 3.3: Simulation of NH R18₁⁷ lineshape with i) Model A: only NH dipolar coupling constant (10.83 kHz) ii) Model B: NH DCC and amide proton CSA ($\delta_\sigma = 8$ ppm, $\eta_\sigma = 1.0$, $\beta = 10^\circ$, $\gamma = 0$) iii) Model C: NH DCC and amide proton CSA and T_{2RF} (1.0 ms). In all three cases, the NH dipolar splitting remains the same.

3.2.7 ¹⁵N T_1 Experiment

The 2D ¹⁵N T_1 -NCA experiment was performed with a pulse sequence shown in Figure 3.4. The excitation frequencies were set at 116.1 ppm and 57.7 ppm for ¹⁵N and ¹³C, respectively. 96 ¹⁵N points were acquired with 120 μ s dwell time. 96 scans were added to acquire each point in the indirect dimension of the 2D experiment. The ¹H $\pi/2$ pulse width was 2.78 μ s. A 1.6 ms contact time was used for ¹H-¹⁵N CP. The ¹H radio frequency field strength was 50 kHz, the ¹⁵N field was linearly ramped 70-100% with the center of the ramp being 40 kHz. Two 90° pulses separated by

relaxation delay τ were applied immediately after ^1H - ^{15}N cross-polarization period; the pulse width was 5 μs . SPECIFIC-CP[19] for ^{15}N - ^{13}C transfer was utilized. The ^{13}C field was tangentially ramped 92-100% with the center of the ramp being 35 kHz; the rf field strength for ^{15}N was 25 kHz; the contact time was 6.2 ms. 90 kHz TPPM decoupling [20] was applied during the t_3 evolution; the TPPM pulse width was 5.3 μs .

Four 2D NCA experiments were performed with T_1 relaxation delays of 0.1, 1, 10, and 20 s. To account for the intensity fluctuations during SPECIFIC-CP, an NCA spectrum with τ delay of 0.1 s was acquired before prior to the acquisition of the 10 and 20 s-delay spectra, and the intensities of the NCA peaks in the 1, 10, 20 s spectra were normalized with respect to those in the 0.1 s spectra.

The T_1 decay curves were fitted to a single exponential with R_1 (longitudinal relaxation rate) being the only variable parameter.

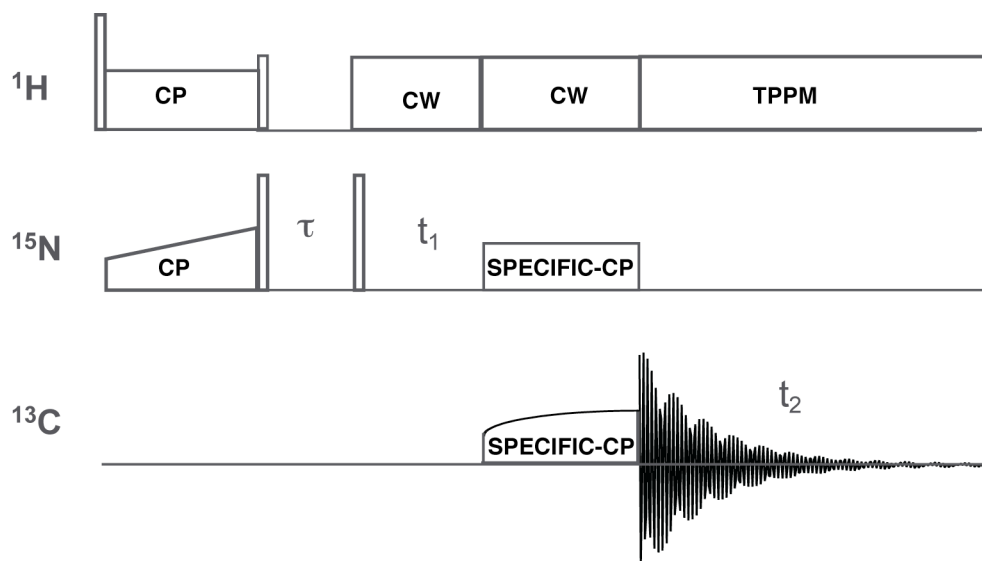


Figure 3.4: 3D ^{15}N T_1 -NCA pulse sequence employed for site-specific ^{15}N T_1 measurements of the C-terminal fragment of the U- ^{15}N -1-73/U- ^{13}C , ^{15}N -74-108 *E. coli* thioredoxin complex. The T_1 relaxation takes place during the τ delay.

3.2.8 ^{13}C - ^{13}C Correlation Spectra at Variable Temperatures

The 2D ^{13}C - ^{13}C DARR spectra were acquired at four temperatures; -5, -15, -25, and -35 °C. The spectra were collected with 512 t_1 points and 16 scans per t_1 point. The ^{13}C excitation frequency was 124.9 ppm. ^1H 90° pulse width was 3.1 μs . The contact time for the ^1H - ^{13}C CP was 1.25 ms. The ^1H radio frequency field strength was 50 kHz, the ^{13}C field was linearly ramped 80-100% with the center of the ramp being 40 kHz. The DARR mixing time was 10 ms. TPPM decoupling was used during t_2 ; the TPPM decoupling pulse width was 6 μs .

3.3. Results and Discussion

3.3.1 ^{15}N Chemical Shift Anisotropy

The chemical shift interaction is a sensitive probe of the local electronic environment around the nucleus. In particular, the backbone amide ^{15}N chemical shifts of proteins are extremely sensitive to several factors, such as the local conformation of the polypeptide chain, hydrogen bonding and dynamics. Although isotropic chemical shifts are directly available from the spectra in both solids and in solution, full CSA tensors could not be measured routinely in solids until recently in molecules containing multiple sites, including peptides and proteins. In MAS NMR, the advent of ROCSA, and more recently, *R*-symmetry based sequences, have made it possible to recouple the full CS tensor under MAS conditions [16,22,26,27]. In this section, we discuss the results of the site-specific ^{15}N CSA measurements of the *E. coli* thioredoxin complex using ROCSA, and the sensitivity of ^{15}N CSA tensors to internal dynamics, secondary structure and hydrogen bonding.

The first 2D NCA plane of the 3D ^{15}N ROCSA-NCA spectrum is shown in Figure 3.5. The experimental ^{15}N ROCSA lineshapes of 27 residues of the 35-residue C-terminal fragment of U- ^{15}N -1-73/U- ^{13}C , ^{15}N -74-108 labeled *E. coli* thioredoxin reassembly are shown in Figure 3.6 and 3.7 along with the best-fit lineshapes extracted from numerical simulations. The best-fit values of the reduced anisotropy and asymmetry parameter are given in Table 1.1 along with the three principal components of the ^{15}N CSA tensor.

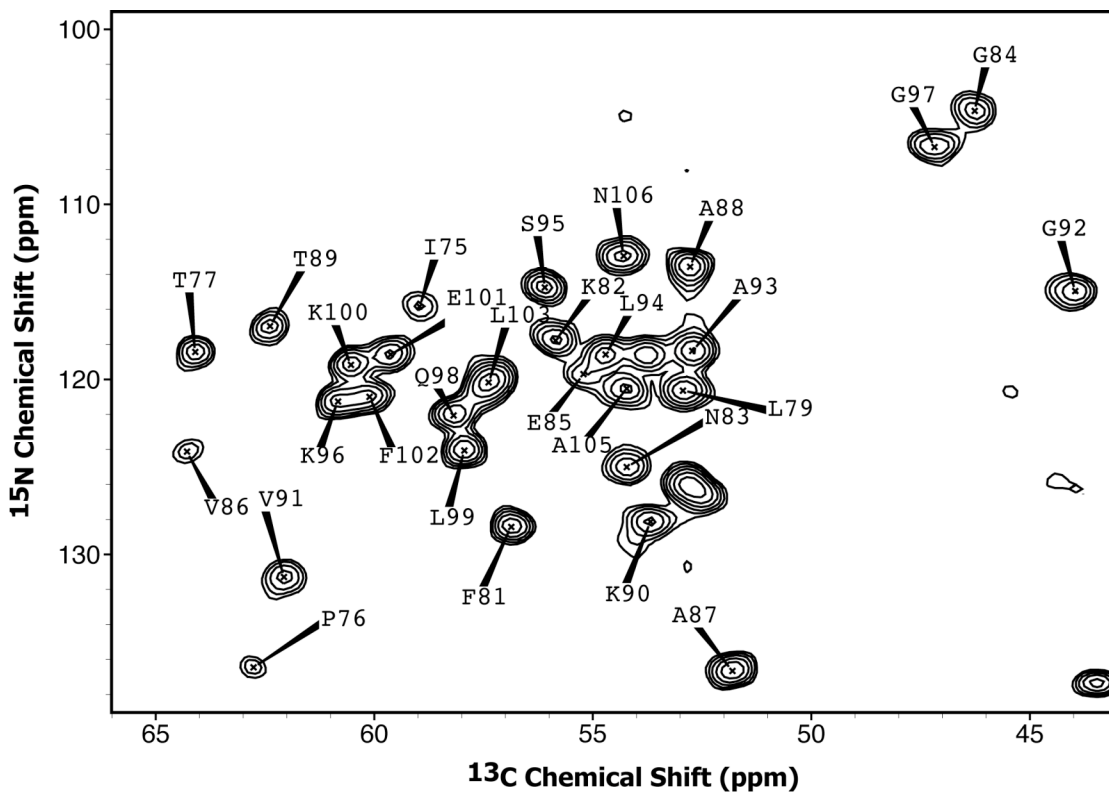


Figure 3.5: The first 2D NCA plane of the 3D ROCSA/NH-dipolar/ R_1 -NCA spectrum. A total of 27 peaks were resolved for the C-terminal fragment of U - ^{15}N -1-73/ U - ^{13}C , ^{15}N -74-108 labeled *E. coli* thioredoxin reassembly.

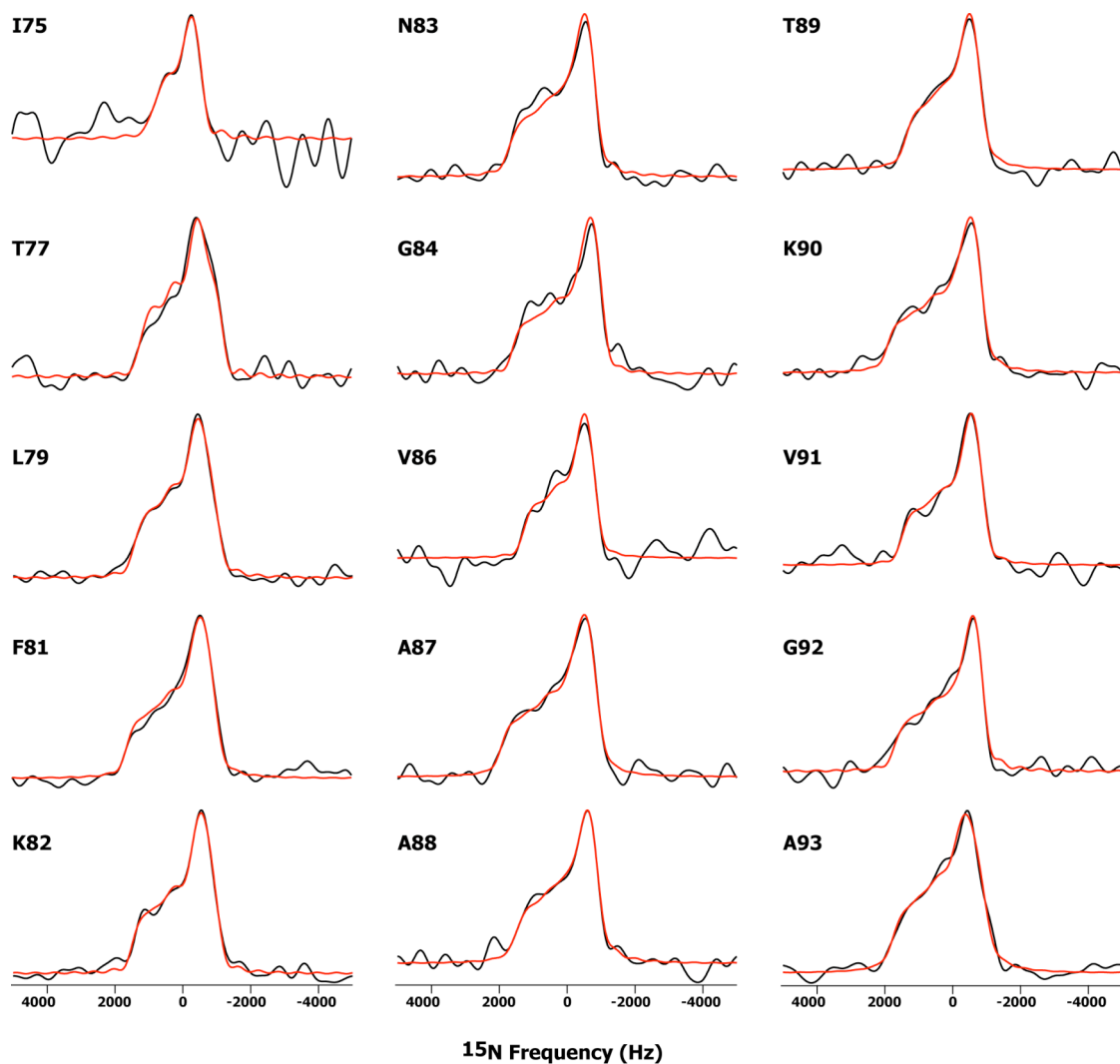


Figure 3.6: Site-specific backbone amide ^{15}N ROCSA lineshapes encompassing residues I75-A93 of the C-terminal fragment of U- ^{15}N -1-73/U- ^{13}C , ^{15}N -74-108 labeled *E. coli* thioredoxin reassembly. The experimental lineshapes are in black, the numerical simulations in red.

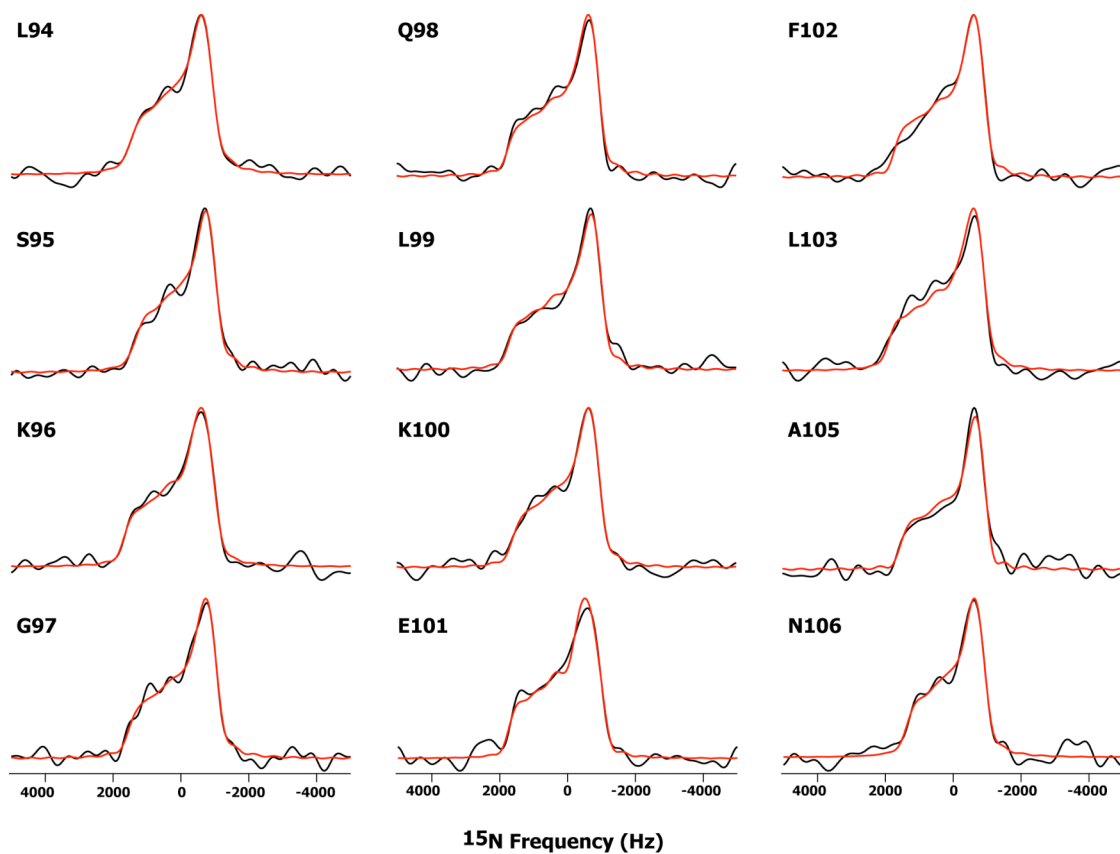


Figure 3.7: Site-specific backbone amide ^{15}N ROCSA lineshapes encompassing residues L94-N106 of the C-terminal fragment of U- ^{15}N -1-73/U- ^{13}C , ^{15}N -74-108 labeled *E. coli* thioredoxin reassembly. The experimental lineshapes are in black, the numerical simulations in red.

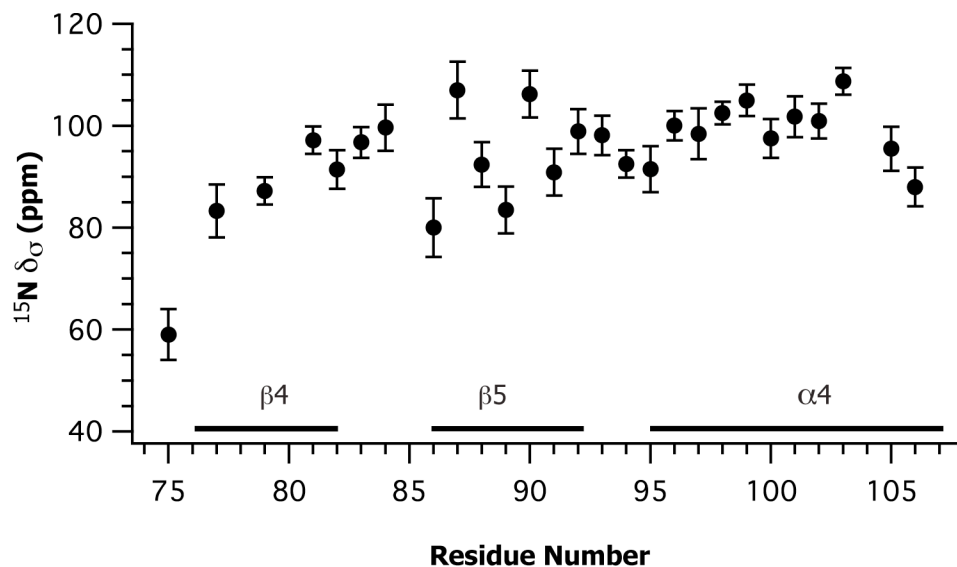


Figure 3.8: Variation of backbone amide $^{15}\text{N } \delta_{\sigma}$ as a function of residue number in $\text{U-}^{15}\text{N-1-73/U-}^{13}\text{C,}^{15}\text{N-74-108}$ *E. coli* thioredoxin reassembly.

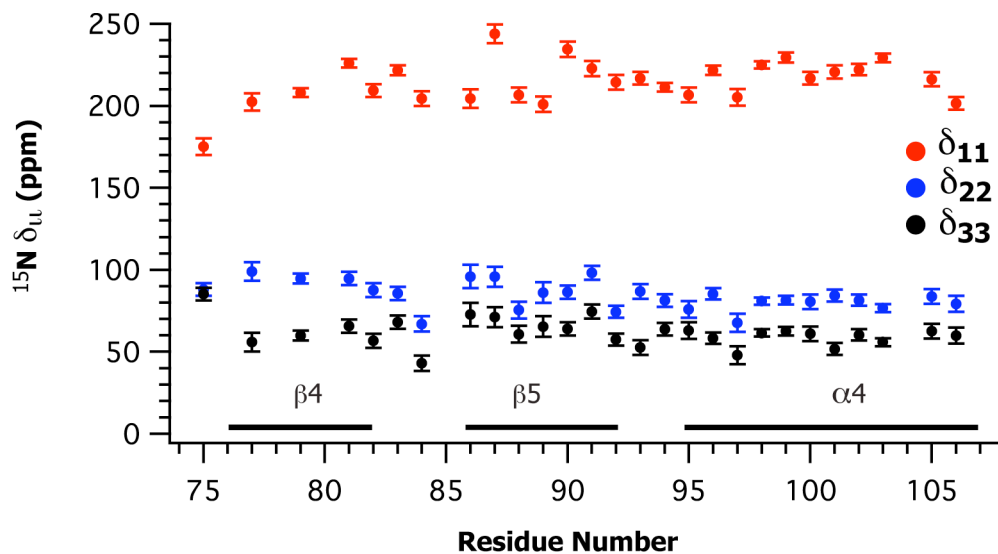


Figure 3.9: Variation of the principal components of the backbone amide ^{15}N CSA tensor as a function of residue number in $\text{U-}^{15}\text{N-1-73/U-}^{13}\text{C,}^{15}\text{N-74-108}$ *E. coli* thioredoxin reassembly.

Table 3.1 Summary of ^{15}N Chemical Shift Parameters for the C-terminal Fragment of U- ^{15}N -1-73/U- ^{13}C , ^{15}N -74-108-labeled *E. coli* Thioredoxin Reassembly.

Residue	δ_{σ} (ppm)	η_{σ}	δ_{11} (ppm)	δ_{22} (ppm)	δ_{33} (ppm)
I75	59.0 ± 5.0	0.05 ± 0.05	175.0 ± 5.0	88.0 ± 3.9	85.0 ± 3.9
T77	83.3 ± 5.2	0.52 ± 0.13	202.3 ± 5.2	99.0 ± 5.8	55.7 ± 5.8
L79	87.2 ± 2.7	0.40 ± 0.05	208.1 ± 2.7	94.7 ± 3.0	59.9 ± 3.0
F81	97.2 ± 2.7	0.30 ± 0.07	225.9 ± 2.7	94.7 ± 4.1	65.5 ± 4.1
K82	91.4 ± 3.8	0.34 ± 0.08	209.2 ± 3.8	87.6 ± 4.2	56.6 ± 4.2
N83	96.7 ± 3.0	0.18 ± 0.07	221.8 ± 3.0	85.5 ± 4.1	68.0 ± 4.1
G84	99.6 ± 4.5	0.24 ± 0.08	204.4 ± 4.5	67.0 ± 4.6	43.0 ± 4.6
V86	80.0 ± 5.8	0.29 ± 0.15	204.3 ± 5.8	95.9 ± 7.1	72.7 ± 7.1
A87	107.0 ± 5.6	0.23 ± 0.09	243.9 ± 5.6	95.7 ± 6.1	71.1 ± 6.1
A88	92.4 ± 4.4	0.16 ± 0.10	206.6 ± 4.4	75.4 ± 5.1	60.6 ± 5.1
T89	83.5 ± 4.6	0.25 ± 0.13	201.0 ± 4.6	86.2 ± 6.3	65.3 ± 6.3
K90	106.2 ± 4.6	0.21 ± 0.07	234.5 ± 4.6	86.4 ± 4.0	64.0 ± 4.0
V91	90.9 ± 4.6	0.26 ± 0.09	222.7 ± 4.6	98.2 ± 4.3	74.5 ± 4.3
G92	98.9 ± 4.4	0.17 ± 0.07	214.3 ± 4.4	74.4 ± 3.7	57.5 ± 3.7
A93	98.1 ± 3.9	0.35 ± 0.09	216.8 ± 3.9	86.8 ± 4.4	52.5 ± 4.4
L94	92.5 ± 2.7	0.19 ± 0.07	211.3 ± 2.7	81.3 ± 3.9	63.8 ± 3.9
S95	91.5 ± 4.5	0.14 ± 0.11	206.6 ± 4.5	75.8 ± 5.1	62.9 ± 5.1
K96	100.0 ± 2.9	0.27 ± 0.06	221.7 ± 2.9	85.2 ± 3.4	58.2 ± 3.4
G97	98.4 ± 5.0	0.20 ± 0.10	205.3 ± 5.0	67.5 ± 5.5	47.9 ± 5.5
Q98	102.5 ± 2.2	0.19 ± 0.04	224.9 ± 2.2	80.9 ± 2.3	61.4 ± 2.3
L99	105.0 ± 3.1	0.18 ± 0.04	229.5 ± 3.1	81.5 ± 2.7	62.6 ± 2.7
K100	97.5 ± 3.8	0.20 ± 0.09	216.9 ± 3.8	80.4 ± 4.4	60.9 ± 4.4
E101	101.8 ± 4.0	0.32 ± 0.05	220.7 ± 4.0	84.3 ± 3.7	51.7 ± 3.7
F102	100.9 ± 3.4	0.21 ± 0.06	222.2 ± 3.4	81.4 ± 3.5	60.3 ± 3.5
L103	108.7 ± 2.6	0.19 ± 0.05	229.2 ± 2.6	76.5 ± 2.5	55.8 ± 2.5
A105	95.5 ± 4.3	0.22 ± 0.08	216.3 ± 4.3	83.6 ± 4.4	62.5 ± 4.4
N106	88.0 ± 3.8	0.22 ± 0.09	201.5 ± 3.8	79.2 ± 4.8	59.8 ± 4.8

3.3.1.1 Dynamic Averaging of the ^{15}N Chemical Shift Anisotropy

The chemical shift interaction is sensitive to internal dynamics when the rate of the internal motion is roughly equal to or faster than the anisotropy of the CS tensor. The anisotropy of the backbone ^{15}N CS interaction (δ_σ) is of the order of 100 ppm, which is 6 kHz when the B_0 field is 14.1 T. Therefore, internal motions occurring on time scales of microseconds and faster give rise to the dynamic averaging of the backbone ^{15}N CSA values. The observed CS tensor in SSNMR bears direct information on the ensemble averaging due to fast internal motions.

As shown in Figure 3.8, the backbone amide ^{15}N CSA parameters exhibit significant variations from residue to residue with δ_σ ranging from 59 to 109 ppm. The mean reduced anisotropy δ_σ (\pm standard deviation) over 27 residues is 94.4 (\pm 10.3) ppm. The mean asymmetry parameter η_σ is 0.25 (\pm 0.08). The small η_σ values (less than 0.3 for most of the residues) are consistent with nearly axially symmetric ^{15}N CSA tensors observed by us and by others for the backbone amide nitrogens of microcrystalline proteins [16,22]. The C-terminal fragment encompassing residues 74-108 starts with a small loop region (G74-I75) near the cleavage site R73. This loop is not covalently bonded to the N-terminal fragment of the thioredoxin complex, but only through a hydrogen bond between R73 (N-terminal fragment) and G74 (C-terminal fragment). The three-dimensional structure of the *E. coli* thioredoxin complex is mainly stabilized by hydrogen bond interactions between the N-terminal β 2 and the C-terminal β 4 strands and hydrophobic interactions. In a previous study conducted on the N-terminal fragment of the thioredoxin complex in our group, Yang et al. have shown that R73 at the cleavage site is also very dynamic on the submicrosecond time scale with a ^{15}N reduced anisotropy δ_σ of 75.0 ppm [16]. In our

studies, we find that the loop containing G74 and I75 exhibits micro- to nanosecond dynamics as well: δ_σ of I75 is 59 ppm, dramatically reduced compared to the rigid-limit value. This is the smallest ^{15}N δ_σ of all the 27 residues of the C-terminal fragment analyzed in this work. We note that G74 is not present in the 2D NCA spectrum, likely due to the dynamic averaging of the C-N dipolar coupling and broadening of the peak beyond detection, which prevented its ^{15}N CSA tensor measurement. Our studies indicate that, in comparison to R73, the loop containing I75 is even more mobile on the submicrosecond time scale with ^{15}N CSA tensor exhibiting greater dynamic averaging.

Some interesting aspects of the highly flexible I75 residue can be inferred from analysis of the principal components of its ^{15}N CSA tensor and the comparison with the corresponding values for other residues in this sample. As illustrated in Table 1, I75 has the following principal components; $\delta_{11} = 175.0$ ppm, $\delta_{22} = 88.0$ ppm, and $\delta_{33} = 85.0$ ppm. The average values of the three principal components of the remaining 26 residues are 216.2 ppm (δ_{11}), 84.0 ppm (δ_{22}), and 60.6 ppm (δ_{33}). If we make a comparison between each of the individual principal components of I75 and the average of the corresponding values for the remaining 26 residues, we see that the deviation of δ_{22} (~4 ppm) is smaller than that of δ_{33} (~24 ppm), which is even smaller than that of δ_{11} (~41 ppm). Both δ_{22} and δ_{33} move downfield by ca. 4 and 24 ppm respectively, while δ_{11} moves upfield by 41 ppm. This reduces the overall breadth of the ^{15}N CS lineshape and hence the reduced anisotropy (δ_σ). Since δ_{22} is the least affected component, the motional axis must be parallel to the δ_{22} axis. A possible explanation for the directionality of the motion in the molecular frame can be given based on this comparison. In the literature on amide ^{15}N CS tensors, the component

δ_{11} is conventionally taken to be nearly parallel to the NH bond vector in the peptide plane (with a small angle in the range of 10° - 20°), and the δ_{22} component is perpendicular to the peptide plane [28,29]. Following this convention, we immediately see that the analysis of the principal CS components for I75 indicates the following:

- i) The internal motion takes place in the peptide plane (perpendicular to δ_{22}) of I75 giving rise to preferential averaging of δ_{11} .
- ii) Since δ_{11} and the NH vector are nearly collinear, we expect to see a motionally averaged NH dipolar coupling for this residue in the NH order parameter measurements. This is indeed the case for this residue, and is discussed in more detail in section 3.3.2 in the context of NH dipolar coupling measurements.

Apart from the loop close to the cleavage site, other loops/turns in the C-terminal fragment of the thioredoxin complex display only weak or no dynamic averaging of ^{15}N CS tensors. The mean reduced anisotropy for the residues lining β -turns (K82, N83, G84 connecting β 4 and β 5) and loops (A93, L94 connecting β 4 and α 4) is 95.7 ppm with a small standard deviation of 3.6 ppm. This value is about same as the average reduced anisotropy for all 27 residues, and indicates that there are no significant large-amplitude, submicrosecond time scale motions in the hairpin turn between β 4 and β 5 as well as in the loop connecting β 5 and α 4. The three residues forming the hairpin turn between strands β 4 and β 5 (K82, N83, G84) exhibit reduced anisotropies in the range between 91 and 100 ppm. In this segment, the NH group of K82 is hydrogen bonded to E85 in the crystal structure of *E. coli* thioredoxin (PDB code 2trx). Similarly, L94 in the loop connecting β 5 and α 4 is hydrogen bonded to

itself in the crystal structure. These hydrogen bond networks could possibly explain the increased rigidity of these residues and hence the lack of pronounced dynamic averaging of ^{15}N CSA tensors.

V86 at the start of β 5 strand has the second lowest reduced anisotropy of 80.0 ppm. The terminal location of V86 and the fact that it is not hydrogen bonded to any other residue are likely reasons for its increased submicrosecond mobility compared to other residues.

3.3.1.2 Secondary Structure Dependence

It has been shown in the literature that, the helical residues have higher ^{15}N δ_{σ} values than sheet residues [30]. Our measurements of ^{15}N CS tensors in U- ^{15}N -1-73/U- ^{13}C , ^{15}N -74-108 labeled *E. coli* thioredoxin reassembly revealed results consistent with prior reports. As illustrated in Table 1.2, the mean reduced anisotropy (\pm standard deviation) for the β -sheet residues (T77, L79, F81, V86, A87, A88, T89, K90, V91, G92) is 92.7 (\pm 9.5) ppm. The mean reduced anisotropy (\pm standard deviation) for the α -helical residues (S95, K96, G97, Q98, L99, K100, E101, F102, L103, A105, N106) is 99.1 (\pm 5.9) ppm. The α -helical residues have, on the average, ca. 6.0 ppm higher anisotropy than β -sheet residues.

The analysis of the principal components of the ^{15}N CS tensors associated with the α -helical and β -sheet residues reveals some interesting features of the dependence of δ_{ii} upon the secondary structure elements. A quick comparison of the average values of the individual principal components corresponding to the two secondary structure elements (helices and sheets) presented in Table 3.2 reveals that the δ_{11} component remains essentially unchanged (within the standard deviation) between α -helix and β -sheet whereas both δ_{22} and δ_{33} move upfield by ca. 10 and 6 ppm,

respectively, in going from β -sheet to α -helix, thus increasing the ^{15}N reduced anisotropy (δ_σ) by ca. 6 ppm.

In Figure 3.10, a histogram is shown illustrating the distribution of deviations of each ^{15}N CSA principal component from their average values (over 26 residues excluding I75). The residues are classified into α -helices (grey) and β -sheets (red). It is clear that the population distributions of both δ_{22} and δ_{33} are more sensitive to the secondary structure type than δ_{11} . In particular, for δ_{22} the population distributions of helices and sheets are well separated. As shown in Table 100, the average δ_{22} value for the helical residues is ca. 80.0 ppm, while that for the sheet residues is ca. 90.0 ppm. The difference of 10.0 ppm between the averages of two distributions of δ_{22} values is more than the overall standard deviation (8.7 ppm) and can be unambiguously interpreted as originating from the secondary structure type.

The δ_{33} component is also sensitive to secondary structure type; however, the population distributions of helical and sheet residues are not as well separated as for δ_{22} . The difference between the average δ_{33} values for the helix (58.5 ppm) and for the sheet (64.7 ppm) is about 6.0 ppm, which is slightly less than the standard deviation (7.2 ppm).

The population distribution of δ_{11} has the least sensitivity to secondary structure type compared to the other principal components. The helical residues have a distribution that centers at 2 ppm, which is much smaller than the standard deviation of δ_{11} (11.2 ppm), while the sheet residues have a much wider distribution with zero mean.

In conclusion, the analysis of the principal components of the backbone amide ^{15}N CSA tensors of *E. coli* thioredoxin reveals that the δ_{22} component of ^{15}N CSA

tensor (which is perpendicular to the peptide plane) is the most sensitive to the secondary structure type and the δ_{11} component (parallel to the NH bond vector) the least sensitive. This statistical observation is also consistent with the analysis of the principal components of ^{15}N CSA tensors of the N-terminal fragment of the U- ^{13}C , ^{15}N -1-73 / U- ^{15}N -74-108 *E. coli* thioredoxin complex (results not shown).

Table 3.2 Summary of the Statistical Mean (\pm Standard Deviation) of the Backbone Amide ^{15}N CSA Parameters of U- ^{15}N -1-73/U- ^{13}C , ^{15}N -74-108 *E. coli* Thioredoxin Reassembly as a Function of Secondary Structure Type.

Secondary structure type	δ_{σ} (ppm)	η_{σ}	δ_{11} (ppm)	δ_{22} (ppm)	δ_{33} (ppm)
Helix	99.1 ± 5.9	0.21 ± 0.05	217.7 ± 9.5	79.7 ± 5.0	58.5 ± 4.9
Sheet	92.7 ± 9.5	0.28 ± 0.11	216.4 ± 14.8	90.0 ± 9.1	64.7 ± 6.5
Others	95.7 ± 3.6	0.26 ± 0.08	212.7 ± 6.8	81.6 ± 8.6	56.8 ± 9.8
All	96.0 ± 7.6	0.25 ± 0.08	216.2 ± 11.2	84.0 ± 8.7	60.6 ± 7.2

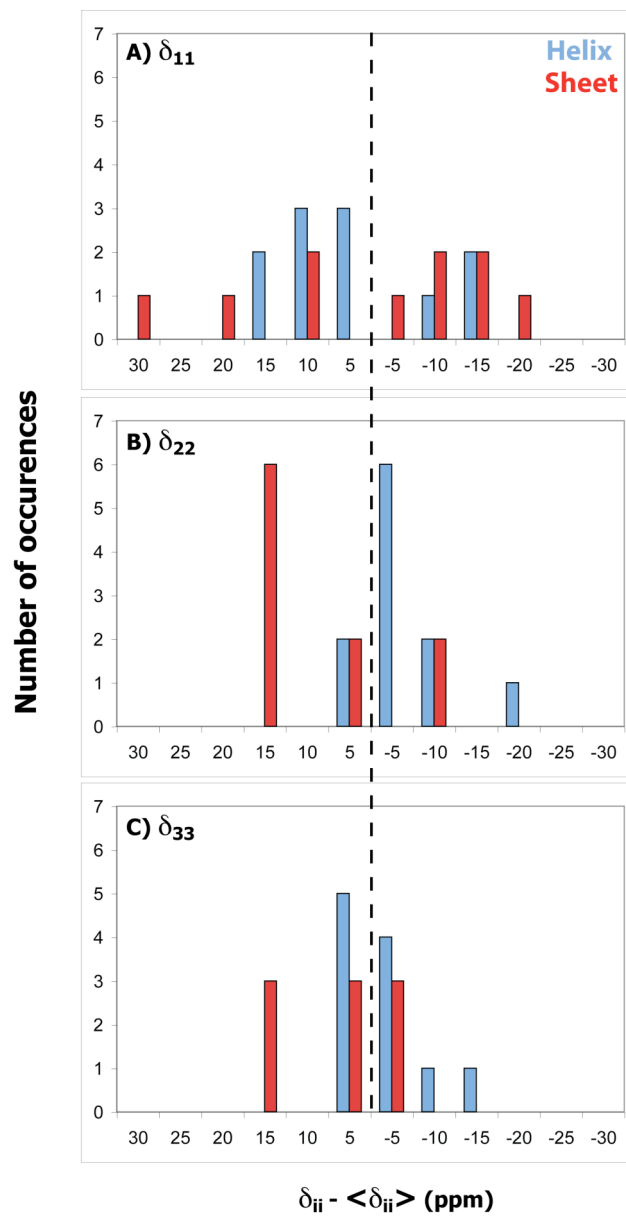


Figure 3.10: A histogram of the deviation of the principal components of the ^{15}N CSA tensor for the two secondary structure types from their mean values. The dashed line indicates the mean value over 26 residues in $\text{U-}^{15}\text{N-1-73}/\text{U-}^{13}\text{C}, ^{15}\text{N-74-108}$ *E. coli* thioredoxin reassembly.

3.3.1.3 Effect of Hydrogen Bonding

It is very well known from previous studies that the CS tensors of both amide nitrogens and amide hydrogens are significantly affected by the hydrogen bond interactions of the NH group with other residues in the protein [31,32]. In the C-terminal fragment of the U-¹⁵N-1-73/U-¹³C,¹⁵N-74-108 *E. coli* thioredoxin reassembly, we observed that hydrogen bonded residues have higher amide ¹⁵N reduced anisotropies (δ_σ) compared to the non-hydrogen bonded residues. Of the 10 residues in β -strands β 4 and β 5, five (L79, F81, A87, K90, G92) are hydrogen bonded. These residues also have the largest δ_σ values ranging between 97.2 and 107.0 ppm with L79 being the only exception ($\delta_\sigma = 87.2$ ppm). The non-hydrogen-bonded residues (T77, V86, A88, T89, V91) have δ_σ in the range between 80.0 and 92.4 ppm. Among the 11 residues in the α 4, eight residues (Q98-N106) are hydrogen bonded. Five of them (Q98, K100, E101, F102, L103) have δ_σ higher than 100.0 ppm. Among these five, L99 and L103 have the largest δ_σ of 105.0 and 108.7 ppm, respectively. In the X-ray crystal structure of *E. coli* thioredoxin, these two residues are doubly-hydrogen bonded. L99 is hydrogen bonded to the carbonyl groups of S95 and K96, while L103 is hydrogen bonded to the carbonyl groups of L99 and K100. Of the remaining three hydrogen bonded residues, A105 and N106 have δ_σ of 95.5 and 88.0 ppm, which are much lower than the average value for the α -helix. This is possibly due to the increased motional averaging at the C-terminal end of the complex.

The analysis of the three principal components of the backbone ¹⁵N CS tensors of hydrogen-bonded versus non-hydrogen-bonded residues (illustrated in Table 3.3) sheds light onto the unique sensitivity of the molecular-frame orientation of the individual components to hydrogen bonding. Table 3.3 reveals that δ_{22} and δ_{33} are essentially invariant (within their standard deviations), regardless of whether a residue

participates in a hydrogen bond or not. It is only δ_{11} that moves downfield from 210 to 220 ppm upon hydrogen bonding, thus increasing the reduced anisotropy (δ_σ) by about 6 ppm. In Figure 3.11, a histogram is shown illustrating the distribution of deviations of each ^{15}N CS principal component from their average values (over 26 residues excluding I75). The residues are classified into two types: hydrogen bonded (grey) and non-hydrogen bonded (red). As shown in A, the hydrogen-bonded residues have a δ_{11} distribution centered around 4.4 ppm, while the center of the δ_{11} distribution for the non-hydrogen bonded residues is at -6.0 ppm. The difference of 10 ppm is significant as it is about the same size as the standard deviation for δ_{11} (11.2 ppm). The deviations in the other two principal components δ_{22} and δ_{33} are not as sensitive to hydrogen bonding as that in δ_{11} . This is evident from Figures 3.11 B and C as there is a equal distribution of populations for both hydrogen-bonded and non-hydrogen-bonded residues on either side with the mean around 0 ppm. The average δ_{22} value for the hydrogen-bonded residues (84.2 ppm) coincides with that of the non-hydrogen-bonded residues (83.9 ppm). The average δ_{33} value of for the hydrogen-bonded residues (60.9 ppm) is also very close to that of the non-hydrogen-bonded residues (61.1 ppm).

In conclusion, the δ_{11} component of the backbone amide ^{15}N CS tensor is observed to be the most sensitive to hydrogen-bond interactions, while both δ_{22} and δ_{33} do not exhibit any significant differences in the presence of hydrogen bonds. The δ_{11} component acquires unique sensitivity to hydrogen bonding, mainly due to its parallel orientation with respect to the NH bond vector (the β angle of 10° - 20°).

Table 3.3 Summary of the Statistical Mean (\pm Standard Deviation) of the Backbone Amide ^{15}N CS Parameters of U- ^{15}N -1-73/U- ^{13}C , ^{15}N -74-108 *E. coli* Thioredoxin Reassembly with respect to Hydrogen Bond Interactions

Type	δ_{σ} (ppm)	η_{σ}	δ_{11} (ppm)	δ_{22} (ppm)	δ_{33} (ppm)
H-bonded	98.7 ± 6.8	0.24 ± 0.07	220.6 ± 11.2	84.2 ± 6.6	60.9 ± 4.6
Non H-bonded	92.2 ± 7.2	0.26 ± 0.11	210.3 ± 8.6	83.9 ± 11.3	60.1 ± 9.9

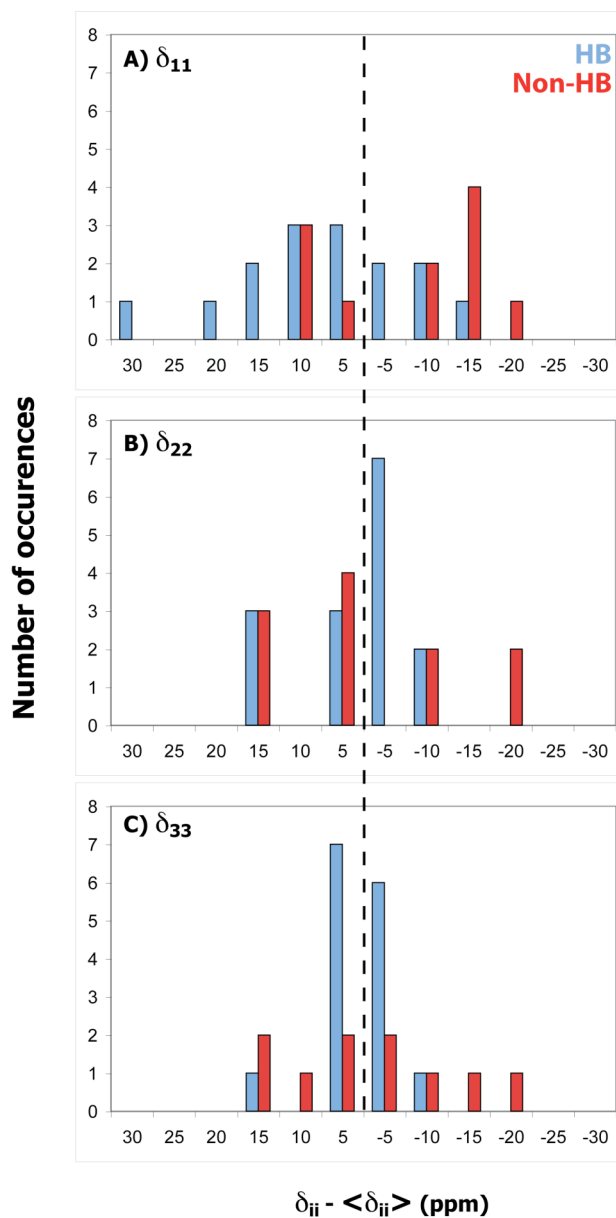


Figure 3.11: A histogram of the deviation of the principal components of the ^{15}N CSA tensor for hydrogen-bonded and non-hydrogen-bonded residues. The dashed line indicates the mean value over 26 residues in U- ^{15}N -1-73/U- ^{13}C , ^{15}N -74-108 *E. coli* thioredoxin reassembly.

3.3.2 NH Dipolar Order Parameters

Site-specific backbone amide NH dipolar couplings are an important source of information about internal dynamics on the micro- to nanosecond time scales both in solution and in solids. When there is no internal motion, the NH dipolar coupling is at its rigid limit value of 10.83 kHz corresponding to an inter-nuclear distance of 1.04 Å. When internal motions are present and their rates are faster than the NH dipolar frequency, the dipolar interaction is scaled according to the amplitude of the motion [33]. The larger the amplitude of the internal motion, the greater the reduction of the NH dipolar interaction. It is important to note that the averaged NH dipolar coupling contains no information about the time scale of the internal motion, but only about the motional amplitude. Thus, site-specific NH dipolar couplings are a direct source of information on the amplitude of internal submicrosecond time scale motions of the NH group of each residue. It is customary to report NH dipolar couplings as order parameters ($\langle S \rangle$), which represent a ratio of the actual NH dipolar coupling to its rigid limit value. Thus $\langle S \rangle$ ranges from 0 (complete isotropic motion) to 1 (motionless rigid NH group).

Site-specific measurements of motional amplitude parameters of proteins in solution is complicated by the overriding isotropic tumbling motion. In the absence of the global tumbling motion in solids, these parameters can be accessed directly by measuring the NH dipolar interaction by a suitable recoupling sequence.

In this section, the solid-state NH order parameters of C-terminal fragment (74-108) of the U- ^{15}N -1-73/U- ^{13}C , ^{15}N -74-108 *E. coli* thioredoxin reassembly are discussed. The experimental NH dipolar lineshapes of the 27 residues resolved in the 2D spectra are shown in Figure 3.12 and 3.13, together with best-fit lineshapes

extracted from numerical simulations. The best-fit NH dipolar couplings are given in Table 3.4.

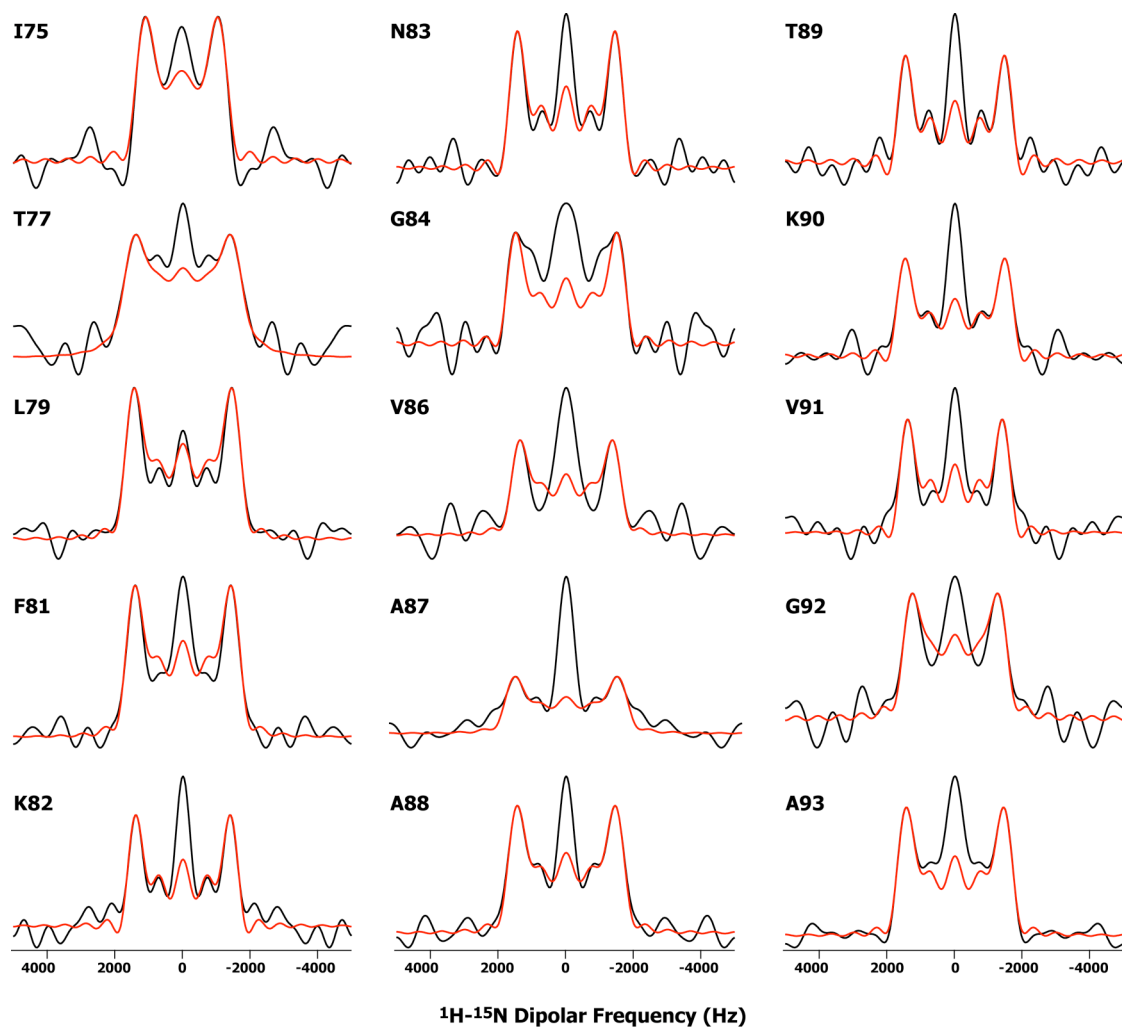


Figure 3.12: Site-specific backbone amide NH R18₁⁷ lineshapes encompassing residues I75-A93 of the C-terminal fragment of U-¹⁵N-1-73/U-¹³C,¹⁵N-74-108 *E. coli* thioredoxin reassembly. The experimental lineshapes are in black, the numerical simulations in red. The zero-frequency peak was not included in the fit.

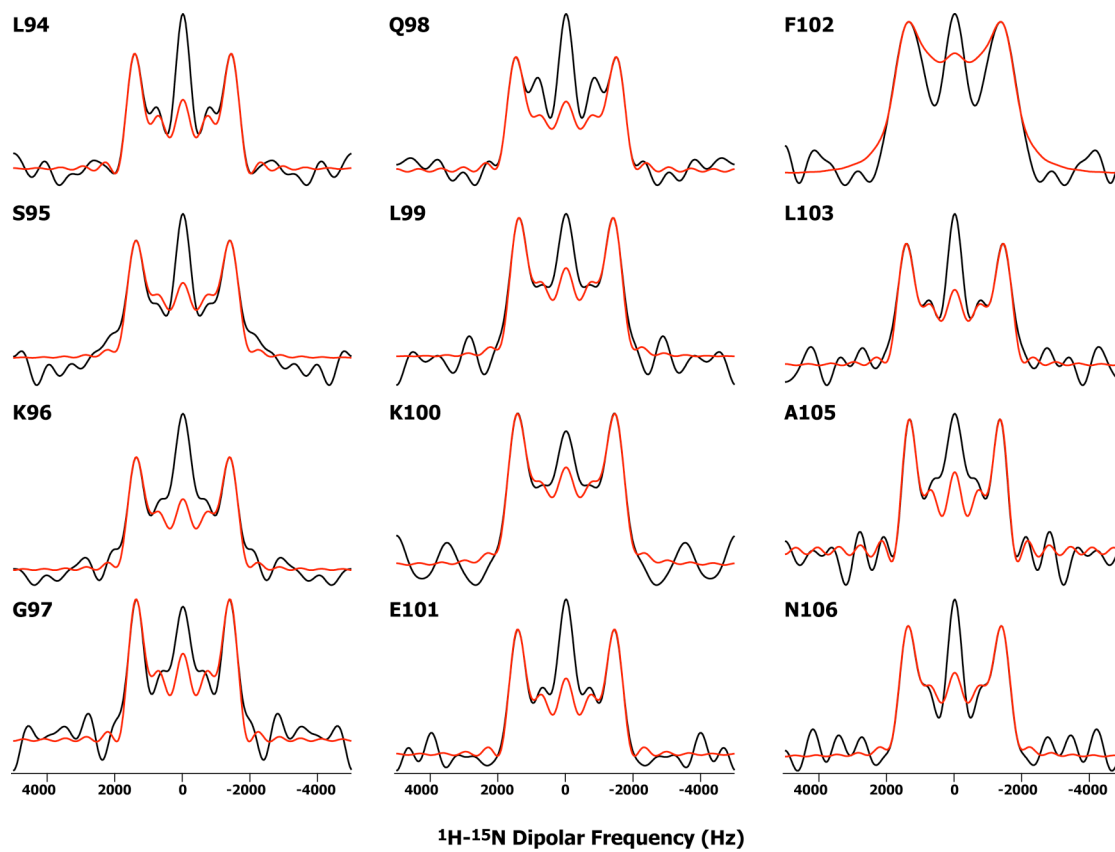


Figure 3.13: Site-specific backbone amide NH R18₁⁷ lineshapes encompassing residues L94-N106 of the C-terminal fragment of U-¹⁵N-1-73/U-¹³C,¹⁵N-74-108 *E. coli* thioredoxin reassembly. The experimental lineshapes are in black, the numerical simulations in red. The zero-frequency peak was not included in the fit.

Table 3.4 Summary of Backbone NH Dipolar Order Parameters for the C-Terminal Fragment of the U-¹⁵N-1-73/U-¹³C, ¹⁵N-74-108 *E. coli* Thioredoxin Reassembly.

Residue	$\langle S \rangle_{\text{NH}}$
I75	0.71
T77	0.92
L79	0.93
F81	0.91
K82	0.89
N83	0.92
G84	0.96
V86	0.88
A87	0.94
A88	0.93
T89	0.93
K90	0.94
V91	0.90
G92	0.81
A93	0.92
L94	0.91
S95	0.90
K96	0.89
G97	0.89
Q98	0.95
L99	0.90
K100	0.93
E101	0.92
F102	0.92
L103	0.92
A105	0.85
N106	0.89

3.3.2.1 Dynamic Averaging of NH Dipolar Couplings

The backbone NH dipolar order parameters extracted from the solid-state DIPSHIFT spectra for the 27 residues of the 35-residue C-terminal fragment of U-¹⁵N-1-73/U-¹³C,¹⁵N-74-108 *E. coli* thioredoxin reassembly are in the range of 0.71–0.96. As discussed in reference 12, the absolute value of the NH dipolar order parameters depends on the choice of rigid-limit value of the NH bond length. In this work, we have used 1.04 Å as the vibration-averaged rigid-limit NH bond length corresponding to the NH dipolar coupling constant of 10.83 kHz [34]. The mean NH dipolar order parameter (\pm standard deviation) over 27 residues is 0.90 (\pm 0.05). The standard deviation is only about 5.5% of the average value, which indicates that most of the residues have essentially the same NH order parameter without much site-to-site variation due to internal dynamics. This is illustrated in Figure 3.14.

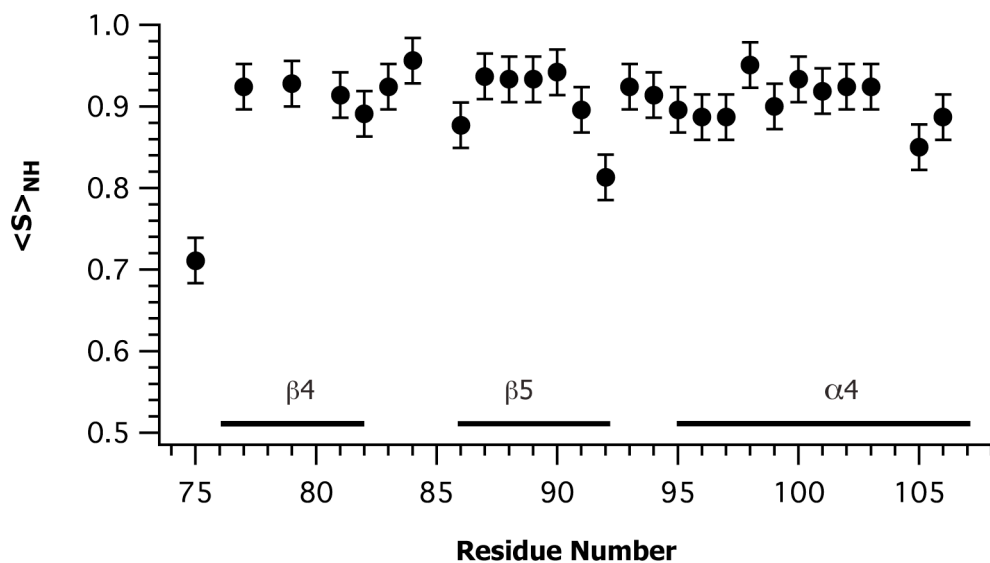


Figure 3.14: Variation of backbone NH dipolar order parameter as a function of residue number in U- ^{15}N -1-73/U- ^{13}C , ^{15}N -74-108 *E. coli* thioredoxin reassembly.

Similar to our observation of the highly reduced ^{15}N CS tensor in I75 (see above), this residue located in the loop close to the cleavage site (R73) exhibits the smallest NH dipolar coupling of 7.7 kHz (dipolar order parameter of 0.71), indicating that it is very dynamic on the submicrosecond time scale. For comparison, the mean order parameter $\langle S \rangle$ over 27 residues is 0.90.

Apart from I75, the remaining residues in the C-terminal fragment of U- ^{15}N -1-73/U- ^{13}C , ^{15}N -74-108 *E. coli* thioredoxin reassembly display only weak or no dynamic averaging of the NH dipolar interaction, indicating that the C-terminal fragment is largely rigid on the submicrosecond time scale. This trend is consistent with our results for the amide ^{15}N CSA values. Apart from I75, only 9 residues (K82, V86, V91, G92, S95, K96, G97, A105, N106) out of 26 have NH order parameters less than or equal to the mean value 0.90. Interestingly, these residues are located either in turns or termini of regular secondary structure elements, which are expected to exhibit

increased internal mobility on the submicrosecond time scale and, hence, lower dipolar order parameters. K82 is located at the start of the turn connecting $\beta 4$ and $\beta 5$. V86 is at the start of $\beta 5$, while V91 and G92 are the end residues of $\beta 5$. S95, K96, G97 are at the initial portion of $\alpha 4$ and have no hydrogen bonding partners while both A105 and N106 are close to the C-terminal end of the complex ($\alpha 4$).

There is no noticeable secondary structure dependence of NH dipolar order parameters: the average values for both helical and sheet residues are equal to 0.91. The loop/turn residues excluding I75 have an average order parameter of 0.92, which is about the same as that for helices and sheets. Overall the NH order parameter data indicate that the backbone of the C-terminal fragment of U- ^{15}N -1-73/U- ^{13}C , ^{15}N -74-108 *E. coli* thioredoxin reassembly is rigid on submicrosecond time scales with flexible portions located only at the loop/turn regions and the termini of $\beta 4$ and $\alpha 4$.

Since the amide ^{15}N CSA and NH dipolar couplings are about the same order of magnitude (6.0 kHz and 10.8 kHz, respectively), dynamic averaging of these two parameters by local motions of the backbone can be correlated, if the same motion is responsible for the averaging of the two parameters. For the ten residues (I75, K82, V86, V91, G92, S95, K96, G97, A105, N106) whose NH dipolar order parameters are smaller than or equal to 0.90, we have compared the order parameters with the ^{15}N CSA values to assess whether there is any significant correlation between these two parameters for the above residues. Interestingly, six of these ten residues (I75, K82, V86, V91, S95, N106) exhibit ^{15}N reduced anisotropy values (δ_σ) smaller than the overall average (94.4 ppm) for the C-terminal fragment of the (I75, K82, V86, V91, S95, N106). The remaining four residues (G92, K96, G97, A105) exhibit ^{15}N δ_σ in the range of 96-100 ppm.

3.3.2.2 Comparison with Solution NMR Order Parameters

Backbone dynamics of *E. coli* thioredoxin has been studied in solution.[35] Using the Lipari-Szabo model-free formalism (which is discussed in section 3.3.3), Stone et al. reported site-specific values for generalized solution NH order parameters (S) and correlation times for fast internal motions extracted from ^{15}N R_1 , R_2 and ^1H - ^{15}N NOE rates. A comparison between generalized solution and dipolar solid-state NH order parameters could reveal the degree of correlation between the internal motions in the two states. Figure 3.15 illustrates the comparison between the generalized solution and the dipolar solid-state order parameters. There is no clear trend between the variation of solution and solid-state order parameters along the backbone, which suggests that the differences could be due to the fact that solution results emphasize nanaosecond to picosecond time scale motions and are insensitive to microsecond time scale dynamics, while solid-state NMR is sensitive to both time scales. This observation is consistent with other micro-crystalline proteins such as ubiquitin [15].

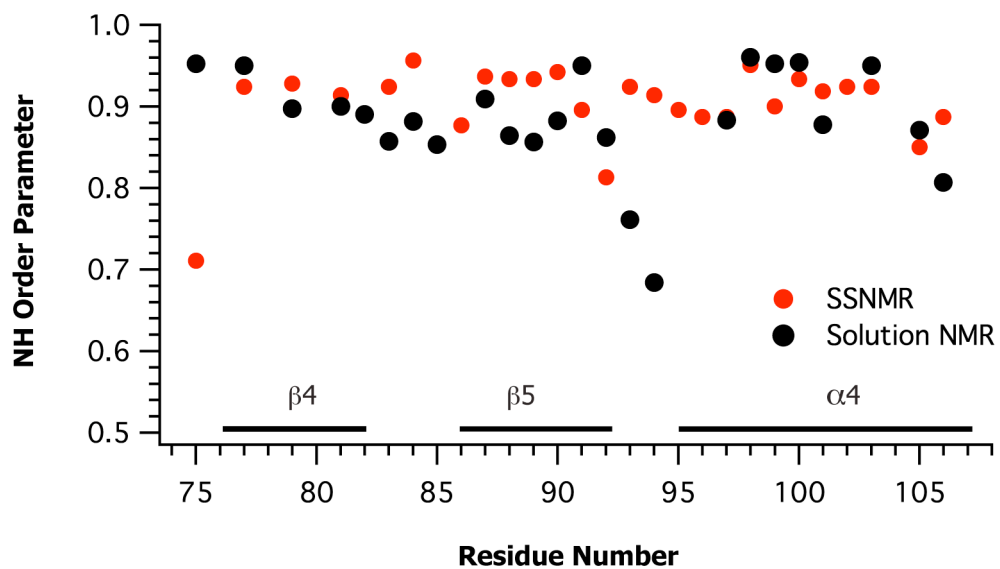


Figure 3.15: Comparison of solid-state NH dipolar order parameters with generalized solution order parameters for the C-terminal fragment of U- ^{15}N -1-73/U- ^{13}C , ^{15}N -74-108 *E. coli* thioredoxin reassembly.

3.3.2.3 NH Bond Lengths and Hydrogen Bonding

In the absence of any significant internal dynamics, the NH dipolar couplings can be quite sensitive to structural perturbations such as the elongation of the NH bond distance due to hydrogen bonding interactions [36]. This could also contribute to lower order parameters and hence allow for a possible distinction between hydrogen bonded versus non-hydrogen bonded residues. In our analysis of the NH order parameters of the C-terminal fragment of the U-¹⁵N-1-73/U-¹³C,¹⁵N-74-108 *E. coli* thioredoxin reassembly, we observed no correlation between the NH dipolar couplings and hydrogen bonding interactions. Regardless of whether a particular residue is hydrogen bonded or not, the average NH order parameter is equal to 0.91.

3.3.3 ¹⁵N Longitudinal Relaxation Rates (R_1)

NMR relaxation measurements have long been in use to study dynamics of proteins. The backbone amide ¹⁵N relaxation rates (both longitudinal and transverse) are measured site-specifically to probe picosecond-to-nanosecond time scale motions in solution [35]. The relaxation rates (which are reciprocal of the relaxation times) are directly proportional to the spectral density of the motion, which is a function of both the amplitude and the time scale of the internal motion. Thus, relaxation rates complement order-parameter and CSA measurements in the solid state in that they provide additional information on the time scale of the internal motion. The random local fields that contribute to the relaxation of the amide ¹⁵N nucleus originate primarily from the fluctuating NH dipolar interaction and secondarily from the ¹⁵N CSA interaction [37]. In solids, longitudinal relaxation rates (R_1) are more widely used to study the motional processes than transverse relaxation rates (R_2) which have

contributions mainly from the static dipolar interactions [38]. It has been shown previously that the spin diffusion between backbone ^{15}N nuclei of two neighboring residues does not interfere significantly with ^{15}N R_1 measurements in the solid state [39].

In this section, we present the measurements of the ^{15}N longitudinal relaxation rates of the C-terminal fragment (74-108) of U- ^{15}N -1-73/U- ^{13}C , ^{15}N -74-108 *E. coli* thioredoxin reassembly, and discuss the results in terms of internal backbone dynamics.

The cross peak intensity decay was examined for the 29 resolved residues in the 2D NCA spectrum. However, due to the inherently low sensitivity of the heteronuclear correlation experiments on the C-terminal fragment of the complex, magnetization decay curves for nine residues could not be extracted with high enough precision to permit accurate determination of the longitudinal relaxation rates. As a result, the decay curves for only 20 of the 29 residues were analyzed. The cross-peak intensity decay for each of these residues was fitted to a single exponential function (with a fixed coefficient of one). The resulting R_1 values with their uncertainties are presented in Table 3.5. Considering the inherent intensity fluctuations in the T_1 decay curves, we further restricted the T_1 analysis to 13 residues, which exhibit the exponential fit correlation coefficient $R^2 \geq 0.96$. The T_1 decay curves of these 13 residues along with the exponential fits are presented in Figure 3.16, and a summary of R_1 values as a function of residue number is given in Figure 3.17.

Of the thirteen residues under analysis, three belong to loops (I75, A93, L94), five are part of the helix α_4 , and the remaining five comprise the β -strands β_4 and β_5 .

The average R_1 values are 0.040 s^{-1} for the helix, 0.020 s^{-1} for the β -strands, and 0.055 s^{-1} for the loops. Consistent with the results of both ^{15}N CSA and NH dipolar coupling experiments, I75 is the most dynamic residue with the highest R_1 value of 0.346 s^{-1} , which corresponds to a T_1 of ca. 3 s. The cross-peak corresponding to this residue is present only in the spectra acquired with a τ delay of 100 ms and 1 s, and disappears completely at longer τ delays. The two other loop residues A93, L94 connecting β_4 and α_4 have R_1 values 0.0318 and 0.0405 s^{-1} , respectively. The turn residues K82, N83, G84 connecting the two strands β_4 and β_5 are not included in the analysis as their R^2 values are smaller than 0.96 s^{-1} . However, their R_1 values show an interesting trend. Among these three, K82 appears to be rigid with the R_1 value of 0.014 s^{-1} . As discussed previously, this residue is hydrogen bonded to E85 in the X-ray crystal structure of *E. coli* thioredoxin. The residues N83 and G84 have higher R_1 values ($\geq 0.044\text{ s}^{-1}$) compared to K82, which indicate higher flexibility of these two residues in the turn region and in the absence of any hydrogen bonding interaction.

Among the residues lining the two secondary structure elements, there is no significant difference observed in their R_1 values. However, there are notable outliers. First, G92 stands out as having a relatively high R_1 of 0.0399 s^{-1} among the β -sheet residues. This is the terminal residue of β_5 . It is interesting to note that this residue has an NH order parameter of 0.81, which is much lower than the average value over the 27 residues (0.90). Second, A105 and N106 located at the C-terminal end of α_4 helix with exhibit high R_1 values in the range $0.046 - 0.064\text{ s}^{-1}$. These residues also have relatively lower order parameters (0.85 for A105 and 0.89 for N106).

In summary, the backbone amide ^{15}N longitudinal relaxation rates suggest increased flexibility of residues in the loop/turn regions and also at the termini of the

secondary structure elements. This trend is consistent with the variation of NH order parameters along the backbone in the C-terminal fragment of thioredoxin.

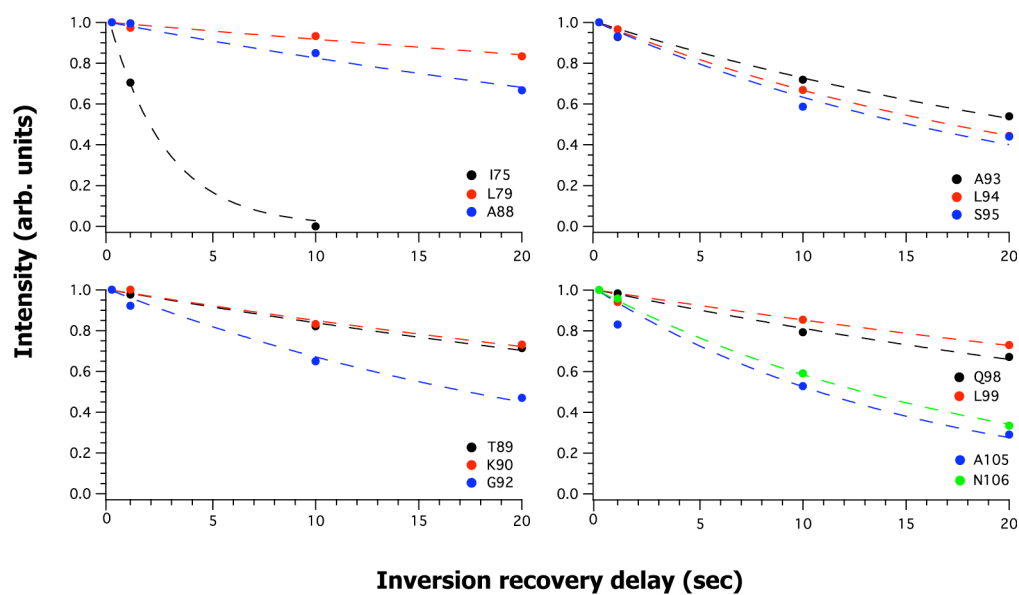


Figure 3.16: ^{15}N T_1 decay curves obtained from the 3D T_1 -NCA experiment in $\text{U-}^{15}\text{N-1-73}/\text{U-}^{13}\text{C,}^{15}\text{N-74-108}$ *E. coli* thioredoxin reassembly. The experimental points were fit to exponential functions.

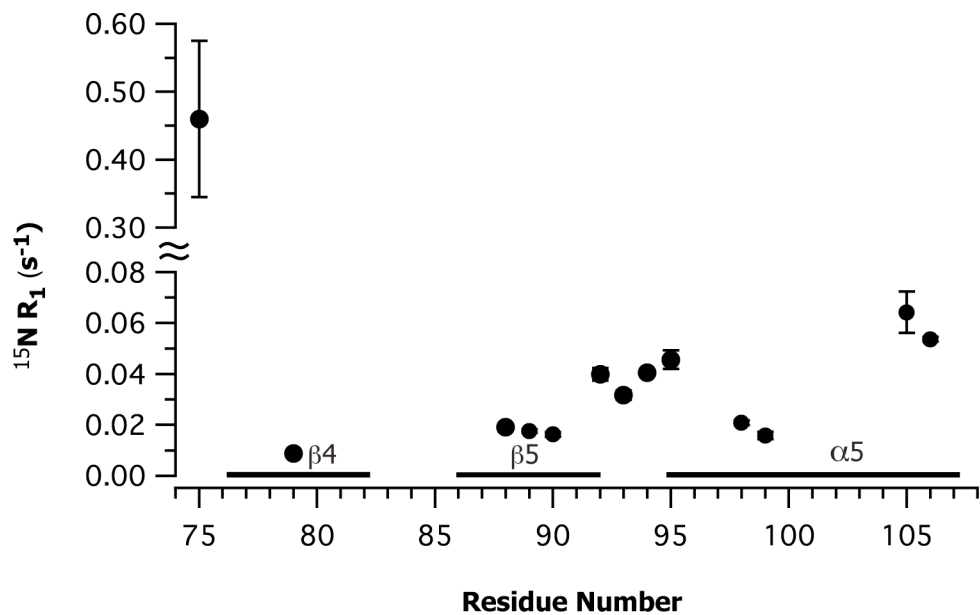


Figure 3.17: Variation of ^{15}N R_1 values as a function of residue number in U- ^{15}N -1-73/U- ^{13}C , ^{15}N -74-108 *E. coli* thioredoxin reassembly.

Table 3.5 Summary of Backbone ^{15}N R_1 values for the C-terminal Fragment of the U- ^{15}N -1-73/U- ^{13}C , ^{15}N -74-108 *E. coli* Thioredoxin Reassembly.

Residue	^{15}N R_1 (s^{-1})
I75	0.4600±0.1150
L79	0.0086±0.0007
A88	0.0192±0.0012
T89	0.0176±0.0007
K90	0.0163±0.0009
G92	0.0399±0.0025
A93	0.0318±0.0019
L94	0.0405±0.0004
S95	0.0457±0.0037
Q98	0.0208±0.0009
L99	0.0159±0.0015
A105	0.0643±0.0081
N106	0.0537±0.0009

3.3.4. Correlation Between Solid-State NH Dipolar Order Parameters and ^{15}N R_1

As discussed above, longitudinal relaxation experiments are sensitive to the motions on the picosecond-to-nanosecond time scales, while the anisotropic lineshape experiments (CSA, dipolar) are sensitive to motions on the microsecond and faster time scale. In principle, a comparison between these experimentally determined parameters (^{15}N CSA, NH dipolar coupling, and ^{15}N R_1) performed in a site-specific manner could reveal important information on the correlation between motions on submicrosecond and picosecond-to-nanosecond time scales. For example, I75 is

found to be very dynamic with a strong correlation between motions on all time scales recorded in our experiments (from submicroseconds to picoseconds), as it has the smallest ^{15}N CSA, and NH order parameter, and ^{15}N T_1 value. However, for other residues (whose SSNMR parameters exhibit weaker motional averaging), the ^{15}N CSA is, in addition to dynamics, sensitive to several other factors, such as hydrogen bonding and secondary structure type as discussed in section 3.3.1. For this reason, it would be more reasonable to compare the solid-state NH dipolar order parameters directly with the ^{15}N R_1 values to determine the degree of correlation between motions on submicrosecond and picosecond-to-nanosecond time scales.

To find out the correlation between relaxation and NH order parameters, we have applied the model-free formalism of Lipari and Szabo [40,41] which has been widely used in the literature for the interpretation of solution NMR relaxation and NOE rates in the context of internal dynamics of proteins in solution. Recently, solid-state NMR dipolar order parameters and relaxation rates have also been interpreted in the literature using the same model-free formalism [42]. Assuming that the NH dipolar coupling is the only relaxation mechanism, ^{15}N R_1 is directly proportional to the spectral density at three frequencies: the zero-quantum frequency, the ^{15}N single-quantum frequency, and the double-quantum frequency.

$$R_1 = \frac{1}{10} \omega_D^2 \{J_0(\omega_H - \omega_N) + 3J_1(\omega_N) + 6J_2(\omega_H + \omega_N)\} \quad (3.1)$$

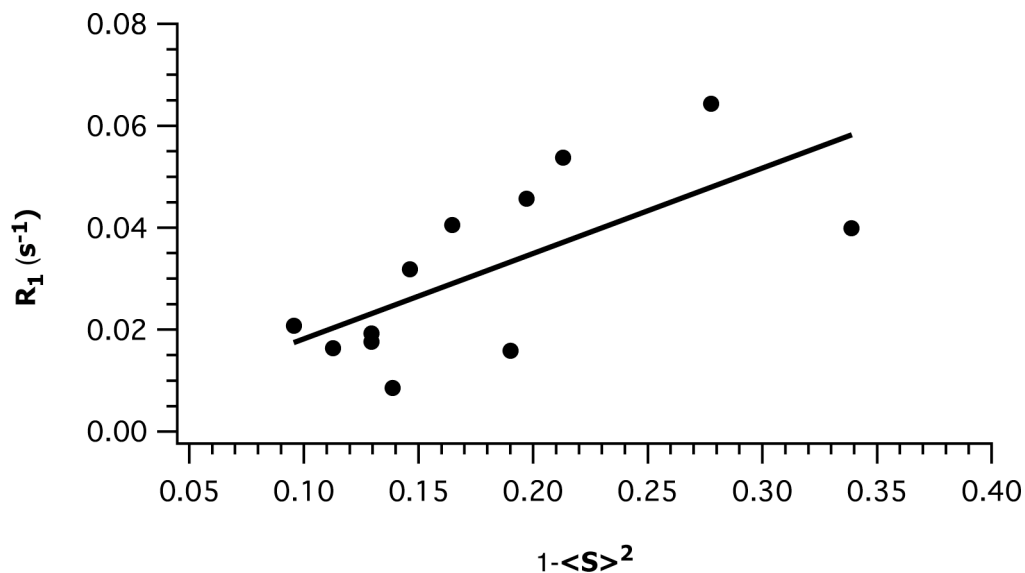


Figure 3.18: Correlation between ^{15}N R_1 and solid-state NH order parameters in the C-terminal fragment of U- ^{15}N -1-73/U- ^{13}C , ^{15}N -74-108 *E. coli* thioredoxin reassembly.

In the model-free formalism, the spectral density $J(\omega)$ is a Lorentzian function described by two model-free dynamics parameters, the order parameter (S) (which is a measure of the spatial restriction of motion) and the correlation time (τ_f) for the internal motions.

$$J(\omega) = (1 - S^2) \frac{\tau}{1 + (\omega\tau)^2} \quad (3.2)$$

In the fast-limit regime, when the correlation time is much shorter than the inverse of the Larmor frequency ω , R_1 reduces to:

$$R_1 = \omega_D^2 (1 - S^2) \tau_f \quad (3.3)$$

Since both R_1 and S are experimentally determined parameters, one can immediately get an estimate of the correlation time for the internal motions (τ_f) using Equation 1.3. Figure 3.18 illustrates the correlation between R_1 and $(1 - \langle S \rangle^2)$ for the twelve residues (excluding I75) for which both R_1 and S are available. There is a weak linear correlation between R_1 and $(1 - \langle S \rangle^2)$ with an R^2 of 0.47, as shown by the best-fit line. The residues above the best-fit line exhibit a clear linear trend while residues below tend to deviate from the simple two-parameter model-free formalism. There are two possible reasons for the discrepancy. First, the simple two-parameter model-free approach may not be sufficient enough for those residues possibly due to additional motions on slower time scales. Model-free formalism can account for such motions with an additional Lorentzian function in the spectral density, which has a characteristic slower time scale in the nanosecond regime and an order parameter for slower motions (such that the measured order parameter is the product of faster and slower time scale order parameters). However, since there are more dynamics parameters included in the model, this approach requires additional experimental parameters such as ^{15}N relaxation measurements at two different B_0 fields. Second, the assumption that the NH dipolar coupling is the only relaxation mechanism for ^{15}N relaxation may not be fully valid, and the ^{15}N CSA could make significant contribution to the ^{15}N longitudinal relaxation process. However, in this work, we have not performed a detailed calculation of the spectral density with contributions from the ^{15}N CSA; this will be the subject of future studies.

A plot of the internal correlation time in the fast limit as a function of residue number is shown in Figure 3.19. Except for I75, all residues have correlation times of the same order of magnitude, in the range of 15-70 ps. This indicates that all residues (except I75) undergo fast motions relatively uniformly with only mild variations along the backbone.

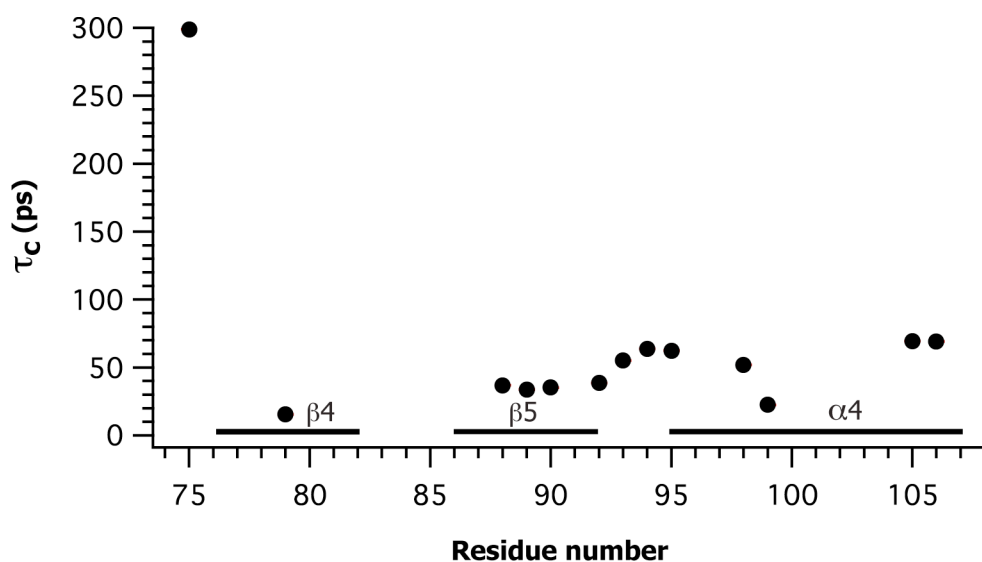


Figure 3.19: Summary of correlation time for fast internal motions using the model-free formalism in U-¹⁵N-1-73/U-¹³C,¹⁵N-74-108 *E. coli* thioredoxin reassembly

3.3.5 Dynamics on Intermediate Time Scales

Relaxation and dipolar order parameter measurements probe motions on submicrosecond-to-picosecond time scales. These intermediate time scale motions are typically studied by rotating-frame relaxation ($T_{1\rho}$) experiments in the solid state, in which the relaxation of magnetization is monitored under an applied rf field [43].

Another alternative for obtaining a qualitative estimate of intermediate time scale motions is to monitor the peak intensities in 1D CP and 2D correlation spectra as well as to record ^{13}C - ^{15}N dipolar couplings directly. The peak intensities in these spectra are affected by several factors such as the averaged HX and XX dipolar couplings (where $X = ^{15}\text{N}, ^{13}\text{C}$) due to the intermediate time scale motions (as well as fast limit motions) and their interference with MAS and decoupling frequencies. The inverse strength of all these interactions fall in the millisecond-to-microsecond time scale range and thus are sensitive probes of the intermediate time scale motions. By monitoring the cross-peak intensities of each residue as a function of an external parameter such as temperature, one can follow intermediate time scale dynamics along the backbone as well as side chains [44].

In this section, temperature dependence of the 2D ^{13}C - ^{13}C DARR spectra of the C-terminal fragment (74-108) of U- ^{15}N -1-73/U- ^{13}C , ^{15}N -74-108 *E. coli* thioredoxin reassembly is discussed. The variation of cross peak intensities as a function of temperature is analyzed.

In the range of temperatures from -5 to -35 °C, the cross peaks in 2D DARR spectra acquired with the mixing time of 10 ms have generally higher intensities at -5 and -15 °C; the intensities decrease significantly at lower temperatures. A careful analysis of the temperature-dependent DARR spectra reveals that the majority of the cross peaks show systematic chemical shift and/or intensity changes upon cooling the sample from -5 to -35 °C, as illustrated in Figure 3.20. The attenuation of cross-peak intensity can be caused by motions occurring on time scales that matches the experimental time scales at a given temperature. In this case, the experimental time scale is determined by ^1H - ^{13}C CP and proton decoupling during ^{13}C chemical shift

evolution. The rf field strengths used for CP and decoupling range between 50 and 100 kHz, which falls into the submillisecond or intermediate time scales. Hence, disappearance or weakening of cross-peak intensities indicates that the corresponding residues undergo motion on the corresponding time scales.

The depressed cross peak intensities are illustrated in Figure 3.20 showing an overlay of the DARR spectra recorded at -5 and -35 °C. Interestingly, most of the residues exhibiting large intensity variations with temperature are located in turns, loops, and the solvent-exposed surface of the $\alpha 4$. Only a few terminal residues of the β -strands $\beta 4$ and $\beta 5$ display such intensity variations. This is illustrated in Figure 3.21 depicting examples of the temperature dependencies of the cross peak intensities for residues located in the different secondary structure elements. We conclude that these residues (the loop, turn, and solvent-exposed $\alpha 4$) enter the intermediate time scale dynamics regime at temperatures below -25 °C.

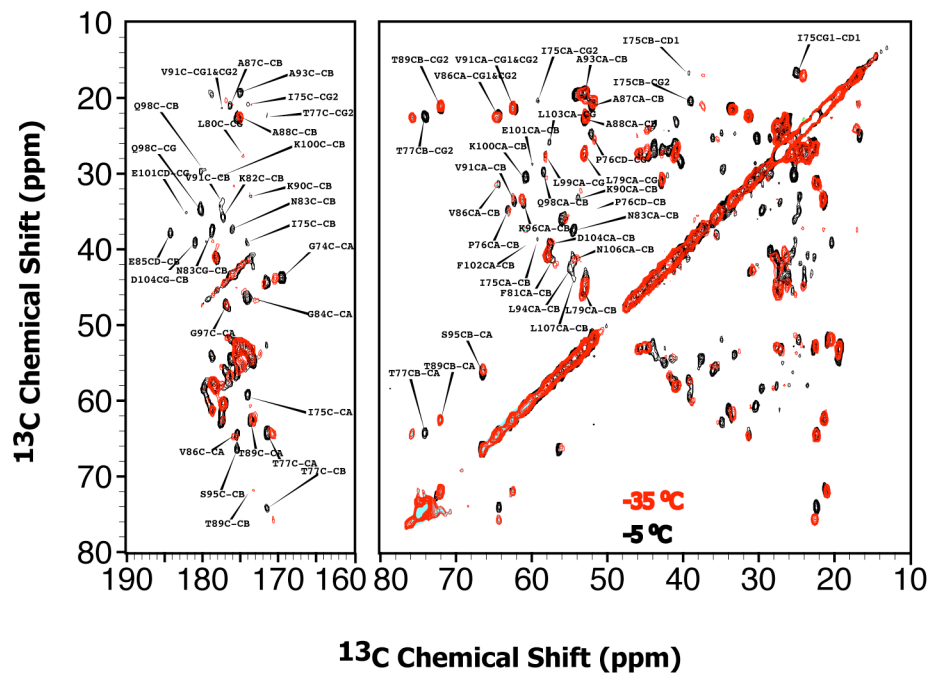


Figure 3.20: Overlay of 2D ^{13}C - ^{13}C DARR spectra of $\text{U-}^{15}\text{N-1-73}/\text{U-}^{13}\text{C}, ^{15}\text{N-74-108}$ *E. coli* thioredoxin reassembly at $-5\text{ }^\circ\text{C}$ (black) and $-35\text{ }^\circ\text{C}$ (red).

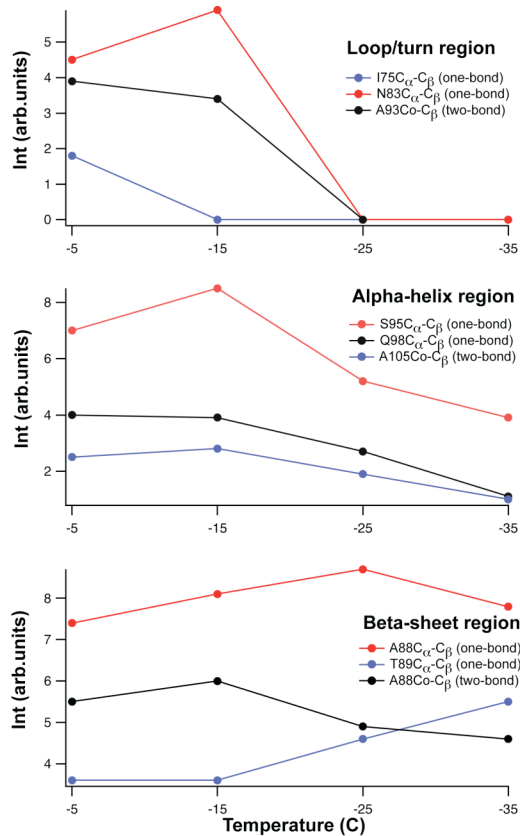


Figure 3.21: Intensity variation of DARR cross peaks as a function of temperature for different secondary structure elements of C-terminal fragment of U-¹⁵N-1-73/U-¹³C,¹⁵N-74-108 *E. coli* thioredoxin reassembly. Reproduced with permission from ref [44].

3.4 Conclusions

Backbone amide ^{15}N CSA and NH dipolar lineshapes have been measured in a site-specific manner for the C-terminal fragment of the U- ^{15}N -1-73/U- ^{13}C , ^{15}N -74-108 *E. coli* thioredoxin reassembly. These parameters, in addition to residue-specific ^{15}N R_1 measurements are excellent probes of internal dynamics of proteins in the solid state on a wide range of time scales from submicroseconds to picoseconds. ^{15}N CSA interaction is found to be very sensitive to the secondary structure type as well as to the hydrogen bonding interaction. A weak, but significant correlation between R_1 and solid-state dipolar order parameters obtained using the two-parameter model-free formalism indicates that NH dipolar coupling is the primary source of ^{15}N relaxation and also that the motions on the submicrosecond and pico-to-nanosecond time scales are correlated. The absence of any significant correlation between solution and solid-state order parameters is primarily due to the difference in the time scales of the two methods. A number of residues in the loop/turn regions and in the surface exposed α 4 undergo intermediate (micro- to millisecond) time scale motions at temperatures below $-25\text{ }^\circ\text{C}$.

3.5 References

- (1) Palmer, A. G.; Rance, M.; Wright, P. E. *J. Am. Chem. Soc.* **1991**, *113*(12), 4371-4380.
- (2) Palmer, A. G.; Williams, J.; McDermott, A. *J. Phys. Chem.* **1996**, *100*(31), 13293-13310.
- (3) McDermott, A.; Polenova, T. *Curr. Opin. Struct. Biol.* **2007**, *17*(5), 617-622.
- (4) Long, J. R.; Sun, B. Q.; Bowen, A.; Griffin, R. G. *J. Am. Chem. Soc.* **1994**, *116*(26), 11950-11956.
- (5) Gall, C. M.; Cross, T. A.; DiVerdi, J. A.; Opella, S. J. *PNAS* **1982**, *79*(1), 101-105.
- (6) Sandstrom, D.; Hong, M.; Schmidt-Rohr, K. *Chem. Phys. Lett.* **1999**, *300*(1-2), 213-220.
- (7) Hologne, M.; Faelber, K.; Diehl, A.; Reif, B. *J. Am. Chem. Soc.* **2005**, *127*(32), 11208-9.
- (8) Hologne, M.; Chen, Z.; Reif, B. *J. Magn. Reson.* **2006**, *179*(1), 20-8.
- (9) Gu, Z.; Druceckhammer, D. G.; Kurz, L.; Liu, K.; Martin, D. P.; McDermott, A. *Biochemistry* **1999**, *38*(25), 8022-8031.
- (10) Gu, Z.; McDermott, A. *J. Am. Chem. Soc.* **1993**, *115*(10), 4282-4285.
- (11) Gu, Z.; Zambrano, R.; McDermott, A. *J. Am. Chem. Soc.* **1994**, *116*(14), 6368-6372.
- (12) Tycko, R.; Dabbagh, G.; Mirau, P. A. *J. Magn. Reson.* **1989**, *85*(2), 265-274.
- (13) Franks, W. T.; Zhou, D. H.; Wylie, B. J.; Money, B. G.; Graesser, D. T.; Frericks, H. L.; Sahota, G.; Rienstra, C. M. *J. Am. Chem. Soc.* **2005**, *127*(35), 12291-12305.
- (14) Giraud, N.; Blackledge, M.; Goldman, M.; Bockmann, A.; Lesage, A.; Penin, F. o.; Emsley, L. *J. Am. Chem. Soc.* **2005**, *127*(51), 18190-18201.
- (15) Lorieau, J. L.; McDermott, A. E. *J. Am. Chem. Soc.* **2006**, *128*(35), 11505-11512.
- (16) Yang, J.; Tasayco, M. L.; Polenova, T. *J. Am. Chem. Soc.* **2009**, *131*(38), 13690-13702.
- (17) Neue, G.; Dybowski, C. *Solid State Nucl. Magn. Reson.* **1997**, *7*(4), 333-336.
- (18) Chan, J. C. C.; Tycko, R. *J. Chem. Phys.* **2003**, *118*(18), 8378-8389.
- (19) Baldus, M.; Petkova, A. T.; Herzfeld, J.; Griffin, R. G. *Mol. Phys.* **1998**, *95*(6), 1197-1207.
- (20) Bennett, A. E.; Rienstra, C. M.; Auger, M.; Lakshmi, K. V.; Griffin, R. G. *J. Chem. Phys.* **1995**, *103*(16), 6951-6958.
- (21) Bak, M.; Rasmussen, J. T.; Nielsen, N. C. *J. Magn. Reson.* **2000**, *147*(2), 296-330.
- (22) Wylie, B. J.; Franks, W. T.; Rienstra, C. M. *J. Phys. Chem. B* **2006**, *110*(22), 10926-10936.
- (23) Zhao, X.; Eden, M.; Levitt, M. H. *Chem. Phys. Lett.* **2001**, *342*(3-4), 353-361.

- (24) Hohwy, M.; Jaroniec, C. P.; Reif, B.; Rienstra, C. M.; Griffin, R. G. *J. Am. Chem. Soc.* **2000**, *122*(13), 3218-3219.
- (25) Veshtort, M.; Griffin, R. G. *J. Magn. Reson.* **2006**, *178*(2), 248-282.
- (26) Wylie, B. J.; Franks, W. T.; Graesser, D. T.; Rienstra, C. M. *J. Am. Chem. Soc.* **2005**, *127*(34), 11946-11947.
- (27) Wylie, B. J.; Schwieters, C. D.; Oldfield, E.; Rienstra, C. M. *J. Am. Chem. Soc.* **2009**, *131*(3), 985-992.
- (28) Brender, J. R.; Taylor, D. M.; Ramamoorthy, A. *J. Am. Chem. Soc.* **2001**, *123*(5), 914-922.
- (29) Loth, K.; Pelupessy, P.; Bodenhausen, G. *J. Am. Chem. Soc.* **2005**, *127*(16), 6062-6068.
- (30) Yao, L.; Grishaev, A.; Cornilescu, G.; Bax, A. *J. Am. Chem. Soc.* **2010**, *132*(12), 4295-4309.
- (31) Yao, L.; Grishaev, A.; Cornilescu, G.; Bax, A. *J. Am. Chem. Soc.* **2010**, *132*(31), 10866-10875.
- (32) Sharma, Y.; Kwon, O. Y.; Brooks, B.; Tjandra, N. *J. Am. Chem. Soc.* **2001**, *124*(2), 327-335.
- (33) Torchia, D. A.; Szabo, A. *J. Magn. Reson.* **1985**, *64*(1), 135-141.
- (34) Yao, L.; VoÅgeli, B.; Ying, J.; Bax, A. *J. Am. Chem. Soc.* **2008**, *130*(49), 16518-16520.
- (35) Stone, M. J.; Chandrasekhar, K.; Holmgren, A.; Wright, P. E.; Dyson, H. J. *Biochemistry* **1993**, *32*(2), 426-435.
- (36) Zhao, X.; Sudmeier, J. L.; Bachovchin, W. W.; Levitt, M. H. *J. Am. Chem. Soc.* **2001**, *123*(44), 11097-11098.
- (37) Torchia, D. A.; Szabo, A. *J. Magn. Reson.* **1982**, *49*(1), 107-121.
- (38) Giraud, N.; Bockmann, A.; Lesage, A.; Penin, F. o.; Blackledge, M.; Emsley, L. *J. Am. Chem. Soc.* **2004**, *126*(37), 11422-11423.
- (39) Giraud, N.; Blackledge, M.; B^ckmann, A.; Emsley, L. *J. Magn. Reson.* **2007**, *184*(1), 51-61.
- (40) Lipari, G.; Szabo, A. *J. Am. Chem. Soc.* **1982**, *104*(17), 4546-4559.
- (41) Lipari, G.; Szabo, A. *J. Am. Chem. Soc.* **1982**, *104*(17), 4559-4570.
- (42) Schanda, P.; Meier, B. H.; Ernst, M. *J. Am. Chem. Soc.* **2010**, *132*(45), 15957-15967.
- (43) Krushelnitsky, A.; Zinkevich, T.; Reichert, D.; Chevelkov, V.; Reif, B. *J. Am. Chem. Soc.* **2010**, *132*(34), 11850-11853.
- (44) Yang, J.; Paramasivam, S.; Marulanda, D.; Cataldi, M.; Tasayco, M. L.; Polenova, T. *Magn. Reson. Chem.* **2007**, *45*(S1), S73-S83.

Chapter 4

MAS NMR STUDIES OF DYNEIN LIGHT CHAIN 8

4.1 Introduction

Cytoplasmic dynein is a multi-subunit microtubule-dependent motor protein involved in the motility of a large variety of cellular cargo such as organelles and vesicles [1-3]. It consists of two or three high molecular weight heavy chains (DHC) (~500 kD), several intermediate chains (DIC) (~74 kD), several light intermediate chains (DLIC) (~52-61 kD), and three light chains (DLC) (10-14 kD). The DHCs contain ATP binding sites and are responsible for microtubule binding and motor activity by converting chemical energy into mechanical force. The DICs bind to cargo through interaction with the p150^{Glued} subunit of another complex, dynactin [4]. Direct DIC-cargo interactions have also been reported [5]. DLCs are presumed to play key roles in regulating the motor activity. Other than being an integral part of dynein complex, DLC8 also binds to a number of other proteins. (nNOS [6,7], N-terminal regulatory domain of I κ B α [8], Bim [9], Swallow [10], GKAP [11]). It has also been shown that the amino acid sequences of the binding domains of these various DLC8 target proteins are not similar, suggesting that DLC8 is capable of binding to different proteins with diverse amino acid sequences. Recently, DLC8 has been shown to interact with both Ebolavirus VP35 [12] and bovine immunodeficiency virus BIV [13], potentially affecting the early transcription and/or the localization of the virus [14,15].

DLC8 homologs from different species have remarkable sequence identity. *Drosophilla* LC8 is 94%, 71%, and 50% identical to LC8 from human, *Aspergillus nidulans*, and yeast, respectively.

The three-dimensional structure of DLC8 has been solved by both X-ray crystallography and solution NMR methods [16-22]. The crystal structure (pdb code 1CMI) of human DLC8 shows that it exists as a tight dimer, while solution NMR structure (pdb code 1F3C) from rat DLC8 shows that it exists as a moderately tight dimer ($K_D = 12\mu\text{M}$). Both crystal and solution NMR structures reveal that each monomer consists of five contiguous β -strands and two helices, and that dimerization involves $\beta 3$ - $\beta 2'$ interaction. The solution NMR structure of the DLC8 monomer from rat has also been solved at low pH (3.0) [20].

DLC8 also forms a tight complex with TcTex1, another LC in the dynein complex. The recent report of the crystal structure of DLC8 in complex with TcTex1 and 32-residue fragment of IC has been solved (pdb code 2PG1) (shown in Figure 4.1) by Williams et. al. [21]. The results from this study indicate that the binding sites in DLC8 and in TxTex1 are effectively blocked by interactions with ICs, which thus prohibit them from interacting with cellular cargo proteins.

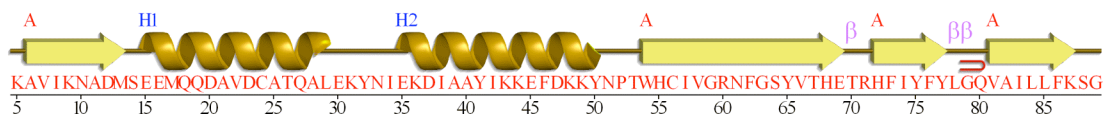


Figure 4.1: Amino acid sequence and secondary structure of *Drosophila* dynein light chain 8 generated by PDBsum from the X-ray coordinates deposited in the PDB file 2PG1. Residues M1, S2, D3 and R4 are not included.

Even though there are a number of solution NMR studies of DLC8 reported in the literature [17,18,20], the entire dynein complex is too large to be studied by solution methods because of their very large molecular weight (ca. 2MDa) and the associated spin-spin relaxation problems. Similarly, other LC8 binding partners, such as retroviral Gag [23], microtubule-binding protein syntaphilin [24] and nuclear pore complex [25], cannot be studied in complex with LC8 in solution because they are also too large and/or insoluble. Furthermore, many of these assemblies are difficult to crystallize and therefore not amenable to X-ray diffraction studies.

To the best of our knowledge, there are no solid-state NMR studies of dynein complex yet. Hence, in our laboratory, we have initiated structural and dynamics investigation of the dynein and dynactin by MAS NMR spectroscopy in collaboration with Prof. John Williams's laboratory at Beckman Research Institute, CA. Recently Sun et al. have completed the resonance assignments of both DLC8 of dynein and CAP-Gly of the dynactin in the solid state as a first step toward the characterization of these multisubunit complexes [26].

In this chapter, we present backbone ^{15}N CSA and ^1H - ^{15}N dipolar lineshape analysis of select DLC8 residues in the context of internal backbone dynamics in the solid state. For the same residues, we additionally present the direct determination of backbone torsion angles Φ by correlated ^1H - ^{15}N and ^1H - ^{13}C dipolar lineshapes; this torsion angle presents an independent structural probe complementary to the distance constraints commonly used in the determination of protein structures by solid-state NMR spectroscopy.

4.2 Experimental Methods

4.2.1 Sample Preparation

The microcrystalline DLC8 preparation has been discussed in detail in ref [27].

4.2.2 Solid-State NMR Spectroscopy

All SSNMR spectra presented in this chapter were acquired at 14.1 T on a narrow bore Varian InfinityPlus spectrometer operating at Larmor frequencies of 599.8 MHz for ^1H , 150.8 MHz for ^{13}C , and 60.8 MHz for ^{15}N . The instrument was outfitted with a 3.2 mm T3 MAS probe. The MAS frequency was 10 kHz for ^{15}N CSA, ^1H - ^{15}N dipolar lineshape experiments, and 8 kHz for HN-CAHA lineshape experiments, and was controlled to be within ± 1 Hz by a Varian MAS controller. The temperature was kept at 0 °C. The temperature reported includes a MAS frequency-dependent correction determined experimentally by using PbNO_3 as the temperature sensor [28]. The conditions pertaining to the individual experiments are given below.

4.2.3 ^{15}N ROCSA Experiment

The ^{15}N CSA recoupling was performed by the symmetry based ROCSA method [29]. The pulse sequence for 3D NCA-ROCSA experiment is the same as used for reassembled thioredoxin experiments discussed in Chapter 3. The excitation frequencies were set at 122.4 ppm for ^{15}N , and at 58.5 ppm for ^{13}C . Sixteen ROCSA points were acquired with the dwell time equal to one rotor period, and 48 ^{15}N t_2 points with the dwell time of 120 μs dwell time. 32 scans were added to record each point in the indirect dimensions of the 3D spectra. ^1H 90° pulse width was 2.78 μs . The contact time for the ^1H - ^{15}N CP was 1.6 ms. The ^1H radio frequency field strength was 52 kHz, the ^{15}N field was linearly ramped from 56-100% with the center of the

ramp being 42 kHz. A ROCSA sequence was used with a window $\tau_a = 3.29 \mu\text{s}$, and 42.8 kHz rf irradiation was employed. The Z-filter pulses were placed after the ROCSA block; the rf field strength was 50 kHz. The Z-filter delay was set equal to one rotor period. XY-16 decoupling on the ^{13}C channel was performed with an rf field strength of 67.9 kHz. 105 kHz CW decoupling was performed on the ^1H channel during ROCSA. SPECIFIC-CP [30] for ^{15}N - ^{13}C transfer was utilized. The rf field strength for ^{15}N was 35 kHz, and the ^{13}C field was tangentially ramped 88-100% with the center of the ramp being 25 kHz; the contact time was 6.2 ms. 100 kHz CW decoupling was applied during SPECIFIC-CP. The Z-filter pulses were incorporated on the ^{13}C channel immediately after SPECIFIC-CP; the rf field strength was 67.9 kHz. 92 kHz TPPM [31] decoupling was applied during t_3 evolution; the TPPM pulse width was 5.4 μs pulse width.

The NCA dimension was processed with a 60° sine-bell apodization function, followed by a Lorentzian-to-Gaussian transformation in both dimensions. A forward linear prediction to twice the number of the experimental points was employed in the ^{15}N dimension followed by zero-filling up to 256 points. The ROCSA dimension was processed with 100-200 Hz exponential line-broadening.

4.2.4 ^{15}N ROCSA Numerical Simulations

The details of the numerical simulation and the error analysis of the ^{15}N CSA lineshapes have been described in Chapter 3.

4.2.5 3D DIPSHIFT Experiment

The pulse sequence for the 3D NCA-DIPSHIFT experiment is the same as used for the reassembled thioredoxin in Chapter 3. The ^1H - ^{15}N dipolar recoupling was

achieved by the symmetry-based $R18_1^7$ sequence [32,33]. The excitation frequencies were set at 122.4 ppm for ^{15}N , and at 55.5 ppm for ^{13}C . Sixteen dipolar points were acquired with the dwell time equal to one rotor period, and 64 ^{15}N t_2 points were acquired with the dwell time of 120 μs . 64 scans were added to acquire each point in the indirect dimensions of the 3D spectra. ^1H 90° pulse width was 2.78 μs . The contact time for the ^1H - ^{15}N CP was 1.6 ms. The ^1H radio frequency field strength was 52 kHz, the ^{15}N field was linearly ramped 61-100% with the center of the ramp being 42 kHz. A $R18_1^7$ block was used for ^1H - ^{15}N dipolar recoupling; the rf field was 90 kHz. The total length of the 2τ period was set equal to 32 rotor periods. SPECIFIC-CP [30] for ^{15}N - ^{13}C transfer was utilized. The ^{15}N field was 35 kHz; the ^{13}C field was tangentially ramped 90-100% with the center of the ramp being 25 kHz; the contact time was 6.2 ms. 90 kHz CW decoupling was applied during SPECIFIC-CP. 91 kHz TPPM [31] decoupling was applied during t_3 evolution; the TPPM pulse width was 5.4 μs .

The NCA dimension was processed with a 60° sine-bell apodization function, followed by a Lorentzian-to-Gaussian transformation in both dimensions. A forward linear prediction to three times the number of the experimental points was employed in the ^{15}N dimension followed by zero-filling up to 256 points.

4.2.6 NH Dipolar Lineshape Simulations

The details of the numerical simulation of the $R18_1^7$ NH dipolar lineshapes have been described in Chapter 3.

4.2.7 HN-CAHA Dipolar Experiment

The 3D HNCH-NCA experiment was performed with the pulse sequence shown in Figure 4.2. The ^1H - ^{15}N and ^1H - ^{13}C dipolar recoupling was performed by the symmetry based T-MREV (Transverse-Mansfield Rhim Elleman Vaughan) sequence [34]. C4-symmetry was employed where each quarter of a rotor period (cycle) was a MREV block. The MAS frequency was 8 kHz controlled to within ± 0.001 kHz. The excitation frequencies were set at 121.4 ppm for ^{15}N and at 58.2 ppm for ^{13}C . Sixteen dipolar points were acquired in the dipolar evolution (t_1) dimension with a dwell time of $\tau_r/2$ ($r = 2$) during ^1H - ^{15}N dipolar evolution (t_1) and $\tau_r/4$ during ^1H - ^{13}C dipolar evolution, respectively. 64 ^{15}N t_2 points were acquired with the dwell time of 120 μs . 160 scans were added per dwell point in the 3D experiment. ^1H 90° pulse width was 2.6 μs . The contact time for the ^1H - ^{15}N CP was 1.6 ms. The ^1H radio frequency field strength was 52 kHz, the ^{15}N field was linearly ramped 62-100% with the center of the ramp being 42 kHz. The rf field during the T-MREV-4 block was 96 kHz (12 times the MAS frequency). SPECIFIC-CP [30] for ^{15}N - ^{13}C transfer was utilized. The ^{15}N field was 35 kHz; the ^{13}C field was tangentially ramped 89-100% with the center of the ramp being 25 kHz; the contact time was 6.2 ms. 99 kHz CW decoupling was applied during SPECIFIC-CP. 96 kHz TPPM [31] decoupling was applied during t_3 evolution; the TPPM pulse width was 5.2 μs .

The NCA dimension was processed with a 60° sine-bell apodization function, followed by a Lorentzian-to-Gaussian transformation in both dimensions. A forward linear prediction to three times the number of the experimental points was employed in the ^{15}N dimension followed by zero-filling up to 256 points.

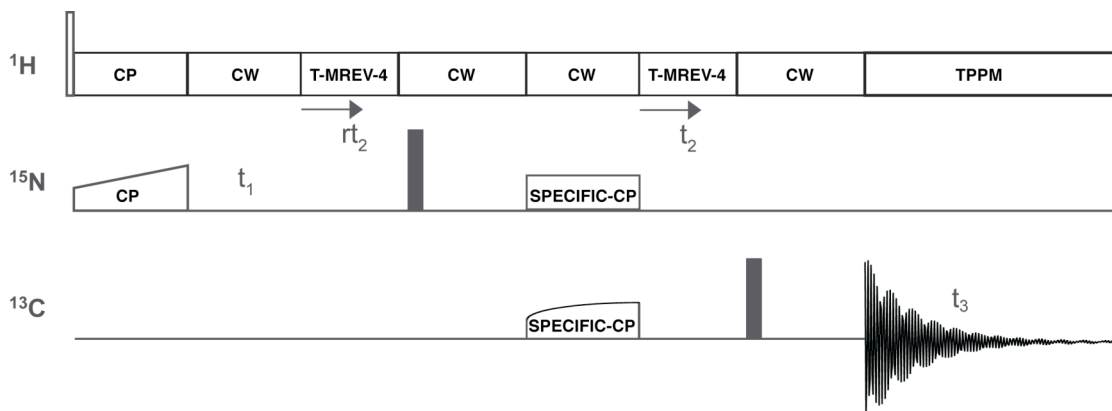


Figure 4.2: 3D HN-CAHA pulse sequence for site-specific backbone torsion angle Φ measurements. ^1H - ^{15}N and ^1H - ^{13}C dipolar recoupling is performed using the T-MREV-4 scheme.

4.2.8 HN-CAHA Dipolar Lineshape Simulations

The HN-CAHA dipolar lineshape simulations were performed using a home-written SCILAB program where the first-order average Hamiltonian was used to calculate the spin dynamics under the T-MREV irradiation. As discussed previously [35], the dipolar lineshapes obtained using the first-order average Hamiltonian agree very well with the full numeric simulation of the T-MREV pulse sequence. Additionally, the average Hamiltonian simulations are much faster than the full Hamiltonian approach, which requires significant computational time.

The first-order average Hamiltonian for the T-MREV sequence for an isolated NH spin system is

$$\bar{H}^{(1)} = (\kappa\omega^{(-1)}\hat{H}_+ + \kappa^*\omega^{(1)}\hat{H}_-)\hat{N}_z \quad (4.1)$$

where κ is a complex scaling factor for the T-MREV sequence determined by the symmetry number and the details of the C-elements and $\omega^{(1)} = (\omega^{(-1)})^* = (b_{HN} / 2\sqrt{2})\sin(2\beta)e^{i\gamma}$. The dipolar coupling constant is given by $b_{NH} = -(\mu_0 / 4\pi)\gamma_H\gamma_N\hbar / r_{HN}^3$ where r_{HN} is the N-H internuclear distance. The γ -encoded nature of the T-MREV average Hamiltonian is evident from the expression for $\omega^{(1)}$ in which the magnitude of the recoupled dipolar interaction depends only on β (the angle between the NH dipolar vector and the rotor axis) and the azimuthal angle γ around the rotor axis only affects the phase factor, but not the magnitude. The theoretical value of the magnitude of the complex scaling factor is 0.485. In practice, this value slightly varies as a function of MAS frequency and the strength of the dipolar interaction (NH vs CH).

At time $t=0$, the spin system is in a transverse ^{15}N spin state. Then $\hat{\rho}(0) = \hat{N}_x$, and the evolution of the density operator under the T-MREV average Hamiltonian is given by

$$\hat{\rho}(t) = \cos(\omega t)\hat{N}_x + \sin(\omega t)(2\hat{H}_\psi\hat{N}_y) \quad (4.2)$$

where $\omega = |\kappa\omega^{(-1)}|$ is the scaled dipolar frequency and $\hat{H}_\psi = \cos(\psi)\hat{H}_x + \sin(\psi)\hat{H}_y$, $\psi = \gamma - \lambda - \pi/2$, where γ is the powder angle and λ is the phase of the complex scaling factor κ . The value of λ is usually taken to be zero.

In the above expression for the evolution of the density operator, only the first term (containing \hat{N}_x) produces experimentally observable cosine modulated dipolar oscillations at the scaled dipolar frequency ω , and the second term (containing $2\hat{H}_\psi\hat{N}_y$) is not observable. Hence, the T-MREV dipolar FID contains only the real

part and its Fourier transform (or the dipolar lineshape) is symmetric with respect to zero frequency.

As discussed in detail by Hohwy et al. in ref [34], the coherence $2\hat{H}_\psi \hat{N}_y$ in the density operator decays much faster than the pure heteronuclear term \hat{N}_x due to the residual homonuclear proton-proton dipolar interactions which are not completely averaged to zero by the T-MREV irradiation. This is described this as a *differential* relaxation process by which a phenomenological relaxation time T_2^{NH} must be taken into account in the following manner in the evolution of the density operator:

$$\frac{d}{dt} \begin{pmatrix} \langle \hat{N}_x \rangle \\ \langle 2\hat{H}_\psi \hat{N}_y \rangle \end{pmatrix} = \begin{pmatrix} 0 & -\omega \\ \omega & -1/T_2^{NH} \end{pmatrix} \begin{pmatrix} \langle \hat{N}_x \rangle \\ \langle 2\hat{H}_\psi \hat{N}_y \rangle \end{pmatrix} \quad (4.3)$$

where T_2^{NH} is related to the width of the proton spectrum. The value of T_2^{NH} is adjusted along with NH dipolar coupling constant to obtain the best fit to the experimental T-MREV NH dipolar lineshape.

The above treatment only applies to an isolated NH spin system which is usually rare in real solids. In the case of HN-CAHA experiments, there are two T-MREV periods for HN and HA-CA dipolar recoupling, respectively. During each T-MREV period, each heteronucleus (^{15}N or ^{13}C) interacts with two protons (H^{N} , H^{A}) simultaneously, so it is necessary to calculate the evolution of the density operator for a three-spin system (I_2S). If the H^{N} and H^{A} protons are labeled as H_1 and H_2 , respectively, the evolution of the density operator under the T-MREV irradiation for a three-spin ($\text{N}, \text{H}^{\text{N}}, \text{H}^{\text{A}}$) system is given by

$$\frac{d}{dt} \begin{pmatrix} \langle \hat{N}_x \rangle \\ \langle 2\hat{H}_{1\psi} \hat{N}_y \rangle \\ \langle 2\hat{H}_{2\psi} \hat{N}_y \rangle \\ \langle 4\hat{H}_{1\psi} \hat{H}_{2\psi} \hat{N}_x \rangle \end{pmatrix} = \begin{pmatrix} 0 & -\omega_1 & -\omega_2 & 0 \\ \omega_1 & -\Gamma_2 & 0 & -\omega_2 \\ \omega_2 & 0 & -\Gamma_2 & -\omega_1 \\ 0 & \omega_2 & \omega_1 & -\Gamma_3 \end{pmatrix} \begin{pmatrix} \langle \hat{N}_x \rangle \\ \langle 2\hat{H}_{1\psi} \hat{N}_y \rangle \\ \langle 2\hat{H}_{2\psi} \hat{N}_y \rangle \\ \langle 4\hat{H}_{1\psi} \hat{H}_{2\psi} \hat{N}_x \rangle \end{pmatrix} \quad (4.4)$$

where ω_1 and ω_2 are the N-H^N and the N-H^A dipolar couplings respectively, and Γ_j is the phenomenological rate of decay of coherences involving $j-1$ protons. Γ_3 is related to Γ_2 as follows: $\Gamma_3 = \left(\frac{27}{16}\right)\Gamma_2$

The system of differential equations in eq. (4.4) can also be set up for an (C^A, H^A, H^N) spin system and solved independently. The calculation of both $\langle \hat{N}_x(t) \rangle$ and $\langle \hat{C}_x^A(t) \rangle$ involves diagonalizing the two 4x4 Liouvillian matrices for each crystallite. The total evolution of the (H^N-N-C^A-H^A) four-spin system up to an arbitrary time point t is the product of two coherences $\langle \hat{N}_x(t) \rangle$ and $\langle \hat{C}_x^A(t) \rangle$ scaled by the intermediate N-CA transfer efficiency of the SPECIFIC-CP pulse sequence. However, numerical simulations indicate that even the isotropic polarization model for N-CA transfer works as well as the anisotropic polarization models in HN-CAHA lineshape simulations. This has also been discussed in detail by Rienstra et al. [35]. Hence, we have done all the HN-CAHA dipolar lineshape simulations assuming isotropic N-CA transfer for all the crystallites in the powder averaging. Each point in the HN-CAHA dipolar FID of a single crystallite can be written merely as a product of the HN dipolar fid and the CA-HA dipolar FID.

$$FID_{HN-CAHA}(t) = FID_{HN}(t) * FID_{CA-HA}(t) \quad (4.5)$$

As shown in the original report [35], doubling the ^{15}N evolution time with respect to the ^{13}C evolution (also known as coupling amplification [36]) results in HN-CAHA dipolar lineshapes that are more sensitive to the torsion angle Φ_{H} . Hence,

$$FID_{\text{HN-CAHA}}(t) = FID_{\text{HN}}(2t) * FID_{\text{CA-HA}}(t) \quad (4.6)$$

The above expression is used along with powder averaging to generate the T-MREV HN-CAHA dipolar lineshapes as a function of three adjustable parameters: i) torsion angle (Φ_{H}), ii) relaxation rate (Γ_2), and iii) HX dipolar scaling factor (κ).

The best fits to the experimental spectra were found by performing a grid-search in the three-dimensional parameter space with the following boundaries;

i) Φ_{H} ranges from 0° to 180° in steps of 5° . It is to be noted that Φ_{H} ranging from 0° to -180° produces the same HN-CAHA dipolar lineshapes. In other words, the HN-CAHA dipolar lineshapes are insensitive to the sign of Φ_{H} , and this is a fundamental property of the dipolar interactions.

ii) Γ_2 ranges from 1.0 to 6.7 ms^{-1} in steps of 0.2 ms^{-1} , and

iii) κ ranges from 80-120% of its optimum value (0.4779 for NH, 0.4535 for CH) in steps of 2% increments.

The observed torsion angle Φ_{H} (H-N-CA-HA) is related to the backbone torsion angle Φ (CO-N-CA-CO) as follows:

$$\Phi = \Phi_{\text{H}} + 60^\circ \quad (4.7)$$

Since the sign of Φ_H is undetermined in the T-MREV experiment, each observed value of Φ_H gives rise to two possible values of Φ .

Additional details of the numerical simulations are as follows: Standard peptide geometry was used to define the dipolar tensors in the PAS frame [35]. The ZCW986 powder set was used with only one γ -angle (since T-MREV is γ -encoded). All the experimental spectra were apodized by 200-500 Hz exponential linebroadening in order to reduce the noise amplitude. The fitting was performed in the frequency domain with either only amplitude or a combination of amplitude and baseline scaling factors. Best-fit parameters were iteratively searched by minimizing the RMSD at each step until the last iteration yielded no further decrease in RMSD. The torsion angle Φ_H was found to be mildly covariant (within a few degrees) with rest of the fit parameters, while the scaling factor (κ) and relaxation rate (Γ_2) are strongly covariant with each other.

4.3 Results and Discussion

4.3.1 ^{15}N Chemical Shift Anisotropy Tensors of Dynein Light Chain 8

The first 2D NCA plane of 3D ^{15}N ROCSA-NCA spectrum of DLC8 is shown in Figure 4.3. Out of 89 residues of DLC8, ^{15}N ROCSA lineshapes were extracted for 15 residues that produced resolved cross-peaks in the NCA plane of the 3D spectra, I8, A11, V22, C24, I42, N51, W54, I57, V58, G59, G63, S64, Y75, L84, and L85. They are fairly uniformly distributed along the primary sequence of the protein. In terms of the distribution in secondary structure elements, most of these residues are located on either α -helices or β -strands (with reference to the crystal structure 2PG1 and TALOS predictions). Only one residue (N51) is located in the loop.

The experimental ^{15}N ROCSA lineshapes of these 15 residues together with the numerical best-fit simulations are shown in Figure 4.4. The best-fit values of the reduced anisotropy and asymmetry parameter are given in Table 4.1 along with the three principal components of the ^{15}N CSA tensor. The variation of the ^{15}N δ_{σ} and the three principal components as a function of residue number is plotted in Figure 4.5 and 4.6 respectively.

As discussed in Chapter 3, the amide ^{15}N CSA values are sensitive to the internal backbone dynamics occurring on time scales of microseconds and faster.

The ^{15}N δ_{σ} values range from 92 to 100 ppm for the 15 residues of DLC8 analyzed in this work. The mean (\pm standard deviation) is 95.4 (\pm 3.0) ppm. This value is close to the average of ^{15}N CSA of the *E. coli* thioredoxin fragment (96.0 ± 7.6 ppm). The small range (and also the small standard deviation) of the ^{15}N δ_{σ} in DLC8 indicates that the almost all of these 15 residues have little dynamics and are almost rigid on time scales of microseconds and faster, or the motional amplitudes are small resulting in little averaging of the CSA tensor.

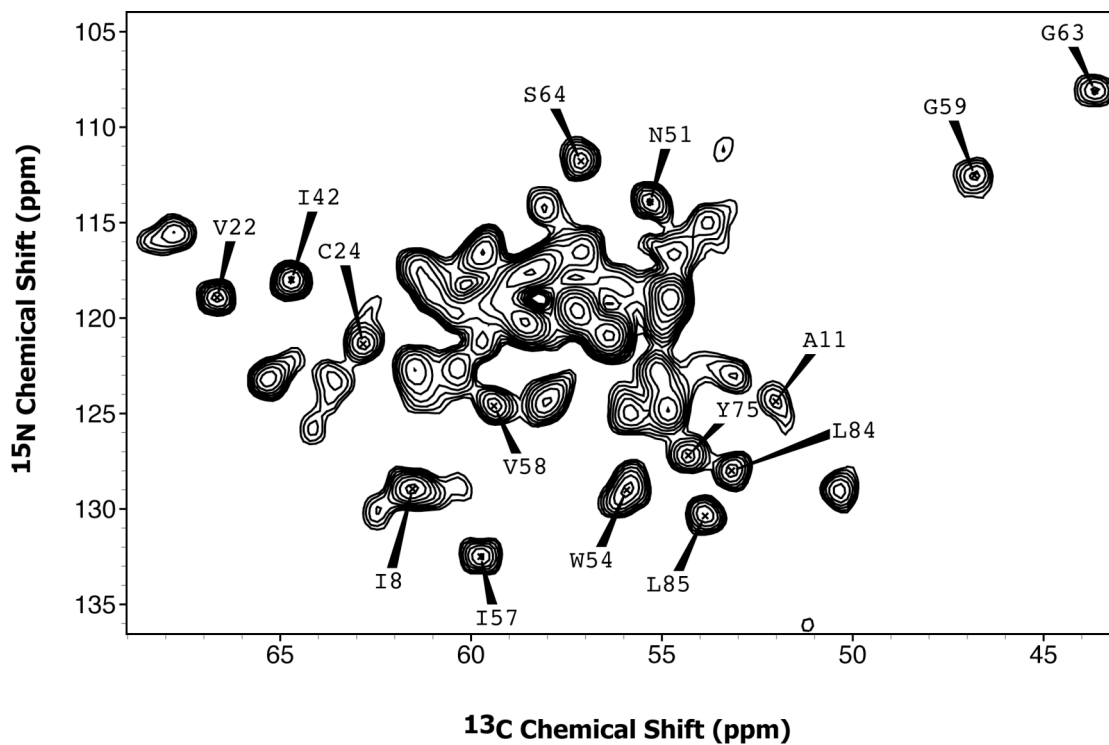


Figure 4.3: The first 2D NCA plane of the 3D ROCSA (or DIPSHIFT or HN-CAHA)-NCA spectrum of DLC8. A total of 15 cross-peaks were resolved.

We next turn our attention to the CSA parameters for the individual residues. A11 located close to the C terminus of the first β -strand has the lowest δ_σ of 91.6 ppm. Among the 15 residues, this residue also exhibits the lowest intensity in the 2D NCA spectrum. These two observations suggest that A11 undergoes motions both on the intermediate (millisecond to microsecond) and on the faster time scales (microseconds and faster) such that it has a reduced cross-peak intensity as well as a small ^{15}N chemical shift anisotropy.

Interestingly, N51 which is located in the loop between $\alpha 2$ and $\beta 2$, does not show significant dynamic averaging. The δ_{σ} value for this residue is 94.0 ppm which is close to the mean value for the 15 residues.

Apart from N51, the other fourteen residues are located in regular secondary structure elements and anticipated to exhibit rigid-like behavior with smaller motional amplitude which is indeed observed experimentally.

In conclusion, the ^{15}N CSA analysis of DLC8 indicates a rigid backbone structure of the 15 residues whose lineshapes have been recorded, and for their immediate neighboring residues. In the future, in order to obtain a complete motional profile for all residues in DLC8, we intend to acquire higher-resolution spectra, by conducting experiments at high magnetic fields, where enhanced sensitivity permits an increase in the inherent digital resolution in the NCA planes.

We have also attempted an analysis of the CS parameters in terms of the secondary structure and hydrogen bonding. For the 15 residues under study, the secondary structure is as follows: three residues (V22, C24, I42) are located in helices, and eleven (I8, A11, W54, I57, V58, G59, G63, S64, Y75, L84, L85) are in in β -sheets. The relatively small number of residues in helices, as compared to β -sheets structure does not allow for a statistical comparison of ^{15}N chemical shift anisotropies and the three individual principal component values of the ^{15}N CSA tensor between the two types of secondary structure. Similarly, eleven of the fifteen residues are hydrogen-bonded, and the remaining three are not (N51 which is part of a loop is excluded in this analysis). Again, the small number of non-hydrogen-bonded residues versus hydrogen-bonded residues does not warranty the statistical comparison of their ^{15}N CSA values.

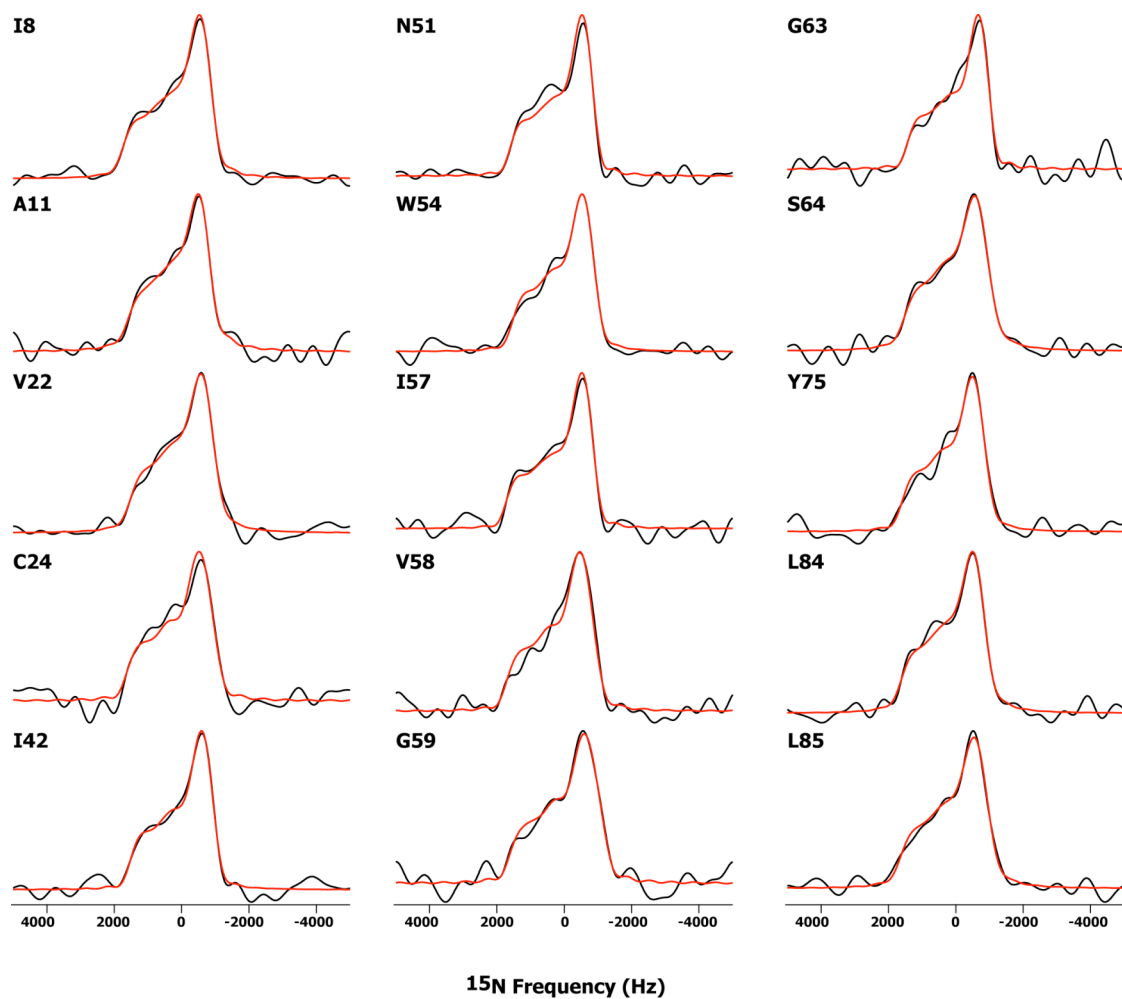


Figure 4.4: Site-specific backbone amide ^{15}N ROCSA lineshapes for 15 residues of DLC8. The experimental lineshapes are in black, the numerical simulations in red.

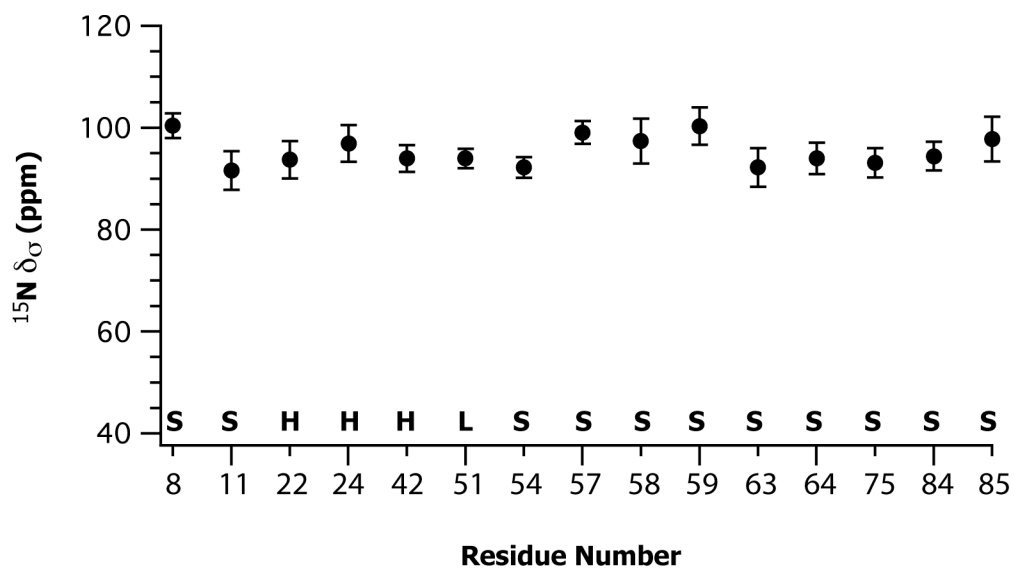


Figure 4.5: Variation of backbone amide $^{15}\text{N } \delta_{\sigma}$ as a function of the residue number.

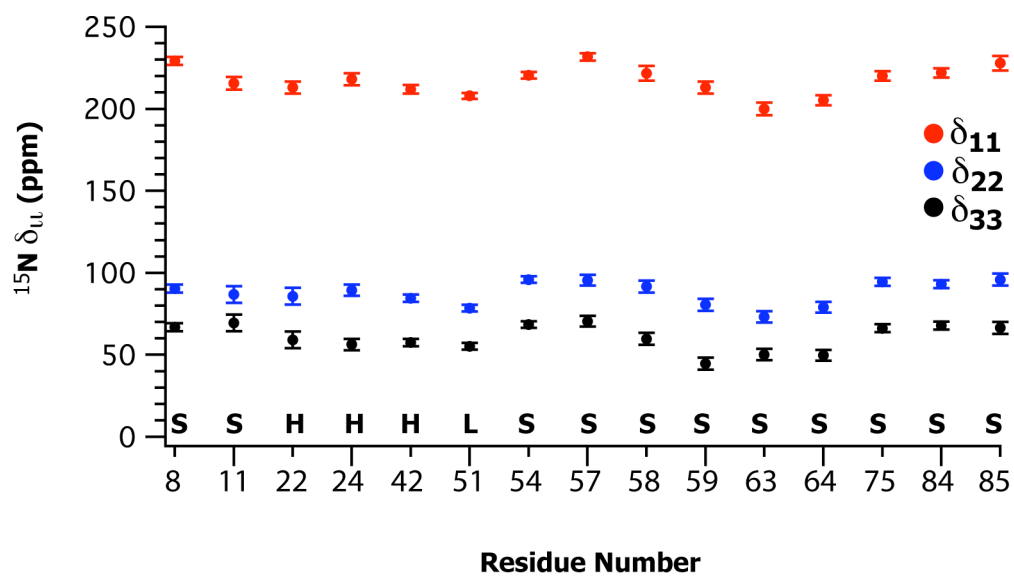


Figure 4.6: Variation of the principal components of the backbone amide ^{15}N CSA tensor as a function of the residue number.

Table 4.1 Summary of the ^{15}N Chemical Shift Parameters for DLC8

Residue	δ_σ (ppm)	η_σ	δ_{11} (ppm)	δ_{22} (ppm)	δ_{33} (ppm)
I8	100.4 ± 2.4	0.24 ± 0.05	229.2 ± 2.4	90.4 ± 2.4	66.8 ± 2.4
A11	91.6 ± 3.8	0.19 ± 0.10	215.5 ± 3.8	86.7 ± 5.0	69.5 ± 5.0
V22	93.7 ± 3.7	0.29 ± 0.10	212.9 ± 3.7	85.7 ± 5.1	59.0 ± 5.1
C24	96.9 ± 3.6	0.34 ± 0.06	218.1 ± 3.6	89.3 ± 3.5	56.2 ± 3.5
I42	94.0 ± 2.6	0.29 ± 0.03	211.9 ± 2.6	84.8 ± 2.3	57.4 ± 2.3
N51	94.0 ± 1.9	0.25 ± 0.04	207.8 ± 1.9	78.5 ± 2.1	55.1 ± 2.1
W54	92.2 ± 2.0	0.30 ± 0.03	220.4 ± 2.0	95.8 ± 2.1	68.4 ± 2.1
I57	99.1 ± 2.2	0.25 ± 0.06	231.6 ± 2.2	95.5 ± 3.2	70.4 ± 3.2
V58	97.4 ± 4.4	0.33 ± 0.06	221.8 ± 4.4	91.7 ± 3.7	59.7 ± 3.7
G59	100.3 ± 3.7	0.36 ± 0.06	212.9 ± 3.7	80.4 ± 3.6	44.5 ± 3.6
G63	92.2 ± 3.8	0.25 ± 0.07	199.9 ± 3.8	73.0 ± 3.4	50.2 ± 3.4
S64	94.0 ± 3.1	0.31 ± 0.05	205.3 ± 3.1	79.0 ± 3.2	49.6 ± 3.2
Y75	93.1 ± 2.9	0.30 ± 0.05	220.0 ± 2.9	94.5 ± 2.4	66.2 ± 2.4
L84	94.4 ± 2.8	0.27 ± 0.05	222.0 ± 2.8	93.0 ± 2.4	67.8 ± 2.4
L85	97.8 ± 4.4	0.30 ± 0.06	227.8 ± 4.4	95.9 ± 3.7	66.3 ± 3.7

4.3.2 Solid-State NMR NH Dipolar Order Parameters of Dynein Light Chain 8

As discussed in detail in Chapter 3, the site-specific NH dipolar couplings are a direct source of the amplitude of internal motion in the solid state. In this section the NH dipolar lineshape analysis of the 15 residues of DLC8 discussed above is presented.

The experimental NH dipolar lineshapes, together with numerical best-fit simulations, are shown in Figure 4.7. The best-fit values of the NH dipolar couplings

are reported in terms of order parameters ($\langle S \rangle_{\text{NH}}$) in Table 4.2. The variation of solid-state NH order parameters as a function of the residue number is plotted in Figure 4.8. The rigid-limit value of the NH dipolar coupling is taken to be 10.83 kHz, which corresponds to a NH distance of 1.04 Å. The NH dipolar order parameters range from 0.85-0.98 with a mean value (\pm standard deviation) of 0.94 ± 0.03 .

Consistent with the observations from the ^{15}N CSA recoupling experiment, the residue A11 is found to be more mobile than other residues under analysis in the NH dipolar coupling measurement as well. A11 has the smallest NH dipolar order parameter of 0.85, which corresponds to a NH dipolar coupling of 9.2 kHz. This value is considerably lower than the average value (0.94) of the fifteen residues under analysis, which suggests that A11 undergoes motions of considerable amplitude on time scales of microseconds and faster.

Apart from A11, the remaining fourteen dipolar order parameters range from 0.91 to 0.98. Considering the inherent uncertainties in the measurement of NH dipolar order parameters, which is from ± 0.02 to ± 0.03 , it is not feasible to make a one-to-one comparison of $\langle S \rangle_{\text{NH}}$ and interpret the difference in terms of dynamics details. Hence, we refrain from such analysis and conclude that the backbone of DLC8 at the positions of the 15 residues analyzed in this work is rigid, with little dynamic averaging on microsecond and faster time scales.

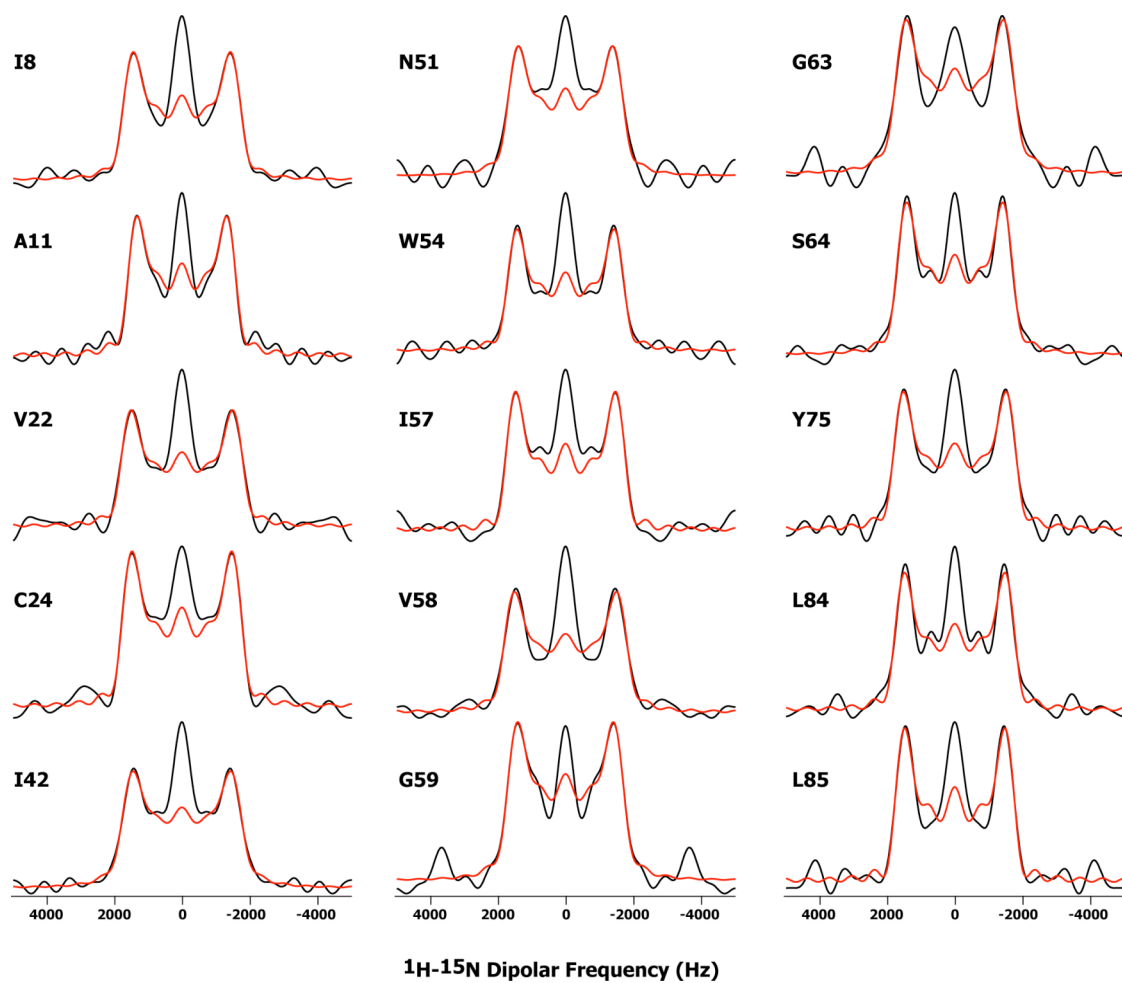


Figure 4.7: Site-specific backbone amide NH R18₁⁷ ROCSA lineshapes for 15 residues of DLC8. The experimental lineshapes are in black, the numerical simulations in red. The zero-frequency peak was not included in the fit.

Table 4.2 Summary of Backbone NH Order Parameters for DLC8.

Residue	$\langle S \rangle_{\text{NH}}$
I8	0.93
A11	0.85
V22	0.97
C24	0.95
I42	0.94
N51	0.91
W54	0.93
I57	0.95
V58	0.98
G59	0.92
G63	0.94
S64	0.92
Y75	0.98
L84	0.96
L85	0.95

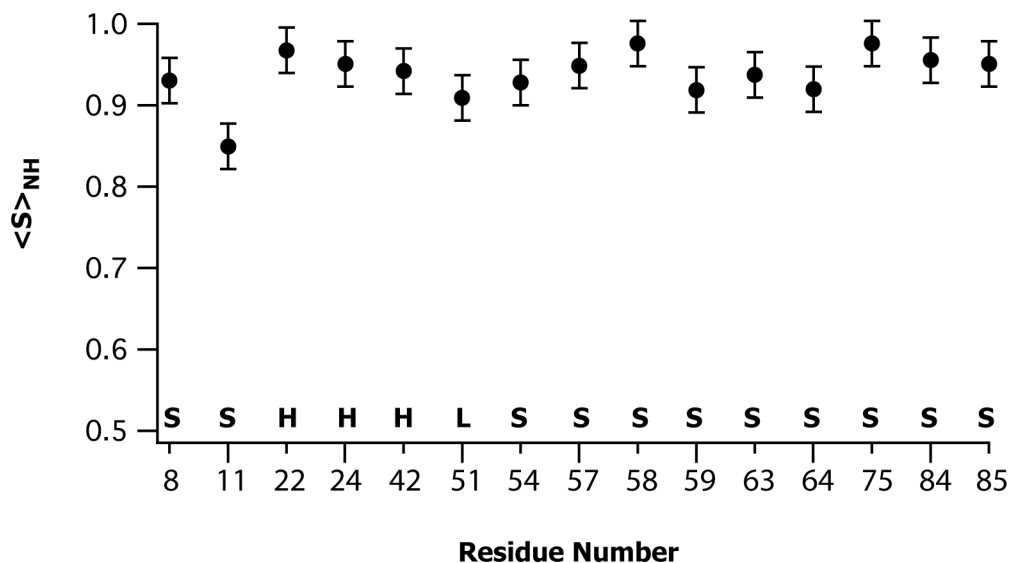


Figure 4.8: Variation of SSNMR NH dipolar order parameters in DLC8 as a function of the residue number.

4.3.3 HN-CAHA Dipolar Lineshapes of Dynein Light Chain 8

Protein structure determination protocols using NMR methods have traditionally relied on a large number of inter-nuclear distance constraints obtained by NOEs [37] in solution state and spin-diffusion based dipolar transfers [38] in the solid state. It has been established by multiple investigators that the quality of such proteins structures using distance constraints alone can be greatly improved by additional structural constraints such as backbone and side-chain torsion angles, as well as projection angles between distant bond vectors [39-41]. In addition, torsion angle measurements provide direct information on the local conformation of the polypeptide chain. For example, with standard bond lengths and bond angles, the backbone

conformation of the protein can be uniquely determined if the torsion angles ϕ and ψ are known for each residue. Hence, methods for the determination of torsion angles are particularly useful in the structural analysis of proteins.

Several NMR approaches have been developed to determine torsion angles in proteins. For example, in solution the J -coupling constant between the amide proton and the alpha proton is particularly sensitive to the torsion angle Φ between the NH and the CH bond vectors. The J -coupling between the alpha proton and the beta proton is sensitive to the side-chain torsion angle χ_1 . It has also been established that chemical shifts of the backbone nuclei, together with the amino acid sequence identity can also be used to predict torsion angles. Programs such as TALOS [42,43] use this information and compare the chemical shifts against a large database of known protein structures with known chemical shift assignments to predict the backbone torsion angles of unknown protein structures.

Solid-state NMR offers a number of tools to measure torsion angles directly in proteins and peptides. The inherently anisotropic nature of the chemical shift and the dipolar interactions, as well as their unique dependence on orientations can be exploited to relate torsion angles to observable parameters [34-36,44-48]. One of the earliest MAS-based approaches to measuring torsion angles, called RACO (Relayed Anisotropy COrrrelation) was reported by Ishii et al. [46] where the torsion angle ψ was determined by finding the relative orientation of the CS tensor of the carbonyl carbon and the CA-HA dipolar vector. Since the measurement of the orientation of the CS tensor in the molecular frame is not often straightforward, this approach was later modified to correlate two dipolar tensors such as NH and CA-HA and was shown to be more sensitive to the torsion angle ϕ . Hohwy et al. showed that the torsion angle

determination methods can be improved with symmetry-based H-X dipolar recoupling schemes such as T-MREV [34]. They also showed in their work that the explicit consideration of the proton relaxation during the T-MREV irradiation is crucial in extracting molecular parameters such as bond lengths and angular information from the dipolar lineshapes. Later, Rienstra et al. demonstrated the feasibility of this approach by measuring backbone (ϕ , ψ) as well as side-chain torsion (χ_1) angles on a model tripeptide (f-MLF-OH) [35,48]. Recently, Franks et al. have shown that the angular constraints such as NH(i)-NH(i+1) and NH-CAHA measured by T-MREV recoupling on a per-residue basis greatly improves the resolution of protein structures [49]. In the streptococcal B1 immunoglobulin-binding domain of protein G (GB1), the backbone rmsd improved from 0.50 Å to 0.31 Å with the addition of the NH(i)-NH(i+1) and NH-CAHA angular constraints.

In this section, we present the analysis of the correlated HN and HACA dipolar lineshapes recoupled by T-MREV for select eleven residues. From these lineshapes, we extract the torsion angle Φ by numerical simulations.

The experimental HN-HACA dipolar lineshapes together with numerical best-fit simulations are shown in Figure 4.9. The best-fit values of the torsion angle Φ_H , the differential relaxation constant Γ_2 , and the dipolar scaling factor κ are presented in Table 4.3.

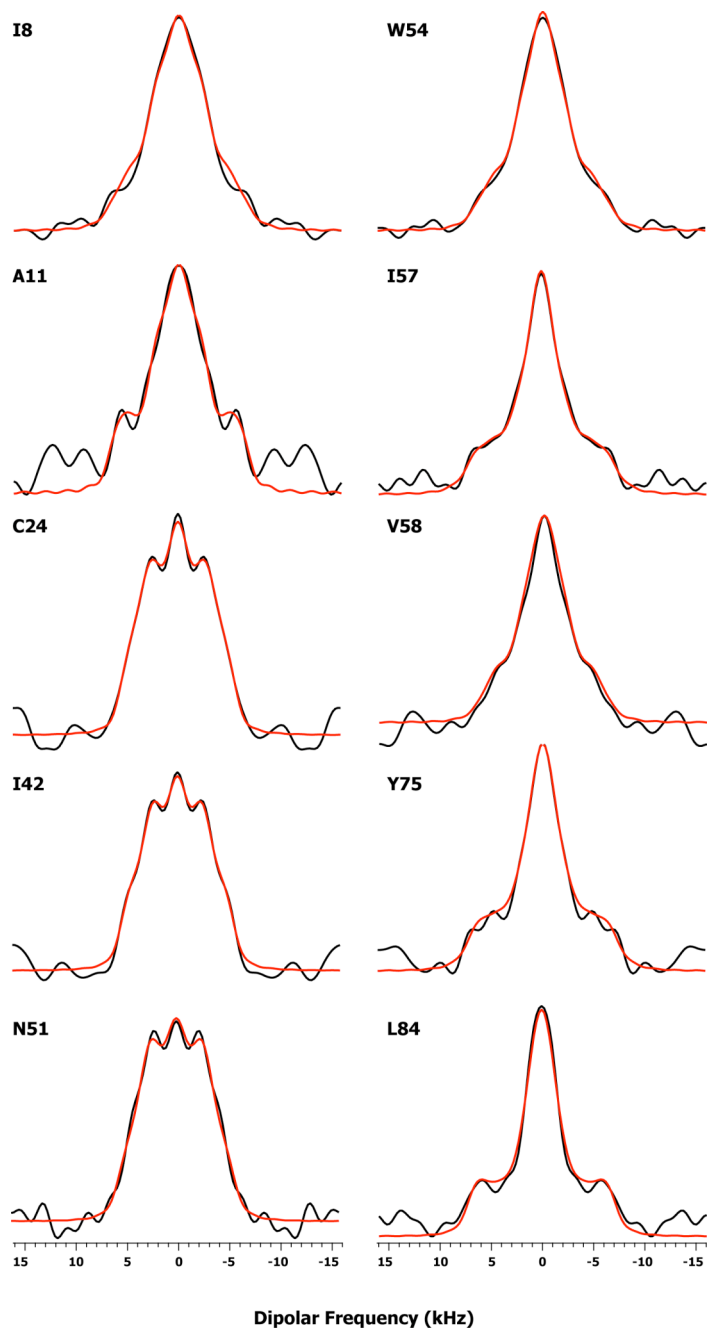


Figure 4.9: Site-specific HN-CAHA dipolar lineshapes for ten residues under analysis in DLC8. The experimental lineshapes are in black, the numerical simulations are in red.

Table 4.3. Summary of T-MREV-4 HN-CAHA Lineshape Fit Parameters for the 11 Residues of DLC8.

Residue	Φ_H (°)	Γ_2 (ms ⁻¹)	$\kappa_{\text{NH,CH}}$
I8	±155	6.7	0.449, 0.426
A11	±155	2.7	0.440, 0.417
C24	±125	1.9	0.382, 0.363
I42	±115	2.4	0.382, 0.363
N51	±120	3.1	0.392, 0.372
W54	±160	6.7	0.440, 0.417
I57	±170	5.7	0.478, 0.454
V58	±160	5.7	0.411, 0.390
Y75	±170	5.0	0.478, 0.454
L84	±170	3.3	0.468, 0.444
L85	±165	5.7	0.449, 0.426

As discussed in section 4.2.8, the HN-HACA dipolar lineshapes are sensitive to the torsion angle Φ_H only through the projection angle θ which has a range of 0°-90°.

In Figure 4.10, the HN-CAHA dipolar lineshapes are depicted for Φ_H ranging from 0° to 180° and for fixed values of Γ_2 (2.0 ms⁻¹) and κ (0.4779 for NH, 0.4535 for CH). As we can see from this Figure, the dipolar lineshapes are very sensitive to the torsion angle Φ_H . However there is some degeneracy in the range of 30°-130° with 80° being the center. In other words, any dipolar lineshape with Φ_H in the range 30°-80° is the same as 160°- Φ_H . This degeneracy arises due to the fact the HN-HACA dipolar lineshapes are sensitive to the torsion angle Φ_H only through the projection angle θ

(also called the pseudo bond angle between NH and CAHA bond vectors), which is the same for both Φ_H and Φ_H+50° in the range 30° - 130° with 80° being the center. The mathematical details of this degeneracy have been extensively discussed by Ishii et al. [50] and are not presented here. The magnitude of Φ_H usually ranges from 120° from 180° for regular secondary structure elements such as right handed helix and β -strands, and therefore only the second solution is acceptable where Φ_H is greater than 80° . As is also evident from Figure 4.10, Φ_H in the range 140° - 180° does not have any degeneracy and the corresponding dipolar lineshapes can be analyzed unambiguously.

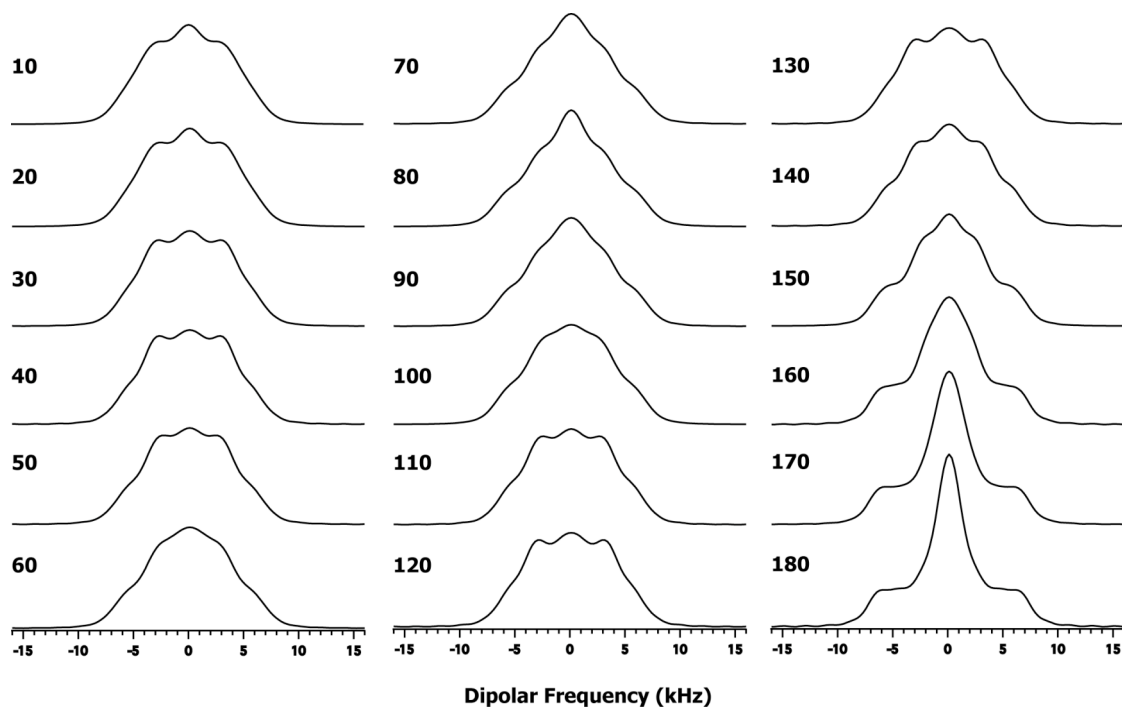


Figure 4.10: Simulated T-MREV-4 HN-CAHA dipolar lineshapes for varying Φ_H from 10° to 180° . The value of Γ_2 was fixed at 4.0 ms^{-1} . HN and HC dipolar couplings were fixed at their rigid limit values. Note that the T-MREV-4 lineshapes are symmetric with respect to $\Phi_H = 80^\circ$ in the range 30° - 130° .

Eight of the thirteen residues under analysis have a unique torsion angle Φ_H ($\geq 155^\circ$) in the range $[0^\circ, 180^\circ]$. These residues include I8, A11, W54, I57, V58, Y75, L84, and L85. Their experimental spectra have no degeneracy in the limit $[0^\circ, 180^\circ]$ as compared to the grid of lineshapes shown in Figure 4.10. However, their lineshapes are invariant to the sign of Φ_H which gives two solutions to backbone torsion angle Φ .

Three of the remaining five residues (C24, I42, N51) have multiple solutions in Φ_H itself. These multiple solutions are in the range $[0^\circ, 131^\circ]$ with 80° roughly being the center of the symmetry. C24 has two solutions with the same RMSD; one at $\Phi_H = 35^\circ$ and the other at $\Phi_H = 125^\circ$. I42 has one solution at 40° and the other at 115° . N51

has one solution at 40° and the other at 120° . Usually the magnitude of Φ_H values range from 120° to 180° in right-handed helices or β -strands. Hence, only the second solution which is greater than 80° is acceptable. In Figure 4.9, the experimental lineshapes of C24, I42, and N51 are plotted along with the simulated spectra for the second solution of Φ_H .

The remaining two residues V22 and S64 have experimental spectra that do not fit very well with simulations, mainly because of the high noise level in their dipolar lineshapes. They are not presented in Figure 4.9. In general, the HN-HACA dipolar lineshapes require high signal-to-noise ratio so that the numerical best-fit spectra can be obtained with minimum RMSD. To illustrate this point, we fitted a simulated spectrum with $\Phi_H = 140^\circ$ to the grid of Φ_H and plotted the resulting RMSD profile in Figure 4.11. As expected, there is one global minimum at $\Phi_H = 140^\circ$ with zero RMSD. However, there are two symmetric local minima around 55° and 105° with 80° being the center. The RMSD at $\Phi_H = 105^\circ$ is only about 2.6%. This small difference gets masked in the presence of the experimental noise, which makes the best-fit parameters deviate quite significantly over a large range of Φ_H . Hence, it is necessary to measure HN-CAHA lineshapes with high signal-to-noise, so that the numerical fits yield unambiguous structural parameters.

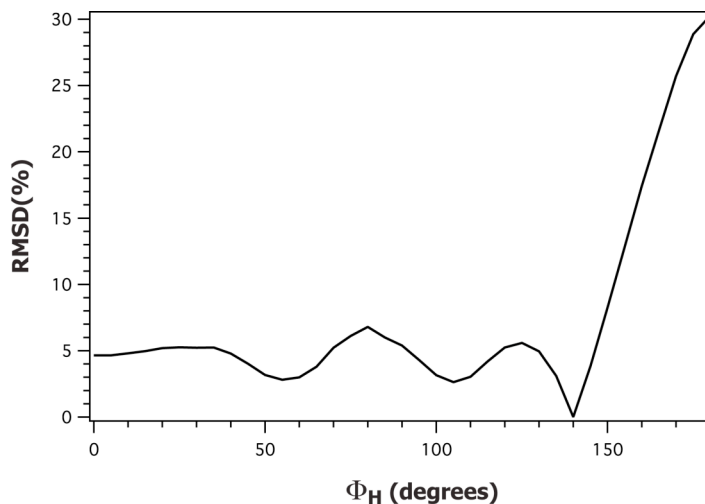


Figure 4.11: RMSD plot of simulated HN-CAHA dipolar lineshape with $\Phi_H = 140^\circ$. The value of Γ_2 is fixed at 2.0 ms^{-1} . NH and CH dipolar couplings were fixed at their rigid limit values.

For all other residues excluding V22 and S64, the agreement between the experimental and the simulated spectra is generally very good, which indicates that the best-fit parameters are reliable and can be analyzed with confidence.

Since NH-HACA lineshapes are insensitive to the sign of Φ_H , each value of Φ_H corresponds to two values of backbone Φ . This degeneracy is a fundamental property of the dipolar couplings and cannot be distinguished without using additional information about the geometry of the spin system. Hence, of the two solutions, we have simply decided to choose the one that agrees with TALOS predictions. However, this need not be done in a general case. Franks et al. [49] have suggested the use of the projection angles (θ) directly (without converting them into torsion angle Φ) in the form of force fields during the simulated annealing of protein structure calculations

[49]. Thus the dipolar projection angles form a third set of constraints after distance and TALOS constraints.

In Table 4.4, the Φ values determined from SSNMR experiments are presented along with the X-ray (2PG1) structure values and TALOS calculations. The deviations from both X-ray- and TALOS-based values are plotted in Figure 4.12. for the 10 residues excluding N51. This residue is in a loop in the crystal structure. The TALOS prediction also suggests the same. However, the SSNMR-based Φ value shows significant deviation from both the X-ray- and TALOS-derived angle. In the crystal structure, this residue is very close to the C-terminal end of $\alpha 2$ and possibly could be part of the $\alpha 2$. The ^{15}N CSA ($\delta_{\sigma} = 94$ ppm) and the solid-state NH dipolar order parameter (0.91) are also quite high, suggesting that the residue is only moderately mobile on the time scales of microseconds and faster. We have therefore ignored this outlier for comparison and plotted the difference for the 10 residues with regular secondary structure elements in Figure 4.12.

The average deviations for the 10 residues against both X-ray and TALOS values are 11.5° and 11.4° respectively, a good agreement between the three methods used to infer this angle. The range of the absolute deviation is from 1° to 24° against the X-ray structure and 1° - 19° against the TALOS values. It is interesting to note that the deviations of residues W54, I57, and L85 against TALOS are the three largest (18° , 19° , 14°), while at the same time they are negligible against the crystal structure values. For residues C24 and V58 it is the other way around; the SSNMR Φ values agree closely with TALOS while deviations from the crystal structure values are the largest (16° , 24°).

Table 4.4. Comparison of SSNMR Φ Values of DLC8 Residues Against X-ray- and TALOS-Based Values.

Residue	$\Phi_{\text{SSNMR}} (^{\circ})$	$\Phi_{\text{X-ray}} (^{\circ})$	$\Phi_{\text{TALOS}} (^{\circ})$
I8	-95	-79	-86
A11	-145	-134	-134
C24	-65	-49	-66
I42	-55	-63	-64
N51	-60	72	60
W54	-100	-99	-118
I57	-130	-128	-111
V58	-140	-116	-134
Y75	-130	-135	-122
L84	-110	-115	-111
L85	-135	-134	-120

Overall, the agreement between SSNMR-derived Φ values and those obtained from the X-ray structure and TALOS predictions methods is rather good, which suggests that the HN-HACA dipolar experiment can be used as an independent tool to measure the torsion angle Φ in proteins and peptides, as has been demonstrated by the prior work [35,48,49]. The HN-CAHA experiment can also be modified to measure the torsion angle Ψ [35]. However the modified experiment suffers from problems associated with low signal-to-noise ratios because of the long-range magnetization transfer from N(i+1) and CA(i). The T-MREV-based recoupling method can also be extended to measure NH(i)-NH(i+1) projection angles [51]. However, this experiment requires excellent resolution in the ^{15}N - ^{15}N correlation spectrum to resolve all the residues, which is quite difficult to achieve in uniformly ^{15}N labeled samples unless the protein size is small and the conformational homogeneity is very high. The

relatively high dipolar scaling factor associated with the T-MREV sequence makes it suitable for lineshape measurements with increased sensitivity to torsion angles. The only drawback of this method is the high rf requirement (12 times the rotor frequency) which restricts the MAS frequency. Despite this minor technical drawback, the method is generally applicable to uniformly labeled spin systems and can serve as an independent probe of protein structure.

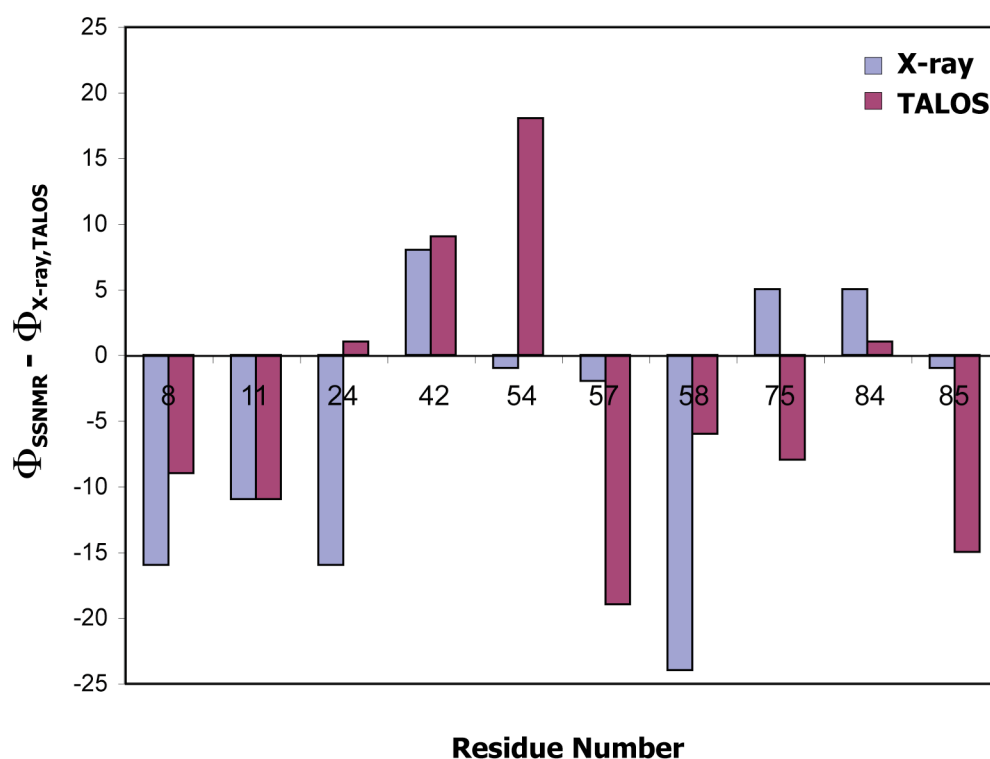


Figure 4.12: Comparison of site-specific Φ values of DLC8 determined from solid-state NMR experiments with X-ray and TALOS values

We are interested in applying these methods to other proteins in our laboratory in the future to enhance the quality of the protein structures, as well as probe local conformations, and the current work on DLC8 provides some insights into optimization of NMR conditions and dipolar lineshape analysis.

4.4 Conclusions

Backbone amide ^{15}N CSA and ^1H - ^{15}N dipolar lineshapes have measured for fifteen select residues of DLC8 exhibiting well-resolved cross-peaks in the NCA planes of the 3D ROCSA and DIPSHIFT spectra.. The results indicate that the DLC8 backbone is mostly rigid at the positions of these residues with very small amplitudes of motions occurring on the microsecond time scales or faster. The backbone torsion angle Φ has also been measured for the same residues by correlated ^1H - ^{15}N and ^1H - ^{13}C dipolar lineshapes. The results compare well with crystal structure values and TALOS-derived values and indicate that the Φ angles measured directly by SSNMR for individual residues in proteins have the potential to serve as additional constraints in protein structure calculations.

4.5 References

- (1) Mallik, R.; Gross, S. P. *Curr. Biol.* **2004**, *14*(22), R971-82.
- (2) Yamamoto, A.; Hiraoka, Y. *J. Cell Sci.* **2003**, *116*(Pt 22), 4501-12.
- (3) Devred, F.; Barbier, P.; Lafitte, D.; Landrieu, I.; Lippens, G.; Peyrot, V.; Leslie, W.; John, J. C. In *Methods in Cell Biology*; Academic Press: 2010; Vol. Volume 95, p 449-480.
- (4) Vaughan, K. T.; Vallee, R. B. *J. Cell Biol.* **1995**, *131*(6 Pt 1), 1507-16.
- (5) Karki, S.; Ligon, L. A.; DeSantis, J.; Tokito, M.; Holzbaaur, E. L. *Mol. Biol. Cell* **2002**, *13*(5), 1722-34.
- (6) Jaffrey, S. R.; Snyder, S. H. *Science* **1996**, *274*(5288), 774-7.
- (7) Fan, J. S.; Zhang, Q.; Li, M.; Tochio, H.; Yamazaki, T.; Shimizu, M.; Zhang, M. *J. Biol. Chem.* **1998**, *273*(50), 33472-81.
- (8) Crepieux, P.; Kwon, H.; Leclerc, N.; Spencer, W.; Richard, S.; Lin, R.; Hiscott, J. *Mol. Cell Biol.* **1997**, *17*(12), 7375-85.
- (9) Puthalakath, H.; Huang, D. C.; O'Reilly, L. A.; King, S. M.; Strasser, A. *Mol. Cell* **1999**, *3*(3), 287-96.
- (10) Schnorrer, F.; Bohmann, K.; Nusslein-Volhard, C. *Nat. Cell Biol.* **2000**, *2*(4), 185-90.
- (11) Naisbitt, S.; Valtschanoff, J.; Allison, D. W.; Sala, C.; Kim, E.; Craig, A. M.; Weinberg, R. J.; Sheng, M. *J. Neurosci.* **2000**, *20*(12), 4524-34.
- (12) Kubota, T.; Matsuoka, M.; Chang, T.-H.; Bray, M.; Jones, S.; Tashiro, M.; Kato, A.; Ozato, K. *J. Virol.* **2009**, *83*(13), 6952-6956.
- (13) Su, Y.; Qiao, W.; Guo, T.; Tan, J.; Li, Z.; Chen, Y.; Li, X.; Li, Y.; Zhou, J.; Chen, Q. *Cell. Microbiol.* **2010**, *12*(8), 1098-1107.
- (14) Tan, G. S.; Preuss, M. A.; Williams, J. C.; Schnell, M. J. *PNAS* **2007**, *104*(17), 7229-34.
- (15) Moseley, G. W.; Roth, D. M.; DeJesus, M. A.; Leyton, D. L.; Filmer, R. P.; Pouton, C. W.; Jans, D. A. *Mol. Biol. Cell* **2007**, *18*(8), 3204-13.
- (16) Beckwith, S. M.; Roghi, C. H.; Liu, B.; Morris, N. R. *J. Cell Biol.* **1998**, *143*(5), 1239-1247.
- (17) Fan, J.-S.; Zhang, Q.; Tochio, H.; Li, M.; Zhang, M. *J. Mol. Biol.* **2001**, *306*(1), 97-108.
- (18) Fan, J.-S.; Zhang, Q.; Tochio, H.; Zhang, M. *J. Biomol. NMR.* **2002**, *23*(2), 103-114.
- (19) Liang, J.; Jaffrey, S. R.; Guo, W.; Snyder, S. H.; Clardy, J. *Nat. Struct. Mol. Biol.* **1999**, *6*(8), 735-740.
- (20) Makokha, M.; Huang, Y. J.; Montelione, G.; Edison, A. S.; Barbar, E. *Protein Sci.* **2004**, *13*(3), 727-34.

- (21) Williams, J. C.; Roulhac, P. L.; Roy, A. G.; Vallee, R. B.; Fitzgerald, M. C.; Hendrickson, W. A. *PNAS* **2007**, *104*(24), 10028-33.
- (22) Lightcap, C. M.; Sun, S.; Lear, J. D.; Rodeck, U.; Polenova, T.; Williams, J. C. *J. Biol. Chem.* **2008**, *283*(40), 27314-24.
- (23) Petit, C.; Giron, M. L.; Tobaly-Tapiero, J.; Bittoun, P.; Real, E.; Jacob, Y.; Tordo, N.; De The, H.; Saib, A. *J. Cell Sci.* **2003**, *116*(Pt 16), 3433-42.
- (24) Chen, Y. M.; Gerwin, C.; Sheng, Z. H. *J. Neurosci.* **2009**, *29*(30), 9429-38.
- (25) Stelter, P.; Kunze, R.; Flemming, D.; Hopfner, D.; Diepholz, M.; Philippsen, P.; Bottcher, B.; Hurt, E. *Nat. Cell Biol.* **2007**, *9*(7), 788-96.
- (26) Sun, S. J.; Siglin, A.; Williams, J. C.; Polenova, T. *J. Am. Chem. Soc.* **2009**, *131*(29), 10113-10126.
- (27) Sun, S. Ph.D. Thesis, University of Delaware, Newark, 2011.
- (28) Neue, G.; Dybowski, C. *Solid State Nucl. Magn. Reson.* **1997**, *7*(4), 333-336.
- (29) Chan, J. C. C.; Tycko, R. *J. Chem. Phys.* **2003**, *118*(18), 8378-8389.
- (30) Baldus, M.; Petkova, A. T.; Herzfeld, J.; Griffin, R. G. *Mol. Phys.* **1998**, *95*(6), 1197-1207.
- (31) Bennett, A. E.; Rienstra, C. M.; Auger, M.; Lakshmi, K. V.; Griffin, R. G. *J. Chem. Phys.* **1995**, *103*(16), 6951-6958.
- (32) Zhao, X.; Eden, M.; Levitt, M. H. *Chem. Phys. Lett.* **2001**, *342*(3-4), 353-361.
- (33) Zhao, X.; Sudmeier, J. L.; Bachovchin, W. W.; Levitt, M. H. *J. Am. Chem. Soc.* **2001**, *123*(44), 11097-11098.
- (34) Hohwy, M.; Jaroniec, C. P.; Reif, B.; Rienstra, C. M.; Griffin, R. G. *J. Am. Chem. Soc.* **2000**, *122*(13), 3218-3219.
- (35) Rienstra, C. M.; Hohwy, M.; Mueller, L. J.; Jaroniec, C. P.; Reif, B.; Griffin, R. G. *J. Am. Chem. Soc.* **2002**, *124*(40), 11908-11922.
- (36) Hong, M.; Gross, J. D.; Rienstra, C. M.; Griffin, R. G.; Kumashiro, K. K.; Schmidt-Rohr, K. *J. Magn. Reson.* **1997**, *129*(1), 85-92.
- (37) Kumar, A.; Wagner, G.; Ernst, R. R.; Wuthrich, K. *Biochem. Biophys. Res. Commun.* **1980**, *96*(3), 1156-1163.
- (38) Szeverenyi, N. M.; Sullivan, M. J.; Maciel, G. E. *J. Magn. Reson.* **1982**, *47*(3), 462-475.
- (39) Lange, A.; Becker, S.; Seidel, K.; Giller, K.; Pongs, O.; Baldus, M. *Angew. Chem. Int. Ed.* **2005**, *44*(14), 2089-92.
- (40) Zech, S. G.; Wand, A. J.; McDermott, A. E. *J. Am. Chem. Soc.* **2005**, *127*(24), 8618-26.
- (41) Zhou, D. H.; Shea, J. J.; Nieuwkoop, A. J.; Franks, W. T.; Wylie, B. J.; Mullen, C.; Sandoz, D.; Rienstra, C. M. *Angew. Chem. Int. Ed.* **2007**, *46*(44), 8380-3.
- (42) Cornilescu, G.; Delaglio, F.; Bax, A. *J. Biomol. NMR.* **1999**, *13*(3), 289-302.
- (43) Shen, Y.; Delaglio, F.; Cornilescu, G.; Bax, A. *J. Biomol. NMR.* **2009**, *44*(4), 213-23.
- (44) Hong, M.; Gross, J. D.; Griffin, R. G. *J. Phys. Chem. B* **1997**, *101*(30), 5869-5874.

- (45) Costa, P. R.; Gross, J. D.; Hong, M.; Griffin, R. G. *Chem. Phys. Lett.* **1997**, *280*(1-2), 95-103.
- (46) Ishii, Y.; Terao, T.; Kainosho, M. *Chem. Phys. Lett.* **1996**, *256*(1-2), 133-140.
- (47) Chan, J. C. C.; Tycko, R. *J. Am. Chem. Soc.* **2003**, *125*(39), 11828-11829.
- (48) Rienstra, C. M.; Tucker-Kellogg, L.; Jaroniec, C. P.; Hohwy, M.; Reif, B.; McMahon, M. T.; Tidor, B.; Lozano-Perez, T.; Griffin, R. G. *PNAS* **2002**, *99*(16), 10260-10265.
- (49) Franks, W. T.; Wylie, B. J.; Schmidt, H. L. F.; Nieuwkoop, A. J.; Mayrhofer, R.-M.; Shah, G. J.; Graesser, D. T.; Rienstra, C. M. *PNAS* **2008**, *105*(12), 4621-4626.
- (50) Ishii, Y.; Hirao, K.; Terao, T.; Terauchi, T.; Oba, M.; Nishiyama, K.; Kainosho, M. *Solid State Nucl. Magn. Reson.* **1998**, *11*(3-4), 169-175.
- (51) Reif, B.; Hohwy, M.; Jaroniec, C. P.; Rienstra, C. M.; Griffin, R. G. *J. Magn. Reson.* **2000**, *145*(1), 132-141.

Chapter 5

MAS NMR SPECTROSCOPIC AND DENSITY FUNCTIONAL THEORY STUDIES OF IONIZATION STATES OF THIAMIN

5.1 Introduction

Thiamin diphosphate (ThDP) is an important coenzyme in a variety of enzyme systems that catalyze the transfer of aldehyde or acyl groups and the decarboxylation of α -keto acids. It is comprised of thiazolium and 4'-aminopyrimidine aromatic rings. Only recently has the participation of the 4'-aminopyrimidine group in enzyme catalysis gained wider acceptance [1,2]. During catalysis by the thiamin diphosphate (ThDP) superfamily of enzymes, the 4'-aminopyrimidine moiety of ThDP can interconvert among four ionization/tautomeric states: the positively charged N1'-protonated 4'-aminopyrimidinium (APH⁺), and the three neutral forms, 4'-aminopyrimidine (AP), 1', 4'-iminopyrimidine (IP) and the ylide (YI) (Figure 5.1). However, not all of these ionization/tautomeric forms have been clearly characterized yet. In particular, previous research has shown that APH⁺ and the ylide forms are not directly detectable by other spectroscopic methods, such as circular dichroism [3] or solution NMR. Therefore, central questions concerning the molecular basis for activation of C2-H bond of ThDP and how the enzymes favorably stabilize the IP form during various steps of the catalytic cycle still remain unanswered [3-10]. Solid-state NMR spectroscopy, which could provide atomic-level information in these large enzymes, would go the farthest in resolving such long-standing

questions, due to the exquisite sensitivity of NMR chemical shifts to both the ionization and tautomeric states [11-13].

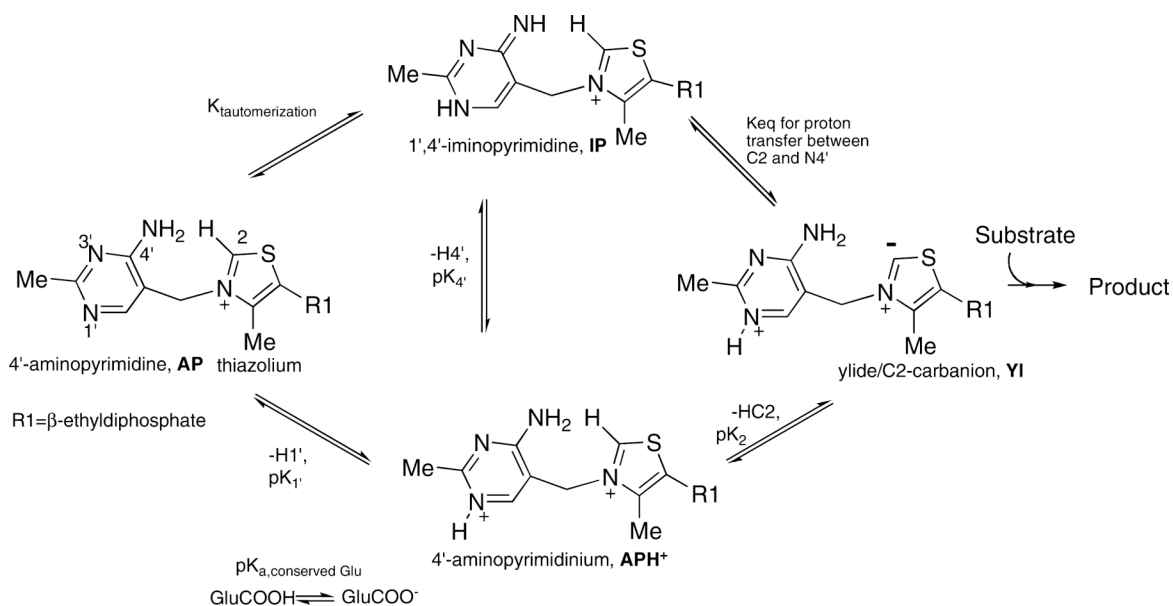


Figure 5.1: Various ionization and tautomerization states of ThDP bound to enzymes. (Adapted from ref. [24] with permission)

Although isotropic chemical shifts available from solution NMR spectra are in many cases sufficient to infer the ionization and tautomeric states [14,15], chemical shift anisotropy (CSA) tensors recorded in the solid state provide much more detailed insight [16-20]. Furthermore, density functional theory (DFT) calculations of the magnetic shielding tensors and their analysis in light of the experimental NMR results yield comprehensive understanding of the electronic structure of a molecule [21-23]. Solid-state NMR measurements are often the only way to record chemical shifts and CS tensors, for example, in large proteins, where solution lines are broadened beyond

detection. The high molecular weight of the ThDP-dependent enzymes (varying between 160,000 and 250,000) has so far limited their solution NMR studies, and solid-state NMR spectroscopy presents a promising alternative for investigation of their catalytic mechanisms.

Despite the enormous potential of solid-state NMR methods, there have been no reports in the literature so far on the use of the CS tensors as probes for various ionization/tautomeric forms of thiamin-dependent enzymes. Therefore, the focus of our work has been the investigation of ^{13}C and ^{15}N chemical shift anisotropy tensors for different ionization states of free thiamin in the solid state as a starting point for subsequent studies of ^{13}C and ^{15}N chemical shifts of several ionization and tautomeric states in a series of thiamin-enzyme complexes. This work represents the first step toward understanding the tautomeric and ionization states among which the protein-bound ThDP cofactor undergoes interconversion during the enzymatic cycle. Thiamin molecules containing selective ^{13}C and ^{15}N isotopic labels at key positions of the 4'-aminopyrimidine ring (C6', N4') and of the thiazolium ring (C2) were synthesized in the Prof. Frank Jordan's laboratory at the Rutgers University. Protonated thiamin is in the 4'-aminopyrimidinium form (APH^+) and unprotonated is in the 4'-aminopyrimidine form (AP), both on and off the enzymes. We have recorded the ^{13}C and ^{15}N CS tensors for each ionization form by magic angle spinning (MAS) NMR spectroscopy and performed DFT calculations of the corresponding magnetic shielding anisotropy tensors. Our results indicate that the isotropic chemical shifts as well as the principal components of the ^{13}C and ^{15}N CS tensors are very sensitive to the protonation states in thiamin and therefore permit one to differentiate between the two forms (AP and APH^+). The calculated magnetic shielding tensors of C2, C6' and

N4' exhibit excellent agreement with the experimental CS tensors. Our findings indicate that MAS NMR spectroscopy in conjunction with DFT calculations is a sensitive probe of ionization states in the ThDP cofactor, and this approach can be applied to studies of the ionization and tautomeric forms in ThDP-dependent enzymes.

5.2 Experimental Methods

5.2.1 Materials

The detailed description of synthesis procedure of [$^{13}\text{C}2$, $^{13}\text{C}6'$] thiamin chloride hydrochloride, [$^{13}\text{C}2$, $^{13}\text{C}6'$] thiamin, [$^{15}\text{N}4'$] thiamin chloride hydrochloride, and [$^{15}\text{N}4'$] thiamin is given in references [24,25].

5.2.2 Preparation of Solid-State NMR Samples

Crystalline [$^{13}\text{C}2$, $^{13}\text{C}6'$] thiamin chloride hydrochloride (10.4 mg, 0.031 mmol) or [$^{15}\text{N}4'$] thiamin chloride hydrochloride (9.0 mg, 0.027 mmol) were packed into 3.2 mm MAS rotors and used in the subsequent MAS NMR experiments as models for the N1' protonated form.

[$^{13}\text{C}2$, $^{13}\text{C}6'$] thiamin (8.0 mg, 0.027 mmol) or [$^{15}\text{N}4'$] thiamin (6.7 mg, 0.022 mmol) were packed into 3.2 mm MAS rotors and used in the subsequent MAS NMR experiments as models for the N1' unprotonated form.

5.2.3 Solid-State NMR Spectroscopy

All ^{13}C and ^{15}N MAS spectra presented in this work were acquired at 9.4 T (400.17 MHz ^1H Larmor frequency) on a Tecmag Discovery spectrometer outfitted with a 3.2 mm wide bore Varian HXY T3 probe. The temperature was kept at 23 °C. The temperature reported includes a MAS frequency-dependent correction determined

experimentally by using PbNO_3 as the temperature sensor [26]. ^{13}C chemical shifts were referenced to the downfield peak of adamantane (38.56 ppm with respect TMS). ^{15}N chemical shifts were referenced to ammonium chloride (39.2 ppm with respect to liquid NH_3).

The low-spinning-frequency ^{13}C CPMAS spectra were acquired on $\text{Th}\cdot\text{HCl}$ at $\omega_r/2\pi = 2900, 4070$ and 5980 Hz. The MAS frequency was controlled with a Tecmag MAS controller: within ± 5 Hz at 2900 kHz, while at 4070 and 5980 Hz the variation was up to ± 100 Hz. The standard CP sequence was used with a 1-ms contact time; the ^1H radio frequency field strength was 60 kHz, the ^{13}C field was linearly ramped 80-100% with the center of the ramp being 50 kHz. The ^1H 90° pulse width was 2.5 ms. The same experimental parameters were used at every spinning frequency. The ^1H decoupling was performed using TPPM [27] with 100 kHz ^1H radio frequency field strength maintained for the duration of the acquisition period, 25.6 ms. The CPMAS spectra were acquired with either 32 scans (at $\omega_r/2\pi = 2900$ Hz) or with 4 scans ($\omega_r/2\pi = 4070$ and 5980 Hz); the recycle delay was 10 s. The spectra were processed without any line broadening, and the intensity of each sideband was extracted for the two carbons in the 2, 6'- ^{13}C $\text{Th}\cdot\text{HCl}$ sample.

The low spinning-frequency ^{13}C CP-MAS spectra of 2, 6'- ^{13}C Th were acquired at $\omega_r/2\pi = 2075, 3810, \text{ and } 5973$ Hz. The rest of the experimental conditions were the same as for the thiamin hydrochloride sample. At all MAS frequencies, 16 scans were used with a 10-sec pulse delay.

The Herzfeld-Berger analysis [28] was performed to calculate the CS parameters from the intensities of the spinning side-band envelopes for the two carbon atoms in both forms of thiamin.

The ^{15}N CP-MAS NMR spectra of $4'-^{15}\text{N}$ Th•HCl and Th were acquired at a spinning frequency of 10 kHz. The standard CP sequence was used with a 1-ms contact; the ^1H radio frequency field strength was 60 kHz, the ^{15}N field was linearly ramped 80-100% with the center of the ramp being 50 kHz. 100 kHz. TPPM decoupling was applied during the acquisition time (30 ms); ^1H radio frequency field strength was 100 kHz. 32 scans were acquired with a recycle delay of 10 s.

The ROCSA (Recoupling Of Chemical Shift Anisotropy) pulse sequence [29] was used to recouple the ^{13}C and ^{15}N CSA interaction at MAS frequencies above 10 kHz. The ^{13}C ROCSA spectra were collected at the MAS frequency of 12 kHz. The ^{13}C radio frequency field strength during the ROCSA period was 51.3 kHz, and that of the ^1H decoupling was 122 kHz. The ^{15}N ROCSA spectra were collected at the MAS frequency of 10 kHz. The ^{15}N rf field strength during the ROCSA period was 42.8 kHz and that of the ^1H decoupling was 100 kHz. 16 transients were added up with a recycle delay of 10 sec for each t_1 point. 32 and 24 t_1 points were acquired using the States method [30] for ^{15}N and ^{13}C ROCSA spectra, respectively. The CS dimension was zero-filled to 512 points; no apodization was applied prior to the Fourier transformation.

5.2.4 ^{13}C , ^{15}N CSA Numerical Simulations

The slow-spinning ^{13}C MAS spectra were simulated in SIMPSON [31], using the CS parameters obtained from HB analysis. An exponential line broadening of 88 Hz was applied to the simulated spectra to match the natural linewidth. SIMPSON was also used to simulate ^{13}C and ^{15}N ROCSA lineshapes. The MINUIT procedure embedded in SIMPSON was applied for fitting the experimental ROCSA spectra using three variable parameters: δ_σ , η_σ and the line-broadening parameter. The

uncertainties for the fitting parameters δ_{σ} and η_{σ} were determined using the Monte Carlo method as described in Chapter 3.

5.2.5 Density Functional Theory Calculations

Quantum chemistry calculations were carried out using the DFT method in Gaussian03 [32]. Geometry optimization [33] was employed using the B3LYP functionals [34-36] and tzvp basis set [37,38]. $^{13}\text{C}/^{15}\text{N}$ shielding tensor calculations were performed using the same functionals and basis set and GIAO approximation [39-42]. The starting structure for Th•HCl geometry optimization was obtained from the X-ray structure of Th•HCl [43]. The starting structure for the unprotonated thiamin used in the subsequent geometry optimization was derived from the crystal structure of Th•HCl by removing the HCl. Two sets of calculations were performed for both Th•HCl and Th: one with chloride anions, the other without the anions (charge of +1 for Th and charge +2 for Th•HCl). The J -coupling constant calculations were performed using B3LYP and IGLO-III basis set [44] with the polarizable continuum model (PCM) [45-47]. Most of the calculations were performed under GridChem computational resources and services, Computational Chemistry Grid [48] (www.gridchem.org).

The ^{13}C chemical shifts were referenced with respect to the downfield resonance of adamantane at 38.56 ppm, whose absolute magnetic shielding tensor was calculated at the same level of theory as those for the thiamin models. The ^{15}N chemical shift was referenced with respect to 244.6 ppm according to the previously described procedure [49].

5.3 Results and Discussion

5.3.1 Selective Labeling of Thiamin Analogs

Thiamin (Th) and thiamin hydrochloride (Th•HCl) correspond to the AP and APH⁺ form of ThDP, respectively, in enzyme catalysis (Figure 5.1). Because only the 4'-aminopyrimidinium ring undergoes a change in ionization, we anticipated that between the two selectively labeled carbon atoms, C2 and C6', the ¹³C CSA tensor of C6' would be the prime reporter of the protonation state of the 4'-aminopyrimidine ring, along with the ¹⁵N CSA tensor of the N4' atom. The chemical structures of Th and Th•HCl with selective ¹³C labels introduced at positions 2 and 6', and with ¹⁵N label incorporated at N4' are depicted in Figure 5.2.

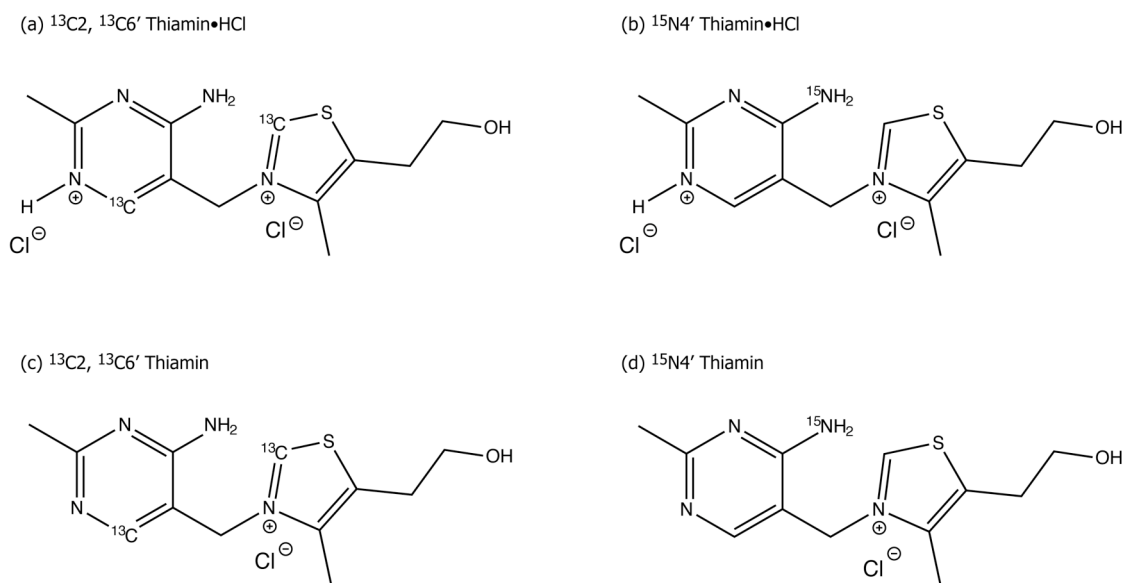


Figure 5.2: Chemical structures of Th•HCl and Th with ¹³C/¹⁵N enrichment at positions C2, C6' and N4'. (Adapted from ref. [24] with permission)

5.3.2 Assignments of ^{13}C Resonances in Different Ionization States of Thiamin

Since there are two ^{13}C isotopically labeled sites (C2 and C6') in both Th and Th•HCl, ambiguity arises in the resonance assignment of the ^{13}C spectra of both samples in the absence of *a priori* knowledge about the two carbon chemical shifts. To resolve this ambiguity, we have measured the $^1J_{\text{C-H}}$ coupling constant for these two carbons by solution NMR, and compared the experimental results with the DFT-computed J -couplings in Th•HCl and Th. The results are summarized in Table 5.1. Based on the DFT calculations, $J_{\text{C2-H}}$ is larger than $J_{\text{C6'-H}}$ by more than 22 Hz in Th•HCl and by 35 Hz in Th. The experimental J -couplings obtained from the proton-coupled ^{13}C solution NMR spectra of Th•HCl and Th are in excellent agreement with the theoretical predictions, and this agreement immediately permits us to assign the two carbons in both ionization states; the corresponding isotropic solution chemical shifts are also indicated in Table 5.1.

Table 5.1 Experimental and Computed J_{CH} Couplings for the 2,6'- $^{13}\text{C}/4'$ - ^{15}N Th•HCl and Th

Sample		J_{CH} (Hz)		δ_{iso} (ppm)
		Solution NMR	DFT	Solution NMR
Th•HCl	C2	214.1	208.8	154.6
	C6'	185.6	186.7	145.1
Th	C2	213.6	210.0	157.8
	C6'	177.5	175.3	161.0

5.3.3 ^{13}C and ^{15}N Chemical Shift Anisotropy Tensors in Different Ionization States of Thiamin: MAS NMR Spectroscopy

The ^{13}C CSA tensors were recorded by two methods: i) slow-MAS spectra at three different spinning frequencies with the subsequent Herzfeld-Berger analysis to extract the CSA tensor components [28]; ii) the symmetry-based recoupling of chemical shift anisotropy (ROCSA) method suitable for high MAS frequencies [29]. The ^{15}N CSA parameters were determined using ROCSA because the much smaller ^{15}N CSA tensor results in rather weak sideband intensities even at slow-MAS frequencies, thus prohibiting their accurate measurement.

The experimental ^{13}C , slow-MAS and ROCSA spectra of both Th•HCl and Th are shown in Figure 5.3 along with numerical simulations. The experimental ^{15}N ROCSA spectra along with numerical simulations are illustrated in Figure 5.4. The ^{13}C , ^{15}N CSA parameters of the key atoms C2, C6' and N4' in the two different ionization states are presented in Table 5.2.

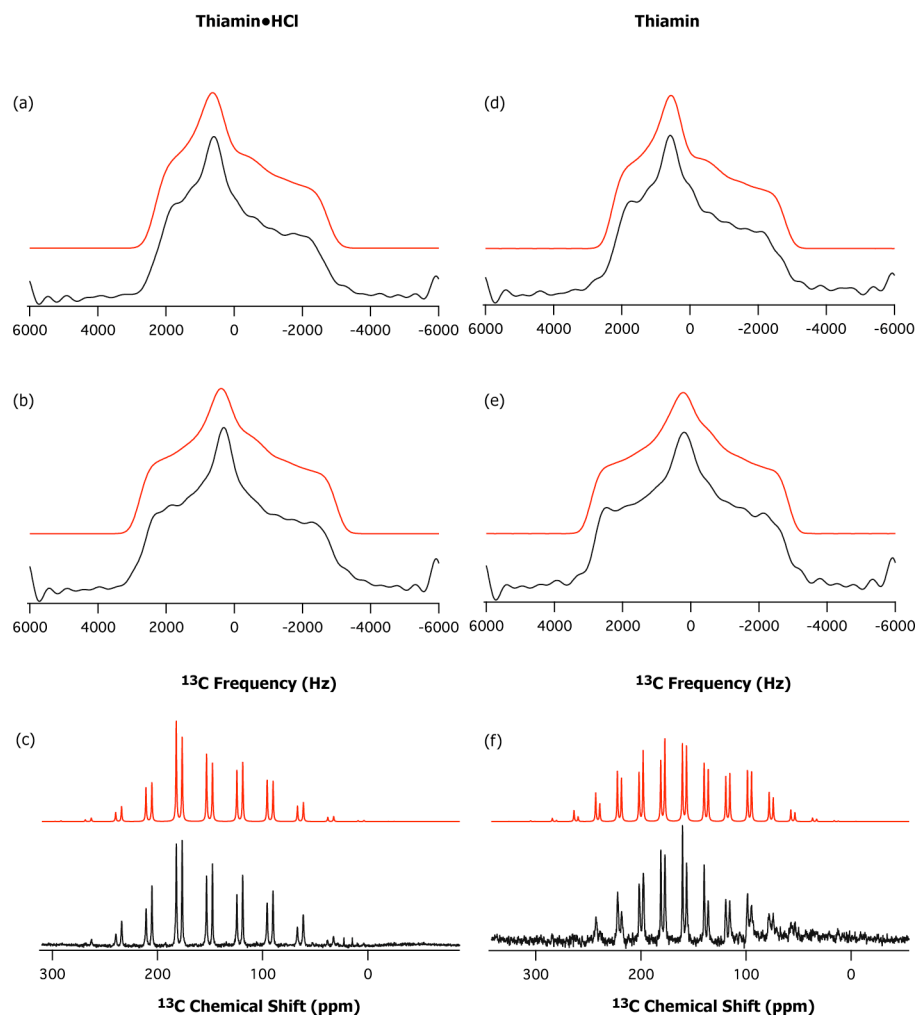


Figure 5.3: ^{13}C ROCSA and slow-MAS spectra of Th•HCl and Th: experimental (black) and simulated (red). (a) ROCSA spectrum of C2 of Th•HCl. (b) ROCSA spectrum of C6' of Th•HCl. (c) Slow-MAS spectrum of C2 and C6' of Th•HCl at 2900 Hz MAS frequency. (d) ROCSA spectrum of C2 of Th. (e) ROCSA spectrum of C6' of Th. (f) Slow-MAS spectrum of C2 and C6' of Th at 2075 Hz MAS frequency. (Adapted from ref. [24] with permission)

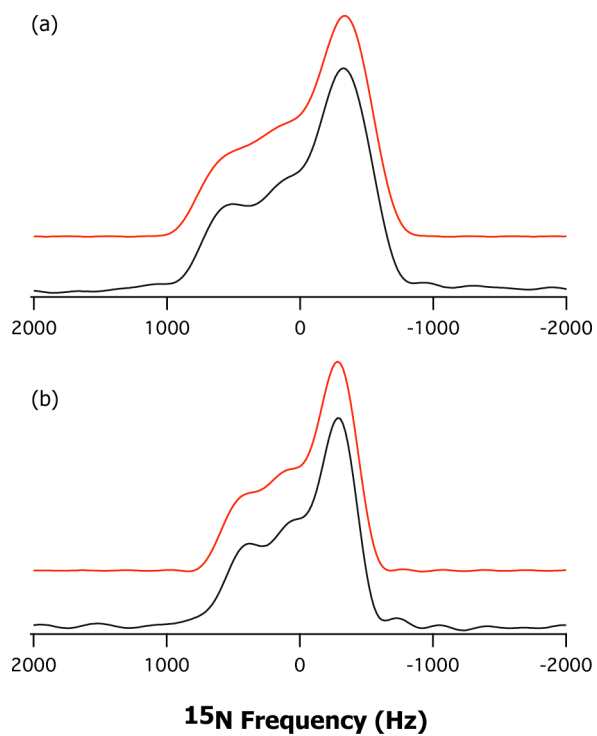


Figure 5.4: ^{15}N ROCSA spectra of $\text{Th}\cdot\text{HCl}$ and Th : experimental (black) and simulated (red). (a) $\text{N4}'$ of $\text{Th}\cdot\text{HCl}$. (b) $\text{N4}'$ of Th . (Adapted from ref. [24] with permission)

Table 5.2 Experimental and Computed ^{13}C and ^{15}N CSA Parameters for 2,6'- $^{13}\text{C}/4'$ - ^{15}N Th•HCl and Th

Sample	Atom	Method	δ_{iso} (ppm)	δ_{σ} (ppm)	η_{σ}	δ_{11} (ppm)	δ_{22} (ppm)	δ_{33} (ppm)
Th•HCl	C2	Slow-MAS	153.4	-98.5 ± 1.6	0.59 ± 0.03	231.7 ± 1.6	173.6 ± 1.7	54.9 ± 1.7
		ROCSA	153.4	-103.8 ± 2.6	0.61 ± 0.04	237.0 ± 2.6	173.6 ± 2.6	49.6 ± 2.6
		DFT/with Cl ⁻	154.9	-105.9	0.80	250.2	165.5	49.0
		DFT/without Cl ⁻	158.7	110.3	1.00	269.0	158.7	48.4
	C6'	Slow-MAS	147.8	-109.6 ± 4.5	0.78 ± 0.03	245.3 ± 4.5	159.9 ± 3.3	38.2 ± 3.3
		ROCSA	147.8	-111.3 ± 3.7	0.81 ± 0.06	248.5 ± 3.7	158.4 ± 4.1	36.5 ± 4.1
		DFT/with Cl ⁻	153.7	-114.0	0.87	260.3	161.1	39.7
		DFT/without Cl ⁻	149.7	-110.2	0.88	253.3	156.3	39.5
	N4'	ROCSA	116.5	74.9 ± 1.8	0.27 ± 0.08	191.4 ± 1.8	89.2 ± 3.1	68.9 ± 3.1
		DFT/with Cl ⁻	113.1	70.8	0.11	183.9	81.6	73.8
		DFT/without Cl ⁻	103.8	78.4	0.25	182.2	74.4	54.8
	Th	C2	Slow-MAS	156.5	-100.8 ± 1.2	0.66 ± 0.05	240.2 ± 1.2	173.6 ± 2.6
ROCSA			156.5	-103.1 ± 2.4	0.62 ± 0.04	240.0 ± 2.4	176.1 ± 2.5	53.4 ± 2.5
DFT/with Cl ⁻			155.6	-107.0	0.75	249.2	169.0	48.6
DFT/without Cl ⁻			162.8	-114.9	0.80	266.2	174.3	47.9
C6'		Slow-MAS	160.4	-107.8 ± 2.2	0.92 ± 0.03	263.9 ± 2.2	164.7 ± 2.2	52.6 ± 2.2
		ROCSA	160.4	-108.7 ± 2.6	0.93 ± 0.04	265.3 ± 2.6	164.2 ± 2.8	51.7 ± 2.8
		DFT/with Cl ⁻	162.2	109.2	0.90	271.4	156.7	58.5
		DFT/without Cl ⁻	163.4	-108.6	0.99	271.5	163.9	54.8
N4'		ROCSA	91.2	59.6 ± 1.6	0.28 ± 0.04	150.8 ± 1.6	69.7 ± 1.5	53.1 ± 1.5
		DFT/with Cl ⁻	98.2	59.5	0.51	157.7	83.6	53.3
		DFT/without Cl ⁻	70.2	-56.2	0.90	123.5	73.0	14.0

From Table 5.2, it is obvious that the two methods give consistent results for ^{13}C CS tensors in both ionization states. The C2 CS tensor is not very different in the two ionization forms. The three principal components (δ_{11} , δ_{22} and δ_{33}) display a small shift of ca. 3.0 ppm in the upfield direction upon protonation, from Th to Th•HCl. As a result, the net change is only in the isotropic chemical shift, from 156.5 ppm to 153.4 ppm, but the reduced anisotropy δ_{σ} and the asymmetry parameter η_{σ} remain nearly the same in the two states. As expected, the CS parameters of C6' are significantly different in the two protonation states. The C6' isotropic chemical shift changes by about 12.5 ppm upfield upon protonation from Th to Th•HCl. The principal components of the CS tensor, δ_{11} and δ_{33} also move upfield by 17.0 and 15.0 ppm, respectively (Figure 5.5 A). The δ_{22} component displays only a small shift of 6.0 ppm. The resulting change in the reduced anisotropy δ_{σ} and the asymmetry parameter η_{σ} are negligible- these remain the same within the error bars in the two protonation states, as the difference between the relative shifts of δ_{iso} and δ_{33} is small.

The ^{15}N ROCSA spectra are presented in Figure 5.4. The N4' CS parameters are found to be even more sensitive to the protonation state than those for C6'. The isotropic chemical shift, δ_{iso} , differs by more than 25.0 ppm in the two forms. Of the three principal components of the CS tensor, the δ_{11} component of N4' CSA tensor is observed to be the most sensitive to the protonation, moving downfield by ca. 40.0 ppm from Th to Th•HCl. As a result, the reduced anisotropy, δ_{σ} , increases by 15 ppm in Th•HCl. The δ_{22} and δ_{33} principal components also display considerable downfield shift of 20.0 and 16.0 ppm, respectively (Figure 5.5 B). We note that it is not possible to measure η_{σ} accurately in our experiments, because this parameter has a strong correlation with the line-broadening parameter used in fitting the experimental ^{15}N

ROCSA lineshapes with nearly axial symmetry. As a consequence, the position of both δ_{22} and δ_{33} is not as well defined as that of δ_{11} , especially when η_{σ} is in the range of 0.1 - 0.4 [50].

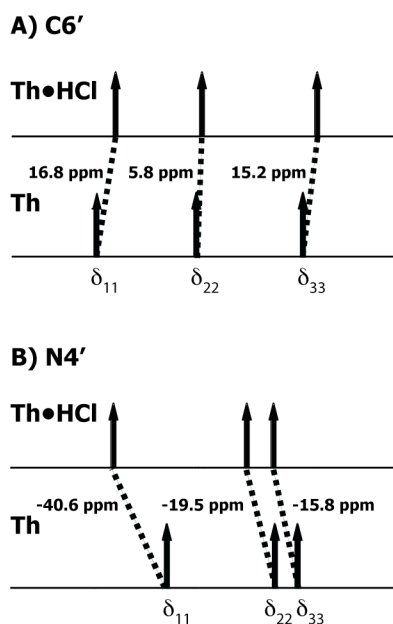


Figure 5.5: Deviation of the A) C6' and B) N4' chemical shift tensor components upon deprotonation from Th•HCl to Th.

5.3.4 ^{13}C , ^{15}N CSA Tensors in Thiamin Hydrochloride: Density Functional Theory

Experimental results and DFT calculations are summarized in Table 5.2. DFT calculations performed on the geometry-optimized structure of Th•HCl predict the experimental trend very well in the following respects: i) C6' is more shielded than C2; and ii) δ_{σ} of C6' is larger than that of C2.

The calculations predict the principal components of the C2 CS tensor to within 9.0 ppm. The calculated isotropic chemical shift of C2, 154.9 ppm, agrees well with the experimental value of 153.4 ppm. The maximum deviation is observed for δ_{11} (13.0 ppm) and δ_{22} (-8.0 ppm) with δ_{33} showing no deviation at all. For C6', the computed principal components of the magnetic shielding tensor are in even better agreement with the experimental results, with the difference being only of the order of 7.0 ppm. Since for C6' the three computed principal components deviate in the same direction (deshielded) with respect to the experimental values, the isotropic chemical shift also differs by 6.0 ppm.

For the N4' CS tensor, the agreement between experiment and theory is excellent, and even tighter agreement is observed than for the ^{13}C tensors. The average deviation of the three principal components is less than 7.0 ppm. The computed δ_{11} and δ_{22} are 7.5 ppm upfield, while the calculated δ_{33} is downfield by 5 ppm compared with experiment. The calculated isotropic chemical shift is therefore only 3.4 ppm different from the experimental value.

The effect of the presence of two chloride anions was also addressed in the DFT calculations. We performed an additional round of calculations with geometry optimization on the twice positively charged Th•HCl without the two chloride anions. The following trends were observed:

1. The predicted C6' CS tensor is in much better agreement with experiment without the two chloride anions. The average deviation between experiment and theory is less than 4.0 ppm for the three principal components. The predicted isotropic chemical shift of 149.7 ppm is in much better agreement with the experimental value of 147.8 ppm.

2. The computed principal components of the C2 CSA tensor show greater deviations from the experimental values (by more than 20.0 ppm on average). As observed in the calculations with neutral thiamin hydrochloride, this deviation can be largely attributed to changes in δ_{11} (30.0 ppm) and to a lesser extent to δ_{22} (-15.0 ppm) with δ_{33} showing no deviation at all.
3. The computed N4' CS tensor in the absence of the chloride anions deviates more from the experimental values with an average difference of 13.0 ppm for the individual principal components. Both δ_{22} and δ_{33} display the maximum deviation from experimental values and also from their computed values in the presence of chloride ions. The δ_{11} component of N4' remains relatively unchanged upon the removal of the chloride ions.

5.3.5 ^{13}C , ^{15}N CSA Tensors in Thiamin: Density Functional Theory

For the DFT calculations on thiamin, we used a starting model that was derived from the Th•HCl X-ray structure by removing the HCl. We performed geometry optimization to obtain the final structure for magnetic shielding tensor calculations.

As in the case of Th•HCl, DFT calculations on the geometry-optimized Th structure correctly predict that C6' is more deshielded than C2, which is consistent with the experimental results. The calculated reduced anisotropy, δ_{σ} , of C6' is higher than that of C2, as observed in experiments.

The calculated principal components of the C2 CS tensor agree with their experimental values to within 7.0 ppm. As in the Th•HCl calculation, δ_{11} of C2 shows greater deviation from experiment (9.0 ppm downfield), while δ_{22} and δ_{33} are upfield compared with experiment. As a result, the calculated isotropic chemical shift is

different by only 1.0 ppm from experiment. For C6', the average deviation of the calculated principal components is also less than 7.0 ppm. δ_{11} and δ_{33} are downfield compared with experiment (by 6.2 and 6.8 ppm, respectively), while δ_{22} is upfield by 7.5 ppm. This results in the calculated isotropic chemical shift (162.2 ppm) in close agreement with the experimental value (160.4 ppm).

The calculated N4' CS tensor components are also in close agreement with experiment, to within 9.0 ppm. As observed in the Th•HCl calculations, both δ_{11} and δ_{22} contribute to the difference between calculations and experiment with δ_{33} showing no deviation.

The perturbation of the carbon CS tensors due to the removal of the chloride anions in Th is nearly the same as in Th•HCl. The C6' CS tensor is observed to agree more closely with the experimental values, but the C2 CS tensor tends to deviate to a greater extent from the experiment; nevertheless, the agreement between theory and experiment is very good.

Conversely, the absence of the two chloride anions has a great effect on the N4' CS tensor in Th. The δ_{11} and δ_{33} components differ from their experimental values by -27.0 and -39.0 ppm, respectively. As a result, the computed isotropic chemical shift is off by more than 20.0 ppm upfield. Moreover, the calculations predict an almost rhombic tensor ($\eta_{\sigma} = 0.90$), whereas in experiments the tensor is close to axial ($\eta_{\sigma} = 0.28$).

The sensitivity of the C2 and N4' CS tensors to the absence of the chloride ions in both AP and APH⁺ forms can be attributed to the chloride ion located close to the sulfur atom in the thiazolium ring (Figure 6.6). The interatomic C2-Cl and N4'-Cl

distances are ca. 3.7 Å and 3.2 Å, respectively, in the X-ray structure as well as in the geometry-optimized structures used in our shielding tensor calculations.

In summary, the calculations predict accurately the C2 and N4' CS tensors in the presence of the chloride anions, and the C6' CS tensor in the absence of chloride anions. This trend is observed to be the same for both Th and Th•HCl. The correlation between the computed and the experimental CS components is shown in Figure 5.6 for both ^{13}C and ^{15}N atoms. As discussed, the correlation between the ^{15}N CS tensor predictions and the experimental values is much better in the presence of the chloride anions than without chloride anions (see Figure 5.6b and 5.6c, respectively).

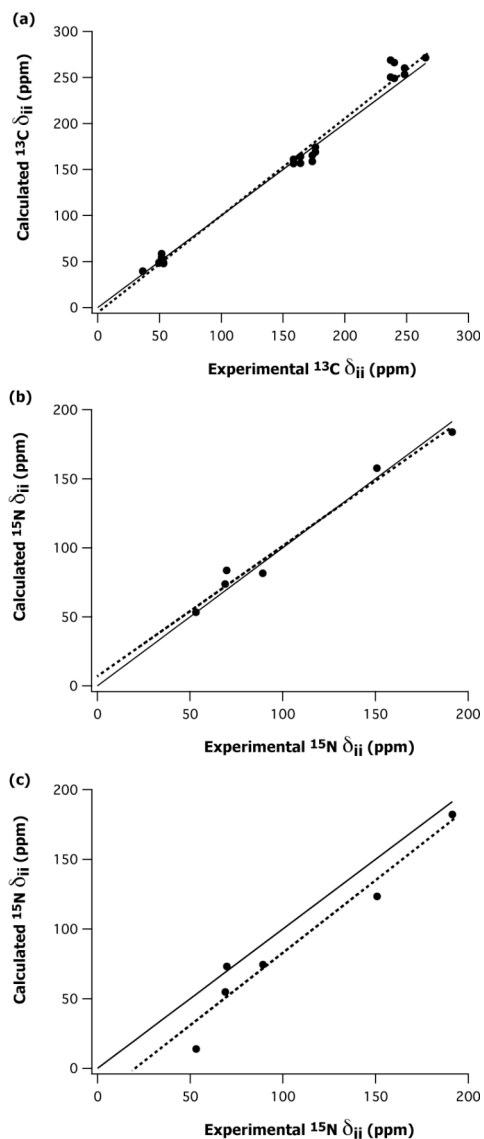


Figure 5.6: Correlation between the principal components δ_{ii} of the calculated (DFT) and the experimental (MAS NMR) chemical shift anisotropy tensors of Th•HCl and Th: (a) ^{13}C of C2 and C6', (b) ^{15}N of 4' with chloride anions, and (c) ^{15}N of N4' without chloride anions. The solid lines in all three figures indicate perfect agreement ($\delta_{\text{cal}} = \delta_{\text{exp}}$), and the dotted lines are the least-square fits: (a) $\delta_{\text{cal}} = 1.05 \cdot \delta_{\text{exp}} - 4.88$, $R^2 = 0.99$, (b) $\delta_{\text{cal}} = 0.94 \cdot \delta_{\text{exp}} + 7.86$, $R^2 = 0.98$; and (c) $\delta_{\text{cal}} = 1.03 \cdot \delta_{\text{exp}} - 20.28$, $R^2 = 0.94$. (Adapted from ref. [24] with permission)

5.3.6 Relative Orientations of ^{13}C , ^{15}N CSA Tensors in the Thiamin Molecular Frame

In an effort to determine whether there is any marked difference in the orientation of CS tensors of the key atoms in the two ionization states, we calculated the C6' and N4' tensor orientations with respect to the molecular frame.

As illustrated in Figure 5.7, the orientation of C6' CS tensor in Th•HCl is such that the δ_{33} component lies perpendicular to the 4'-aminopyrimidine ring, and both δ_{11} and δ_{22} lie in the plane of the ring. The δ_{11} component is inclined at an angle of 18° - 25° with respect to the C6'-H bond vector. Interestingly, the orientation remains largely unchanged upon deprotonation with only the direction of δ_{11} moving closer to the C6'-H bond by about 10° . The absence of the two chloride anions does not affect the orientation of the C6' CS tensor, and each component retains the same position as with chloride anions (figure not shown).

The orientation of the N4' CS tensor is such that the δ_{22} component is perpendicular to the 4'-aminopyrimidine ring. The δ_{11} component is collinear with the C4'-N4' bond vector. Interestingly and similar to the C6' results, this orientation remains unchanged upon deprotonation. However, the absence of the chloride ions significantly affects the N4' CS tensor orientation. In the protonated form, the δ_{22} component moves away from the normal to the 4'-aminopyrimidine plane by about 50° , with only δ_{11} lying in the 4'-aminopyrimidine plane. In thiamin, all three components change their orientation, with both δ_{11} and δ_{33} moving away from the plane by 13° and 10° , respectively, and δ_{22} moves away from the normal by 17° .

In summary, we observed no major differences in the orientation of the C6' and N4' CSA tensors in the two ionization states in the presence of chloride anions. The absence of chloride ions, although having no impact on the ^{13}C tensors, affects the

N4' CSA tensor, resulting in different orientations of the principal components in the protonated and unprotonated forms.

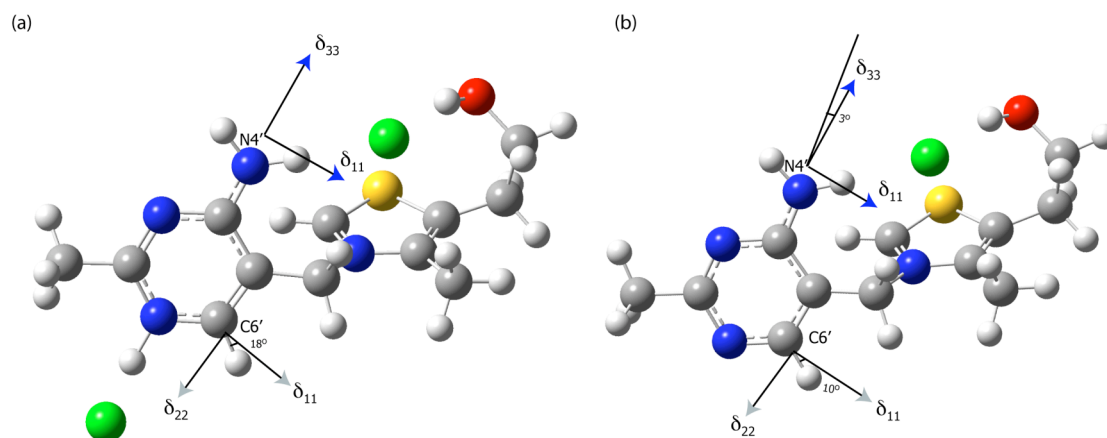


Figure 5.7: Structures of Th.HCl (a) and Th (b) used for DFT calculations and depicting orientations of C6' and N4' CSA tensors. For both atoms, the third principal component (δ_{33} for C6', δ_{22} for N4') is perpendicular to 4'-aminopyrimidine plane. (Adapted from ref. [24] with permission)

5.4 Conclusions

This work demonstrates that the ^{13}C and the ^{15}N CS tensors of C2, C6' and N4' atoms are sensitive probes of the ionization state of thiamin. Both the principal components of the CS tensors and the isotropic chemical shifts exhibit significant changes upon protonation/deprotonation. The density functional theory calculations are in excellent agreement with the experimental findings. The predicted C6' and N4' isotropic chemical shifts are within 6.0 ppm and 7.0 ppm of the experimental values, respectively. Considering that the isotropic chemical shift difference of these atoms in the two ionization states far exceeds this range of deviation, we conclude that the DFT calculation of CS parameters can be used in conjunction with MAS NMR measurements for characterization of the different ionization states of thiamin. The results of this work are expected to guide future investigations of thiamin ionization and tautomeric states in thiamin-dependent enzymes, which will address some of the remaining open questions about their enzymatic mechanisms.

5.5 References

- (1) Jordan, F. *Nat. Prod. Rep.* **2003**, 20(2), 184-201.
- (2) Schellenberger, A. *Biochim. Biophys. Acta* **1998**, 1385(2), 177-86.
- (3) Nemeria, N.; Chakraborty, S.; Baykal, A.; Korotchkina, L. G.; Patel, M. S.; Jordan, F. *PNAS* **2007**, 104(1), 78-82.
- (4) Nemeria, N.; Korotchkina, L.; McLeish, M. J.; Kenyon, G. L.; Patel, M. S.; Jordan, F. *Biochemistry* **2007**, 46(37), 10739-44.
- (5) Nemeria, N.; Baykal, A.; Joseph, E.; Zhang, S.; Yan, Y.; Furey, W.; Jordan, F. *Biochemistry* **2004**, 43(21), 6565-75.
- (6) Jordan, F.; Nemeria, N. S.; Zhang, S.; Yan, Y.; Arjunan, P.; Furey, W. *J. Am. Chem. Soc.* **2003**, 125(42), 12732-8.
- (7) Kern, D.; Kern, G.; Neef, H.; Tittmann, K.; Killenberg-Jabs, M.; Wikner, C.; Schneider, G.; Hubner, G. *Science* **1997**, 275(5296), 67-70.
- (8) Kaplun, A.; Binshtein, E.; Vyazmensky, M.; Steinmetz, A.; Barak, Z.; Chipman, D. M.; Tittmann, K.; Shaanan, B. *Nat. Chem. Biol.* **2008**, 4(2), 113-8.
- (9) Meshalkina, L. E.; Kochetov, G. A.; Brauer, J.; Hubner, G.; Tittmann, K.; Golbik, R. *Biochem. Biophys. Res. Commun.* **2008**, 366(3), 692-7.
- (10) Tittmann, K.; Neef, H.; Golbik, R.; Hubner, G.; Kern, D. *Biochemistry* **2005**, 44(24), 8697-700.
- (11) Reynolds, W. F.; Peat, I. R.; Freedman, M. H.; Lyster, J. R. *J. Am. Chem. Soc.* **1973**, 95(2), 328-331.
- (12) Rabenstein, D. L.; Sayer, T. L. *J. Magn. Reson.* **1976**, 24(1), 27-39.
- (13) Surprenant, H. L.; Sarneski, J. E.; Key, R. R.; Byrd, J. T.; Reilley, C. N. *J. Magn. Reson.* **1980**, 40(2), 231-243.
- (14) Bachovchin, W. W.; Roberts, J. D. *J. Am. Chem. Soc.* **1978**, 100(26), 8041-8047.
- (15) Sudmeier, J. L.; Bradshaw, E. M.; Haddad, K. E. C.; Day, R. M.; Thalhauser, C. J.; Bullock, P. A.; Bachovchin, W. W. *J. Am. Chem. Soc.* **2003**, 125(28), 8430-8431.
- (16) Naito, A.; Ganapathy, S.; Akasaka, K.; McDowell, C. A. *J. Chem. Phys.* **1981**, 74(6), 3190-3197.
- (17) Haberkorn, R. A.; Stark, R. E.; Van Willigen, H.; Griffin, R. G. *J. Am. Chem. Soc.* **1981**, 103(10), 2534-2539.
- (18) Smith, S. O.; Farr-Jones, S.; Griffin, R. G.; Bachovchin, W. W. *Science* **1989**, 244(4907), 961-964.
- (19) Gu, Z.; McDermott, A. *J. Am. Chem. Soc.* **1993**, 115(10), 4282-4285.
- (20) Gu, Z.; Zambrano, R.; McDermott, A. *J. Am. Chem. Soc.* **1994**, 116(14), 6368-6372.
- (21) Bagno, A.; Scorrano, G. *J. Phys. Chem.* **1996**, 100(5), 1545-1553.
- (22) Ooms, K. J.; Bolte, S. E.; Smees, J. J.; Baruah, B.; Crans, D. C.; Polenova, T. *Inorg. Chem.* **2007**, 46(22), 9285-9293.

- (23) Ooms, K.; Polenova, T.; Shough, A.-M.; Doren, D. J.; Nash, M. J.; Lobo, R. F. *J. Phys. Chem. C* **2009**, *113*(24), 10477-10484.
- (24) Paramasivam, S.; Balakrishnan, A.; Dmitrenko, O.; Godert, A.; Begley, T. P.; Jordan, F.; Polenova, T. *J. Phys. Chem. B* **2011**, *115*(4), 730-6.
- (25) Balakrishnan, A. Ph.D. Thesis, Rutgers University, Newark, 2011.
- (26) Neue, G.; Dybowski, C. *Solid State Nucl. Magn. Reson.* **1997**, *7*(4), 333-336.
- (27) Bennett, A. E.; Rienstra, C. M.; Auger, M.; Lakshmi, K. V.; Griffin, R. G. *J. Chem. Phys.* **1995**, *103*(16), 6951-6958.
- (28) Herzfeld, J.; Berger, A. E. *J. Chem. Phys.* **1980**, *73*(12), 6021-6030.
- (29) Chan, J. C. C.; Tycko, R. *J. Chem. Phys.* **2003**, *118*(18), 8378-8389.
- (30) States, D. J.; Haberkorn, R. A.; Ruben, D. J. *J. Magn. Reson.* **1982**, *48*(2), 286-292.
- (31) Bak, M.; Rasmussen, J. T.; Nielsen, N. C. *J. Magn. Reson.* **2000**, *147*(2), 296-330.
- (32) Gaussian 03, R. C., Frisch, M. J.; Trucks, G. W.; Schlegel, H. B.; Scuseria, G. E.; Robb, M. A.; Gaussian, Inc., Wallingford, CT, 2004.
- (33) Schlegel, H. B. *J. Comput. Chem.* **1982**, *3*(2), 214-218.
- (34) Becke, A. D. *Phys. Rev. A* **1988**, *38*(6), 3098-3100.
- (35) Becke, A. D. *J. Chem. Phys.* **1993**, *98*(7), 5648-5652.
- (36) Lee, C. T.; Yang, W. T.; Parr, R. G. *Phys. Rev. B* **1988**, *37*(2), 785-789.
- (37) Schafer, A.; Horn, H.; Ahlrichs, R. *J. Chem. Phys.* **1992**, *97*(4), 2571-2577.
- (38) Schafer, A.; Huber, C.; Ahlrichs, R. *J. Chem. Phys.* **1994**, *100*(8), 5829-5835.
- (39) Wolinski, K.; Hinton, J. F.; Pulay, P. *J. Am. Chem. Soc.* **1990**, *112*(23), 8251-8260.
- (40) McWeeny, R. *Phys. Rev.* **1962**, *126*(3), 1028.
- (41) Wolinski, K.; Sadlej, A. J. *Mol. Phys.* **1980**, *41*(6), 1419 - 1430.
- (42) Ditchfield, R. *Mol. Phys.* **1974**, *27*(4), 789 - 807.
- (43) Te, R. L.; Griesser, U. J.; Morris, K. R.; Byrn, S. R.; Stowell, J. G. *Cryst. Growth Des.* **2003**, *3*(6), 997-1004.
- (44) Kutzelnigg, W.; Fleischer, U.; Schindler, M. *The IGLO-Method: Ab Initio Calculation and Interpretation of NMR Chemical Shifts and Magnetic Susceptibilities* Springer Verlag, 1990; Vol. 23.
- (45) Cossi, M.; Barone, V.; Cammi, R.; Tomasi, J. *Chem. Phys. Lett.* **1996**, *255*(4-6), 327-335.
- (46) Miertus, S.; Tomasi, J. *Chem. Phys.* **1982**, *65*(2), 239-245.
- (47) Miertus, S.; Scrocco, E.; Tomasi, J. *Chem. Phys.* **1981**, *55*(1), 117-129.
- (48) Dooley, R.; Milfeld, K.; Guiang, C.; Pamidighantam, S.; Allen, G. *J. Grid Comput.* **2006**, *4*(2), 195-208.
- (49) Brender, J. R.; Taylor, D. M.; Ramamoorthy, A. *J. Am. Chem. Soc.* **2001**, *123*(5), 914-922.
- (50) Wylie, B. J.; Franks, W. T.; Rienstra, C. M. *J. Phys. Chem. B* **2006**, *110*(22), 10926-10936.

Chapter 6

ASSIGNMENT OF IONIZATION AND TAUTOMERIC STATES IN THE THIAMIN DIPHOSPHATE FAMILY OF ENZYMES BY MAS NMR SPECTROSCOPY

6.1 Introduction

In the thiamin diphosphate (ThDP) superfamily of enzymes, ThDP interconverts among several ionization and tautomeric states during the catalytic reaction [1-6]. Identification and characterization of these various ionization/tautomeric states of ThDP by spectroscopic techniques are essential to understand their catalytic mechanism.

In the previous chapter, MAS NMR spectroscopy was applied to characterize two of the ionization states (AP and APH⁺) of thiamin in terms of ¹³C and ¹⁵N chemical shift tensors of the key atoms using specifically labeled thiamin analogs. In particular, it was shown that, in addition to the anisotropy parameter (δ_o), the isotropic chemical shifts (δ_{iso}) of C6' and N4' are also uniquely sensitive to the two ionization states (with ca.12 ppm difference for C6' and 25 ppm for N4')[7]. These results, obtained from the analog compounds, can be extended to infer ionization/tautomeric states of ThDP, the biologically active form of thiamin, because the β -diphosphate moiety in ThDP is located too far from the heterocyclic rings to make any significant contribution to the chemical shifts of the key atoms.

In this chapter, we use the model chemical shifts of the AP and APH⁺ forms to interpret the ¹³C and ¹⁵N MAS NMR spectra of ThDP bound to: (1) yeast pyruvate

decarboxylase (YPDC, EC 4.1.1.1); (2) the E1 components of the pyruvate (E1p, EC 1.2.4.1), and (3) 2-oxoglutarate (E1o, EC 1.2.4.2) dehydrogenase complexes from *E. coli*. The molecular masses of these enzymes are in the range 160 – 250 kDa, which excludes the possibilities of solution NMR applications to these enzyme systems. MAS NMR spectroscopy is a suitable technique for the study of such large molecular systems with the independence of resonance linewidths on the molecular size [8,9].

6.2 Experimental Methods

6.2.1 Materials

The detailed description of enzymatic synthesis of [$^{13}\text{C}_2,^{13}\text{C}_6$] and [$^{15}\text{N}_4$] labeled ThDP from labeled thiamin, protein expression, purification procedures, and incorporation of labeled ThDP into enzymes are given in ref [10].

6.2.2 Solid-State NMR Spectroscopy

All ^{13}C CPMAS spectra were acquired at 9.4 T (400.17 MHz ^1H Larmor frequency) on a Tecmag Discovery spectrometer outfitted with a 3.2 mm wide bore Varian HXY T3 probe. The MAS frequency was 10.000 ± 0.010 kHz, controlled by a Tecmag MAS controller. The temperature calibration was done using a PbNO_3 temperature sensor [11]. For both ^{13}C and ^{15}N CPMAS experiments, the actual sample temperature includes a correction of +5 °C taking into account sample spinning. ^{13}C chemical shifts were referenced to the most deshielded peak of adamantane (38.56 ppm with respect to TMS). The ramped CP sequence was used with 1.0 -1.5 ms contact time. The ^1H radio frequency field strength was 50-60 kHz, and the ^{13}C field was linearly ramped from 80-100% with the center of the ramp being $\omega_{\text{rf}}(^{13}\text{C}) = \omega_{\text{rf}}(^1\text{H}) \pm \omega_{\text{r}}$. The ^1H 90° pulse length was 2.5-3.65 ms. The ^1H decoupling was

performed using TPPM [12] with $\omega_{rf} = 70$ -100 kHz. The number of transients and the recycle delay for each spectrum are given in the figure captions. All ^{13}C spectra were processed with 20 Hz exponential broadening.

All ^{15}N CPMAS spectra were acquired at 14.1 T (599.78 MHz ^1H Larmor frequency) on a Varian InfinityPlus spectrometer outfitted with a standard bore 3.2 mm HXY T3 probe. The MAS frequency was 10.000 ± 0.001 kHz, controlled by a Varian MAS controller. ^{15}N chemical shifts were referenced ammonium chloride (39.2 ppm with respect to liquid NH_3). The ramped CP sequence was used with 1.5-1.6 ms contact time. The ^1H radio frequency field strength was 50-60 kHz and the ^{15}N field was linearly ramped from 80-100% with the center of the ramp being $\omega_{rf}(^{15}\text{N}) = \omega_{rf}(^1\text{H}) \pm \omega_r$. The ^1H 90° pulse length was 2.50-2.78 ms. ^1H decoupling was performed using TPPM [12] with $\omega_{rf} = 90$ -100 kHz. The number of transients, the recycle delay, and the apodization parameters for each spectrum are given in the figure captions.

6.3 Results and Discussion

6.3.1 ^{13}C CPMAS NMR on ThDP-Dependent Enzymes

Our previous work on thiamin analogs suggests that the isotropic chemical shift of the C6' atom is a direct marker of the ionization state of the 4'-aminopyrimidine ring, as it shifts downfield from ca. 148 ppm in APH^+ form to ca. 160 ppm in AP form. This observation is complementary to the CD experiments where only the AP and IP forms can be detected.

6.3.1.1 ^{13}C CPMAS NMR Spectra of ThDP-YPDC Complex

When the ^{13}C MAS NMR spectrum of YPDC reconstituted with [$^{13}\text{C}2, ^{13}\text{C}6'$]-ThDP was compared with the YPDC (with unlabeled ThDP) spectrum (Figure 6.1 a

and b), two new resonances stood out: One resonance at 162.2 ppm; and another at 146.5 ppm, the latter reminiscent of the C6' carbon in the protonated form of thiamin. With reference to the model chemical shifts reported in chapter 5, as well as experiments on E1o reconstituted with [$^{13}\text{C}2,^{13}\text{C}6'$]-ThDP (Figure 6.3a) and E1p reconstituted with [$^{13}\text{C}2$]-ThDP (Figure 6.2a) discussed later, these two resonances can be immediately assigned to individual atoms of ThDP bound to YPDC, the one at 162.2 ppm to C2 and the one at 146.5 ppm to C6' in the APH⁺ form.

Based on these observations, we draw the following conclusions: (a) ThDP is in its APH⁺ form according to the chemical shift of the C6' atom, and (b) the C2-H bond of the thiazolium ring is in its undissociated form, not in the ylide form. No evidence could be found for any resonances near 250 ppm previously assigned to a Ylide model by solution NMR spectroscopy [13].

We have also addressed the effect of substrate surrogate activation of YPDC on the ionization/tautomeric states of enzyme-bound ThDP. YPDC activity is known to be regulated by substrate binding at a distinct regulatory site Cys 221 [14-17]. Pyruvamide, a non-decarboxylating analog, is a known substrate activator surrogate [18]. In a spectrum of apo-YPDC reconstituted with [$^{13}\text{C}2,^{13}\text{C}6'$]-ThDP and pyruvamide (200 mM) (Figure 6.1c), there was no change in chemical shift of the C2 and C6' resonances, which were found at 162.2 ppm and 146.5 ppm, respectively. From this observation, it can be concluded that substrate surrogate activation does not affect the ionization/tautomeric states of enzyme bound ThDP.

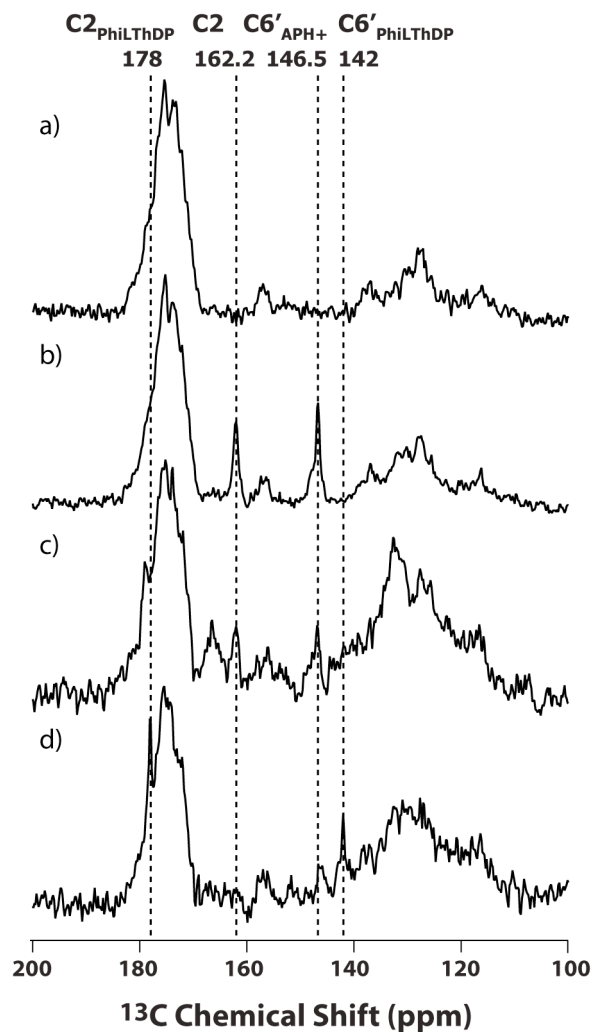


Figure 6.1: ^{13}C CPMAS NMR spectra of YPDC with a) unlabeled ThDP (control spectrum), b) only $[^{13}\text{C}_2, ^{13}\text{C}_6']$ -ThDP, c) $[^{13}\text{C}_2, ^{13}\text{C}_6']$ -ThDP and pyruvamide (100 mM). The broad resonance at ~ 166 ppm is from excess pyruvamide. d) $[^{13}\text{C}_2, ^{13}\text{C}_6']$ -ThDP and acetyl phosphinate (60 mM). All spectra were acquired at 5°C with 16,384 transients and 5 s recycle delay.

The Rutgers group has taken advantage of the fact that 2-oxophosphonates and 2-oxophosphinates are excellent 2-oxoacid analogs that form stable pre-decarboxylation intermediate analogs [19,20]. In this work, two analogs were used for this purpose; i) methyl acetylphosphonate (MAP with a single negative charge at the phosphonate monoester), and ii) acetyl phosphinate which is an even better steric approximation to pyruvate [21]. Both of these pyruvate analogs gave strong indication that in their covalent adducts with ThDP on enzymes, the IP tautomeric form predominates.

Addition of AcPhi to YPDC resulted in the spectrum in Figure 6.1d. Three prominent changes were observed. (1) The C2 resonance at 162 ppm disappears. (2) Two new resonances at 142 ppm and 178 ppm appear. (3) The resonance at 146.5 ppm for the C6' in the APH⁺ form of ThDP is significantly diminished. The disappearance of the 162 ppm resonance and the appearance of a new one at 178 ppm could be attributed to the C2 atom in the enzyme-bound C2- α -phosphinolactyl-ThDP intermediate. The most novel finding is the strong resonance at 142 ppm, seen along with the weaker yet clear resonance at 146.5 ppm. Firstly, the resonance at 146.5 ppm (C6') corresponds to a fraction of unreacted enzyme-bound ThDP, seen as a Michaelis complex in CD experiments by the Rutgers group on YPDC, while the one at 142 ppm most likely pertains to the 4'-aminopyrimidine ring of C2 α -phosphinolactylThDP. The chemical shift for C6' resonance in the IP form is 136 ppm from model studies, and the chemical shift observed is a value between the IP (136 ppm) and the APH⁺ (146.5 ppm), suggesting an averaging due to fast exchange between these two forms in the active sites containing the tetrahedral intermediate analog. No unambiguous evidence was obtained for the IP tautomeric form from the C6' chemical shifts,

however, the C2 chemical shifts provided evidence for direct detection of enzyme bound tetrahedral intermediate of ThDP by NMR spectroscopy.

6.3.1.2 ^{13}C CPMAS NMR Spectra of ThDP-E1p Complex

For the purposes of unambiguous resonance assignment of C2, C6' of ThDP bound to E1p, the Rutgers group used two labeling strategies: one with singly labeled [$^{13}\text{C}2$]-ThDP and the other with doubly labeled [$^{13}\text{C}2,^{13}\text{C}6'$]-ThDP. In figure 6.2a, the MAS spectrum of [$^{13}\text{C}2$]-ThDP bound to E1p is presented. A weak signal at 162 ppm in the absence of MAP confirms the bound C2 resonance also seen in the case of YPDC (Figures 6.1d).

Two experiments were carried out with the addition of MAP: the middle spectrum (Figure 6.2b) is with the singly labeled [$^{13}\text{C}2$]-ThDP, the bottom spectrum with the doubly labeled [$^{13}\text{C}2,^{13}\text{C}6'$]-ThDP (Figure 6.2c). The spectra provide unambiguous assignment of C2 and C6', 184.2 ppm for the former and 145.5 ppm for the latter in the presence of MAP.

Based on the model chemical shifts of C6', it is clear that C6' is in the APH^+ form. The C2 resonance at 184.2 ppm displays a 22 ppm deshielding on formation of the tetrahedral PLThDP, appropriate for replacement of H by C [22].

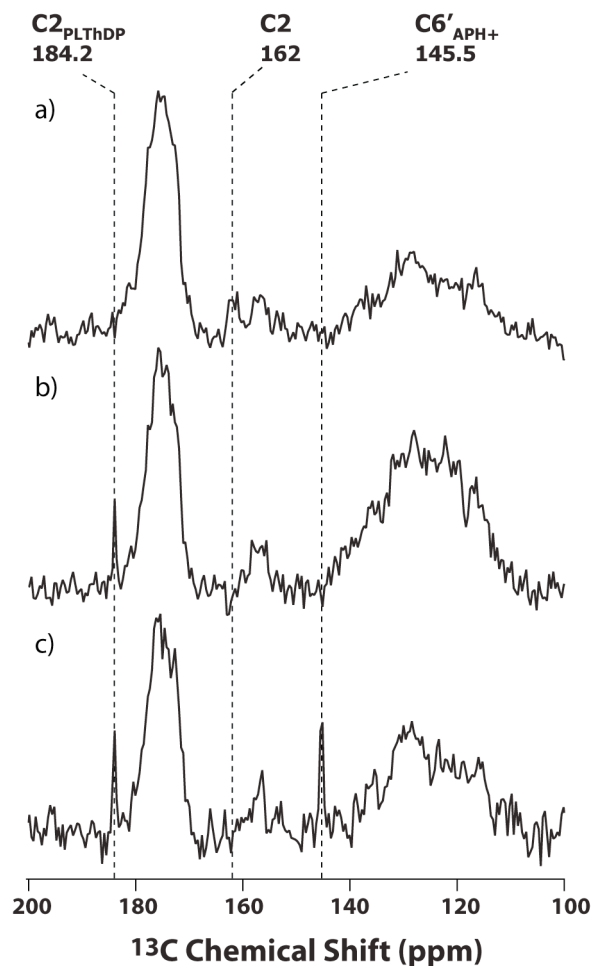


Figure 6.2: ^{13}C CPMAS NMR spectra of E1p reconstituted with $[^{13}\text{C}_2]$ -ThDP or $[^{13}\text{C}_2, ^{13}\text{C}_6']$ -ThDP. E1p reconstituted with: a) $[^{13}\text{C}_2]$ -ThDP, b) $[^{13}\text{C}_2]$ -ThDP and additional 10 mM methyl acetylphosphonate, c) $[^{13}\text{C}_2, ^{13}\text{C}_6']$ -ThDP and additional 10 mM methyl acetylphosphonate. The spectra were acquired at 15 °C with 16,384 transients and recycle delay was 10 s (spectrum a) and 5 s (spectra b and c).

6.3.1.3 ^{13}C CPMAS NMR Spectra of ThDP-E1o Complex

Based on the pH titration experiments conducted on E1o by the Rutgers group [5], it is expected that increasing the pH decreases the relative concentration of the APH^+ form, and only the $\text{C6}'$ resonance should be affected. This idea was tested by acquiring ^{13}C MAS NMR spectra of E1o reconstituted with [$^{13}\text{C2}, ^{13}\text{C6}'$]-ThDP at pH 7.0 and at pH 8.0 (Figure 6.3). The spectra reveal that the resonance at 146–147 ppm pertaining to the $\text{C6}'$ carbon diminishes in intensity significantly (relative to protein backbone), whereas the resonance at ~161 ppm pertaining to the C2 carbon is relatively unaffected. Moreover, a broad new resonance is seen at 167.2 ppm which is assigned to $\text{C6}'$ of enzyme bound ThDP in the AP form.

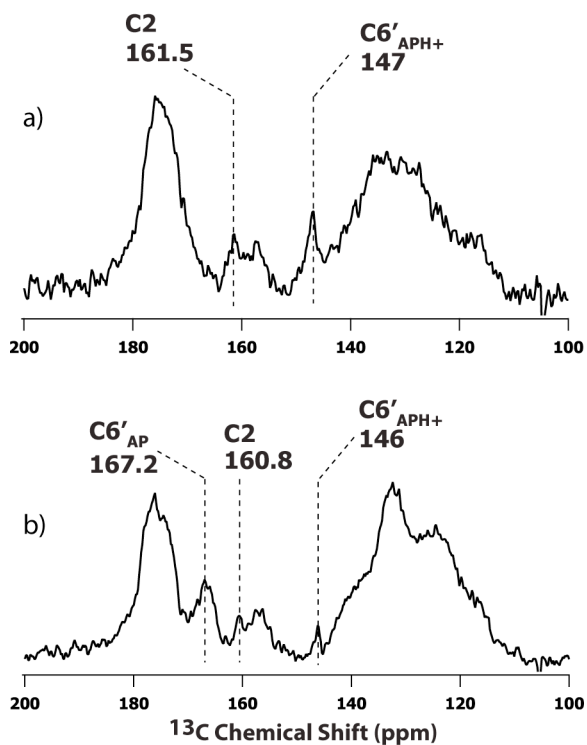


Figure 6.3: ^{13}C CPMAS NMR spectra of *E. coli* 2-oxoglutarate dehydrogenase E1 reconstituted with $[^{13}\text{C}_2, ^{13}\text{C}_6']$ -ThDP. a) Spectrum acquired at pH 7.0 at 8 °C with 32,768 transients. b) Spectrum acquired at pH 8.0 at 10 °C with 28,900 transient. Recycle delay was 5 s for both spectra.

6.3.2 ^{15}N CPMAS NMR on ThDP-dependent Enzymes

Based on the significantly large isotropic chemical shift difference (ca. 25 ppm) of $^{15}\text{N}_4'$ between AP and APH^+ form observed in the thiamin models, observation of the $^{15}\text{N}_4'$ resonance from ThDP bound to the enzymes may provide the most direct evidence for the state of tautomerization/ionization of the 4'-

aminopyrimidine ring. This experiment is even more challenging than the ^{13}C experiments described above because of the inherently low sensitivity of the ^{15}N spectra of ThDP bound to enzymes. We present ^{15}N CPMAS spectra acquired on two ThDP bound enzymes, E1p and YPDC.

6.3.2.1 ^{15}N CPMAS NMR Spectra of ThDP-E1p Complex

The ^{15}N resonance of [$^{15}\text{N}4'$]-ThDP in the APH^+ ionization state appears at 116.5 ppm from models, which falls within the envelope of the enzyme backbone amide resonances. Although the enzyme bound ThDP is predicted to be in the APH^+ form according to ^{13}C experiments at pH 7.0, no clear evidence for a ^{15}N resonance pertaining to the enzyme-bound APH^+ form could be obtained. Nevertheless, the spectra presented in Figures 6.4 and 6.5 provide important insight: in the presence of MAP, we observe a clear indication of a new signal around 141.2 ppm at pH 7.0, a chemical shift between the 212 ppm for the IP form and APH^+ at 116.5 ppm (91.2 ppm for the AP form).

The pH dependence of CD experiments on the ThDP family of enzymes and the pH dependent ^{13}C SSNMR experiments on E1o predict a shift to the AP form for the enzyme-bound ThDP at higher pH values. Raising the pH from 7.0 to 8.0 gives indication for the existence of the AP form (84.6 ppm) of the enzyme-bound ThDP in E1p. In the presence of MAP at pH 8.0, there is also evidence for coexistence with other forms (141.2 ppm).

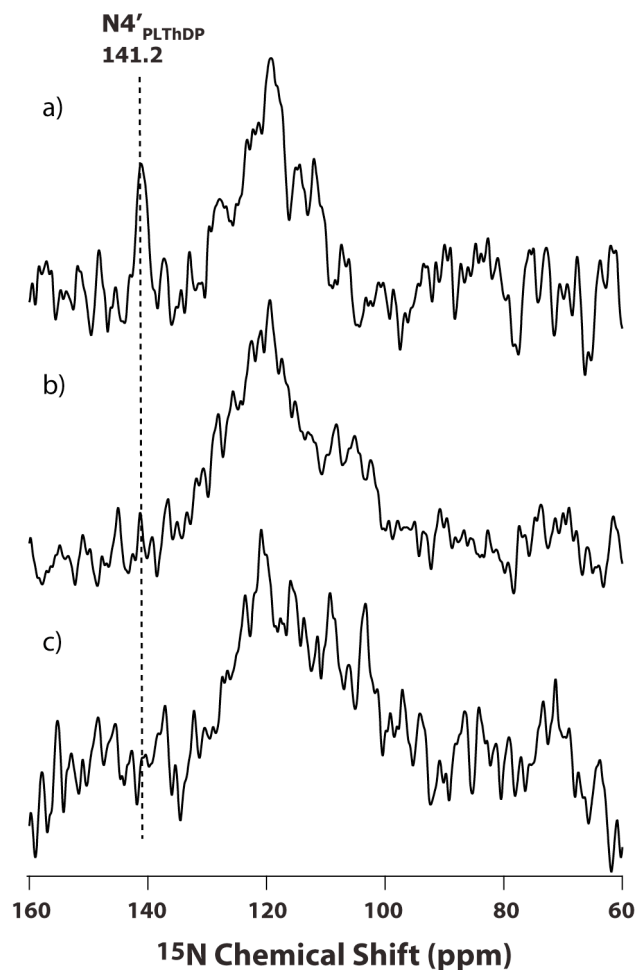


Figure 6.4: ^{15}N CPMAS NMR spectra of E1p reconstituted with $[^{15}\text{N}4']\text{-ThDP}$ at pH 7.0. E1p reconstituted with: a) 3 eq. $[^{15}\text{N}4']\text{-ThDP}$ and additional 10 mM methyl acetylphosphonate at $-25\text{ }^{\circ}\text{C}$. b) 3 eq. $[^{15}\text{N}4']\text{-ThDP}$ at $-25\text{ }^{\circ}\text{C}$. c) 1 eq. $[^{15}\text{N}4']\text{-ThDP}$ at $-23\text{ }^{\circ}\text{C}$. The spectra a sum of 30,720 transients (spectrum a), 16,384 scans (spectrum b), and 14,336 transients (spectrum c); the recycle delay was 5 s. All spectra were processed with 50 Hz exponential broadening.

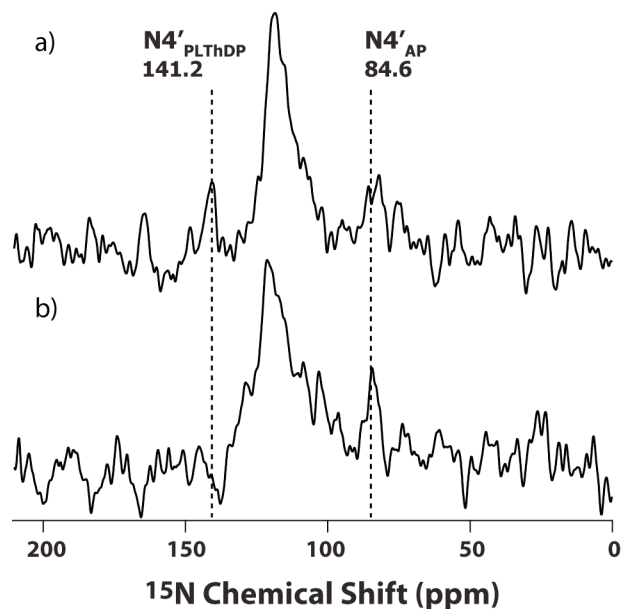


Figure 6.5: ^{15}N CPMAS NMR spectra of E1p reconstituted with $[^{15}\text{N}4']\text{-ThDP}$ at pH 8.0. E1p reconstituted with: a) 3 eq. $[^{15}\text{N}4']\text{-ThDP}$ and additional 10 mM methyl acetylphosphonate. b) 3 eq. $[^{15}\text{N}4']\text{-ThDP}$. The spectra were acquired at $-25\text{ }^{\circ}\text{C}$ with 32,768 scans and 5 s recycle delay. Both spectra were processed with 100 Hz exponential broadening.

Considering the CD and SSNMR data, one may postulate a plausible explanation for the observed value of 141.2 ppm as follows. The tetrahedral adduct formed between the ThDP and these phosphonate- or phosphinate-based substrate analogs is predominantly in the IP form (presumably in a pH-dependent equilibrium with the APH^+ form). At the higher pH of 8.0, we observe a resonance at 84.6 ppm corresponding to the enzyme with the AP form of ThDP, and one at 141.2 ppm which we attribute to a fast protolytic equilibrium between the APH^+ and IP forms of ThDP. Similar chemical shift averaging due to fast exchange on pyridoxal model systems and

also between two-site and three-site equilibria are seen by solid-state NMR studies on the pyridoxal-5'-phosphate dependent tryptophan synthase when the active-site is occupied by a quinonoid intermediate [23-26].

6.3.2.2 ^{15}N CPMAS NMR Spectra of ThDP-YPDC Complex

On YPDC, the ^{15}N spectra also suggest the presence of the IP form (Figure 6.6). In spectra of YPDC reconstituted with [$^{15}\text{N}4'$]-ThDP in the absence or presence of pyruvamide, no evidence is found for the enzyme bound ThDP at pH 6.0. On addition of acetylphosphinate, there is evidence of a signal centered at 176 ppm. This resonance is assigned to the IP form, which is in protolytic equilibrium with the APH^+ form, as discussed earlier.

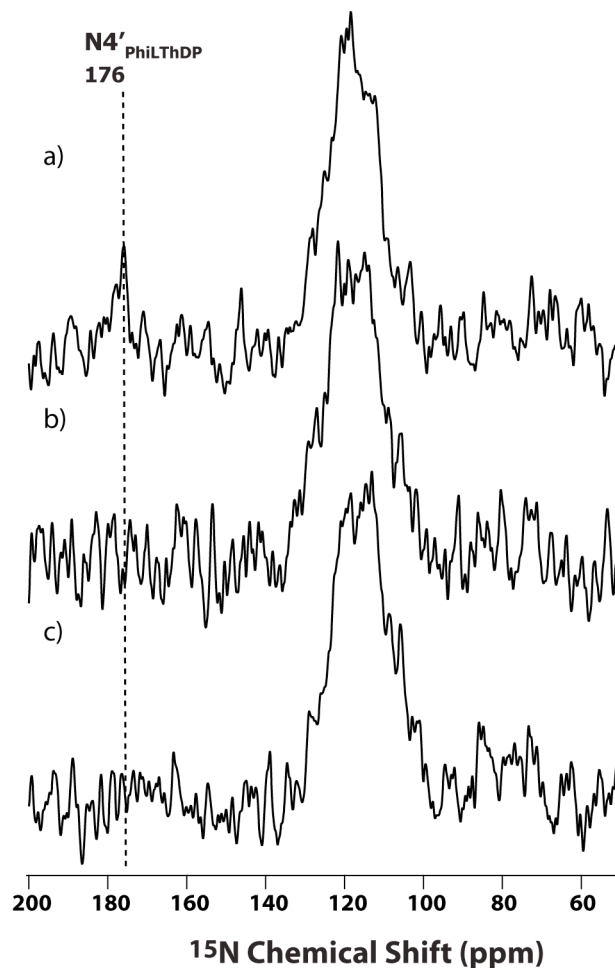


Figure 6.6: ^{15}N CPMAS NMR spectra of YPDC reconstituted with $^{15}\text{N}4'$ -ThDP with: a) in the presence of 60 mM acetyl phosphinate. b) in the presence of 300 mM pyruvamide. c) nothing added. The spectra were acquired at $-25\text{ }^{\circ}\text{C}$ with a) 57,344 scans and 4 s recycle delay, b) 23,552 scans with 5 s recycle delay, c) 27, 648 transients with 5 s recycle delay. All spectra were processed with 50 Hz exponential broadening.

6.4 Conclusions

MAS NMR has been applied for the first time to assign ionization/tautomeric states in ThDP family of enzymes. Although the CD methods have been used to identify AP and IP forms, ^{13}C and ^{15}N CPMAS spectra, specifically the isotropic chemical shifts of labeled C6' and N4', have been used for the first time to observe the APH+ form in all three enzymes used in this work. The isotropic chemical shift of the specifically labeled C2 carbon is also shown to be very sensitive to the addition of substrate analogs, providing strong evidence for the formation of tetrahedral intermediate on two enzymes. This study demonstrates the feasibility of application of MAS NMR spectroscopy to large molecular systems such as ThDP family of enzymes and its ability to infer atomic-level details from the uniquely sensitive chemical shift parameters.

6.5 References

- (1) Jordan, F. *Nat. Prod. Rep.* **2003**, 20(2), 184-201.
- (2) Jordan, F.; Nemeria, N. S.; Zhang, S.; Yan, Y.; Arjunan, P.; Furey, W. *J. Am. Chem. Soc.* **2003**, 125(42), 12732-8.
- (3) Nemeria, N.; Baykal, A.; Joseph, E.; Zhang, S.; Yan, Y.; Furey, W.; Jordan, F. *Biochemistry* **2004**, 43(21), 6565-75.
- (4) Nemeria, N.; Chakraborty, S.; Baykal, A.; Korotchkina, L. G.; Patel, M. S.; Jordan, F. *PNAS* **2007**, 104(1), 78-82.
- (5) Nemeria, N.; Korotchkina, L.; McLeish, M. J.; Kenyon, G. L.; Patel, M. S.; Jordan, F. *Biochemistry* **2007**, 46(37), 10739-44.
- (6) Tittmann, K.; Neef, H.; Golbik, R.; Hubner, G.; Kern, D. *Biochemistry* **2005**, 44(24), 8697-700.
- (7) Paramasivam, S.; Balakrishnan, A.; Dmitrenko, O.; Godert, A.; Begley, T. P.; Jordan, F.; Polenova, T. *J. Phys. Chem. B* **2011**, 115(4), 730-6.
- (8) Han, Y.; Ahn, J.; Concel, J.; Byeon, I. J.; Gronenborn, A. M.; Yang, J.; Polenova, T. *J. Am. Chem. Soc.* **2010**, 132(6), 1976-87.
- (9) Sun, S.; Siglin, A.; Williams, J. C.; Polenova, T. *J. Am. Chem. Soc.* **2009**, 131(29), 10113-26.
- (10) Balakrishnan, A. Ph.D. Thesis, Rutgers University, Newark, 2011.
- (11) Neue, G.; Dybowski, C. *Solid State Nucl. Magn. Reson.* **1997**, 7(4), 333-336.
- (12) Bennett, A. E.; Rienstra, C. M.; Auger, M.; Lakshmi, K. V.; Griffin, R. G. *J. Chem. Phys.* **1995**, 103(16), 6951-6958.
- (13) Arduengo, A. J.; Goerlich, J. R.; Marshall, W. J. *Liebigs Annalen* **1997**, 1997(2), 365-374.
- (14) Baburina, I.; Dikdan, G.; Guo, F.; Tous, G. I.; Root, B.; Jordan, F. *Biochemistry* **1998**, 37(5), 1245-55.
- (15) Baburina, I.; Gao, Y.; Hu, Z.; Jordan, F.; Hohmann, S.; Furey, W. *Biochemistry* **1994**, 33(18), 5630-5.
- (16) Baburina, I.; Li, H.; Bennion, B.; Furey, W.; Jordan, F. *Biochemistry* **1998**, 37(5), 1235-44.
- (17) Kutter, S.; Weiss, M. S.; Wille, G.; Golbik, R.; Spinka, M.; Konig, S. *J. Biol. Chem.* **2009**, 284(18), 12136-44.
- (18) Hubner, G.; Weidhase, R.; Schellenberger, A. *Eur. J. Biochem.* **1978**, 92(1), 175-81.
- (19) O'Brien, T. A.; Kluger, R.; Pike, D. C.; Gennis, R. B. *Biochem. Biophys. Acta* **1980**, 613(1), 10-7.
- (20) Kluger, R.; Pike, D. C. *J. Am. Chem. Soc.* **1977**, 99(13), 4504-6.
- (21) Nemeria, N. S.; Korotchkina, L. G.; Chakraborty, S.; Patel, M. S.; Jordan, F. *Bioorg. Chem.* **2006**, 34(6), 362-79.

- (22) Gallo, A. A.; Sable, H. Z. *J. Biol. Chem.* **1976**, *251*(9), 2564-70.
- (23) Lai, J.; Niks, D.; Wang, Y.; Domratcheva, T.; Barends, T. R. M.; Schwarz, F.; Olsen, R. A.; Elliott, D. W.; Fatmi, M. Q.; Chang, C.-e. A.; Schlichting, I.; Dunn, M. F.; Mueller, L. J. *J. Am. Chem. Soc.* **2010**, *133*(1), 4-7.
- (24) Sharif, S.; Fogle, E.; Toney, M. D.; Denisov, G. S.; Shenderovich, I. G.; Buntkowsky, G.; Tolstoy, P. M.; Huot, M. C.; Limbach, H. H. *J. Am. Chem. Soc.* **2007**, *129*(31), 9558-9.
- (25) Sharif, S.; Schagen, D.; Toney, M. D.; Limbach, H. H. *J. Am. Chem. Soc.* **2007**, *129*(14), 4440-55.
- (26) Sharif, S.; Denisov, G. S.; Toney, M. D.; Limbach, H. H. *J. Am. Chem. Soc.* **2007**, *129*(19), 6313-27.

APPENDIX

AMERICAN CHEMICAL SOCIETY LICENSE
TERMS AND CONDITIONS

May 16, 2011

This is a License Agreement between Sivakumar Paramasivam ("You") and American Chemical Society ("American Chemical Society") provided by Copyright Clearance Center ("CCC"). The license consists of your order details, the terms and conditions provided by American Chemical Society, and the payment terms and conditions.

All payments must be made in full to CCC. For payment instructions, please see information listed at the bottom of this form.

License Number	2653780354564
License Date	Apr 21, 2011
Licensed content publisher	American Chemical Society
Licensed content publication	Journal of the American Chemical Society
Licensed content title	Magic Angle Spinning Solid-State NMR Spectroscopy for Structural Studies of Protein Interfaces. Resonance Assignments of Differentially Enriched Escherichia coli Thioredoxin Reassembled by Fragment Complementation
Licensed content author	Dabeiba Marulanda et al.
Licensed content date	Dec 1, 2004
Volume number	126
Issue number	50
Type of Use	Thesis/Dissertation
Requestor type	Not specified
Format	Print
Portion	
Table/Figure/Micrograph	
Number of Table/Figure/Micrographs	1
Author of this ACS article	No
Order reference number	

Title of the thesis / dissertation	Insights into Structure, Dynamics of Thioredoxin Reassembly and Dynein Light Chain 8 and Ionization States of Thiamin Cofactor by MAS NMR Spectroscopy
Expected completion date	May 2011
Estimated size(pages)	250
Billing Type	Invoice
Billing Address	041 Brown Laboratory Chemistry and Biochemistry Department Newark, DE 19711 United States
Customer reference info	
Total	0.00 USD
Terms and Conditions	

Thesis/Dissertation

ACS / RIGHTS LINK TERMS & CONDITIONS THESIS/DISSERTATION

INTRODUCTION

The publisher for this copyrighted material is the American Chemical Society. By clicking "accept" in connection with completing this licensing transaction, you agree that the following terms and conditions apply to this transaction (along with the Billing and Payment terms and conditions established by Copyright Clearance Center, Inc. ("CCC"), at the time that you opened your Rightslink account and that are available at any time at <<http://myaccount.copyright.com>>).

LIMITED LICENSE

Publisher hereby grants to you a non-exclusive license to use this material. Licenses are for one-time use only with a maximum distribution equal to the number that you identified in the licensing process.

GEOGRAPHIC RIGHTS: SCOPE

Licenses may be exercised anywhere in the world.

RESERVATION OF RIGHTS

Publisher reserves all rights not specifically granted in the combination of (i) the license details provided by you and accepted in the course of this licensing transaction, (ii) these terms and conditions and (iii) CCC's Billing and Payment terms and conditions.

PORTION RIGHTS STATEMENT: DISCLAIMER

If you seek to reuse a portion from an ACS publication, it is your responsibility to examine each portion as published to determine whether a credit to, or copyright notice of, a third party owner was published adjacent to the item. You may only obtain permission via Rightslink to use material owned by ACS. Permission to use any material published in an ACS publication, journal, or article which is reprinted

with permission of a third party must be obtained from the third party owner. ACS disclaims any responsibility for any use you make of items owned by third parties without their permission.

REVOCATION

The American Chemical Society reserves the right to revoke a license for any reason, including but not limited to advertising and promotional uses of ACS content, third party usage, and incorrect figure source attribution.

LICENSE CONTINGENT ON PAYMENT

While you may exercise the rights licensed immediately upon issuance of the license at the end of the licensing process for the transaction, provided that you have disclosed complete and accurate details of your proposed use, no license is finally effective unless and until full payment is received from you (by CCC) as provided in CCC's Billing and Payment terms and conditions. If full payment is not received on a timely basis, then any license preliminarily granted shall be deemed automatically revoked and shall be void as if never granted. Further, in the event that you breach any of these terms and conditions or any of CCC's Billing and Payment terms and conditions, the license is automatically revoked and shall be void as if never granted. Use of materials as described in a revoked license, as well as any use of the materials beyond the scope of an unrevoked license, may constitute copyright infringement and publisher reserves the right to take any and all action to protect its copyright in the materials.

COPYRIGHT NOTICE: DISCLAIMER

You must include the following copyright and permission notice in connection with any reproduction of the licensed material: "Reprinted ("Adapted" or "in part") with permission from REFERENCE CITATION. Copyright YEAR American Chemical Society."

WARRANTIES: NONE

Publisher makes no representations or warranties with respect to the licensed material.

INDEMNITY

You hereby indemnify and agree to hold harmless publisher and CCC, and their respective officers, directors, employees and agents, from and against any and all claims arising out of your use of the licensed material other than as specifically authorized pursuant to this license.

NO TRANSFER OF LICENSE

This license is personal to you or your publisher and may not be sublicensed, assigned, or transferred by you to any other person without publisher's written permission.

NO AMENDMENT EXCEPT IN WRITING

This license may not be amended except in a writing signed by both parties (or, in the case of publisher, by CCC on publisher's behalf).

OBJECTION TO CONTRARY TERMS

Publisher hereby objects to any terms contained in any purchase order, acknowledgment, check endorsement or other writing prepared by you, which terms are inconsistent with these terms and conditions or CCC's Billing and Payment terms and conditions. These terms and conditions, together with CCC's Billing and Payment terms and conditions (which are incorporated herein), comprise the entire agreement between you and publisher (and CCC) concerning this licensing transaction. In the event of any conflict between your obligations established by these terms and conditions and those established by CCC's Billing and Payment terms and conditions, these terms and conditions shall control.

JURISDICTION

This license transaction shall be governed by and construed in accordance with the laws of the District

of Columbia. You hereby agree to submit to the jurisdiction of the courts located in the District of Columbia for purposes of resolving any disputes that may arise in connection with this licensing transaction.

THESES/DISSERTATION TERMS

Regarding your request for permission to include **your** paper(s) or portions of text from **your** paper(s) in your thesis/dissertation, permission is now automatically granted; please pay special attention to the **implications** paragraph below. The Copyright Subcommittee of the Joint Board/Council Committees on Publications approved the following:

Copyright permission for published and submitted material from theses and dissertations ACS extends blanket permission to students to include in their theses and dissertations their own articles, or portions thereof, that have been published in ACS journals or submitted to ACS journals for publication, provided that the ACS copyright credit line is noted on the appropriate page(s).

Publishing implications of electronic publication of theses and dissertation material

Students and their mentors should be aware that posting of theses and dissertation material on the Web prior to submission of material from that thesis or dissertation to an ACS journal may affect publication in that journal. Whether Web posting is considered prior publication may be evaluated on a case-by-case basis by the journal's editor. If an ACS journal editor considers Web posting to be "prior publication", the paper will not be accepted for publication in that journal. If you intend to submit your unpublished paper to ACS for publication, check with the appropriate editor prior to posting your manuscript electronically.

Reuse/Republication of the Entire Work in Theses or Collections: Authors may reuse all or part of the Submitted, Accepted or Published Work in a thesis or dissertation that the author writes and is required to submit to satisfy the criteria of degree-granting institutions. Such reuse is permitted subject to the ACS' "Ethical Guidelines to Publication of Chemical Research"

(<http://pubs.acs.org/page/policy/ethics/index.html>); the author should secure written confirmation (via letter or email) from the respective ACS journal editor(s) to avoid potential conflicts with journal prior publication*/embargo policies. Appropriate citation of the Published Work must be made. If the thesis or dissertation to be published is in electronic format, a direct link to the Published Work must also be included using the ACS Articles on Request author-directed link - see <http://pubs.acs.org/page/policy/articlesonrequest/index.html>

* Prior publication policies of ACS journals are posted on the ACS website at <http://pubs.acs.org/page/policy/prior/index.html>

If your paper has not yet been published by ACS, please print the following credit line on the first page of your article: "Reproduced (or 'Reproduced in part') with permission from [JOURNAL NAME], in press (or 'submitted for publication'). Unpublished work copyright [CURRENT YEAR] American Chemical Society." Include appropriate information.

If your paper has already been published by ACS and you want to include the text or portions of the text in your thesis/dissertation in **print or microfilm formats**, please print the ACS copyright credit line on the first page of your article: "Reproduced (or 'Reproduced in part') with permission from [FULL REFERENCE CITATION.] Copyright [YEAR] American Chemical Society." Include appropriate information.

Submission to a Dissertation Distributor: If you plan to submit your thesis to UMI or to another dissertation distributor, you should not include the unpublished ACS paper in your thesis if the thesis will be disseminated electronically, until ACS has published your paper. After publication of the paper by ACS, you may release the entire thesis (**not the individual ACS article by itself**) for electronic

dissemination through the distributor; ACS's copyright credit line should be printed on the first page of the ACS paper.

v1.2

Gratis licenses (referencing \$0 in the Total field) are free. Please retain this printable license for your reference. No payment is required.

IF YOU WOULD LIKE TO PAY FOR THIS LICENSE NOW, PLEASE REMIT THIS LICENSE ALONG WITH YOUR PAYMENT MADE PAYABLE TO "COPYRIGHT CLEARANCE CENTER" OTHERWISE YOU WILL BE INVOICED WITHIN 48 HOURS OF THE LICENSE DATE. PAYMENT SHOULD BE IN THE FORM OF A CHECK OR MONEY ORDER REFERENCING YOUR ACCOUNT NUMBER AND THIS INVOICE NUMBER RLNK10974279. ONCE YOU RECEIVE YOUR INVOICE FOR THIS ORDER, YOU MAY PAY YOUR INVOICE BY CREDIT CARD. PLEASE FOLLOW INSTRUCTIONS PROVIDED AT THAT TIME.

MAKE PAYMENT TO:
COPYRIGHT CLEARANCE CENTER
DEPT 001
P.O. BOX 843006
BOSTON, MA 02284-3006

FOR SUGGESTIONS OR COMMENTS REGARDING THIS ORDER, CONTACT RIGHTSLINK CUSTOMER SUPPORT: CUSTOMERCARE@COPYRIGHT.COM OR +1-877-622-5543 (TOLL FREE IN THE US) OR +1-978-646-2777

JOHN WILEY AND SONS LICENSE
TERMS AND CONDITIONS

May 16, 2011

This is a License Agreement between Sivakumar Paramasivam ("You") and John Wiley and Sons ("John Wiley and Sons") provided by Copyright Clearance Center ("CCC"). The license consists of your order details, the terms and conditions provided by John Wiley and Sons, and the payment terms and conditions.

All payments must be made in full to CCC. For payment instructions, please see information listed at the bottom of this form.

License Number	2630260952897
License date	Mar 15, 2011
Licensed content publisher	John Wiley and Sons
Licensed content publication	Magnetic Resonance in Chemistry
Licensed content title reassemblies	Magic angle spinning NMR spectroscopy of thioredoxin
Licensed content author	Jun Yang,Sivakumar Paramasivam,Dabeiba Marulanda,Marcela Cataldi,Maria Luisa Tasayco,Tatyana Polenova
Licensed content date	Dec 1, 2007
Start page	S73
End page	S83
Type of use	Dissertation/Thesis
Requestor type	Author of this Wiley article
Format	Print and electronic
Portion	Full article
Will you be translating?	No
Order reference number	
Total	0.00 USD

Terms and Conditions

TERMS AND CONDITIONS

This copyrighted material is owned by or exclusively licensed to John Wiley & Sons, Inc. or one of its

group companies (each a "Wiley Company") or a society for whom a Wiley Company has exclusive publishing rights in relation to a particular journal (collectively "WILEY"). By clicking "accept" in connection with completing this licensing transaction, you agree that the following terms and conditions apply to this transaction (along with the billing and payment terms and conditions established by the Copyright Clearance Center Inc., ("CCC's Billing and Payment terms and conditions"), at the time that you opened your Rightslink account (these are available at any time at <http://myaccount.copyright.com>)

Terms and Conditions

1. The materials you have requested permission to reproduce (the "Materials") are protected by copyright.
2. You are hereby granted a personal, non-exclusive, non-sublicensable, non-transferable, worldwide, limited license to reproduce the Materials for the purpose specified in the licensing process. This license is for a one-time use only with a maximum distribution equal to the number that you identified in the licensing process. Any form of republication granted by this licence must be completed within two years of the date of the grant of this licence (although copies prepared before may be distributed thereafter). The Materials shall not be used in any other manner or for any other purpose. Permission is granted subject to an appropriate acknowledgement given to the author, title of the material/book/journal and the publisher and on the understanding that nowhere in the text is a previously published source acknowledged for all or part of this Material. Any third party material is expressly excluded from this permission.
3. With respect to the Materials, all rights are reserved. Except as expressly granted by the terms of the license, no part of the Materials may be copied, modified, adapted (except for minor reformatting required by the new Publication), translated, reproduced, transferred or distributed, in any form or by any means, and no derivative works may be made based on the Materials without the prior permission of the respective copyright owner. You may not alter, remove or suppress in any manner any copyright, trademark or other notices displayed by the Materials. You may not license, rent, sell, loan, lease, pledge, offer as security, transfer or assign the Materials, or any of the rights granted to you hereunder to any other person.
4. The Materials and all of the intellectual property rights therein shall at all times remain the exclusive property of John Wiley & Sons Inc or one of its related companies (WILEY) or their respective licensors, and your interest therein is only that of having possession of and the right to reproduce the Materials pursuant to Section 2 herein during the continuance of this Agreement. You agree that you own no right, title or interest in or to the Materials or any of the intellectual property rights therein. You shall have no rights hereunder other than the license as provided for above in Section 2. No right, license or interest to any trademark, trade name, service mark or other branding ("Marks") of WILEY or its licensors is granted hereunder, and you agree that you shall not assert any such right, license or interest with respect thereto.
5. NEITHER WILEY NOR ITS LICENSORS MAKES ANY WARRANTY OR REPRESENTATION OF ANY KIND TO YOU OR ANY THIRD PARTY, EXPRESS, IMPLIED OR STATUTORY, WITH RESPECT TO THE MATERIALS OR THE ACCURACY OF ANY INFORMATION CONTAINED IN THE MATERIALS, INCLUDING, WITHOUT LIMITATION, ANY IMPLIED WARRANTY OF MERCHANTABILITY, ACCURACY, SATISFACTORY QUALITY, FITNESS FOR A PARTICULAR PURPOSE, USABILITY, INTEGRATION OR NON-INFRINGEMENT AND ALL SUCH WARRANTIES ARE HEREBY EXCLUDED BY WILEY AND ITS LICENSORS AND WAIVED BY YOU.

6. WILEY shall have the right to terminate this Agreement immediately upon breach of this Agreement by you.

7. You shall indemnify, defend and hold harmless WILEY, its Licensors and their respective directors, officers, agents and employees, from and against any actual or threatened claims, demands, causes of action or proceedings arising from any breach of this Agreement by you.

8. IN NO EVENT SHALL WILEY OR ITS LICENSORS BE LIABLE TO YOU OR ANY OTHER PARTY OR ANY OTHER PERSON OR ENTITY FOR ANY SPECIAL, CONSEQUENTIAL, INCIDENTAL, INDIRECT, EXEMPLARY OR PUNITIVE DAMAGES, HOWEVER CAUSED, ARISING OUT OF OR IN CONNECTION WITH THE DOWNLOADING, PROVISIONING, VIEWING OR USE OF THE MATERIALS REGARDLESS OF THE FORM OF ACTION, WHETHER FOR BREACH OF CONTRACT, BREACH OF WARRANTY, TORT, NEGLIGENCE, INFRINGEMENT OR OTHERWISE (INCLUDING, WITHOUT LIMITATION, DAMAGES BASED ON LOSS OF PROFITS, DATA, FILES, USE, BUSINESS OPPORTUNITY OR CLAIMS OF THIRD PARTIES), AND WHETHER OR NOT THE PARTY HAS BEEN ADVISED OF THE POSSIBILITY OF SUCH DAMAGES. THIS LIMITATION SHALL APPLY NOTWITHSTANDING ANY FAILURE OF ESSENTIAL PURPOSE OF ANY LIMITED REMEDY PROVIDED HEREIN.

9. Should any provision of this Agreement be held by a court of competent jurisdiction to be illegal, invalid, or unenforceable, that provision shall be deemed amended to achieve as nearly as possible the same economic effect as the original provision, and the legality, validity and enforceability of the remaining provisions of this Agreement shall not be affected or impaired thereby.

10. The failure of either party to enforce any term or condition of this Agreement shall not constitute a waiver of either party's right to enforce each and every term and condition of this Agreement. No breach under this agreement shall be deemed waived or excused by either party unless such waiver or consent is in writing signed by the party granting such waiver or consent. The waiver by or consent of a party to a breach of any provision of this Agreement shall not operate or be construed as a waiver of or consent to any other or subsequent breach by such other party.

11. This Agreement may not be assigned (including by operation of law or otherwise) by you without WILEY's prior written consent.

12. Any fee required for this permission shall be non-refundable after thirty (30) days from receipt.

13. These terms and conditions together with CCC's Billing and Payment terms and conditions (which are incorporated herein) form the entire agreement between you and WILEY concerning this licensing transaction and (in the absence of fraud) supersedes all prior agreements and representations of the parties, oral or written. This Agreement may not be amended except in writing signed by both parties. This Agreement shall be binding upon and inure to the benefit of the parties' successors, legal representatives, and authorized assigns.

14. In the event of any conflict between your obligations established by these terms and conditions and those established by CCC's Billing and Payment terms and conditions, these terms and conditions shall prevail.

15. WILEY expressly reserves all rights not specifically granted in the combination of (i) the license details provided by you and accepted in the course of this licensing transaction, (ii) these terms and conditions and (iii) CCC's Billing and Payment terms and conditions.

16. This Agreement will be void if the Type of Use, Format, Circulation, or Requestor Type was misrepresented during the licensing process.

17. This Agreement shall be governed by and construed in accordance with the laws of the State of New York, USA, without regards to such state's conflict of law rules. Any legal action, suit or proceeding arising out of or relating to these Terms and Conditions or the breach thereof shall be instituted in a court of competent jurisdiction in New York County in the State of New York in the United States of America and each party hereby consents and submits to the personal jurisdiction of such court, waives any objection to venue in such court and consents to service of process by registered or certified mail, return receipt requested, at the last known address of such party. . BY CLICKING ON THE "I ACCEPT" BUTTON, YOU ACKNOWLEDGE THAT YOU HAVE READ AND FULLY UNDERSTAND EACH OF THE SECTIONS OF AND PROVISIONS SET FORTH IN THIS AGREEMENT AND THAT YOU ARE IN AGREEMENT WITH AND ARE WILLING TO ACCEPT ALL OF YOUR OBLIGATIONS AS SET FORTH IN THIS AGREEMENT.

v1.4

Gratis licenses (referencing \$0 in the Total field) are free. Please retain this printable license for your reference. No payment is required.

If you would like to pay for this license now, please remit this license along with your payment made payable to "COPYRIGHT CLEARANCE CENTER" otherwise you will be invoiced within 48 hours of the license date. Payment should be in the form of a check or money order referencing your account number and this invoice number RLNK10950123.

Once you receive your invoice for this order, you may pay your invoice by credit card. Please follow instructions provided at that time.

Make Payment To:
Copyright Clearance Center
Dept 001
P.O. Box 843006
Boston, MA 02284-3006

For suggestions or comments regarding this order, contact Rightslink Customer Support: customercare@copyright.com or +1-877-622-5543 (toll free in the US) or +1-978-646-2777.

AMERICAN CHEMICAL SOCIETY LICENSE
TERMS AND CONDITIONS

May 16, 2011

This is a License Agreement between Sivakumar Paramasivam ("You") and American Chemical Society ("American Chemical Society") provided by Copyright Clearance Center ("CCC"). The license consists of your order details, the terms and conditions provided by American Chemical Society, and the payment terms and conditions.

All payments must be made in full to CCC. For payment instructions, please see information listed at the bottom of this form.

License Number	2630251034540
License Date	Mar 15, 2011
Licensed content publisher	American Chemical Society
Licensed content publication	The Journal of Physical Chemistry B
Licensed content title	Solid-State NMR and Density Functional Theory Studies of Ionization States of Thiamin
Licensed content author	Sivakumar Paramasivam et al.
Licensed content date	Feb 1, 2011
Volume number	115
Issue number	4
Type of Use	Thesis/Dissertation
Requestor type	Not specified
Format	Print
Portion	Full article
Author of this ACS article	Yes
Order reference number	
Title of the thesis / dissertation	Insights into Structure, Dynamics of Thioredoxin Reassembly and Dynein Light Chain 8 and Ionization States of Thiamin Cofactor by MAS NMR Spectroscopy
Expected completion date	May 2011
Estimated size(pages)	250

Billing Type	Invoice
Billing Address	041 Brown Laboratory Chemistry and Biochemistry Department Newark, DE 19711 United States

Customer reference info

Total	0.00 USD
-------	----------

Terms and Conditions

Thesis/Dissertation

ACS / RIGHTSLINK TERMS & CONDITIONS THESIS/DISSERTATION

INTRODUCTION

The publisher for this copyrighted material is the American Chemical Society. By clicking "accept" in connection with completing this licensing transaction, you agree that the following terms and conditions apply to this transaction (along with the Billing and Payment terms and conditions established by Copyright Clearance Center, Inc. ("CCC"), at the time that you opened your Rightslink account and that are available at any time at <<http://myaccount.copyright.com>>).

LIMITED LICENSE

Publisher hereby grants to you a non-exclusive license to use this material. Licenses are for one-time use only with a maximum distribution equal to the number that you identified in the licensing process.

GEOGRAPHIC RIGHTS: SCOPE

Licenses may be exercised anywhere in the world.

RESERVATION OF RIGHTS

Publisher reserves all rights not specifically granted in the combination of (i) the license details provided by you and accepted in the course of this licensing transaction, (ii) these terms and conditions and (iii) CCC's Billing and Payment terms and conditions.

PORTION RIGHTS STATEMENT: DISCLAIMER

If you seek to reuse a portion from an ACS publication, it is your responsibility to examine each portion as published to determine whether a credit to, or copyright notice of, a third party owner was published adjacent to the item. You may only obtain permission via Rightslink to use material owned by ACS. Permission to use any material published in an ACS publication, journal, or article which is reprinted with permission of a third party must be obtained from the third party owner. ACS disclaims any responsibility for any use you make of items owned by third parties without their permission.

REVOCATION

The American Chemical Society reserves the right to revoke a license for any reason, including but not limited to advertising and promotional uses of ACS content, third party usage, and incorrect figure source attribution.

LICENSE CONTINGENT ON PAYMENT

While you may exercise the rights licensed immediately upon issuance of the license at the end of the licensing process for the transaction, provided that you have disclosed complete and accurate details of your proposed use, no license is finally effective unless and until full payment is received from you (by CCC) as provided in CCC's Billing and Payment terms and conditions. If full payment is not received on a timely basis, then any license preliminarily granted shall be deemed automatically revoked and shall be void as if never granted. Further, in the event that you breach any of these terms and conditions or any of CCC's Billing and Payment terms and conditions, the license is automatically revoked and shall be void as if never granted. Use of materials as described in a revoked license, as well as any use of the materials beyond the scope of an unrevoked license, may constitute copyright infringement and publisher reserves the right to take any and all action to protect its copyright in the materials.

COPYRIGHT NOTICE: DISCLAIMER

You must include the following copyright and permission notice in connection with any reproduction of the licensed material: "Reprinted ("Adapted" or "in part") with permission from REFERENCE CITATION. Copyright YEAR American Chemical Society."

WARRANTIES: NONE

Publisher makes no representations or warranties with respect to the licensed material.

INDEMNITY

You hereby indemnify and agree to hold harmless publisher and CCC, and their respective officers, directors, employees and agents, from and against any and all claims arising out of your use of the licensed material other than as specifically authorized pursuant to this license.

NO TRANSFER OF LICENSE

This license is personal to you or your publisher and may not be sublicensed, assigned, or transferred by you to any other person without publisher's written permission.

NO AMENDMENT EXCEPT IN WRITING

This license may not be amended except in a writing signed by both parties (or, in the case of publisher, by CCC on publisher's behalf).

OBJECTION TO CONTRARY TERMS

Publisher hereby objects to any terms contained in any purchase order, acknowledgment, check endorsement or other writing prepared by you, which terms are inconsistent with these terms and conditions or CCC's Billing and Payment terms and conditions. These terms and conditions, together with CCC's Billing and Payment terms and conditions (which are incorporated herein), comprise the entire agreement between you and publisher (and CCC) concerning this licensing transaction. In the event of any conflict between your obligations established by these terms and conditions and those established by CCC's Billing and Payment terms and conditions, these terms and conditions shall control.

JURISDICTION

This license transaction shall be governed by and construed in accordance with the laws of the District of Columbia. You hereby agree to submit to the jurisdiction of the courts located in the District of Columbia for purposes of resolving any disputes that may arise in connection with this licensing transaction.

THESES/DISSERTATION TERMS

Regarding your request for permission to include **your** paper(s) or portions of text from **your** paper(s) in your thesis/dissertation, permission is now automatically granted; please pay special attention to the

implications paragraph below. The Copyright Subcommittee of the Joint Board/Council Committees on Publications approved the following:

Copyright permission for published and submitted material from theses and dissertations ACS extends blanket permission to students to include in their theses and dissertations their own articles, or portions thereof, that have been published in ACS journals or submitted to ACS journals for publication, provided that the ACS copyright credit line is noted on the appropriate page(s).

Publishing implications of electronic publication of theses and dissertation material

Students and their mentors should be aware that posting of theses and dissertation material on the Web prior to submission of material from that thesis or dissertation to an ACS journal may affect publication in that journal. Whether Web posting is considered prior publication may be evaluated on a case-by-case basis by the journal's editor. If an ACS journal editor considers Web posting to be "prior publication", the paper will not be accepted for publication in that journal. If you intend to submit your unpublished paper to ACS for publication, check with the appropriate editor prior to posting your manuscript electronically.

Reuse/Republication of the Entire Work in Theses or Collections: Authors may reuse all or part of the Submitted, Accepted or Published Work in a thesis or dissertation that the author writes and is required to submit to satisfy the criteria of degree-granting institutions. Such reuse is permitted subject to the ACS' "Ethical Guidelines to Publication of Chemical Research" (<http://pubs.acs.org/page/policy/ethics/index.html>); the author should secure written confirmation (via letter or email) from the respective ACS journal editor(s) to avoid potential conflicts with journal prior publication*/embargo policies. Appropriate citation of the Published Work must be made. If the thesis or dissertation to be published is in electronic format, a direct link to the Published Work must also be included using the ACS Articles on Request author-directed link - see <http://pubs.acs.org/page/policy/articlesonrequest/index.html>

* Prior publication policies of ACS journals are posted on the ACS website at <http://pubs.acs.org/page/policy/prior/index.html>

If your paper has not yet been published by ACS, please print the following credit line on the first page of your article: "Reproduced (or 'Reproduced in part') with permission from [JOURNAL NAME], in press (or 'submitted for publication'). Unpublished work copyright [CURRENT YEAR] American Chemical Society." Include appropriate information.

If your paper has already been published by ACS and you want to include the text or portions of the text in your thesis/dissertation in **print or microfilm formats**, please print the ACS copyright credit line on the first page of your article: "Reproduced (or 'Reproduced in part') with permission from [FULL REFERENCE CITATION.] Copyright [YEAR] American Chemical Society." Include appropriate information.

Submission to a Dissertation Distributor: If you plan to submit your thesis to UMI or to another dissertation distributor, you should not include the unpublished ACS paper in your thesis if the thesis will be disseminated electronically, until ACS has published your paper. After publication of the paper by ACS, you may release the entire thesis (**not the individual ACS article by itself**) for electronic dissemination through the distributor; ACS's copyright credit line should be printed on the first page of the ACS paper.

v1.2

Gratis licenses (referencing \$0 in the Total field) are free. Please retain this printable license for your reference. No payment is required.

If you would like to pay for this license now, please remit this license along with your payment made payable to "COPYRIGHT CLEARANCE CENTER" otherwise you will be invoiced within 48 hours of the license date. Payment should be in the form of a check or money order referencing your account number and this invoice number RLNK10950091.

Once you receive your invoice for this order, you may pay your invoice by credit card. Please follow instructions provided at that time.

**Make Payment To:
Copyright Clearance Center
Dept 001
P.O. Box 843006
Boston, MA 02284-3006**

For suggestions or comments regarding this order, contact Rightslink Customer Support: customercare@copyright.com or +1-877-622-5543 (toll free in the US) or +1-978-646-2777.